THE PETROLOGY, MINERALOGY AND GEOCHEMISTRY OF THE MAIN ZONE OF THE BUSHVELD COMPLEX AT RUSTENBURG PLATINUM MINES, UNION SECTION.

by

ANDREW ALEXANDER MITCHELL
B.Sc. (Hons), M.Sc. (Rhodes)

Thesis submitted in fulfillment of the requirements for the degree of

Doctor of Philosophy

In the Department of Geology,
Rhodes University,
Grahamstown.

DECLARATION

All work in this thesis is the original work of the author, except where specific acknowledgement is made to the work of others.

SIGNED: 

A A Mitchell
Department of Geology
Rhodes University
Grahamstown

December, 1986

ABSTRACT

Union Section of Rustenburg Patinum Mines is situated in the northwestern part of the Bushveld Complex, some twenty kilometres north of the Pilanesberg Alkaline Complex. The mining lease area covers a roughly triangular segment of Lower, Critical and Main Zone rocks, transgressed to the north and south by magnetite-bearing ferrogabbro of the Upper Zone. The Main Zone at Union Section is the focus of this study. The prime source of sample material for the study is the deep exploration borehole SK2, but additional, supplementary samples were collected on surface and underground, as well as from a second surface exploration borehole, SK4.

In line with the recommendations of SACS (1980), the top of the Critical Zone, and therefore the base of the Main Zone, is taken to be the top of the Bastard Cyclic Unit. Sharpe (1985) suggested that the succession from the base of the Main Zone up to the Pyroxenite Marker is an isotopically separate entity from the rest of the Bushveld layered succession. This is not strictly true, as there is evidence that more than one parental magma was involved in the formation of this interval. It is, however, true that there are fundamental differences, particularly in isotopic makeup, between the Main Zone rocks below the Pyroxenite Marker and those above (the latter having been assigned by Molyneux (1970) to subzone C of the Main Zone).

Kruger et al. (1986, in press) suggested that the Pyroxenite Marker marks the base of the Upper Zone, and this convention is adhered to here. The implication of this is that the rocks which formerly constituted subzone C of the Main Zone are now considered part of the Upper Zone. The Main Zone rocks below the Pyroxenite Marker were originally subdivided by Molyneux (1970) into two subzones, A and B. The results of the present study indicate that this subdivision is not justified. Instead, eight units have been distinguished in the Main Zone on geochemical, petrological and mineralogical bases. Each of these units is characterized by a coherent set, or progression, of chemical and petrological characteristics. The specific assignment of genetic connotations to these units has been deliberately avoided, at least until further studies of the Main Zone prove this to be justified. The demarcation of the eight units is illustrated in the composite diagram (Fig. 34) in the back pocket of this work, and the reasons for the subdivisions are listed in Table 6 (at the end of

chapter 7 of this thesis).

Until the late 1970's, it was thought that most layered cumulates formed by crystal settling (Wager and Brown, 1968). More recently, there has been a fundamental conceptual change, and many workers now believe that most cumulate rocks formed by **in situ** crystallization at the floor and walls of the magma chamber (McBirney and Noyes, 1979, Irvine, 1980a; Campbell, 1987). There is, however, some evidence for the physical separation of phases undergoing cotectic crystallization, particularly in the Upper Critical Zone and lower part of the Main Zone (Eales et al., 1986). This process, which has been alluded to in the past by various authors (Ferguson and Botha, 1963; Vermaak, 1976) involves the flotation of early-formed plagioclase crystals due to their positive bouyancy in tholeiitic liquids. The result is an apparent decoupling of the chemistry of pyroxene and plagioclase, as in unit IV of the Main Zone, where plagioclase becomes more anorthitic upwards, whilst pyroxene becomes more iron-rich.

There is some substantial evidence, particularly in reversals in the strontium isotope initial ratio and the orthopyroxene Mg/(Mg+Fe) ratio, for multiple intrusion in the Main Zone. Although the largest and most important magma influx in the Main Zone was a high-R_o aluminous tholeiite, as suggested by Sharpe (1985), the intrusive history of the Main Zone is believed to be far more complex than Sharpe (op. cit.) suggested. Significantly, there is strong evidence for small influxes of Upper Zone-type (Fe-rich tholeiite) magma in the upper reaches of the Main Zone. These are believed to be precursors to the major influx of Upper Zone-type magma at the Pyroxenite Marker (Kruger et al, 1986, in press).

The fate of intercumulus liquids in cumulate rocks has recently recieved substantial attention (Sparks et al., 1985; Morse, 1986; Barnes, 1986: Campbell, 1987). It is believed that the migration, or at least redistribution, of intercumulus liquids has played a vital role in modifying fractionation trends in the Main Zone. More importantly, the accumulation of late-stage intercumulus liquids is believed to be responsible for the formation of the Fe-rich ultramafic pegmatite bodies that interrupt the layered cumulates in borehole SK2.

CONTENTS

1. INTRODUCTION

1.1 Contextual Overview

With an areal extent of some 65 000 km^2, the Bushveld Complex of the Transvaal may justifiably be regarded as "the largest repository of magmatic ore deposits in the world" (Willemse, 1969). The Complex, comprising an acid phase of granites and granophyres and a mafic phase of layered plutonic rocks, is intrusive through the basement of the Kaapvaal craton into the sediments and volcanics of the Transvaal Supergroup. The mafic phase of the Complex, referred to as the Rustenburg Layered Suite by the South African Committee on Stratigraphy (SACS, 1980), has in the past been subdivided according to a zonal scheme of classification (Wager and Brown, 1968, and others). Although SACS recommend the more formal subdivision of the layered suite into units of formation status, the zonal classification is retained in this work, principally in the interests of a less ambiguous correlation and comparison with previous work on the Complex. In addition, capitals are used for the names of zones and stratigraphic markers, in the interests of clarity, although this runs contrary to the SACS recommendations.

Rustenburg Platinum Mines, Union Section is situated in the northwestern part of the Rustenburg Layered Suite (Fig. 1), 18km west of the town of Northam and 20km north of the Pilanesberg Alkaline Complex (south 24° 56'; east 27° 09'). The mining lease area covers a roughly triangular segment of Lower, Critical and Main Zone rocks, transgressed to the north and south by Upper Zone ferrogabbros, these latter being referred to as the Northern and Southern Gap Areas, respectively (Viljoen and Feuchtwanger, 1977).

This study is concerned with the mineralogy, petrology and geochemistry of the Main Zone at Union Section, and deals specifically with the interval between the Bastard Reef and the stratigraphic horizon that is referred to in the eastern part of the Complex as the "Pyroxenite Marker" (Marais,1977). It would appear, from field work by the author, that the Pyroxenite Marker, as such, is not present at Union Section, but the equivalent horizon is marked by very distinct inflections in geochemical trends, similar to those documented by Marais (1977).

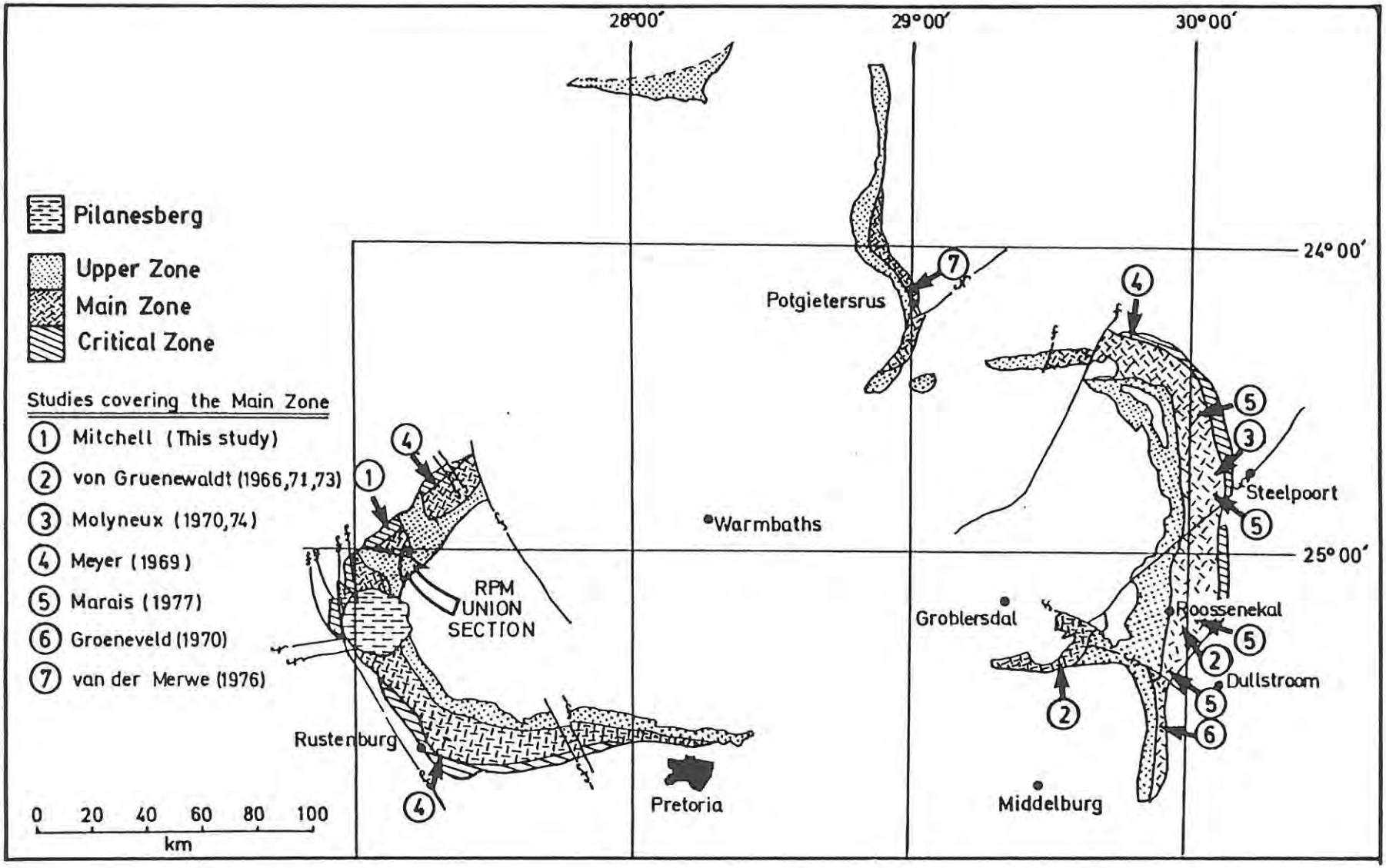

Fig. 1: Sketch map of the Critical, Main and Upper Zones of the Bushveld Complex, showing the localities at which some of the more important studies on the Main Zone have been carried out.

1.2 Previous work on the Main Zone

This section is a review of the more important studies dealing with the Main Zone over the past 56 years. The locality map (Fig. 1) gives an indication of the areas covered by the more significant studies dealing with the Main Zone to date. Stratigraphic subdivisions and marker horizons used in the more important studies on the Main Zone are summarized in Fig. 9 (Section 2.2 of this work).

In two of the earliest reviews of work on the Bushveld Complex, Daly (1928) and Hall (1932) both regarded the Main Zone as by far the thickest of what Hall referred to as the "Main Plutonic Phase" of the Complex. On the basis of Hall's (1932) model, the Main Zone is of the order of 3050 metres thick, and extends from the top of the Critical Zone to the uppermost of the magnetite bands. This leaves an Upper Zone, according to Hall, which consists of 244 metres of bronzite-norites and syenitic rocks, the latter immediately underlying the roof rocks of the Complex. Hall noted that the norites in the lower part of the Main Zone gave rise to a pronounced positive topography, characterized in the eastern part of the Complex (Sekhukhuneland) by the Lulu mountains, and in the area north of Pretoria by the distinctive "pyramid" hills. Hall (op. cit.) subscribed to a mechanism of **in situ** differentiation, primarily, but not entirely, under the influence of gravity, to explain the layering in the Complex. Hall did, however, allude to the possibility that there was a fresh influx of magma at the base of the Main Zone, i.e. just above the Merensky Reef.

B.V. Lombaard (1934) collected samples along traverses across the Complex near Britz and in the vicinity of Lydenburg, covering the interval between the Merensky Reef and the Pyroxenite Marker. Lombaard found that pyroxenitic horizons, such as the Merensky Reef and the Pyroxenite Marker, represent maxima in terms of the pyroxene ratio (opx/(opx+cpx)). On the assumption that the pyroxene ratio can be used directly as an index of fractionation, Lombaard concluded that pyroxenite layers are indicators of new magma influxes.

The Main Zone rocks of the "pyramid" hills in the vicinity of Bon Accord dam, north of Pretoria, were studied by Nel (1940) and van den Berg (1946). Nel's work included some petrological and chemical data,

but inadequate stratigraphic control on sampling renders these data of little value for purposes of comparison with the current study. Van den Berg (op. cit.) undertook a petrofabric analysis of the Main Zone rocks in the Bon Accord area, and noted the optically uniform orientation of orthopyroxene over large areas of gabbro. Both Nel (1940) and van den Berg (1946) classified the Main Zone rocks as gabbros, which contrasts with Hall's (1932) earlier classification of rocks in this interval as norites. In a subsequent study of the Main Zone at Bon Accord, Raal (1965) classified the rocks at the base of the Main Zone as hyperites, containing 50% to 75% hypersthene. Raal's (op. cit.) data suggest that the proportion of plagioclase in the rocks increases steadily upwards through the Main Zone, culminating in an anorthosite layer immediately below the Lower Main Magnetite Band. Raal regarded the Main Magnetite Band as the base of the Upper Zone.

A.F. Lombaard (1949) mapped an area of the Bushveld in the vicinity of Blood River, in the eastern Transvaal. The area mapped includes Critical, Main and Upper Zone lithologies. Within the Main Zone, Lombaard noted the presence of what he termed "gabbro met sferiese struktuur" (gabbro with spherical structure). This rock type is characterized by conspicuous spheroids of mafic minerals, of the order of 40mm in diameter, set in a matrix of spotted leucogabbro. The spheroids consist primarily of altered orthopyroxene, but also contain minor amounts of amphibole, plagioclase, biotite and clinopyroxene. Although Lombaard (1949) was unable to offer an explanation for the origin of the spheroids, his observation was that they occur in bands which are conformable with the gross layering of the Complex. This observation is disputed by more recent workers (Lee and Sharpe, 1979), who regard the spheroids as contact phenomena, not controlled by the igneous layering.

In a palaeomagnetic study on suites of Main Zone gabbro samples from Rustenburg, Britz, Bon Accord and Roossenekal, Gough and van Niekerk (1959) deduced that the Main Zone was emplaced in a horizontal plane. According to Gough and van Niekerk, the characteristic basinward dip of the igneous layering was imposed tectonically, subsequent to crystallization of the rocks.

Ferguson and Botha (1963) investigated the igneous layering in the mafic phase of the Complex, including the fine-scale rhythmic layering

of the Main Zone at Bon Accord and in the Olifants river valley. The rocks referred to by Ferguson and Botha as the Main Zone are the gabbros of the pyramid hills, in which they recognized rhythmic layering on a scale as fine as 2cm. Ferguson and Botha ascribed the fine-scale layering to a process involving combined undercooling and convective overturn of a metastable upper crystallizing layer in the magma chamber. Currents moving along the floor of the chamber were invoked by Ferguson and Botha as the cause of the parallel alignment of orthopyroxene and plagioclase grains in the rocks. The random orientation of clinopyroxene, by contrast, was ascribed to its interstitial nature.

The western lobe of the Bushveld Complex was investigated and mapped by F.J. Coertze (1958, 1960, 1970, 1974) and Coertze and Schumann (1962). In 1958, Coertze first advanced his concept of multiple intrusion, which was to become the central theme of his later work on the Complex. Coertze's concept of multiple intrusion was rather extreme, in that he regarded each separate rock-type as having originated by the sill-like intrusion of a discrete batch of magma of the appropriate composition.

Coertze (1974) subdivided the Rustenburg Layered Suite into eight units, according to dominant rock types. From the base up, these are: the quartz norite sub-unit; the marginal norite sub-unit; the harzburgite unit; the pyroxenite unit; the anorthosite unit; the norite unit; the porphyritic pyroxenite unit; the gabbro unit; and the ferrogabbro unit. Coertze's gabbro unit corresponds closely with the interval which Molyneux (1970) called the Main Zone. Coertze (1974) observed that the base of the gabbro unit (i.e. the Main Zone) is noritic, grading upwards into hyperite (gabbronorite). Coertze (op. cit.) identified anorthosite layers at intervals in the gabbro unit, particularly at approximately 800m above the Merensky Reef.

In one of his earlier publications, Coertze (1960) interpreted a layer of magnetite-bearing anorthosite in the Main Zone south of Pilanesberg as having been emplaced along a shear zone. Cousins (1960) disputed this interpretation, on the basis that anorthosite occurs at the equivalent position in the Main Zone throughout the Complex. On these grounds, Cousins (op. cit.) suggested that anorthosite layers in the Main Zone are concordant with the overall layering, rather than being discordant, later intrusions. The anorthosite layer described by

Coertze (1960) is of interest in that it contains magnetite and sulphides, and is intruded by what Coertze (op. cit.) referred to as dunite pipes. Recent work by Viljoen and Burvenich (1983) indicates that iron-rich ultramafic pegmatite bodies are common in the Main and Upper Mottled Anorthosite layers of the Main Zone, where they give rise to pronounced linear magnetic anomalies.

Throughout all his work, Coertze emphasized the presence of disconformities in the layered succession of the Bushveld, and ascribed them to new influxes of magma. The most obvious of these disconformities are the northern and southern "gap" areas flanking the Union Section segment, in which Upper Zone ferrogabbro transgresses across the Critical and Main Zones. On a smaller scale, Coertze also attributed variations in the stratigraphic sequence along strike, particularly in the Upper Critical Zone, to disconformities associated with influxes of new magma.

Von Gruenewaldt (1966) mapped an area in the vicinity of Groblersdal, in the eastern Bushveld. This locality includes a portion of the Main Zone, in which von Gruenewaldt described an horizon of spherical pyroxenite aggregates, of the type first described by Lombaard (1949). This distinctive lithology von Gruenewaldt referred to as the "Tennis Ball Marker".

Meyer (1969) undertook a petrographic study of the Main Zone at R.P.M. Rustenburg Section, based on borehole core sampling. Included in his study, for comparative purposes, were somewhat shorter intersections of the Main Zone at R.P.M. Atok and Amandelbult sections. Meyer was concerned primarily with the petrographic textures in the Main Zone, to the detriment, as Vermaak (1976) puts it, of "a more intimate regard for the gross layering" of the Main Zone rocks. Meyer's work is nevertheless valuable, in that his thorough petrographic logging of the Rustenburg borehole cores allows for detailed comparison and correlation with the Main Zone at Union Section and elsewhere.

In reviewing the literature on the Bushveld Complex, Wager and Brown (1968) experienced some difficulty in finding consensus on the location of zone boundaries within the layered suite. In an attempt to introduce some conformity to the zonal nomenclature, Wager and Brown started from the premise that the layered suite can be divided,

broadly, into two stages. The first stage, which Wager and Brown called the "integration" stage, was thought to have been characterized by periodic influxes of new magma to the chamber. The top of the Critical Zone was regarded as the end of the integration phase. The second phase, incorporating the Main and Upper Zones, was regarded by Wager and Brown as being an extended period of uninterrupted crystal fractionation from a basaltic magma, with no fresh influxes. Wager and Brown placed the Critical Zone / Main Zone boundary at the top of what they referred to as the Bastard-Merensky-Macro-Rhythmic Unit. The top of the Main Zone was regarded by these authors as being immediately below the first of the magnetite layers in the layered succession. The Main Zone has an estimated thickness, according to Wager and Brown, (1968), of approximately 5180 metres in the eastern Transvaal, and 3050 metres in the Rustenburg area.

Wager and Brown (1968) drew attention to the fact that there are transgressions at both the base and the top of the Main Zone in various parts of the Complex. Willemse (1964) described the transgression of the Critical Zone by the Main Zone in the Potgietersrus limb, whilst the clearly evident transgression of the Main Zone by the Upper Zone in the gap areas of the northwestern Bushveld was noted by Coertze (1958). By contrast with Coertze (1958), Wager and Brown (1968) did not regard these transgressions as evidence of new influxes of magma.

The Main Zone in the Stoffberg area of the southeastern Bushveld was investigated by Groeneveld (1970). The Critical Zone is not present in this part of the Complex, with the result that the Main Zone rests directly on Pretoria Group sediments. Approximately 600m above the base of the Main Zone, Groeneveld mapped a 70 metre thick layer of anorthosite. Groeneveld noted small, but significant, amounts of biotite, amphibole and magnetite for some 200m above the anorthosite layer. From 1370m to 1710m above the base of the Main Zone, Groeneveld found magnetite in the gabbro. In the northern part of the area mapped by Groeneveld (1970), the magnetite is intercumulus, but further south it manifests itself as fine rodlets within plagioclase grains, imparting a dark grey overall colour to the rocks. Marais (1977) correlated the magnetite-bearing gabbros mapped by Groeneveld (1970) with the magnetite gabbronorites which underly the Pyroxenite Marker at Tonteldoos, Roossenekal and Steelpoortpark.

Molyneux (1970) mapped the Main and Upper Zones, as well as the roof rocks of the Complex, in the vicinity of Steelpoort in the Eastern Transvaal. Molyneux's estimate of the thickness of the Main Zone in this part of the Complex is 2860m, compared with 1790m for the Upper Zone. Molyneux (1970) instituted the threefold subdivision of the Main Zone into Subzones A, B and C, a system which is now well entrenched in the literature of the Bushveld Complex. Subzone A, the lowermost of the three subzones, covers the interval from the base of the Merensky Reef to the top of the Upper Mottled Anorthosite, a vertical interval of some 1200m. Within Subzone A, at a height of approximately 600m above the Merensky Reef, is the Main Mottled Anorthosite. Between the Main and Upper Mottled Anorthosite layers, Molyneux (1970) mapped numerous magnetite-bearing pegmatite stringers and magnetite plugs. The presence of magnetite plugs in this part of the succession was also noted by Willemse (1969). Groeneveld's (1970) work south of Steelpoort indicated the presence, if not of ultramafic pegmatite, then at least of magnetite and hydrous minerals, at a similar level in the sequence. Subzone B of the Main Zone consists of approximately 1000m of relatively uniform gabbroic rocks. Although Subzone B is devoid of identifiable stratigraphic markers, Molyneux divided it into six "sheets", each between 100m and 200m thick, on the basis of differential erosion effects. Cumulus magnetite and/or magnetite plugs occur sporadically in the uppermost of these six sheets.

Subzone C, the third and uppermost subzone, starts with the Pyroxenite Marker, which is represented in the Steelpoort area by a 2m thick layer of pyroxenite. Above the Pyroxenite Marker, Subzone C progresses through approximately 600m of equigranular to porphyritic gabbro, interspersed with occasional anorthosite layers. The top of Subzone C, and thus of the Main Zone, was placed by Molyneux at the base of a magnetite anorthosite layer, thirty metres below the lowermost magnetite seam of the Upper Zone. This contrasts with Willemse's (1969) designation of the Main Magnetite as the base of the Upper Zone. In a fairly brief treatment of the mineralogy of the Main Zone, Molyneux (1970) described the primary phase change from hypersthene to pigeonite, which takes place in Subzone B at a composition of Fs_{31}. Higher up in the Main Zone, primary hypersthene reappears at the Pyroxenite Marker, with a composition of Fs_{24}. Molyneux's plagioclase analyses show a gradual change from An_{70} in the Merensky Reef to An_{64} below the Pyroxenite Marker. This is followed by a reversion, in the

Pyroxenite Marker, to a composition of An_{67}, and then a gradual decrease to An_{60} at the top of Subzone C. Molyneux's later (1974) work is essentially a synopsis of his original (1970) research.

In mapping the area around Roossenekal in the eastern Bushveld, von Gruenewaldt (1971) adhered to Molyneux's (1970) threefold subdivision of the Main Zone into Subzones A, B and C. Von Gruenewaldt's estimate of the thickness of the Main Zone at Roossenekal is 3940m, which is somewhat greater than Molyneux's estimate of a thickness of 2860m at Steelpoort, further north. Von Gruenewaldt (1971) described Subzone A of the Main Zone as being gabbronorite, characterized by hypersthene except for a very short interval approximately 93m above the Merensky Reef, where there is a sudden change from Fs_{25} to Fs_{34}. The change to a more iron-rich composition is reflected in a brief appearance of pigeonite. Between 1000m and 1200m above the Merensky Reef, von Gruenewaldt observed noticeable fluctuations in the texture and mineral compositions of the rocks. Von Gruenewaldt (1971) placed the boundary between Subzones A and B within this interval.

Whilst the orthopyroxene in Subzone A is characteristically cumulus, that of Subzone B is typically intercumulus, or ophitic, in texture. Concomitant with the change from cumulus to intercumulus texture, the first inverted pigeonite, apart from the brief occurrence at 93m above the Merensky Reef, appears in the sequence. With increasing height in Subzone B, the proportion of inverted pigeonite to primary orthopyroxene increases steadily, until it is the only Ca-poor variety in the rock.

At the Pyroxenite Marker, there is a reversion from inverted pigeonite to primary hypersthene, reflected in a compositional change from Fs_{44} to Fs_{27}. Cumulus orthopyroxene was found by von Gruenewaldt (1971) to characterize the gabbroic rocks for a vertical interval of 450m above the Pyroxenite Marker. Above 450m, there is a compositional change back to pigeonite, which differs from the underlying hypersthene in being intercumulus. From this point upwards into the Upper Zone, pigeonite is the only Ca-poor pyroxene in the rocks.

Each change in pyroxene composition in the Main Zone is accompanied by a simultaneous change in plagioclase composition (von Gruenewaldt, 1971). Von Gruenewaldt (op. cit.) considered the pegmatites in the

layered suite briefly, mentioning the presence of vermiculite pipes in Subzone B, and magnetite pipes in Subzone C, of the Main Zone. There is also a reference to diallagite pipes in the Main Zone, but these were not investigated. From von Gruenewaldt's map, it appears that the diallagite pegmatite bodies are in the Main Mottled Anorthosite. A synopsis of von Gruenewaldt's (1971) work has been published (von Gruenewaldt, 1973), and in a later paper (von Gruenewaldt and Weber-Diefenbach, 1977), the transition from orthopyroxene to pigeonite in the Main Zone is discussed in some detail.

The compositional variations displayed by the pyroxenes of the Bushveld Complex were studied by Atkins (1969), in the eastern lobe, and by Markgraaf (1976) in the western lobe. These studies are, however, broadly-based reconnaissance studies, of little or no value in the detailed analysis of processes operating within the Bushveld magma chamber.

Marais (1977) sampled a series of 600 to 700 metre long traverses across the Pyroxenite Marker in the eastern Bushveld. Marais showed that the Pyroxenite Marker varies quite considerably in physical appearance along strike. In the northeastern part of the Complex, the Pyroxenite Marker is a single layer of pyroxenite. Further south, at Roossenekal, the Pyroxenite Marker is a single layer of pyroxenite. At Tonteldoos, south of Roossenekal, the Pyroxenite Marker is absent as such, but the equivalent horizon is marked by geochemical and mineralogical inflections. On the basis of trace element chemistry, Marais (1977) postulated a gradual addition of primitive magma towards the top of Subzone B, followed by a sudden, large influx of magma at the level of the Pyroxenite Marker.

Hamilton's (1977) strontium isotope study of the Bushveld Complex returned a Rb-Sr age of 2095± 24 m.y. (this age was based on a decay constant of 1.39×10^{-6}; use of the currently preferred 1.42×10^{-6} decay constant returns an age of 2050 m.y.). The initial $^{87}Sr/^{86}Sr$ ratios of the rocks of the Rustenburg Layered Suite appear to increase upwards in a series of abrupt steps, each associated with a sudden irregularity in cryptic variation in the rocks. Hamilton linked these abrupt changes to new influxes of magma into the chamber. The Sr isotope systematics of the Main Zone appear to be chaotic, the initial ratio (R_o) varying between 0.70592 and 0.70863, but as Hamilton

admitted, his sample density in the Main Zone was not sufficient to illustrate clearly any subtle changes in Rb-Sr isotope systematics.

McCarthy and Cawthorn (1980) suggested that an increase in the Rb/Sr ratio with fractionation of a magma could affect the rate of change of the Sr isotope initial ratio in successive residual melts. According to McCarthy and Cawthorn's reasoning, increasing R_o within the Bushveld Complex need not be due to influxes of fresh magma. Alternatively, according to these authors, it may result from the slow cooling of a single body of magma or, more probably, two large influxes of magma. They suggested that the first influx formed the sequence from the base of the Complex to the top of the Merensky Reef, whilst the second formed the succession from the top of the Merensky Reef to the top of the Upper Zone. Crystallization times of the order of 10 to 20 million years were envisaged for the first magma batch, and 20 to 40 million years for the second batch. This is in extreme contrast to Irvine's (1970) estimated crystallization time of 0.2 million years for the entire Bushveld Complex.

Using the optical spectrographic data produced by Liebenberg (1961), Cawthorn (1983) attempted to model the effects of new magma influxes within the Bushveld on the basis of incompatible element systematics. Apart from the inherently imprecise nature of the analytical technique used by Liebenberg, the exact geographical positions of the sampling localities are not known. On these grounds, Cawthorn's geochemical plots against stratigraphic height should be treated with caution, especially as regards a thick, broadly uniform sequence like the Main Zone.

Sharpe (1981) discussed the evolution of the Bushveld Complex by reviewing evidence for and against various single- and multiple-intrusion models. Sharpe concluded that the Main Zone is the product of a series of magma influxes of varying intensity and composition, his main line of evidence being Hamilton's (1977) Sr isotope data. Sharpe's model later evolved to explain the entire layered succession by the intrusion and double diffusive mixing of only two magma types, of an ultramafic (U-type) and an anorthositic (A-type) lineage (Sharpe and Irvine, 1983). In a recent refinement of his model, Sharpe (1985) has used newly available Sr isotope data to propose that the layered rocks between the Merensky Reef and the

Pyroxenite Marker formed from a massive inflow of fresh, A-type magma into a density-stratified magma chamber.

Klemm et al. (1985) sampled three traverses across the eastern Bushveld, in the vicinity of Roossenekal, from approximately half way up Main Zone Subzone B to the Main Magnetite layer. Klemm et al. presented data which indicate a reversal in the fractionation trends of orthopyroxene and plagioclase some way below the Pyroxenite Marker. The zone of reversed fractionation wedges out southwards from Roossenekal. The reversal is explained as the product of the intrusion and mixing of a new influx of magma in a density-stratified magma chamber. The Pyroxenite Marker, and the magnetite-rich gabbro which underlies it, are interpreted as manifestations of an anomalous, short-lived change in pressure and oxygen fugacity at the crystal-liquid interface, some time after intrusion of the new magma.

Whilst the Main Zone succession of the western lobe of the Bushveld is strikingly similar to that of the eastern lobe, no Main Zone rocks have been identified in the Bethal area (Buchanan, 1975). In the Potgietersrus limb of the Complex, the Main Zone, i.e. the layered succession between the Platreef and the Pyroxenite Marker, exhibits significant differences from the equivalent succession elsewhere in the Complex (van der Merwe, 1976). Most significant of these differences is the presence of a 110 metre thick noritic troctolite some 1100 metres above the Platreef. Van der Merwe (op. cit.) identified three macro-rhythmic units within the 2000 metre thick Main Zone succession in the Potgietersrus limb, each of which he ascribed to an influx of new, but chemically similar, magma.

1.3 Sources of Sample Material

1.3.1 Introduction

With the exception of the Pyramid hills, outcrop of the Main Zone in the western Bushveld is very poor, and is restricted to small, scattered pavements of rock. Consequently, a field-based sampling programme is inadequate for a detailed geochemical study. These considerations have led to this study being based, to a very large extent, on material from exploration boreholes.

The research programme was initiated using material from surface exploration boreholes SK2 and SK4, both of which were collared on the farm Spitzkop 410KQ, within the mining lease area of R.P.M. Union Section. This material was supplemented with underground samples from 11 level 6^S crosscut, and surface samples collected within the mining lease area. The positions of boreholes SK2 and SK4, 11 level 6^S crosscut and the surface sampling sites are shown in Fig. 2. The stratigraphic column (Fig. 3) shows the positions of samples from borehole SK2, and of the MZ series of samples, which were analyzed in the course of this study.

1.3.2 Surface Exploration Borehole SK2

Borehole SK2 was collared on the farm Spitzkop 410KQ, in a down-dip direction from Richard shaft at Union Section along line 7^S, and some five kilometres from Merensky Reef outcrop. The collar elevation of the hole is 1005.79m (above sea level), and collar coordinates on the local grid are: X+63970.53; Y-19412.42 (Fig. 2). The hole was drilled to a depth of 2139.01m, at which point it had penetrated to below the UG1 chromitite. At the Merensky Reef intersection, SK2 deviates from the vertical by 36° (up dip) on a bearing of 310°. Sampling for this project is based on measured core length, rather than calculated vertical depth. The SK2 core was logged in detail by the author in August 1981, and samples were collected at intervals of five to ten metres, with closer-spaced sampling in zones of specific interest. In all, 350 samples were collected from SK2, covering the vertical interval from the Bastard Reef to surface.

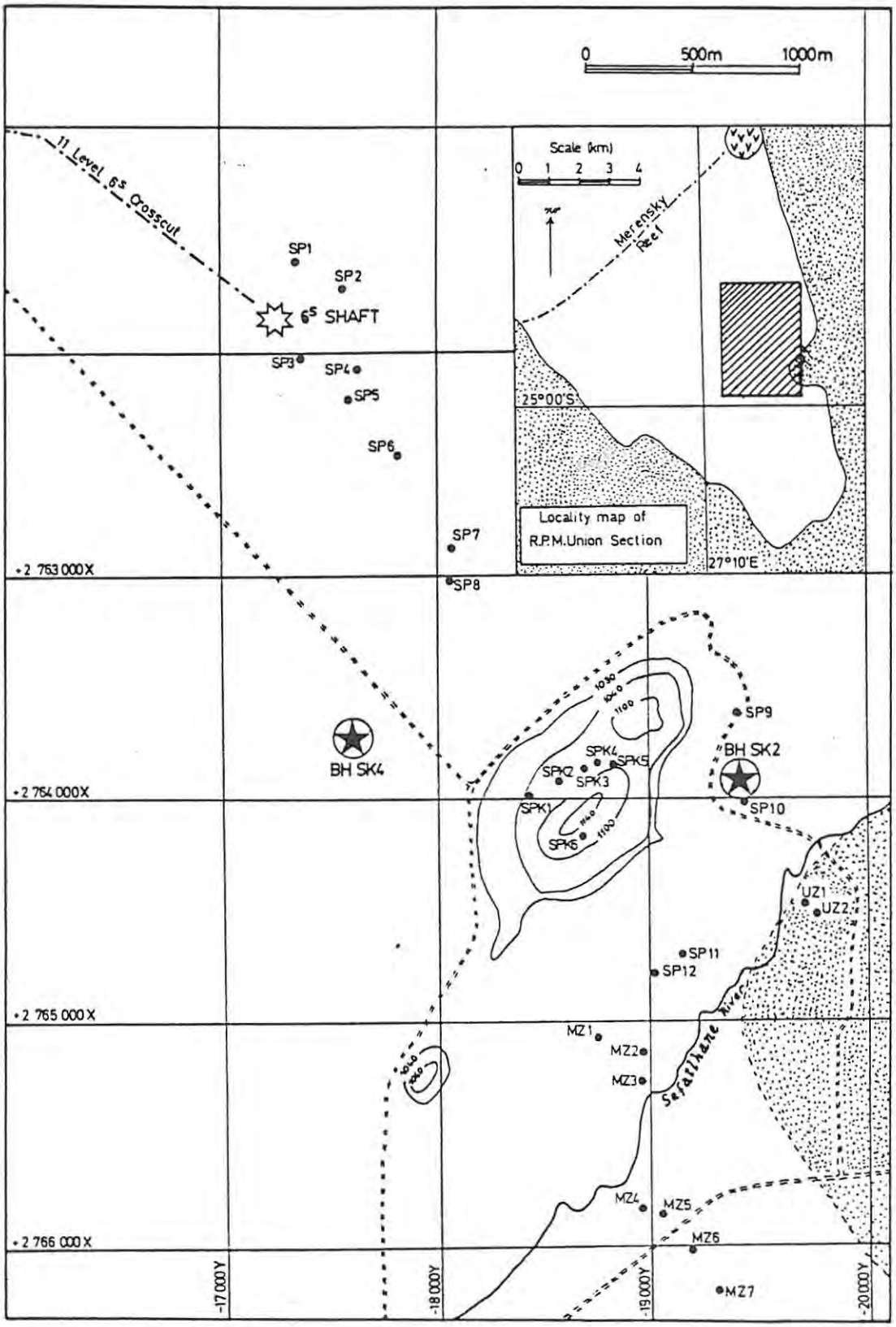

Fig. 2: Map of sample localities on the farm Spitzkop 410 KQ.

1.3.3 Surface Exploration Borehole SK4

As with SK2, borehole SK4 was collared on the farm Spitzkop 410KQ. SK4 is 4.5 kilometres from Merensky Reef outcrop in a down-dip direction along Richard shaft line $12A^S$. The collar elevation of the hole is 1024.50 metres above sea level, and the local grid coordinates are: X+63714; Y-17600. The final uncorrected depth of SK4 is 1336.4 metres. The maximum deflection of the hole is 15^o to the north-west, and the calculated true vertical depth 1314 metres.

As the layered cumulates in borehole SK2 are severely disrupted in many places by ultramafic pegmatite, it was hoped that SK4 would provide a more "normal" succession for comparison. Parts of the SK4 core are, however, extremely altered, especially in the more plagioclase-rich intervals. This factor interfered with sampling, as samples were not normally collected from the more highly altered portions of the core. In all, 105 samples were taken from SK4, covering the 1277.85m interval from the Bastard Reef to surface.

1.3.4 11 Level 6^S Crosscut, R.P.M. Union Section

11 level 6^S crosscut, which is of the order of 1.4 kilometres long, provided access to the lower few hundred metres of the Main Zone at Union Section. A true stratigraphic thickness of 415m was calculated, on the basis of a regional dip of 20^o. The predominant lithology encountered in the crosscut is norite or leuconorite, intercalated with spotted or mottled anorthosite, particularly in the lowermost part of the sequence. In parts of the succession, igneous lamination is evident, and may become so pronounced as to produce thin, almost monomineralic layers of pyroxenite and anorthosite on a centimetre scale. Eighty samples were collected from the crosscut, twenty-five of which were analyzed for trace elements.

1.3.5 Surface Sampling on Spitzkop 410KQ

Surface outcrop of the Main and Upper Zones in the western Bushveld is sparse in the extreme, especially by comparison with the eastern Bushveld. This, combined with the very uniform appearance of the Main Zone rocks in the field, makes detailed mapping a difficult and rather

unproductive exercise. Despite this, a limited sampling exercise was mounted.

The locality map (Fig. 2) shows the positions of surface sampling sites (shaded circles, with sample numbers prefixed by the letters SP, SPK, UZ or MZ). The MZ group of samples (Fig. 2, Fig. 3) are particularly important, in that they straddle a major petrological and geochemical discontinuity at a stratigraphic level equivalent to the Pyroxenite Marker of the eastern Bushveld (Marais, 1977). Although the MZ samples display graphically the sharp changes in petrology and geochemistry across this horizon, the Pyroxenite Marker was not physically identified in the field. The position of the discontinuity is immediately northwest of the Sefatlhane river, between samples MZ1 and MZ2 (Fig. 2).

2. GEOLOGICAL SETTING AND STRATIGRAPHY

2.1 Geological setting

On a regional scale, the most notable feature of the northwestern part of the Bushveld Complex is the existence, in two areas, of major transgressions of the Critical and Main Zones by Upper Zone ferrogabbro (Fig. 4). These two transgressions, referred to as the northern and southern gap areas, effectively isolate the roughly triangular segment of Main and Critical Zone rocks that constitute R.P.M. Union Section. Although surface outcrop of Main and Upper Zone rocks is extremely poor, the Upper Zone ferrogabbro weathers to a reddish soil, which contrasts sharply with the black "turf" or "cotton soil" of the Main Zone (Fig. 5).

In the gap areas, Feringa (1959) and Cousins (1959) concluded that the Lower, Critical and Main Zones were displaced by faulting, with the younger ferrogabbro of the Upper Zone being emplaced after the faulting event. Coertze (1974) ascribed the gap areas to the intrusion of Upper Zone material, which effectively obliterated the Main and Critical Zones in these areas. From their interpretation of the structure of the acid rocks of the western Bushveld, Walraven and Darracott (1976) postulated an anticlinal axis trending through the Union Section segment, flanked by synclinal axes in the gap areas. De Klerk (1982) postulated anticlines running through the gap areas. The implication of de Klerk's statement is that the Critical and Main Zones may never have existed in the gap areas.

Viljoen and Feuchtwanger (1977) concluded that the gap areas originated, in part, through graben faulting. This faulting is postulated to have been pivotal, with the hinge axis parallel to the strike of the Magaliesberg quartzites. Viljoen and Feuchtwanger believed that the throw of the fault increases basinwards into the Complex, thus increasing the dip of the floor rocks, and allowing the emplacement of Upper Zone material in the gap areas. As de Klerk (1982) pointed out, the trend of the graben faults parallels the major direction of faulting and dyke emplacement at Union Section. These features are clearly seen from the airborne magnetic survey of the mining lease area (Fig. 6), in which dykes show up as prominent linear anomalies. Underground workings along the northern and southern

margins of Union Section (particularly in the southwestern part of the mine) have exposed numerous faults parallel to the trend of the postulated graben faults (de Klerk, 1982, and personal observations by the author), which tend to support the essence of Viljoen and Feuchtwanger's model.

The magnetic contour map of Union Section (Fig. 6) and the Landsat image of the area (Fig. 7) both show that the northern margin of the Union Section segment is virtually a straight line, which lends support to a graben faulting model. On the Landsat image, in particular, this linear feature can be traced north into the Magaliesberg quartzites (Fig. 7; Fig. 8). Intersecting this major lineament is a second linear feature, expressed in the almost perfectly straight course of the Sefatlhane river, which flows across the Union Section segment 500 metres east of the prominent Spitzkop hill (Fig. 7; Fig. 8). This latter lineament is of particular significance in that it marks the transition from Subzone B to Subzone C of Molyneux's (1970) Main Zone classification, i.e. it marks the stratigraphic horizon characterized by the Pyroxenite Marker in the north-eastern and eastern parts of the Bushveld (Marais, 1977). The Pyroxenite Marker was not encountered in the field at Union Section, but this does not imply that it does not exist in this part of the Complex. The lineament along the Sefatlhane river could well represent a strike-slip fault, of the type postulated in the Main Zone of the eastern Bushveld by von Gruenewaldt (1973), with the resultant elimination of the Pyroxenite Marker. Marais (1977) described changes to more primitive chemistry which begin to appear well below the Pyroxenite Marker in the eastern Bushveld. Similar effects have been documented in the southwestern Bushveld (Kruger et al., 1986). The changes documented by Marais (op. cit.) and Kruger et al. (op. cit.) are not evident in the MZ group of samples at Union Section (this study). The implication is that a fairly substantial part of the Main Zone succession in the vicinity of the Pyroxenite Marker may have been eliminated by the postulated Sefathlane river fault.

Borehole SK2 lies close to the intersection of the Sefatlhane river lineament and the apparently faulted northern margin of the Union Section segment. This is likely to be a highly fractured area, in which a high incidence of ultramafic pegmatite development, as seen in SK2, is to be expected (Viljoen and Burvenich, 1983).

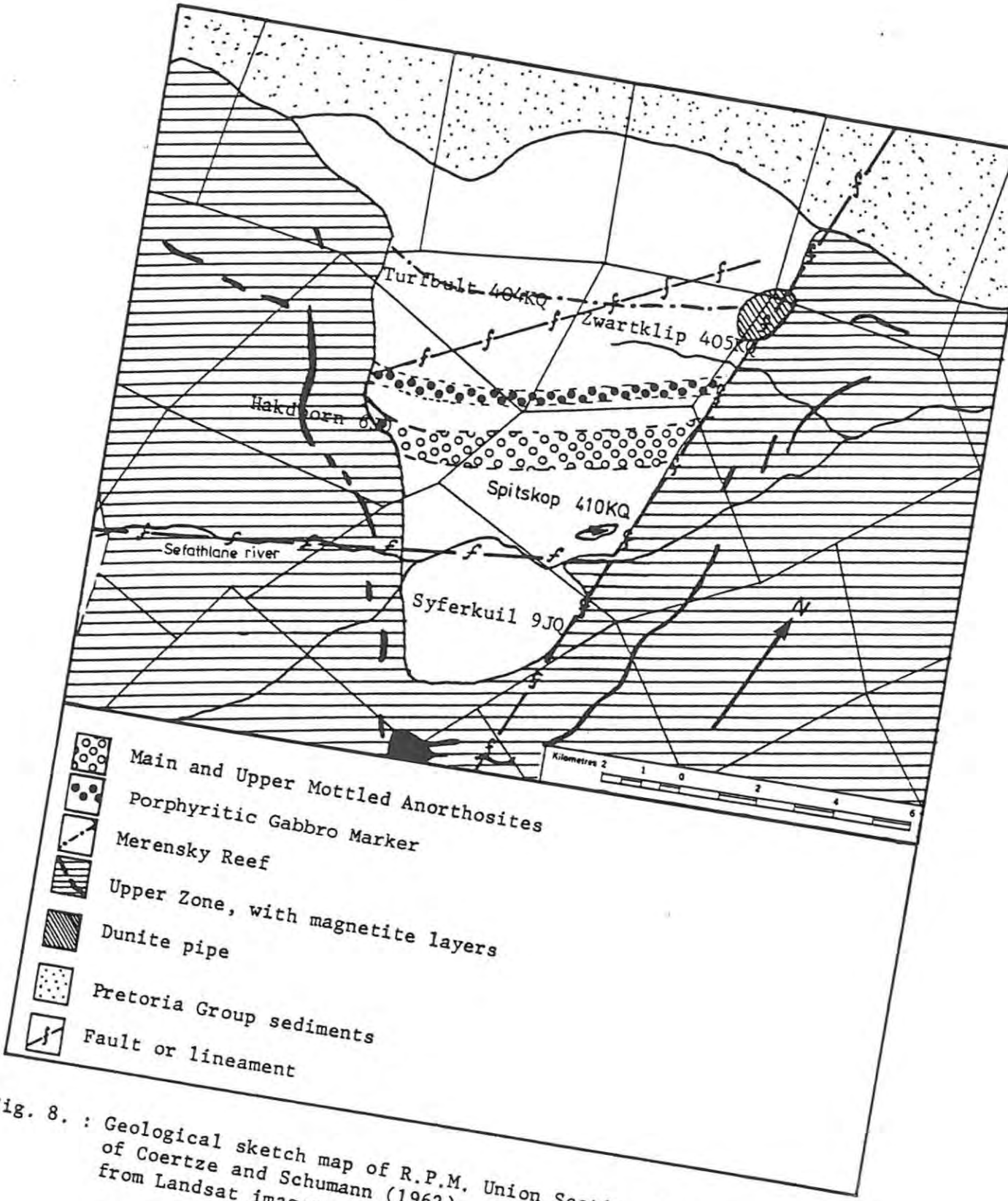

Fig. 8. : Geological sketch map of R.P.M. Union Section, based on the work of Coertze and Schumann (1962), and modified using information from Landsat imagery and airborne magnetic data.

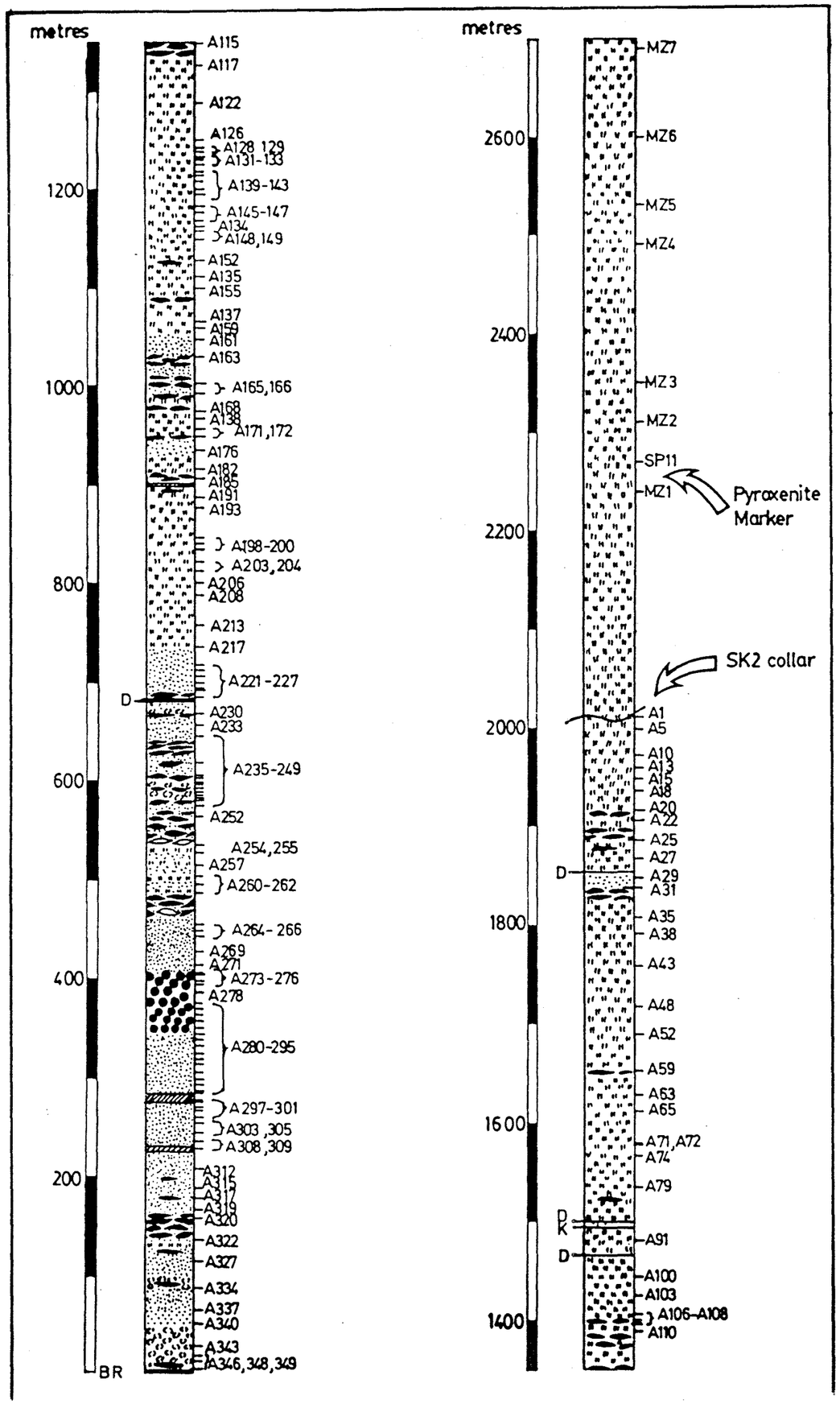

Fig. 3. : Stratigraphic column of the Main Zone succession covered by this study, showing the positions of all analyzed samples. Samples prefixed by "A" are from borehole SK2. Samples prefixed by "MZ" or "SP" are surface samples, collected down-dip from the collar position of SK2. The detailed log of SK2 may be found in appendix 1 of this work, and the exact stratigraphic position of each sample analyzed, together with a brief petrological description, is given in appendix 2. The ornamentation used in figure 3 (see key below) has been used as a standard throughout this thesis.

KEY TO FIG. 3

- Fe-rich ultramafic pegmatite
- Mottled anorthosite
- Leucogabbro or leuconorite
- Gabbro or norite
- Porphyritic gabbro
- Pyroxenite
- D — Dolerite sill
- K — Kimberlitic sill
- BR — Bastard Reef

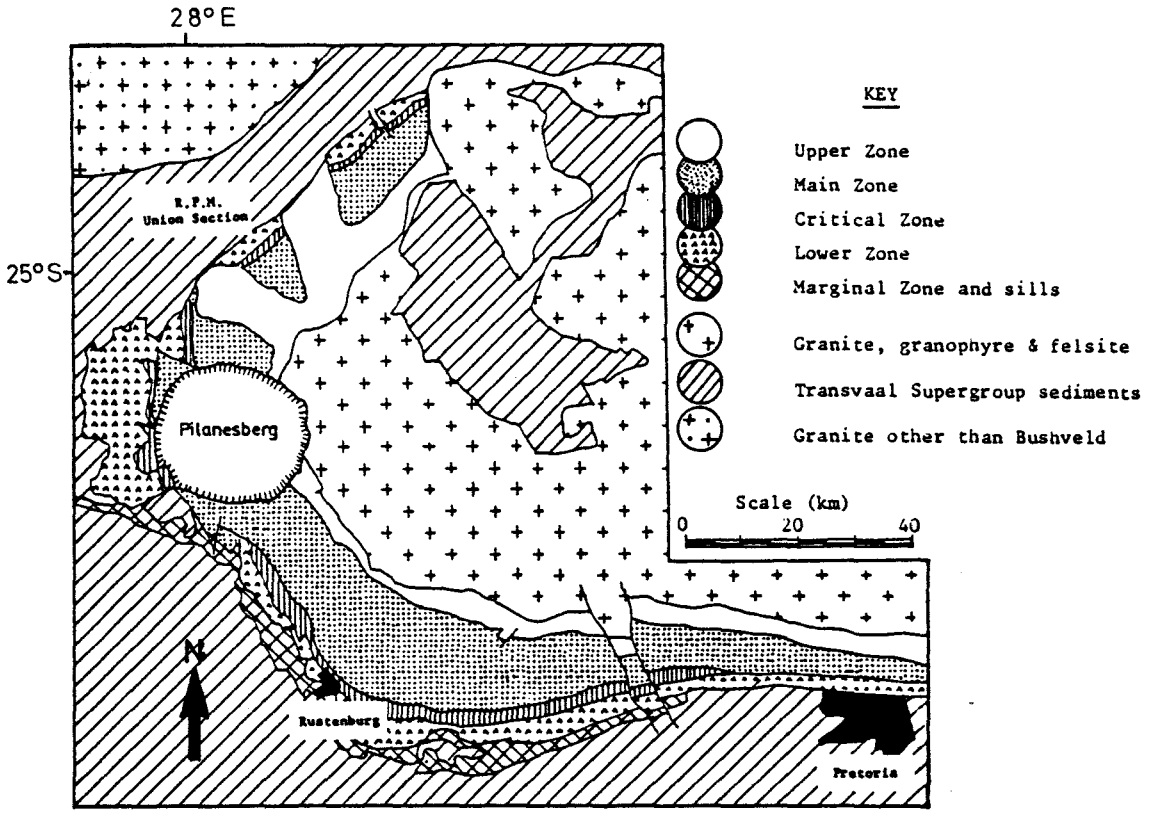

Fig. 4: Sketch map of the western Bushveld Complex.

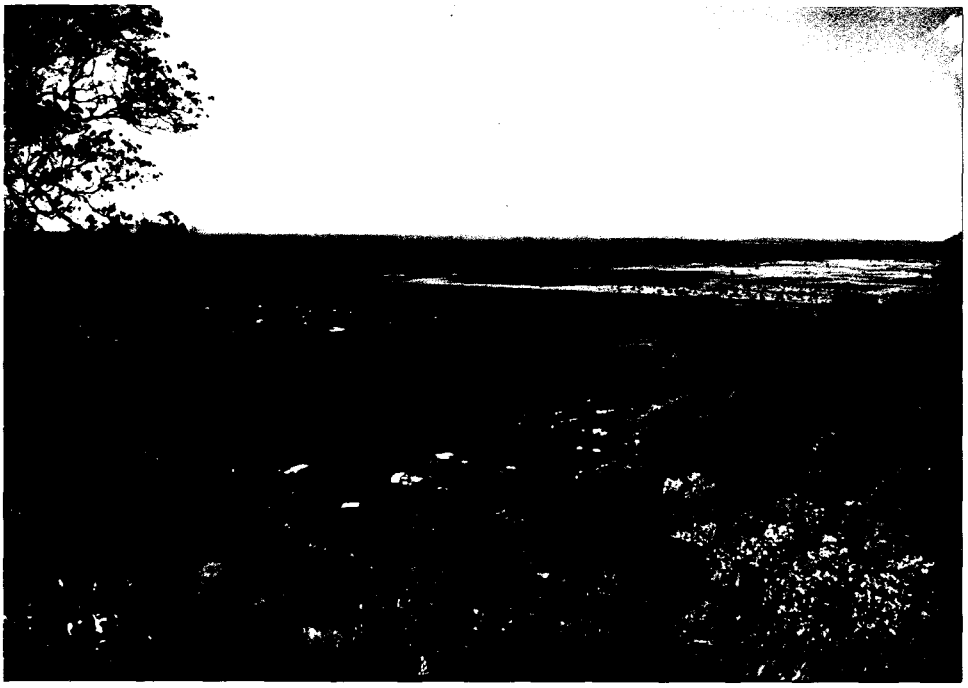

Fig. 5: View east from the top of Spitskop, showing the vivid contrast between the "black turf" of the Main Zone and the red soil of the Upper Zone, in the promontary of Upper Zone material immediately south of the Sefatlhane river.

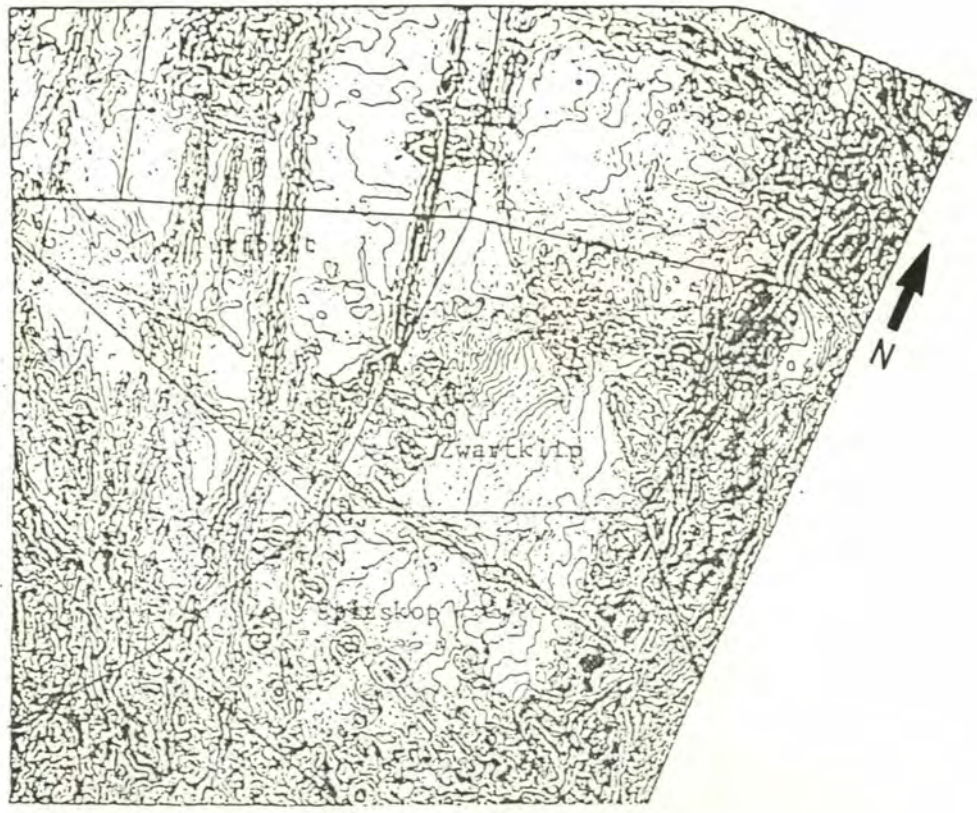

Fig. 6 : Airborne magnetic map of R.P.M. Union Section

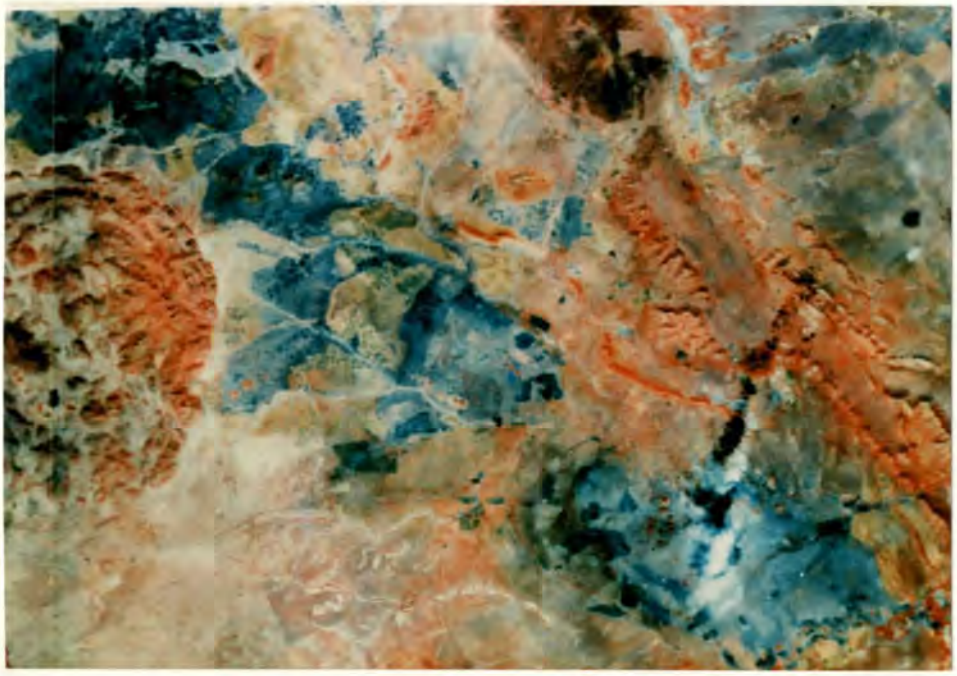

Fig. 7 : Landsat image of the northwestern sector of the Bushveld Complex. Lower, Critical and Main Zone outcrop is dark blue. Ridges of Magaliesberg quartzite to the north of Union Section are deep red.

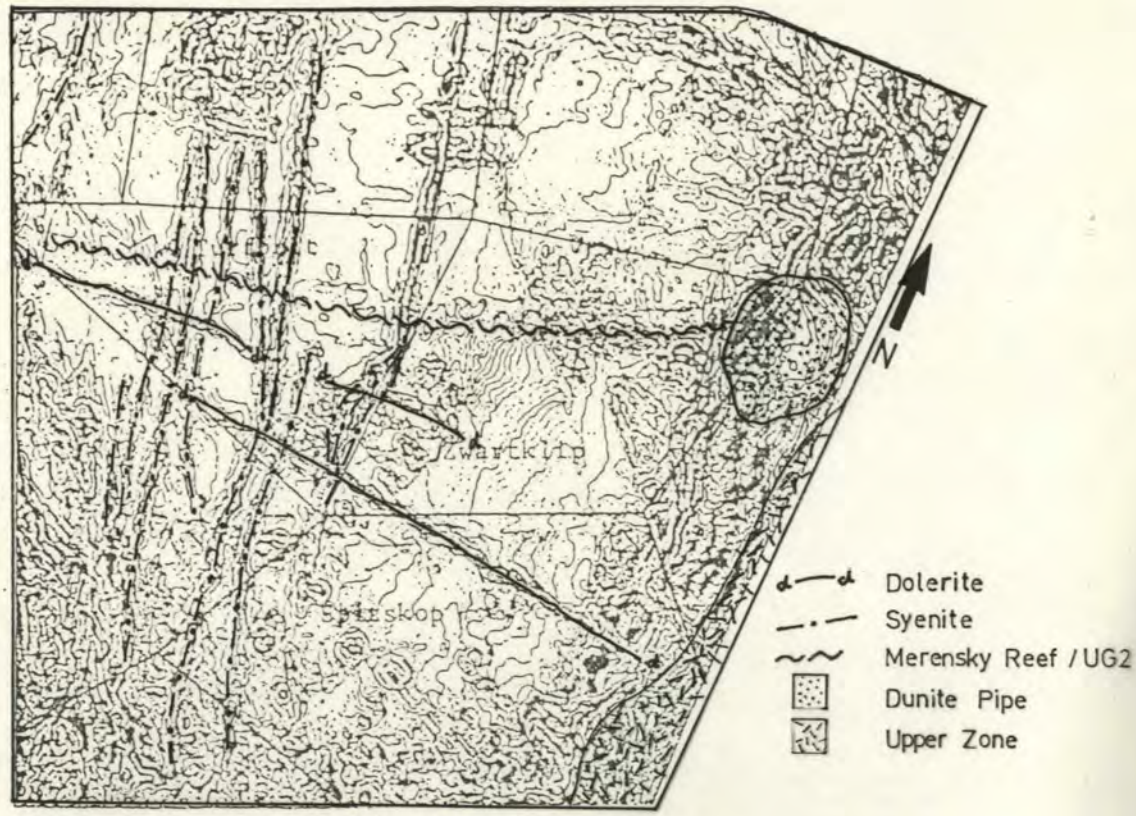

Fig. 6 : Airborne magnetic map of R.P.M. Union Section

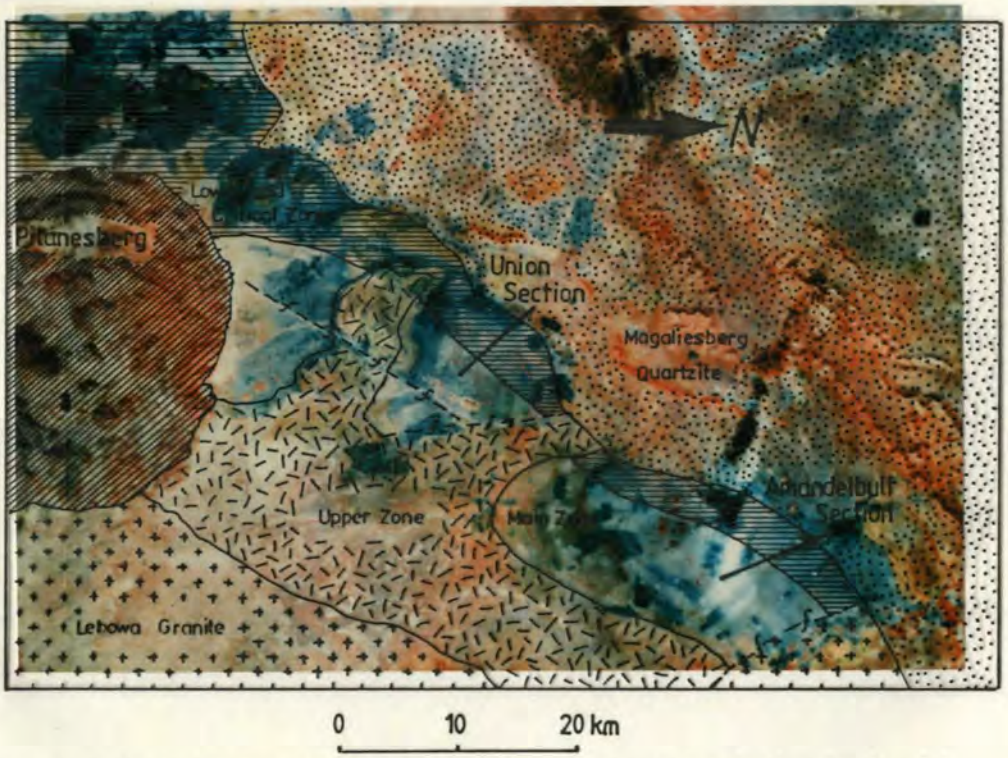

Fig. 7 : Landsat image of the [illegible] sector of the Bushveld Complex. Lower, Critical and Main Zone outcrop is dark blue. Ridges of Magaliesberg quartzite to the north of Union Section are deep red.

2.2 Stratigraphy of the Main Zone

2.2.1 Introduction

The South African Committee for Stratigraphy (SACS, 1980) recommend the formal classification of the Main Zone in the western Bushveld as the "Pyramid Gabbronorite", with no formal subdivisions. In the eastern Bushveld, the Main Zone is subdivided by SACS into three units, from the bottom up the Winnaarshoek Norite Anorthosite, the Leolo Mountain Gabbronorite, and the Mapoch Gabbronorite. These three subdivisions represent Subzones A, B and C, respectively, of Molyneux's (1970) subdivision of the Main Zone (Fig. 9).

As originally defined by Molyneux, Subzone A extends from the base of the Merensky Reef to the top of the Upper Mottled Anorthosite. Norite is the proportionally dominant rock type in this lowermost subzone, but anorthosite, generally the characteristic "spotted" and "mottled" varieties, and pyroxenite, are locally significant. Subzone A is characterized by a number of prominent lithological markers. This is particularly so if the Merensky and Bastard Cyclic Units are included in the Main Zone, as in the case of Molyneux's (1970) classification. At a stratigraphic height of approximately 300 metres above the Merensky Reef, Molyneux (op. cit.) identified a zone in which the gabbronorite contains large orthopyroxene macrocrysts, which impart a porphyritic appearance. This lithology, known colloquially as the "Porphyritic Gabbro Marker", is also found in the SK2 succession, between approximately 350 and 410 metres above the Merensky Reef.

Below the Porphyritic Gabbro Marker in the SK2 succession, at 230 and 280 metres above the Merensky Reef, are two pyroxenite layers, respectively 4.5 and 10 metres thick. Neither Molyneux (1970) nor von Gruenewaldt (1971) mentioned equivalent layers in the eastern Bushveld, but Meyer (1969) indicated the presence of a single pyroxene-rich layer at a similar stratigraphic position in the Rustenburg area. Even at Union Section, the two pyroxenite layers which characterize the lower 300 metres of the SK2 succession do not appear to be continuous. In borehole SK4, up-dip from SK2, the two pyroxenites are not present, but there is a definite coarsening of the grain size of orthopyroxene in the norite at the equivalent stratigraphic heights, giving a texture

similar to that of the Porphyritic Gabbro Marker.

Approximately 300 metres above the Porphyritic Gabbro Marker, Molyneux (1970, 1974) identified a zone approximately 150 metres thick in which layers of anorthosite alternate with gabbronorite. This interval, Molyneux (op. cit.) termed the "Main Mottled Anorthosite". The Main Mottled Anorthosite is clearly evident in SK2, but is disrupted by numerous bodies of ultramafic pegmatite. Disruption of the Main Mottled Anorthosite by ultramafic pegmatite is not restricted to the SK2 succession, and has been described in other parts of the Complex, notably by Willemse (1969), Molyneux (1970), von Gruenewaldt (1971) and Viljoen and Burvenich (1983). The Main Mottled Anorthosite is overlain by roughly 200 metres of gabbronorite, followed by the "Upper Mottled Anorthosite", which is very similar in appearance to the Main Mottled Anorthosite. In the SK2 succession, the base of the Upper Mottled Anorthosite is defined by a 100mm thick layer of fine-grained pyroxenite, not documented in other parts of the Complex. The Upper Mottled Anorthosite is similar to the Main Mottled Anorthosite in being disrupted by ultramafic pegmatite bodies.

Subzone B of the Main Zone starts at the top of the Upper Mottled Anorthosite, according to Molyneux (1970). Subzone B appears in the field to be a rather monotonous succession of gabbronorite, approximately 1000m thick. On the basis of differential erosion effects, Molyneux (1970, 1974) identified six successive "sheets" in Subzone B, but did not explicitly attach any significance to them. Perhaps the most noteworthy feature of Subzone B, in petrological terms, is the transition from primary hypersthene to inverted pigeonite as the dominant Ca-poor pyroxene variety (von Gruenewaldt, 1971, 1973; von Gruenewaldt and Weber-Diefenbach, 1976).

Subzone C of Molyneux's Main Zone classification starts at an horizon marked in some parts of the Bushveld Complex by one, or even two, pyroxenite layers (Marais, 1977). This horizon is known as the Pyroxenite Marker. The term "Pyroxenite Marker" appears to some extent to be a misnomer, as a pyroxenite layer is not everywhere apparent at this level in the stratigraphy (Marais, 1977; this study). The possibility does exist, however, that the absence of the Pyroxenite Marker from some parts of the Complex may be fault-related, rather than being a genetic feature.

Regardless of whether or not the Pyroxenite Marker is developed at the base of Subzone C, the equivalent horizon is always marked by sharp changes in geochemical parameters (Marais, 1977; Sharpe, 1985; Kruger et al., 1986; this study). Above the Pyroxenite Marker, the gabbronorite succession of Subzone C represents, in very broad terms, a repetition of Subzones A and B combined. There is a progression from primary hypersthene at the base of the subzone, through progressively more iron-rich orthopyroxene, to inverted pigeonite at the top of the subzone. The top of Subzone C, and thus of the Main Zone according to Molyneux (1970), is marked by the first appearance of cumulus magnetite in the layered rocks.

Molyneux's (1970) system of subdivision of the Main Zone has been used in Fig. 9, simply because it forms a familiar and ready basis for the comparison of the Main Zone succession in various parts of the Bushveld Complex. Molyneux's is, however, strictly a field-based system, and is replaced in this work by a new classification scheme, based on stratigraphic units which are characterized by more or less coherent geochemical and petrological patterns. Each unit is defined on the basis of as many coincident geochemical and petrological parameters as possible. Some of the more important of these parameters are depicted in a composite diagram (Fig. 34, in the back pocket of this thesis).

Although Molyneux (1970), von Gruenewaldt (1971) and others have suggested that the Merensky Cyclic Unit forms the base of the Main Zone, there are various arguments against this point of view. One of these is that the Merensky and Bastard Cyclic Units are strongly developed cyclic units, more in the style of the underlying UG1, UG2 and Pseudo Reef Cyclic Units of the Upper Critical Zone than of the overlying Main Zone. In addition, the Merensky and Bastard Cyclic Units contain the uppermost chromitite layers in the Bushveld Complex. Chromitite layers typify the Critical Zone, and it would seem rather incongruous to include the Bastard and Merensky Cyclic Units in the (essentially spinel-free) Main Zone. In the SK2 succession, disruption of the cumulus rocks by ultramafic pegmatite makes it difficult to determine the top of the Bastard Cyclic Unit, and thus the top of the Upper Critical Zone. In the 11 level 6^S crosscut section, the top of the Giant Mottled Anorthosite, which also marks the top of the Bastard Cyclic Unit, is fifty-three metres above the Bastard Reef. In the

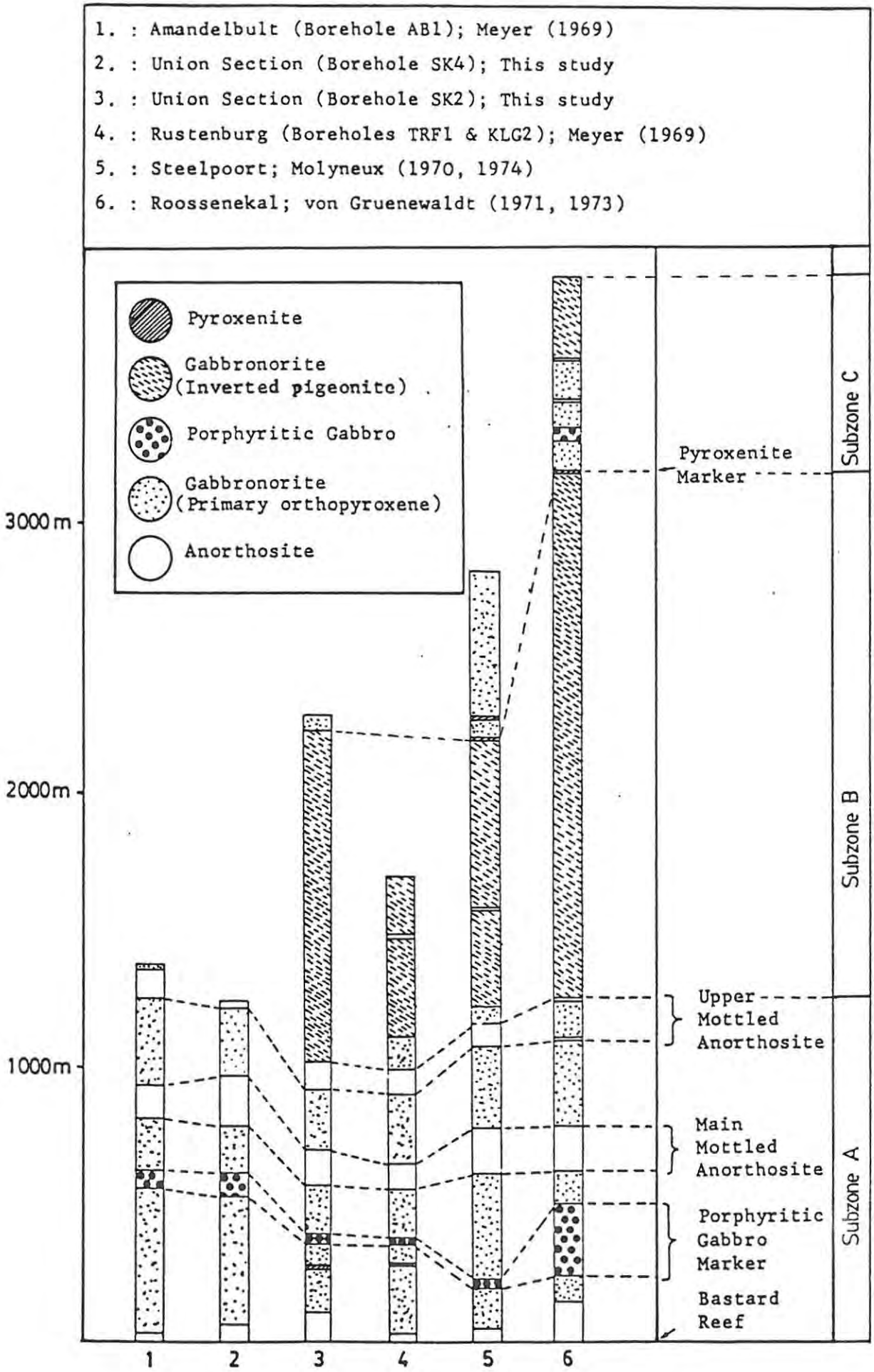

Fig. 9 : Generalised Main Zone stratigraphies for various parts of the Bushveld Complex, showing important marker horizons, and also the threefold subdivision of the Main Zone as suggested by Molyneux (1970).

absence of any more appropriate measure, the Main Zone is regarded in this thesis as beginning at height of fifty-three metres above the Bastard Reef. For ease of reference, stratigraphic heights in this work are quoted in metres above the Bastard Reef. There is no genetic implication in the choice of this datum point. Eight Main Zone units are defined in this work for the interval between the top of the Bastard Cyclic Unit and the Pyroxenite Marker.

2.2.2 Main Zone Unit I

The Giant Mottled Anorthosite, which ends 53 metres above the Bastard Reef, marks the top of the Bastard Cyclic Unit. Above the Giant Mottled Anorthosite, there is a series of rather poorly defined and discontinuous felspathic pyroxenite layers, interspersed with spotted anorthosite, over a vertical interval of approximately 500mm. This layering, visible in the 11 level 6^S crosscut section, but not in SK2, marks the base of Main Zone Unit I. It is difficult to characterize Unit I in SK2, because of disruption by ultramafic pegmatite. In the 11 level 6^S crosscut section, Unit I consists of leuconorite and norite, in which conspicuous centimetre-scale layering is often apparent. The top of Unit I is placed at 113m in SK2, on the basis of geochemistry rather than any distinct petrographic changes.

2.2.3 Main Zone Unit II

Unit II is petrographically similar to Unit I, but the two units are separated on the basis of geochemistry. Unit II extends from 113m to 223.5m above the Bastard Reef, and consists of leuconorite, in which grains of cumulus orthopyroxene up to 3mm in diameter impart a speckled appearance.

2.2.4 Main Zone Unit III

The base of Unit III in SK2 is marked by the development of a rather coarse-grained feldspathic orthopyroxenite, which extends from 223.5m to 229.15 metres above the Bastard Reef. The pyroxenite has sharp upper and basal contacts, and is succeeded upwards by a leucogabbro, which in turn grades into a thin mottled anorthosite layer, approximately 1m thick. The mottled anorthosite is succeeded at 272.6m by a second pyroxenite layer, some ten metres thick. Many geochemical

parameters might justify the definition of a new unit at the base of the pyroxenite at 272.6m (Fig. 34), and there is certainly petrographic justification for such a division. The unit has been defined as the entire interval from 223.5 to 325 metres, however, on the basis that, apart from the two pyroxenites, the leuconorite in this interval is fairly uniform, both petrographically and geochemically. In addition, the two pyroxenite layers have only been identified in SK2, and are not known in the Main Zone succession elsewhere in the Bushveld Complex.

2.2.5 Main Zone Unit IV

The base of Unit IV is somewhat below the gradational base of the distinctive Porphyritic Gabbro Marker, a gabbronorite interval in which large (up to 5mm diameter) oikocrysts of orthopyroxene impart a spotted, or porphyritic, appearance. The upper and lower contacts of the Porphyritic Gabbro Marker are gradational over several metres, and the base of Unit IV has been determined on geochemical, rather than petrological, grounds. The Porphyritic Gabbro Marker extends from 345 to 407 metres above the Bastard Reef. Above the Porphyritic Gabbro Marker, Unit IV consists of gabbronorite and leucogabbronorite. Petrologically, Unit IV and the overlying units have substantially higher proportions of clinopyroxene than do the lowermost three units of the Main Zone (Fig. 34). The top of Unit IV is difficult to determine in SK2, due to the influence of ultramafic pegmatite, but has been arbitrarily placed at 550m on the basis of the limited information available.

2.2.6 Main Zone Unit V

The interlayered sequence of gabbronorite and anorthosite which Molyneux (1970) named the Main Mottled Anorthosite begins somewhere between 550m and 580m above the Bastard Reef. In borehole SK2, this unit has suffered severe disruption by ultramafic pegmatite bodies. It does, however, appear to form a distinct unit, if only because its chaotic geochemical and isotopic systematics do not relate to those of the over- and underlying units.

2.2.7 Main Zone Unit VI

Unit VI extends from the top of the Main Mottled Anorthosite, at 715m,

to 897.7m above the Bastard Reef. This unit is characterized petrologically by fairly substantial variations in modal mineralogy. Geochemically, Unit VI is distinguished by a very strong fractionation trend in the V/Cr ratio.

2.2.8 Main Zone Unit VII

At 897.7m, there is a fine-grained orthopyroxenite, of the order of 100mm thick. This pyroxenite is taken to represent the base of what Molyneux (1970) called the Upper Mottled Anorthosite. The Upper Mottled Anorthosite is similar to the Main Mottled Anorthosite, according to Molyneux, being a sequence of interlayered anorthosite and gabbronorite. In SK2, the Upper Mottled Anorthosite, in common with the Main Mottled Anorthosite, is disrupted by ultramafic pegmatite bodies. The Upper Mottled Anorthosite forms the lowermost part of Unit VII, and grades upward into gabbronorite at approximately 1060m. From the top of the Upper Mottled Anorthosite upwards to 1600m, unit VII consists of a rather unremarkable sequence of gabbronorite.

Although there is some geochemical variation within the unit, particularly in parameters such as the V/Cr ratio, these variations are not substantial. It was decided not to further subdivide this part of the succession, so as not to introduce unnecessary complications. Petrographically, the most notable feature of Unit VII is the appearance, at approximately 1400m, of inverted pigeonite. From 1400m to 1600m, primary hypersthene and inverted pigeonite coexist in the gabbronorite. Von Gruenewaldt and Weber-Diefenbach (1976) discussed the coexistence of the two species of Ca-poor pyroxene. On the basis of texture, these authors postulated that the hypersthene in these rocks is the product of the interaction of early-formed pigeonite with a relatively more Mg-rich magmatic liquid.

2.2.9 Main Zone Unit VIII

At the base of Unit VIII, 1600m above the Bastard Reef, pigeonite gains complete ascendancy over hypersthene as the Ca-poor pyroxene species in the gabbronorite. There are no obvious textural or mineralogical variations within Unit VIII. Probably the most notable feature of this unit is that the inverted pigeonite is optically continuous over tens of centimetres in the rock (Raal, 1965; von Gruenewaldt, 1973). In the

western Bushveld, the gabbronorite of Unit VIII forms the erosional remnants known as the pyramid hills. Unit VIII ends 2250m above the Bastard Reef, immediately below the Pyroxenite Marker.

2.2.10 The Pyroxenite Marker and above

The Pyroxenite Marker has been studied in some detail by Marais (1977), and more recently by Klemm et al. (1985) and Kruger et al. (1986). From Marais's work, it is evident that the Pyroxenite Marker varies considerably along strike, both physically and geochemically, in the eastern lobe of the Bushveld Complex. At Union Section, no evidence was found in the field for the existence of the Pyroxenite Marker **per se**. This does not mean, however, that the Pyroxenite Marker does not exist as a physical entity at Union Section, because outcrop is very sparse. Alternatively, the Pyroxenite Marker may have been eliminated at Union Section by faulting, as discussed in section 2.1 of this work.

The succession above the Pyroxenite Marker in the eastern Bushveld consists mainly of gabbronorite, interspersed periodically with layers of leuconorite or anorthosite. For approximately the first 600m above the Pyroxenite Marker, the Ca-poor pyroxene variety is hypersthene. Above this point in what Molyneux (1970) and von Gruenewaldt (1971) refer to as Subzone C of the Main Zone, inverted pigeonite supplants primary hypersthene. Inverted pigeonite remains the dominant Ca-poor pyroxene throughout the rest of the Main Zone, and into the Upper Zone. The lack of adequate surface sample material at Union Section has meant that only the first 450m above the Pyroxenite Marker are represented in this study, and then only by sparsely distributed samples.

2.2.11 Summary of the Stratigraphy of the Main Zone

The threefold subdivision of the Main Zone into Subzones A, B and C, instituted by Molyneux (1970), is essentially a field-based system. As such, it does not take account of detailed geochemical processes which resulted in the formation of the Main Zone. Meyer's (1969) petrographic study of the Main Zone is extremely detailed, and is potentially a sound basis for a genetic classification of the Main Zone. Meyer was, however, exclusively interested in a textural classification of the rocks of the Main Zone, to the exclusion of any broader genetic considerations.

At risk of complicating the nomenclature of the Bushveld Complex further than is necessary, a new system of subdivision of the Main Zone is used in this thesis, based essentially on geochemistry, integrated with petrography. The criteria employed in making these subdivisions are summarized in Table 11, at the end of chapter 7 of this thesis. It is difficult to estimate the degree to which the succession in SK2 is representative of the Main Zone in general, or even within the Union Section segment. This means that the system used here can only be regarded as provisional, until corroborated by similar studies in other parts of the Complex. Even within Union Section, there are variations in the thickness and exact physical manifestations of successive lithological units (Fig. 10). The two pyroxenite layers which characterize Unit III in the SK2 succession, for example, are also present in the 6^S shaft succession, although somewhat closer together, but manifest themselves as layers of coarse, macrocrystic gabbronorite, rather similar to the Porphyritic Gabbro Marker, in borehole SK4. In SK4, both the Main Mottled Anorthosite and the Upper Mottled Anorthosite have thin pyroxenite layers at their bases, whilst in SK2, only the Upper Mottled Anorthosite begins with a pyroxenite layer.

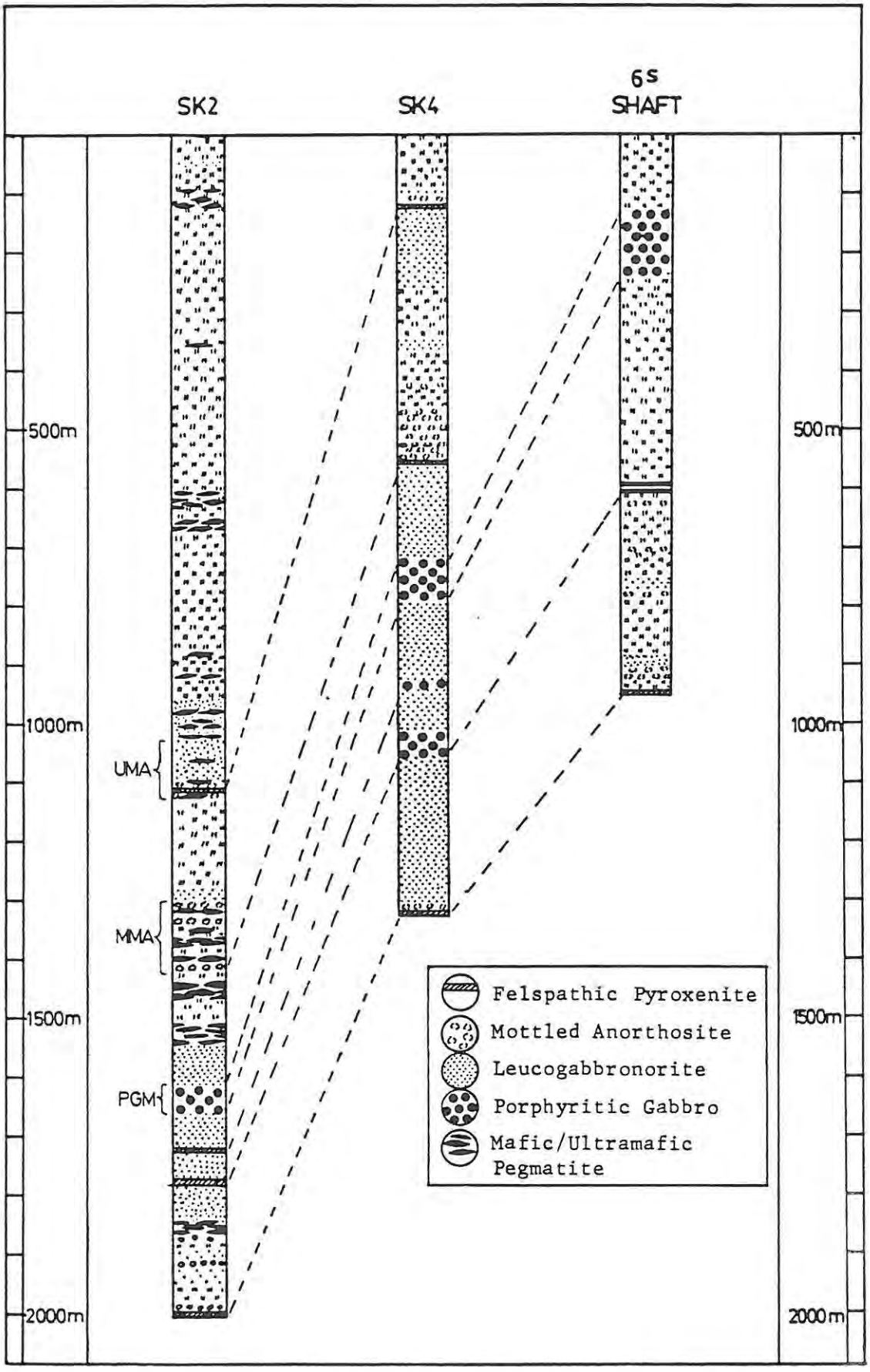

Fig. 10 : Main Zone stratigraphy as intersected in boreholes at Union Section. (PGM = Porphyritic Gabbro Marker; MMA = Main Mottled Anorthosite; UMA = Upper Mottled Anorthosite) Datum in each case is the Bastard Reef.

3. PETROGRAPHY OF THE MAIN ZONE

3.1 Introduction

By contrast with the sharply defined cyclic layering of the underlying Critical Zone, lithological changes in the Main Zone are often very subtle. The layering in the Main Zone conforms more to what McBirney and Noyes (1979) referred to as intermittent layering, in which layers are separated from one another by successions of relatively homogeneous rock. A layer, as defined by McBirney and Noyes, is a sheet-like discontinuity in the crystalline assemblage making up a sequence of rocks.

Meyer's (1969) work on the lowermost 1700m of the Main Zone at R.P.M. Rustenburg Section probably represents the most comprehensive petrographic analysis of the Main Zone to date. Apart from minor differences in detail, the Main Zone succession at Rustenburg corresponds remarkably well with that at Union Section. When Meyer's petrographic classification of the Main Zone is applied at Union Section, it corresponds in a broad, but significant, way with the scheme of subdivision used in this work. This is because petrographic changes reflect changes in the environment of crystallization, which are generally closely linked to geochemical changes.

The petrography of the Main Zone has been illustrated in Fig. 11, in which diagram an attempt has been made to represent all the more important textural varieties within the Main Zone. The samples illustrated were selected using Meyer's (1969) study as a primary reference point. The conceptual framework for petrographic nomenclature suggested by Irvine (1982) is used in this work, but it has been found expedient to revert to the earlier IUGS nomenclature (Streckeisen, 1973) in certain cases. One of the primary reasons for this, in the Main Zone context, is that Irvine (1982) used the term "gabbro" both for rocks which contain only monoclinic pyroxene, and for those which contain both clinopyroxene and orthopyroxene. In this respect, the IUGS term "gabbronorite", synonymous with the older term "hyperite", is more apt for describing a two-pyroxene gabbro. Certain colloquial terms have become accepted usage in the Bushveld literature (examples are "spotted" and "mottled" anorthosite), and these terms are retained where appropriate.

3.2 Units I and II

Unit I begins at the top of the Giant Mottled Anorthosite, which is represented by sample C55 in Fig. 11, and extends to 113m in SK2. Unit II begins at 113m, and extends to the base of the feldspathic pyroxenite at 223.55m. Units I and II are petrographically similar, and are separated only on the basis of geochemistry. These two units consist predominantly of leuconorite, which generally has a spotted appearance, produced by subhedral orthopyroxene primocrysts up to 3mm in diameter in a matrix of cumulus and intercumulus plagioclase and minor intercumulus clinopyroxene. Although not illustrated in Fig. 11, the leuconorite of units I and II is similar to the leuconorite of unit III (A295, Fig. 11).

3.3 Unit III

At the base of unit III, between 223.55m and 229.15, is a coarse-grained feldspathic pyroxenite. In the pyroxenite, subhedral to euhedral primocrysts of orthopyroxene (En_{72}) constitute 80% to 90% of the rock. The orthopyroxene grains vary between 0.5mm and 4mm in diameter, and are commonly characterized by the development of granulated margins. Interstitial phases are plagioclase, clinopyroxene and minor opaque oxides. There is a second pyroxenite layer, approximately 10m thick, at 272.6m, which is similar in composition and texture to the basal pyroxenite of unit III. Apart from the pyroxenite layers, and a one metre thick layer of mottled anorthosite immediately below the uppermost of the two pyroxenites, the bulk of unit III is made up of leuconorite.

The leuconorite of unit III, represented in Fig. 11 by sample A295, contains orthopyroxene and plagioclase as primocrysts, together with interstitial plagioclase and clinopyroxene. The proportion of clinopyroxene in the rock is invariably less than ten percent. Plagioclase constitutes 60 to 70 percent of the rock, whilst orthopyroxene accounts for the remaining 25 to 30 percent. The leuconorite is phanerocrystalline and equigranular, with a median grain size of approximately 1.5mm, although the plagioclase primocrysts, which are sometimes enclosed in orthopyroxene, are substantially smaller than this. Granulation of plagioclase grain boundaries is common, giving rise to a mortar texture, which is often associated with

extreme deformation of the plagioclase grains (Fig. 13c).

3.4 Unit IV

The base of unit IV, at 327 metres above the Bastard Reef, is slightly below the gradational base of the Porphyritic Gabbro Marker. The Porphyritic Gabbro Marker, referred to by Meyer (1969) as a subophitic hypidiomorphic hyperite, is very distinctive in hand specimen. This is due to the presence of brown spots of macrocrystic bronzite that attain 10mm in diameter, distributed throughout the rock. The bronzite macrocrysts are surrounded by distinctive white rims, possibly caused by the mortar texture developed in the plagioclase grains surrounding the macrocrysts.

In thin section, the bronzite macrocrysts reveal themselves as oikocrysts that enclose small, euhedral grains of plagioclase. In general, the plagioclase chadacrysts tend to increase in size towards the margins of the pyroxene oikocrysts, and the cores of the oikocrysts are often free of plagioclase (Fig. 11, sample A284). McBirney and Noyes (1979) described a similar texture in rocks from the Skaergaard intrusion, and interpreted it as evidence that both pyroxene and plagioclase grew **in situ**, the growth of the plagioclase primocrysts being arrested when they were surrounded by orthopyroxene. The groundmass of the Porphyritic Gabbro Marker is an allotriomorphic-granular framework of augite and plagioclase.

The Porphyritic Gabbro Marker does not have sharply defined contacts, but grades almost imperceptibly into the more equigranular lithologies above and below it. A significant feature of the Porphyritic Gabbro Marker, not documented by Meyer (1969), is that it marks the point in the Main Zone at which augite crystallization increases sharply (Fig. 12). The Porphyritic Gabbro Marker extends from approximately 345m to 407m, and grades upwards into more equigranular, fine- to medium-grained gabbronorite. Above 550m, the gabbronorite is extensively disrupted by Fe-rich ultramafic pegmatite bodies. The top of unit IV is placed, somewhat arbitrarily, at 550m, i.e. at the point where substantial pegmatite development begins.

3.5 Unit V

The Main Mottled Anorthosite (Molyneux, 1970) constitutes unit V of the Main Zone in borehole SK2. It is a succession of spotted and mottled anorthosites, extending from approximately 550m to 715m above the Bastard Reef. Like the Porphyritic Gabbro Marker, the Main Mottled Anorthosite is remarkably persistent laterally, and has been documented at many sites in both the eastern and the western Bushveld Complex (Meyer, 1969; Molyneux, 1970; von Gruenewaldt, 1971).

In both boreholes SK2 and SK4, the Main Mottled Anorthosite has been affected by fairly extensive alteration subsequent to crystallization, with the added complication, in SK2, of the presence of numerous bodies of ultramafic pegmatite. These features result in a blurring of the detailed petrographic variation within this unit. Sample A248 (Fig. 11) is fairly typical of the mottled anorthosite encountered within this unit. In A248, augite and biotite are intercumulus, whilst plagioclase and hypersthene are cumulus. The plagioclase grains have been enlarged by adcumulus growth, resulting in subhedral to anhedral grain shapes. The hypersthene grains are altered, and are often replaced by biotite. An horizon of gabbronorite, particularly notable for its fine grain size, occurs in unit V between 607m and 625m above the Bastard Reef (Fig. 13a).

3.6 Unit VI

Unit VI extends from the top of the Main Mottled Anorthosite to the base of the Upper Mottled Anorthosite. The interval involved stretches from 715m to 897m above the Bastard Reef. On balance, the gabbronorite of this unit is relatively leucocratic, although there is a fairly large range in modal plagioclase, from 50 to 82 modal percent (Fig. 12). Plagioclase and orthopyroxene are primocryst phases, with clinopyroxene intercumulus (sample A200, Fig. 11).

3.7 Unit VII

A 10cm thick, fine-grained orthopyroxenite at 897.7m marks the base of the Upper Mottled Anorthosite. The Upper Mottled Anorthosite consists of a series of alternating layers of leucogabbronorite and gabbronorite, grading upwards into more uniform gabbronorite at

approximately 1060m. Texturally, the most notable feature of the rocks of unit VII is that plagioclase, grains of which attain 2mm in length, is the only primocryst phase. Clinopyroxene and orthopyroxene are both intercumulus (samples A138 and A147, Fig. 11). At approximately 1350m, inverted pigeonite first appears in the gabbronorite. From this point upwards to 1600m, inverted pigeonite and primary hypersthene alternate with one another over short distances. This gradual transition to inverted pigeonite over a stratigraphic interval of 250 metres or more has been documented by von Gruenewaldt and Weber-Diefenbach (1977). These latter authors concluded that the hypersthene was produced by the reaction of early-formed pigeonite with a relatively Mg-rich liquid, and that the inverted pigeonite grains in the rock are relicts of the early-formed pigeonite.

3.8 Unit VIII

Pigeonite finally gains complete ascendancy over hypersthene at the base of unit VIII, approximately 1600m above the Bastard Reef. This appears to reflect a fairly significant event in the evolution of the Main Zone, as it also marks the return of low-Ca pyroxene to cumulus status (sample A13, Fig. 11). Pigeonite grains in this unit are generally subhedral, and tend to be elongated in the direction of igneous lamination. As noted by Raal (1965) and von Gruenewaldt (1971, 1973), amongst others, the pigeonite in these rocks is in optical continuity over large areas of the rock, and boundaries between grains are difficult to define. This feature, allied to the often irregular shape and orientation of the augite exsolution lamellae (Fig. 13e-g), is explained by Cameron and Papike (1981) on the basis that, at the point of inversion from pigeonite to hypersthene, one nucleus of the orthorhombic structure formed, and a single crystallization front swept through adjacent pigeonite grains, ignoring grain boundaries. Subsequent exsolution of augite parallel to (100) in these composite grains overprints the randomly-orientated (001) lamellae. Inverted pigeonite continues to characterize the Main Zone gabbronorite up to the base of the Pyroxenite Marker, at 2250m.

3.9 Above the Pyroxenite Marker

At the Pyroxenite Marker, or the equivalent horizon, there is a reversion from the inverted pigeonite ($En_{58.5}$) of unit VIII to primary

hypersthene ($En_{68.5}$ to En_{70}). The hypersthene grains are poikilitic, with chadacrysts of plagioclase occurring within the margins of the pyroxene grains, in what appears to be the incipient development of a texture similar to that of the Porphyritic Gabbro Marker. Hypersthene oikocrysts attain 3mm in diameter, and are probably primocrysts, although adcumulus overgrowths often give them the appearance of being an intercumulus phase. Augite, grains of which attain 1.5mm in length, also appears to be a primocryst phase, whilst plagioclase is an interstitial phase (sample MZ6, Fig. 11).

3.10 Overview of the Petrography of the Main Zone

The lowermost part of the Main Zone, from the top of the Bastard Cyclic Unit to the base of the Porphyritic Gabbro Marker, consists almost entirely of leuconorite. Clinopyroxene is an intercumulus phase in these rocks, accounting for less than ten percent by volume, whilst opaque phases are virtually absent, except in the immediate vicinity of Fe-rich ultramafic pegmatite bodies. At 223.5m and 272m in borehole SK2, the leuconorite is interrupted by orthopyroxenite layers between six and ten metres thick. These pyroxenite layers do not appear to be present everywhere in the Bushveld Complex, or even in the Union Section segment.

From 325m above the Bastard Reef in SK2, the size of orthopyroxene primocrysts begins to increase, by the mechanism of adcumulus growth. As the size of the orthopyroxene grains increases, they poikilitically enclose increasing numbers of plagioclase grains. Ultimately, the pyroxene oikocrysts reach 10mm in diameter, giving rise to the distinctive spotted appearance of the Porphyritic Gabbro Marker. The gradational upper contact of the Porphyritic Gabbro Marker occurs at approximately 407m. A petrographically significant feature is that the modal proportion of augite increases sharply, from less than 10% in the underlying leuconorite, to between 15% and 30% in the Porphyritic Gabbro Marker. It could therefore be said that the Main Zone rocks below the Porphyritic Gabbro Marker are norites, whereas those in and above the Porphyritic Gabbro Marker are gabbronoritic. It might be noted here that the term "porphyritic" is not strictly applicable to cumulus rocks, but the Name "Porphyritic Gabbro Marker" has become widely used, and so is retained in this work.

Further noteworthy intervals in the Main Zone succession are the Main Mottled Anorthosite, between 550m and 715m, and the Upper Mottled Anorthosite, between 898m and 1060m. In borehole SK4, both these intervals have thin pyroxenite layers at their bases, but in SK2, only the Upper Mottled Anorthosite has a pyroxenitic basal layer. The term "Mottled Anorthosite" conjures up images of the distinctive Giant Mottled Anorthosite of the Bastard Cyclic Unit. The Main and Upper Mottled Anorthosites are less distinctive than this, however, at least at Union Section, and consist of interlayered spotted leucogabbronorite and gabbronorite. Both the Main and the Upper Mottled Anorthosites are severely disrupted by ultramafic pegmatite in the SK2 succession. This connection between the ultramafic pegmatite bodies and the more leucocratic layers in the cumulate succession is discussed by Viljoen and Burvenich (1983).

Inverted pigeonite first appears in the Main Zone 1060m above the Bastard Reef. By 1600m, pigeonite has completely replaced hypersthene in the Main Zone gabbronorite, and continues up to the base of the Pyroxenite Marker. At this point, the composition of orthopyroxene changes abruptly, from pigeonite ($En_{58.5}$) below the Pyroxenite Marker to hypersthene (En_{70}) above. Superficially, the rocks above the Pyroxenite Marker resemble those in the lowermost 550m of the Main Zone. The distinguishing feature is the significantly higher modal proportion of clinopyroxene in the former group of rocks (Fig. 12). The Pyroxenite Marker was not identified as a physical entity at Union Section, but its equivalent position was defined on the basis of sharp geochemical and petrographic changes.

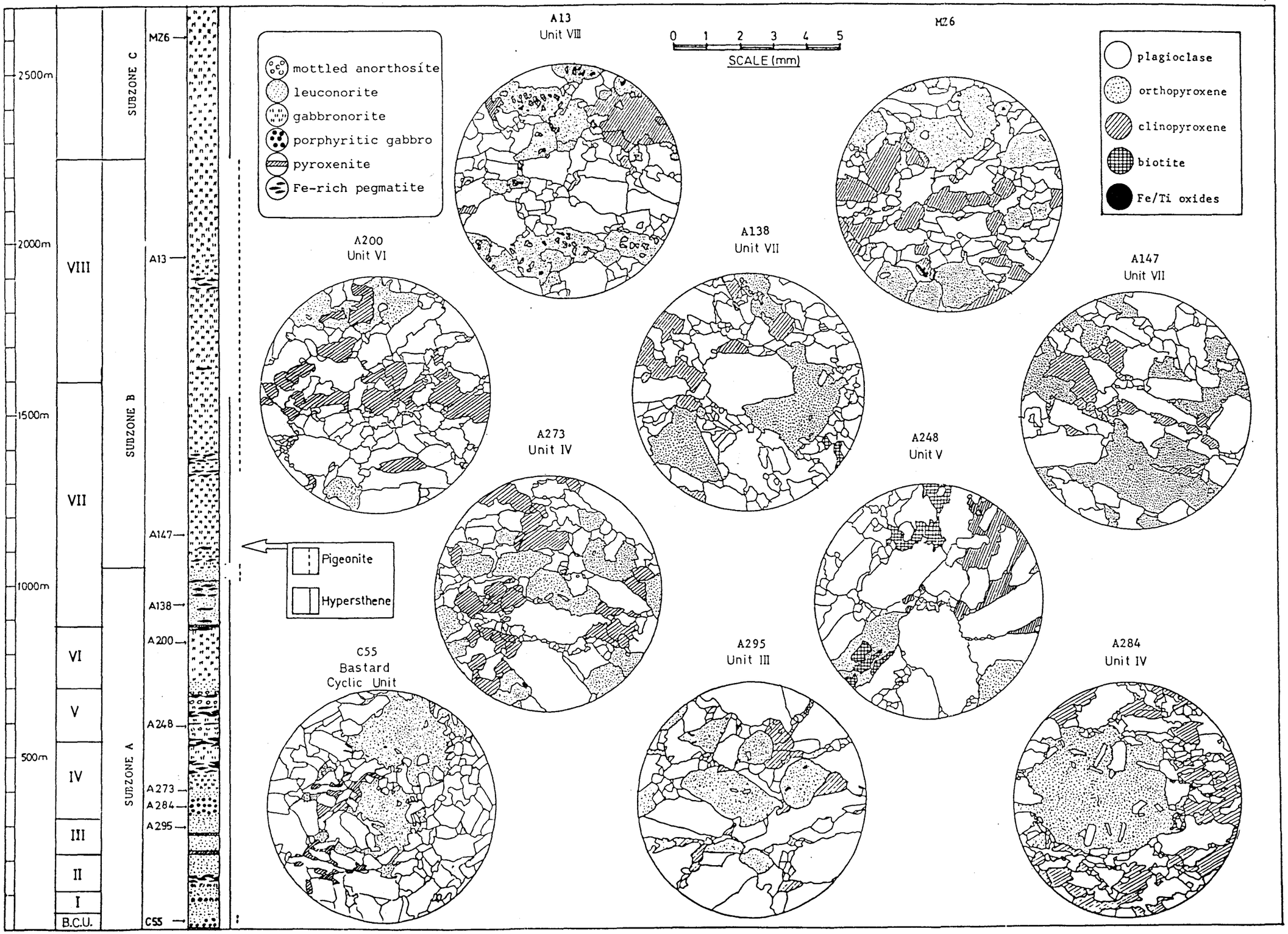
2500m
2000m
1500m
1000m
500m
SUBZONE C
SUBZONE B
SUBZONE A
VIII
VII
VI
V
IV
III
II
I
B.C.U.
MZ6
A13
A147
A138
A200
A248
A273
A284
A295
C55
mottled anorthosite
leuconorite
gabbronorite
porphyritic gabbro
pyroxenite
Fe-rich pegmatite
Pigeonite
Hypersthene
0 1 2 3 4 5
SCALE (mm)
plagioclase
orthopyroxene
clinopyroxene
biotite
Fe/Ti oxides
A13
Unit VIII
MZ6
A200
Unit VI
A138
Unit VII
A147
Unit VII
A273
Unit IV
A248
Unit V
C55
Bastard
Cyclic Unit
A295
Unit III
A284
Unit IV

FIG. 11

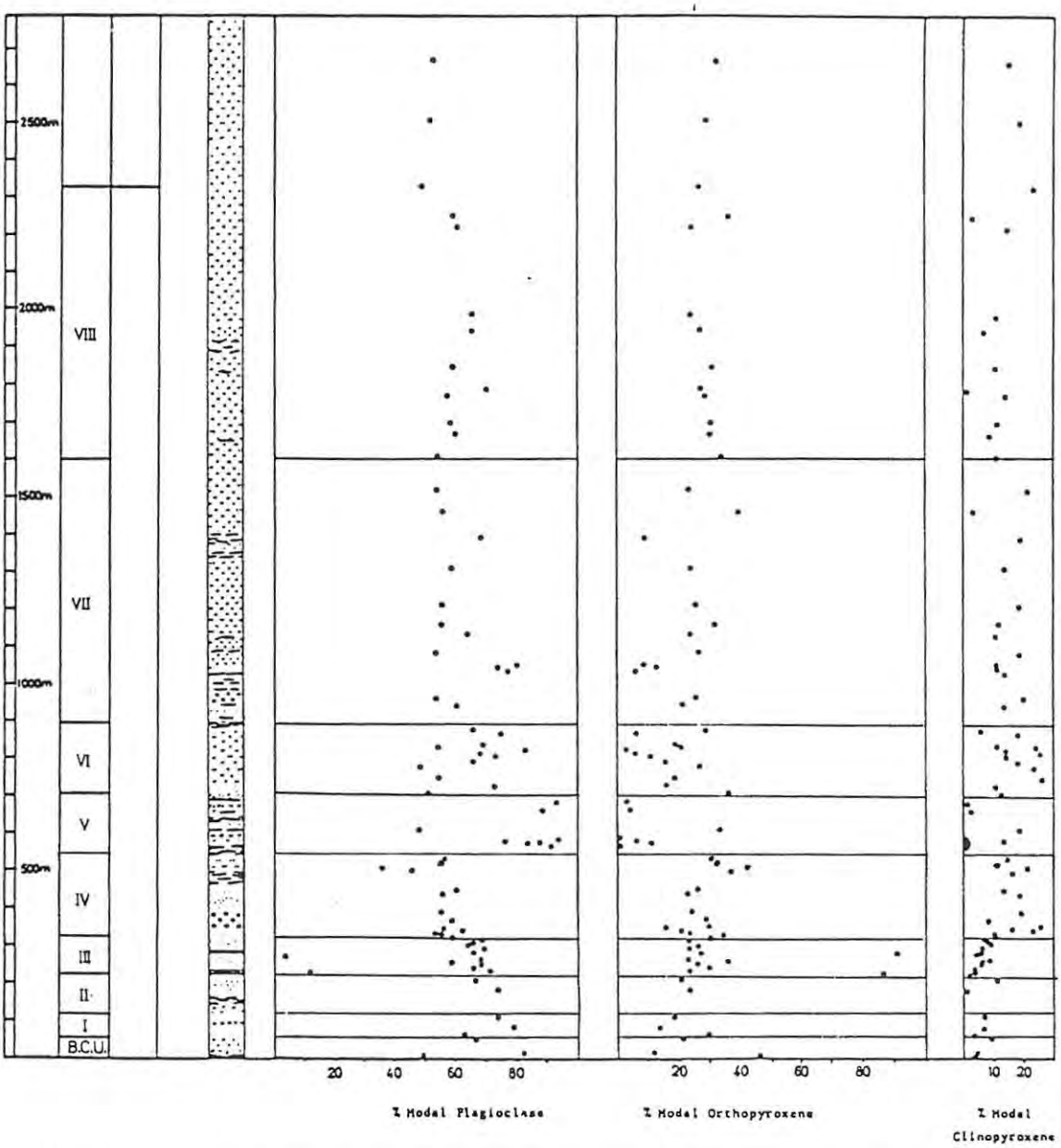

Fig. 12 : Point counted modal analyses of the Main Zone at R.P.M. Union Section. (Modal data are presented in appendix 5.)

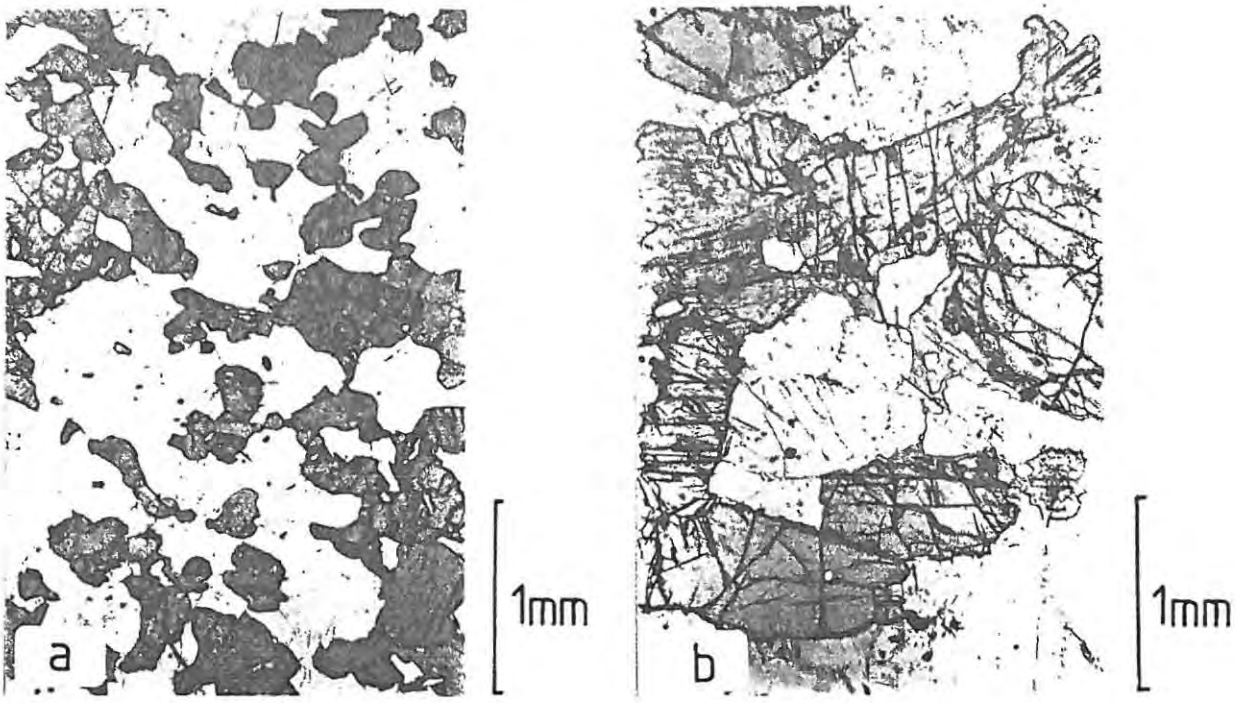

Fig. 13 (a & b) : The abnormally fine-grained nature of the pyroxene (dark grey) in sample A236 (619m above the Bastard Reef) is contrasted with the more "normal" grain size of the overlying gabbros (A235, 646m above the Bastard Reef).

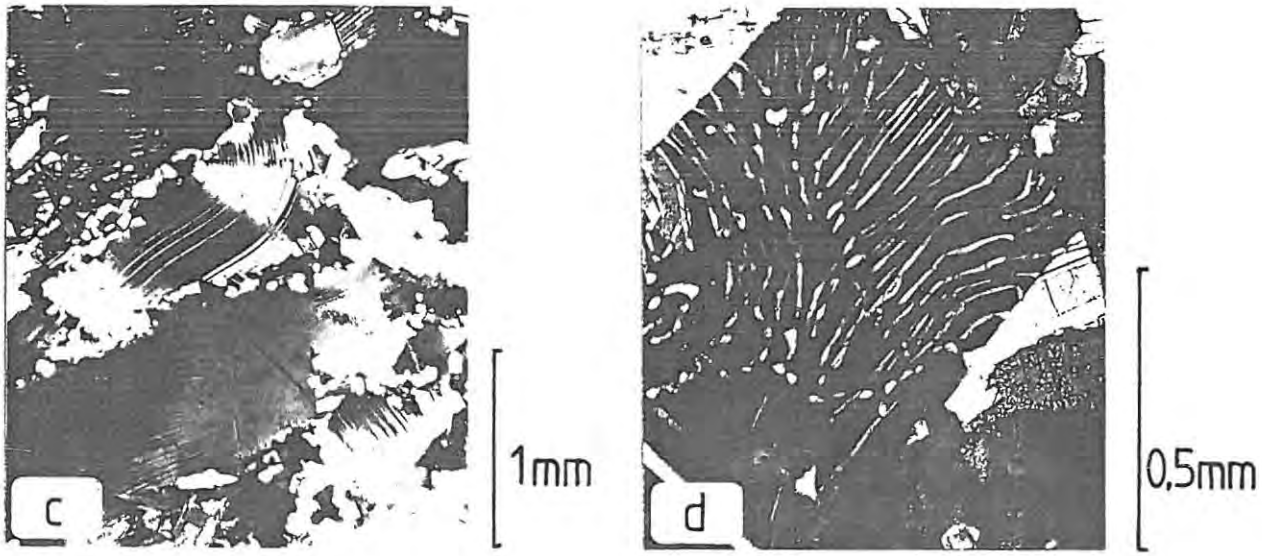

Fig. 13 (c & d) : Features of plagioclase in the Main Zone: in sample A340 (50m above Bastard Reef), plagioclase grains are often bent, and larger grains are surrounded by a mortar texture of smaller sub-grains (Fig. 13, c). In sample A35 (1804m above Bastard Reef), myrmekite is common.

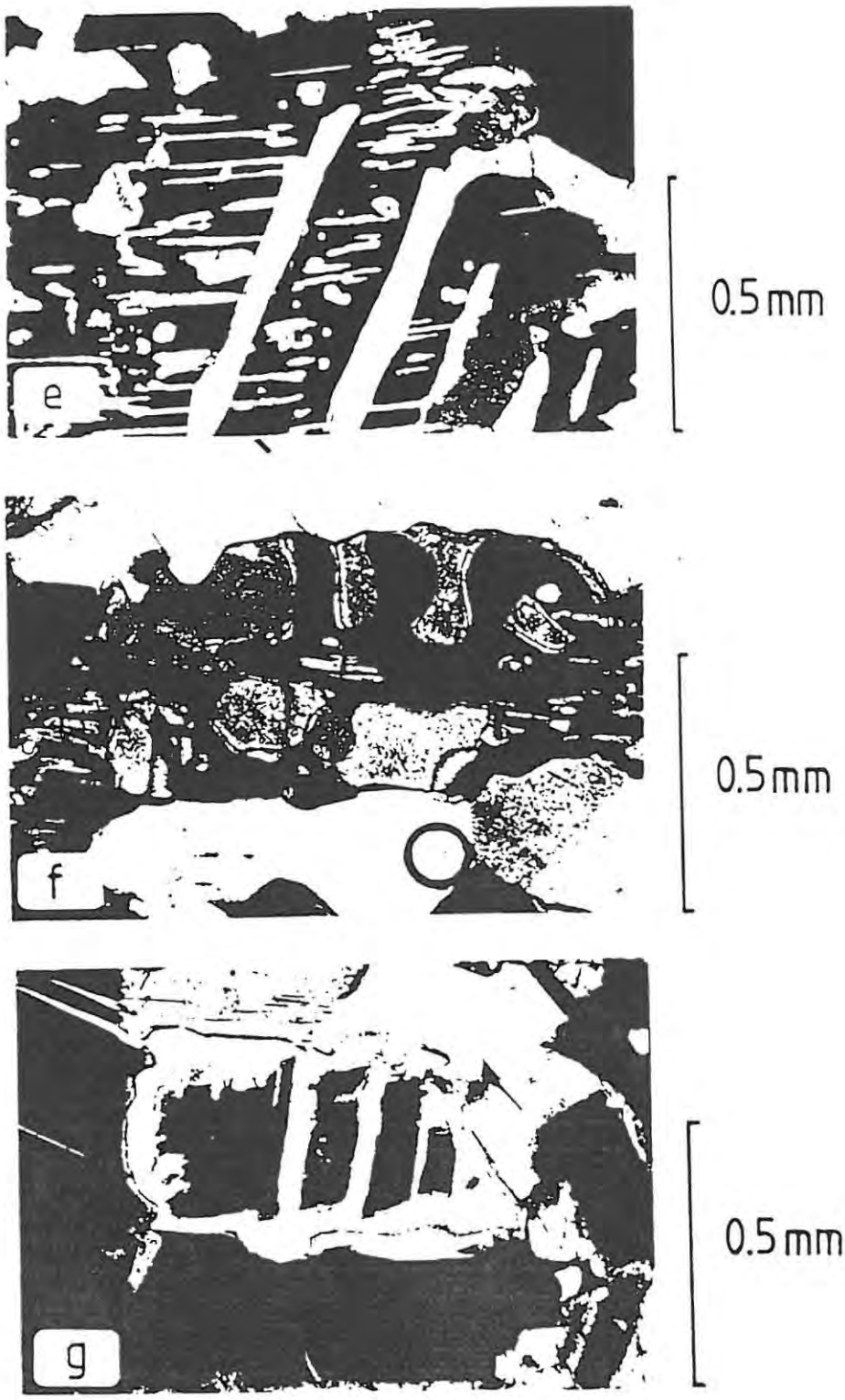

Fig.13 e-g. A study of progressive exsolution of augite (light grey) from inverted pigeonite (black). In Fig.13e, fine exsolution of augite along (100) is complemented by coarser augite lamellae along (001). In Fig.13f, fine lamellae along (100) are still present, but (001) exsolution has the form of amorphous blebs. Ultimately, augite forms a halo around the inverted pigeonite (Fig.13g), with augite lamellae along (001) remaining intact. Fig.13 e-g all from sample A35.

4. MINERAL CHEMISTRY

4.1 Introduction

There is a limited amount of analytical data available on the composition of the pyroxenes in the Main Zone (**inter alia** Atkins, 1969; Markgraaf, 1976; von Gruenewaldt, 1977). Apart from these reconnaissance-type studies, mineralogical data have until now had to be gleaned from the optical determinations by Meyer (1969), Molyneux (1970) and von Gruenewaldt (1971). New electron microprobe data presented in this work (appendix 6) represent a fairly detailed coverage of compositional variations in plagioclase, orthopyroxene and clinopyroxene in the Main Zone. The compositional variations in these three minerals with stratigraphic height are represented, in the first instance, in terms of the ionic Mg/(Mg+Fe) ratio (MMF) in the case of the pyroxenes, and in terms of the end members albite and anorthite in the case of plagioclase. In addition, variations in the concentration of various minor elements in the respective minerals are illustrated and described. In this discussion pigeonite, which is invariably inverted to hypersthene with the concomitant exsolution of augite along (001), is included with primary orthopyroxene under the subsection on orthopyroxene. Accessory and secondary minerals (opaque oxides, amphiboles and biotite) are generally present only as very small grains, and have not been analyzed. Where a single value is quoted for a composition or a ratio, this value is the mean for the given sample, unless stated otherwise.

4.2 Orthopyroxene

Data presented by von Gruenewaldt (1973) show an overall trend of steady iron-enrichment in orthopyroxene through the Main Zone, from the top of the Bastard Cyclic Unit to approximately 100 metres below the Pyroxenite Marker. There are minor perturbations in this trend at the Upper Mottled Anorthosite, which marks the beginning of the zone of transition from primary hypersthene to inverted pigeonite. The hypersthene/pigeonite transition is reported in some more detail by von Gruenewaldt and Weber-Diefenbach (1977). The Union Section orthopyroxene data, presented here, conform in general terms to the trend of iron-enrichment through the Main Zone observed by von Gruenewaldt (1973). There are, however, significant departures from

the gross iron-enrichment trend in the data presented here, particularly in the lowermost 700 metres of the Main Zone (Fig. 14).

At Roossenekal, von Gruenewaldt (1973) noted the apparently anomalous appearance of pigeonite (En_{66}) in a sample from within the Giant Mottled Anorthosite, 93 metres above the Merensky Reef. Molyneux (1970) reported a similar brief occurrence of pigeonite, this time at approximately 300 metres above the Merensky Reef, in the Steelpoort area. In the present study, brief occurrences of pigeonite were observed within the Bastard Cyclic Unit, at 30m above the Bastard Reef, and again at the base of Main Zone unit II (sample A322). In sample A322, the composition of the pigeonite is En_{62}.

4.2.1 The Orthopyroxene MMF Ratio

Orthopyroxene from two samples of the Bastard Cyclic Unit, underlying Main Zone unit I, have been analyzed in this study, mainly to provide continuity with de Klerk's (1982) work on the Upper Critical Zone. The first of these samples is A349, which represents the melanorite immediately above the Bastard Reef. A349, with an MMF ratio of 0.807, is substantially more magnesian than any of the Main Zone orthopyroxene analyses. Orthopyroxene becomes rapidly more iron-rich upwards in the Bastard Cyclic Unit, and by 18 metres above the Bastard Reef, the MMF ratio is 0.676 in sample A346. In Main Zone unit I, orthopyroxene has been analyzed from only three samples. There is no definite trend apparent in these three samples, but MMF ranges from a minimum of 0.665 to a maximum of 0.743, the highest value being recorded in sample A327, at the top of unit I.

Across the boundary between units I and II, there is a rapid decrease in the MMF ratio, and in sample A322, at the base of unit II, the orthopyroxene MMF ratio of 0.643 is relatively iron-rich. From sample A322, there is a progresive increase in the orthopyroxene MMF ratio throughout unit II, culminating in a ratio of 0.720 (sample A312) at 208.5 metres. The possible reasons for the apparently reversed trend of fractionation of the orthopyroxene in unit II will not be discussed here, but it is worth mentioning that there is a substantial development of ultramafic pegmatite bodies in this unit.

The pyroxenite layer at 223.55m marks the base of unit III (Fig. 14).

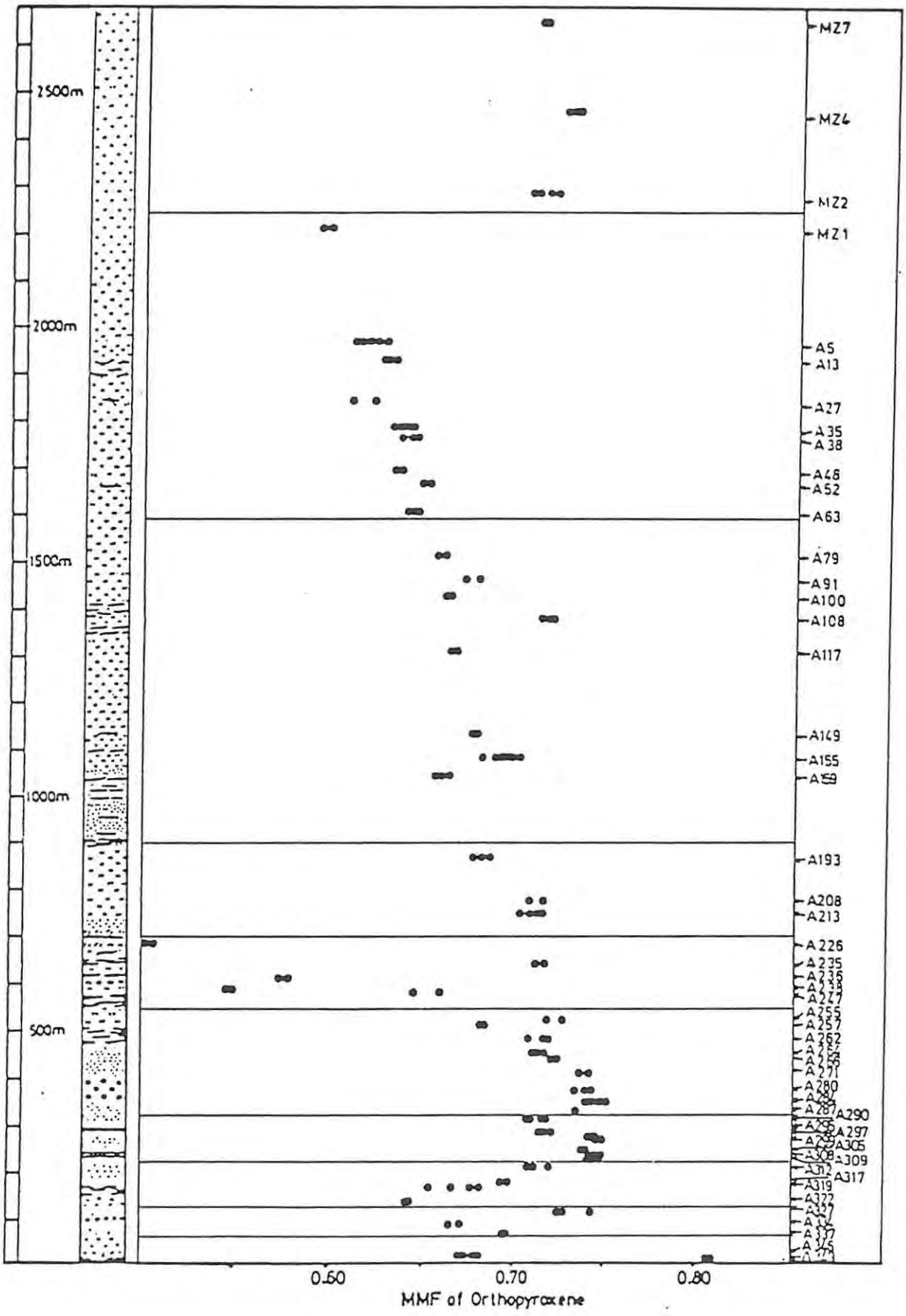

Fig. 14 : Variations in the ratio Mg/(Mg+Fe) with stratigraphic height in the Main Zone.

From the pyroxenite at 223.55m (sample A309) to the pyroxenite at 275m (sample A297), the orthopyroxene MMF ratio is fairly constant at a mean of 0.744, with a standard deviation of 0.003. Above the pyroxenite layer at 275m, there is a noticeable decrease in the orthopyroxene MMF ratio, and the remaining two samples in unit III (A295 and A290) have orthopyroxene MMF ratios which average 0.715, with a standard deviation of 0.004.

Near the base of unit IV, the orthopyroxene MMF ratio increases to 0.735 in sample 287, 332m above the Bastard Reef. In sample A284, which is within the Porphyritic Gabbro Marker at 350m, the orthopyroxene MMF ratio reaches a maximum of 0.751 (Fig. 14). From sample A284 upwards through unit IV, there is a steady decrease in MMF, to 0.684 in sample A257, 517 metres above the Bastard Reef. In sample A255, at the top of unit IV, the MMF ratio increases sharply to 0.723.

In the Main Mottled Anorthosite (unit V), all but one of the samples analyzed are anomalously enriched in iron to varying degrees, the most Fe-rich being sample A226 (MMF=0.501), a leucogabbro near the top of unit V. The exception in unit V is sample A235, which has an MMF ratio of 0.715. This latter ratio is more or less the value predicted for this part of the succession by the extrapolation of the overall trend in the Main Zone orthopyroxene MMF ratios (Fig. 14).

Barring local aberrations, the orthopyroxene MMF ratio decreases steadily throughout Main Zone units VI, VII and VIII,culminating in a ratio of 0.596 in sample MZ1 (Fig. 14). The orthopyroxene MMF ratio increases dramatically across the Pyroxenite Marker, from 0.596 in sample MZ1 to a mean of 0.713 in sample MZ2 (Fig. 14). Above the Pyroxenite Marker, the samples analyzed display a range of MMF ratios from 0.706 to 0.728.

4.2.2 Minor Elements in Orthopyroxene

In Fig. 15, the variations of the minor elements (represented as the oxides Cr_2O_3, TiO_2 and Al_2O_3) in orthopyroxene are shown relative to stratigraphic height in the Main Zone. Nickel is excluded from this diagram, not because of its lesser importance, but because its concentration in orthopyroxene is below detection limit over much of the Main Zone.

4.2.2(a) $\underline{Cr_2O_3}$

The concentration of Cr_2O_3 in orthopyroxene displays fairly large within-sample variations in the Main Zone, particularly in the lowermost few hundred metres. In sample A349, near the base of the Bastard Cyclic Unit, a concentration of 0.5 weight percent Cr_2O_3 was recorded in orthopyroxene (not indicated in Fig. 15). This Cr_2O_3 concentration is substantially higher than those in any of the Main Zone samples (Fig. 15), but accords with orthopyroxene Cr_2O_3 concentrations recorded by de Klerk (1982) over much of the Upper Critical Zone at Union Section. In sample A346, 18.2m above the Bastard Reef, but still within the Bastard Cyclic Unit, Cr_2O_3 in orthopyroxene is sharply lower, at between 0.11 and 0.20 weight percent. There is an overall decrease in orthopyroxene Cr_2O_3 from sample A346 through the rest of the Bastard Cyclic Unit, and continuing upwards through Main Zone units I, II and III. This trend ends at sample A290, 313m above the Bastard Reef, in which the orthopyroxene Cr_2O_3 content ranges from 0.08% to 0.11%.

In sample A287 (332m), near the base of unit IV, orthopyroxene Cr_2O_3 increases sharply to above 0.13% (Fig. 15). From the base of unit IV, the orthopyroxene Cr_2O_3 content is consistently more than 0.12% up to 455m (sample A264). This interval comprises the Porphyritic Gabbro Marker and its immediate hanging- and footwall. The Cr_2O_3 content of orthopyroxene in sample A264 ranges between 0.12 and 0.14 weight percent. Thirty-two metres above A264, the Cr_2O_3 in sample A262 is sharply lower at between 0.06 and 0.10 weight percent. Samples A257 and A255, the remaining samples in unit IV, also have orthopyroxene Cr_2O_3 contents of 0.10 weight percent or less (Fig. 15).

In sample A247 (580.9m), near the base of unit V, the orthopyroxene Cr_2O_3 content is 0.07 to 0.08 weight percent. Above this, orthopyroxene Cr_2O_3 rarely exceeds 0.06% for the entire interval up to 2250 (the base of the Pyroxenite Marker. In some samples in this interval, orthopyroxene Cr_2O_3 may be as low as 0.01 weight percent (sample A226, at 691.5m). Orthopyroxene Cr_2O_3 increases from 0.05% in sample MZ1 (at the top of unit VIII) to between 0.09% and 0.14% in sample MZ2, above the Pyroxenite Marker. Samples MZ2, MZ4 and MZ7, representing the first 440m above the Pyroxenite Marker, have a mean

orthopyroxene Cr_2O_3 content of 0.11 weight percent, with a standard deviation of 0.018.

4.2.2(b) $\underline{TiO_2}$

Variations in orthopyroxene titanium content in the Main Zone are less well defined than is the case for Cr_2O_3 (Fig. 15). There is a particularly wide scatter in orthopyroxene TiO_2 concentrations through units I, II and III. The range in this interval is from 0.15 weight percent TiO_2 (in sample A317, at 283.5m), to 0.88 weight percent TiO_2 (sample A319, at 165.5m). The high TiO_2 contents of the A319 orthopyroxene might possibly be related to the close proximity of an ultramafic pegmatite body. Towards the top of unit III, however, samples A295 (283.5m) and A290 (312.9m) have high orthopyroxene TiO_2 contents (0.63 and 0.53 weight percent, respectively), which cannot be related directly to the close proximity of ultramafic pegmatite bodies. At the base of unit IV, there is a noticeable change in the pattern of orthopyroxene TiO_2 concentration variations (Fig. 15). Most noticeably, there is only one isolated case, in the entire interval from unit IV to unit VIII, in which TiO_2 exceeds 0.3 weight percent (viz. sample A155).

Microprobe analyses by de Klerk (1982) indicate that TiO_2 regularly exceeds 0.3 weight percent in orthopyroxene in the Upper Critical Zone. The one high TiO_2 analysis (0.49 weight percent) in sample A155 is considered aberrant (the mean of eight other analyses on the same sample is 0.21 weight percent). On this basis, the absence of high-Ti orthopyroxene above the base of unit IV may well be significant. There is no notable change in orthopyroxene TiO_2 across the Pyroxenite Marker.

4.2.2(c) $\underline{Al_2O_3}$

Analyses of orthopyroxene from the Lower Critical Zone (de Klerk, 1982) indicate that below the Bastard Reef, the concentration of Al_2O_3 in orthopyroxene is almost invariably higher higher than 1.2 weight percent. In sample A349, a norite 5.7m above the Bastard Reef, the mean concentration of Al_2O_3 in orthopyroxene is 1.22 weight percent. Slightly higher up, in sample A346 (18.2m), the Al_2O_3 content of orthopyroxene decreases to a mean of 0.67%. Samples A337, A334 and

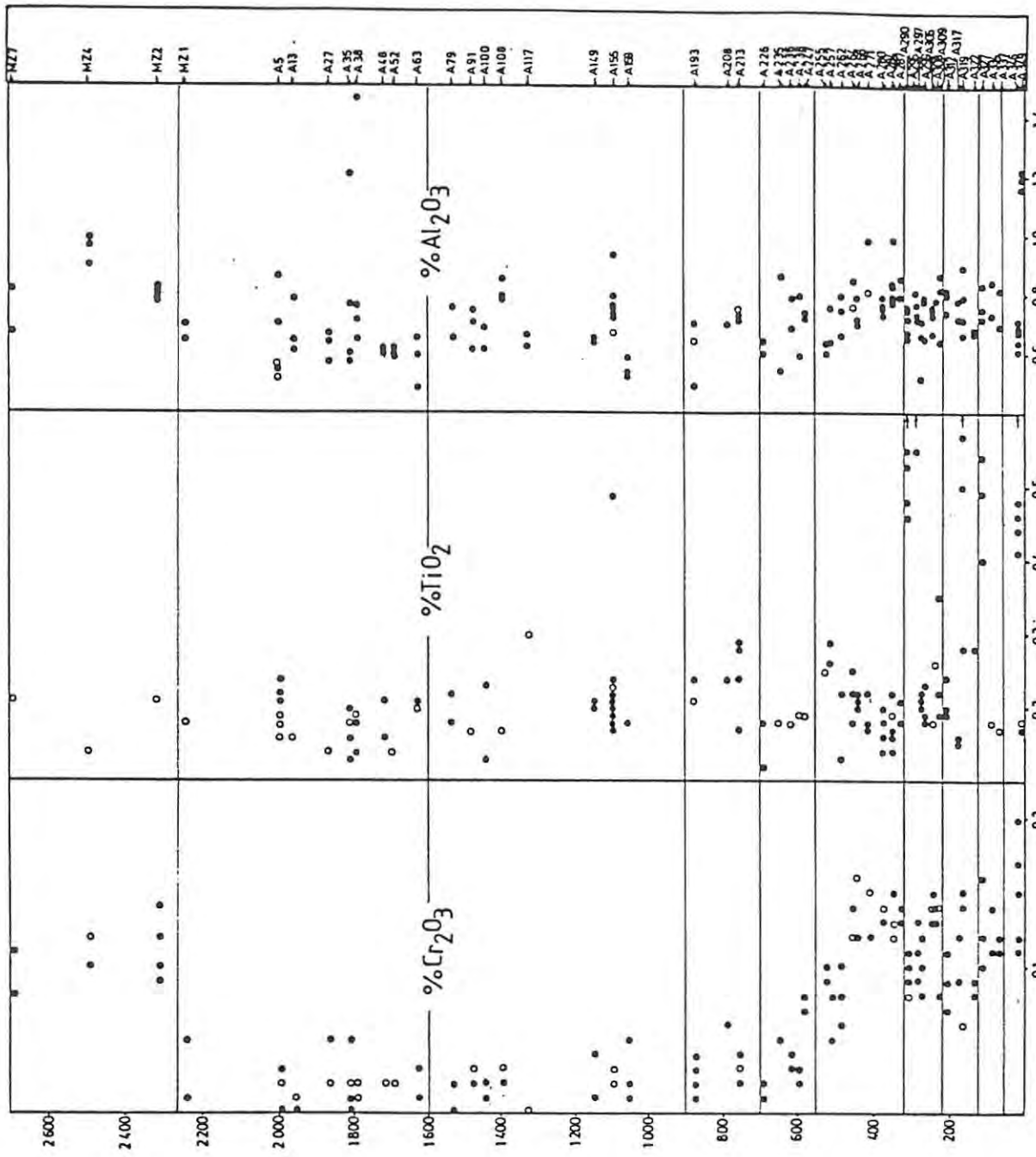

Fig. 15 : Variations in the concentration of Cr_2O_3, TiO_2 & Al_2O_3 in orthopyroxene versus stratigraphic height in the Main Zone. Data points represented on the diagram by open circles are the result of two or more equivalent analyses on the same sample. Shaded circles represent single analyses. Small arrows along the righthand margins of the Cr_2O_3 and TiO_2 plots indicate concentrations which exceed the limits of the plots. Sample numbers are given on the righthand side of the diagram.

A327, in Main Zone unit I, have orthopyroxene Al_2O_3 concentrations in the range 0.69 to 0.84 weight percent. The range of Al_2O_3 concentrations in unit II is much the same as in unit I, although some samples display wider within-sample ranges than others (A319, for example, displays a range of 0.66 to 0.89 weight percent Al_2O_3).

There is a sharp change in orthopyroxene Al_2O_3 concentrations across the boundary between units III and IV. Sample A290, near the top of unit III, contains 0.71 weight percent Al_2O_3 in orthopyroxene. In sample A287, close to the base of unit IV, orthopyroxene Al_2O_3 is 0.83 weight percent. Similarly, sample A284, also in unit IV, displays a concentration of 0.82 weight percent Al_2O_3 in orthopyroxene. Through unit IV and into unit V, there is a gross trend of decreasing orthopyroxene Al_2O_3, and sample A226, near the top of unit V, has an orthopyroxene Al_2O_3 content of 0.62 weight percent.

Low sample density, combined with relatively large within-sample compositional variations, makes the identification of trends somewhat difficult in units VI, VII and VIII. Nevertheless, there appears to be a distinct change in orthopyroxene across the boundary between unit V and unit VI, from 0.62% in sample A226 to 0.74 weight percent Al_2O_3 in sample A213. Similarly, there is another apparent sharp change across the boundary between units VII and VIII, from a mean of 0.70% in sample A79 to a mean of 0.57 weight percent Al_2O_3 in sample A63. Across the Pyroxenite Marker, there is a progressive increase in orthopyroxene Al_2O_3, from 0.67% in MZ1, through 0.79% in MZ2, to 0.95 weight percent in MZ4 (Fig. 15). Above MZ4, the Al_2O_3 content of orthopyroxene decreases to 0.75 weight percent in sample MZ7, 440 metres above the Pyroxenite Marker.

4.3 Augite

Trends of chemical variation in augite mimic those of orthopyroxene very closely, except in terms of absolute concentration. Whilst the MMF ratio of augite in the Main Zone is higher in absolute terms than the MMF ratio of orthopyroxene from equivalent stratigraphic positions, the broad pattern of variation in MMF ratio is essentially the same for both minerals (Fig. 14; Fig. 16). One of the most pronounced features of the plot of orthopyroxene MMF ratio versus stratigraphic height, namely the extreme iron-enrichment of most samples in unit V, is

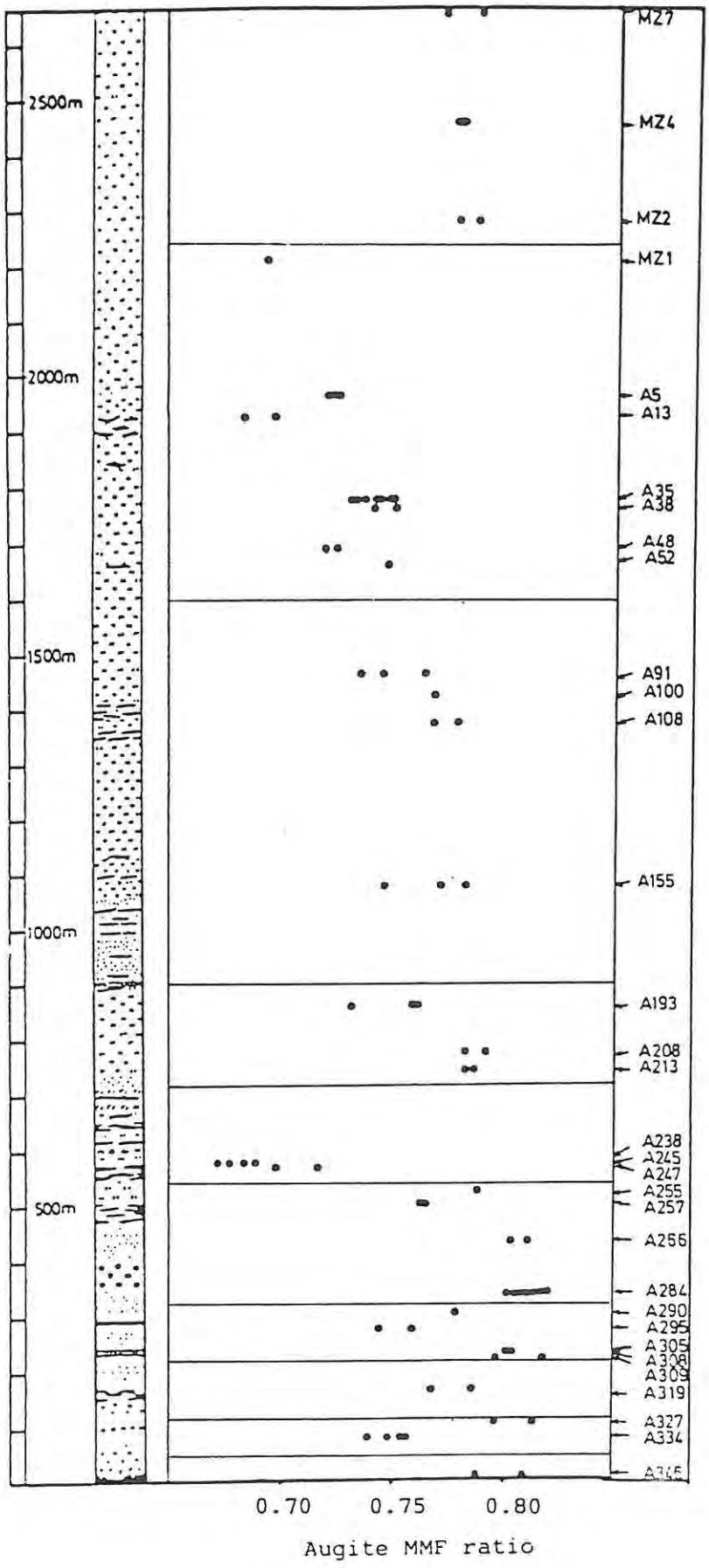

Fig. 16 : Variations in the Mg/(Mg+Fe) ratio of augite with stratigraphic height in the Main Zone.

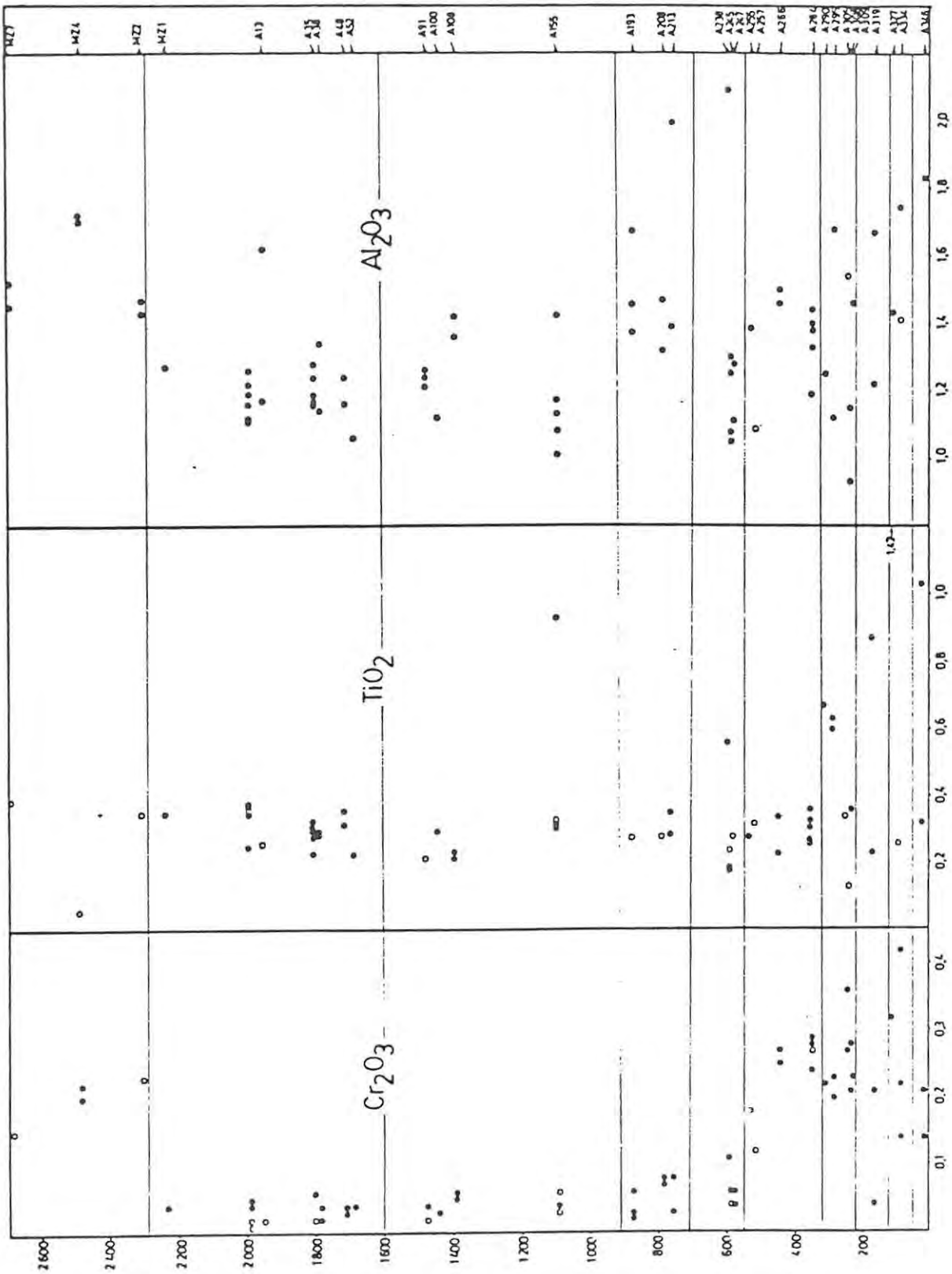

Fig. 17 : Variations in Cr_2O_3, TiO_2 & Al_2O_3 in augite with stratigraphic height in the Main Zone. Open circles are data points representing more than one analysis. Shaded circles represent single analyses.

replicated in the corresponding plot for augite (Fig. 16). A likely explanation for the enhanced iron-enrichment of the majority of the samples analyzed from unit V (the Upper Mottled Anorthosite) lies in the operation of a secondary process, possibly of a late-magmatic nature, and probably linked to the formation of the Fe-rich ultramafic pegmatite bodies.

The lower sample density of the augite analyses compared with the orthopyroxene analyses makes it difficult to determine whether the patterns evident in the MMF plot of orthopyroxene (Fig. 14) are also reflected in the behaviour of augite. The marked increase in the MMF ratio of orthopyroxene at the Pyroxenite Marker is, however, clearly visible in the plot of the MMF ratio of augite (Fig. 16). In broad terms, and excluding the anomalous enhanced iron-enrichment trend, the augite MMF ratio decreases progressively from values of the order of 0.80 in the upper part of the Bastard Cyclic Unit to 0.70 or less at the top of Main Zone unit VIII. Across the Pyroxenite Marker, the augite MMF increases sharply to ratios in the vicinity of 0.78.

In common with the MMF ratio, the behaviour of the minor elements, Cr, Ti and Al, in augite is in sympathy with the behaviour of the same elements in orthopyroxene. The major difference between augite and orthopyroxene in terms of minor elements is, once again, a matter of absolute concentration. In this respect, the concentration of Cr_2O_3 in augite in unit I to IV of the Main Zone is generally in the range 0.1 to 0.4 weight percent (Fig. 17). By comparison, the Cr_2O_3 of orthopyroxene in the same units is between 0.05 and 0.2 weight percent. The behaviour of aluminium is much the same, with the concentration of Al_2O_3 in augite being consistently higher than that of orthopyroxene, by approximately 0.4 weight percent.

4.4 Plagioclase

Von Gruenewaldt (1971) employed both X-ray diffraction and optical methods to determine the composition of plagioclase in the Main and Upper Zones of the eastern Bushveld Complex. His main observation was that the compositional trend of plagioclase with stratigraphic height follows very closely the form of the orthopyroxene compositional trend. Von Gruenewaldt (op. cit.) determined a plagioclase composition of An_{76} for rocks immediately above the Merensky Reef. Upward from this point,

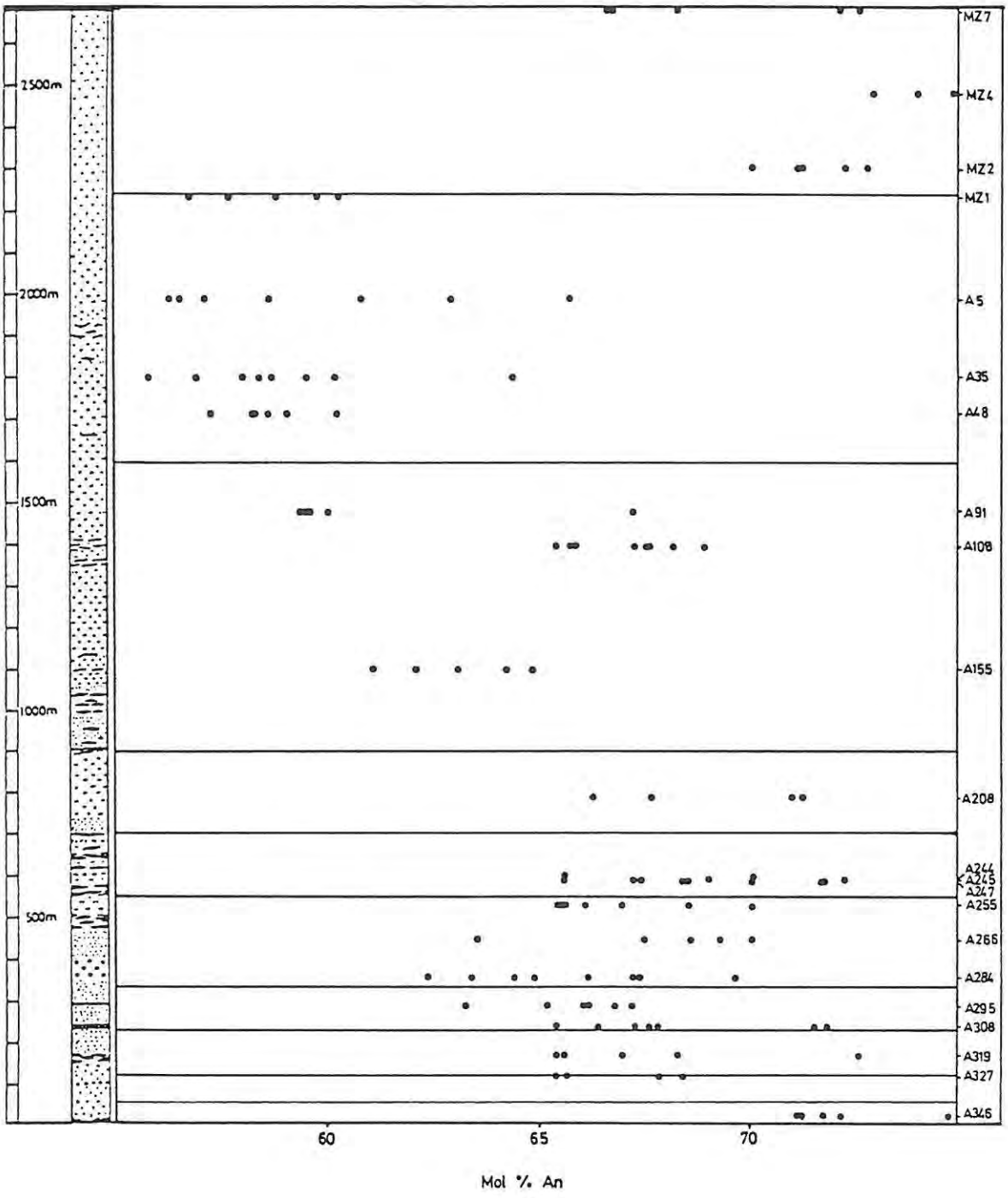

Fig. 18 : Variations in mol% An with stratigraphic height in the Main Zone.

von Gruenewaldt indicated a more or less steady decrease in An content of plagioclase to the base of the Pyroxenite Marker, where he determined a composition of An_{56}. Within this stratigraphic interval, a series of minor inflections in the trend of decreasing An content were identified. Von Gruenealdt (1971) determined the plagioclase composition to be of the order of An_{70} for the first 350m above the Pyroxenite Marker. Above this, the An-content of plagioclase decreases rapidly, reaching An_{60} by the top of Subzone C of Molyneux's (1970) classification of the Main Zone.

At R.P.M. Union Section, the composition of plagioclase in the Merensky Reef is An_{64} or less (de Klerk, 1982). De Klerk's data show plagioclase to become more calcic upwards, reaching An_{77} near the top of the Merensky Cyclic Unit. De Klerk's data represent a relatively small number of analyses, and giveonly a limited idea of the extent of compositional zoning in plagioclase. Kruger (1982) indicated that zoning can produce a compositional spread of between 5 and 15mol percent An within individual Upper Critical Zone samples, especially where the plagioclase is intercumulus. Plagioclase in the Main Zone at Union Section exhibits compositional ranges of the order of 10 to 15 mol percent An within individual samples (Fig. 18; Appendix 6). Zoning of both cumulus and intercumulus plagioclase appears to be fairly complex. The assertion, by a number of researchers into the Bushveld Complex, that cumulus plagioclase exhibits reverse compositional zoning (Liebenberg, 1942; Wager and Brown, 1968; Ferguson and Wright, 1970), is probably an oversimplification of the true situation. There is some evidence that zoning is oscillatory (de Klerk, 1982; this study).

De Klerk (1982) recorded plagioclase compositions of the order of An_{73} in the norite and anorthosite of the Merensky Cyclic Unit. In the present study, plagioclase compositions between $An_{70.2}$ and $An_{74.8}$ have been determined in norite from the Bastard Cyclic Unit (sample A346, 18.2m above the Bastard Reef). In sample A327, near the top of Main Zone unit I, sample A327 contains plagioclase with a range in compositions from $An_{66.5}$ to $An_{69.6}$. Although the within-sample spread of compositions is often fairly considerable, the An content of plagioclase appears to decrease progressively through units I, II and III of the Main Zone (Fig. 18). Sample A295, within unit III, displays a range of plagioclase compositions from $An_{63.2}$ to $An_{67.2}$. In unit IV, although only three samples have been analyzed, there appears to be a

general upward increase in the An content. Sample A284, near the base of unit IV, displays a range of plagioclase compositions from $An_{63.59}$ to $An_{70.60}$. Approximately half way up unit IV, sample A266 displays a range of compositions from $An_{64.5}$ to $An_{71.42}$. The plagioclase composition of sample A255, near the top of unit IV, ranges from $An_{66.23}$ to $An_{71.23}$. The broad upward increase in the Ca-content of plagioclase continues into unit V, where the plagioclase in sample A247 ranges in composition up to $An_{72.59}$.

From the base of unit V, there is a progressive decrease in the Ca-content of plagioclase up to the top of unit VIII, where plagioclase ranges between $An_{56.8}$ and $An_{60.3}$ in sample MZ1. Although there are probably some fairly significant variations over this part of the succession, the restricted number of samples analyzed, coupled to the sometimes extreme within-sample variation in plagioclase composition, precludes any detailed observations. Above the Pyroxenite Marker, the Ca-content of plagioclase increases sharply, to between An_{70} and $An_{72.8}$ in sample MZ2.

Partial trace element analyses were performed on plagioclase separates from twelve Main Zone cumulate rocks (Table 1), covering the elements Zr, Y, Nb, Rb, Sr, Ba and Sc. Scandium has a distribution coefficient substantially less than one for plagioclase, and is used here simply as a guide to the purity of the separates, which appear from optical examination to be more than 95% pure. In table 2, major element analyses are provided for a selection of five plagioclase separates. All analysis of plagioclase separates was done by X-ray fluorescence methods.

Assuming that all the whole-rock Sr is accepted into plagioclase, Sr concentrations in modal plagioclase were calculated, and are plotted against stratigraphic height in Fig. 19. Sr analyses of plagioclase separates are included in the diagram, and correspond closely with values determined for modal plagioclase. The modally determined concentrations are more scattered, as might be expected from inaccuracies in the modal analysis of coarse-grained rocks. The distribution coefficient for Sr into plagioclase is significantly more than one. On this basis, the Sr-content of plagioclase would be expected to decrease with increasing fractionation of a single batch of magma.

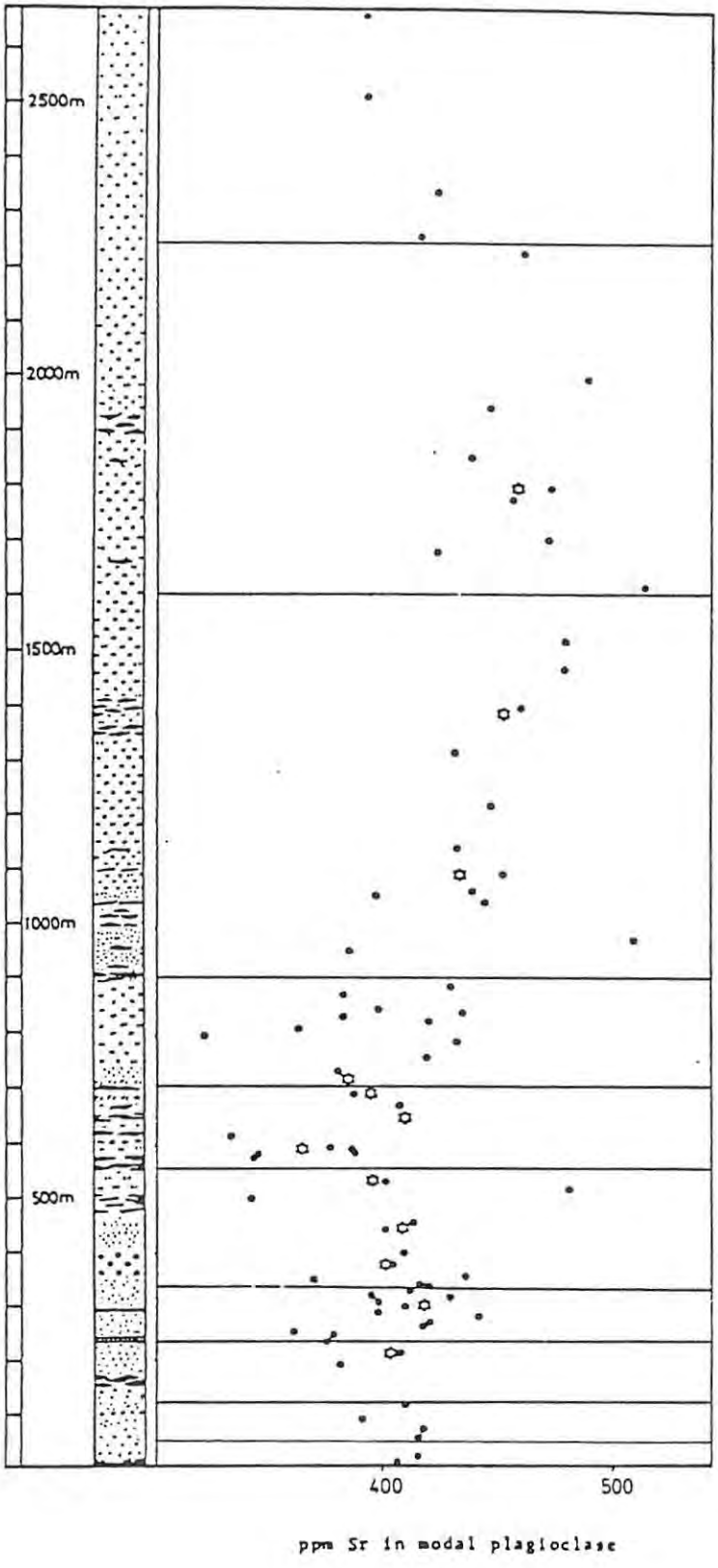

Fig. 19 : Plot of strontium in plagioclase in the Main Zone. Shaded circles represent concentrations calculated from whole-rock analyses on the basis of proportion of modal plagioclase. Stars represent XRF analyses of plagioclase mineral separates.

TABLE 1

PARTIAL TRACE ELEMENT ANALYSES OF PLAGIOCLASE SEPARATES

	A35	A108	A155	A221	A226	A235	A241	A255	A266	A280	A292	A312
Zr	0.0	0.0	0.0	0.0	0.0	3.0	2.6	0.0	0.0	2.6	0.0	3.0
Y	0.0	2.2	2.3	0.0	0.0	0.0	0.0	0.0	0.0	2.1	0.0	0.0
Nb	0.0	0.0	0.0	0.0	0.0	0.0	0.0	0.0	0.0	0.0	0.0	0.0
Rb	3.3	3.0	0.0	4.0	0.0	3.0	0.0	0.0	0.0	0.0	2.3	2.4
Sr	461	454	435	385	395	410	365	397	408	402	418	404
Ba	109	111	107	136	127	197	98	141	106	153	115	114
Sc	2.8	2.4	2.5	3.9	4.2	3.4	3.3	3.7	3.9	2.8	4.4	2.5

TABLE 2

MAJOR ELEMENT ANALYSES OF PLAGIOCLASE SEPARATES

	A35	A108	A155	A280	A312
SiO_2	53.30	52.38	51.41	51.16	51.36
TiO_2	0.04	0.04	0.12	0.04	0.03
Al_2O_3	29.53	30.33	30.71	30.56	30.95
FeO	0.57	0.34	0.28	0.46	0.32
MnO	0.00	0.00	0.00	0.00	0.00
MgO	0.24	0.29	0.28	0.51	0.20
CaO	12.16	12.56	13.29	13.76	13.42
Na_2O	3.81	3.71	3.59	3.18	3.38
K_2O	0.29	0.32	0.28	0.29	0.31
P_2O_5	0.003	0.00	0.003	0.00	0.00
Total	99.94	99.97	99.96	99.96	99.97
Cations per 8 oxygens					
Si	2.414	2.375	2.339	2.331	2.336
Ti	0.001	0.001	0.004	0.001	0.001
Al	1.577	1.621	1.647	1.641	1.659
Fe	0.022	0.013	0.011	0.018	0.012
Mg	0.016	0.020	0.019	0.035	0.014
Ca	0.590	0.610	0.648	0.672	0.654
Na	0.335	0.326	0.317	0.281	0.298
K	0.017	0.019	0.016	0.017	0.018
Mol% An	62.68	63.90	66.05	69.29	67.42
Mol% Ab	35.54	34.18	32.29	28.98	30.73
Mol% Or	1.78	1.94	1.66	1.74	1.85

Throughout units I, II, III and IV of the Main Zone, there is very little change in the Sr-content of plagioclase. Disregarding a certain amount of scatter, plagioclase in most samples in these units contains between 400ppm and 425ppm Sr (Fig. 19). The scatter is particularly wide in unit III, with an apparent trend of increasing Sr, from approximately 360ppm at the base to 430ppm or more at the top of the unit.

At the base of unit V, there is a sharp decrease in the Sr-content of plagioclase, to concentrations of 340ppm or less (Fig. 19). This is the beginning of a major overall trend of increasing plagioclase strontium concentration. The increasing trend culminates in a concentration of more than 500ppm Sr in plagioclase in sample A63, just above the base of unit VIII (Fig. 19). In the remainder of unit VIII, the Sr-content of plagioclase is of the order of 450ppm, disregarding some scatter. Across the Pyroxenite Marker, the Sr-content of plagioclase decreases sharply to less than 425ppm in samples SP11 and MZ3, decreasing further to less than 400ppm in samples MZ5 and MZ7 (Fig. 19).

4.5 Summary of the Mineral Chemistry of the Main Zone

A fairly sizeable body of analytical data has been assembled in this work on the composition of orthopyroxene in the Main Zone. The MMF ratio of orthopyroxene defines a series of strongly defined trends in the Main Zone. In Main Zone unit I, only three samples have been analyzed, but they indicate an upward trend of magnesium enrichment through the unit. In unit II, the trend of upward magnesium enrichment is even more strongly defined than in unit I. Unit III is characterized by a general upward iron-enrichment trend, although the pyroxenite layer at 272.6m, approximately half way up the unit, marks a definite point of inflection to more iron-rich compositions (Fig. 14).

Across the boundary between units III and IV, there is a sharp inflection to increased MMF ratios. Most of unit IV is characterized by a trend of fractionation of orthopyroxene MMF ratios to more iron-rich compositions. Near the top of unit IV, there is a sudden change to more magnesian compositions in sample A255.

Many of the samples in unit V of the Main Zone are characterized by anomalous iron-enrichment, which is probably the product of a late magmatic event, possibly connected with the discordant iron-rich ultramafic pegmatite bodies that disrupt the layering in unit V. A general trend of progressive iron-enrichment of orthopyroxene starts at the base of unit VI, and continues throughout units VI, VII and VIII, barring minor local aberrations (Fig. 14). Sample MZ1, at the top of unit VIII, has a 0.596 MMF ratio. Across the Pyroxenite Marker, the MMF ratio increases dramatically from 0.596 to 0.713, and stays at ratios of between 0.706 and 0.728 up to sample MZ7, 440m above the Pyroxenite Marker.

As regards the minor elements in orthopyroxene, there is a notable break in compositional trends at the base of unit IV. This applies equally to Cr_2O_3, TiO_2 and Al_2O_3 (Fig. 15). The Pyroxenite Marker, which is clearly defined by a sharp break in the orthopyroxene MMF ratio, is also characterized by a pronounced increase in the Cr_2O_3 content of orthopyroxene. Al_2O_3 increases progressively across the Pyroxenite Marker, but TiO_2 displays no apparent changes in concentration. In general terms, the patterns of variation are the same for augite as for orthopyroxene, except in terms of absolute concentration.

Von Gruenewaldt (1971) identified a trend of increasing Na-content in plagioclase in the Main Zone of the Eastern Bushveld. This is the case, in very broad terms, in the SK2 succession at Union Section. There is, however, a notable deviation from this trend in unit IV and the lower parts of unit V, where there is an overall <u>decrease</u> in Ab-content with stratigraphic height. This relatively localized phenomenon could be due to a variety of factors, including the flotation of early-formed plagioclase in the magma (Vermaak, 1976), or various forms of contamination, either by late-stage liquids within the magma chamber itself or from external sources. Sr in modal plagioclase displays two notable inflection in the Main Zone.

The first of the these is a sharp decrease in plagioclase Sr at the base of unit V, an the second is a sharp decrease in the Sr-content of plagioclase across the Pyroxenite Marker. From the base of unit V to the top of unit VIII, there is a general trend of increasing plagioclase Sr-content. This trend is contrary to what is expected,

considering the high distribution coefficient of Sr for plagioclase.

5. WHOLE-ROCK CHEMISTRY

5.1 Introduction

In this section, x-ray fluorescence analyses of 191 Main Zone cumulate rocks are presented. Of these, sixty-nine samples were analysed for both major and trace elements, while the balance were analyzed for trace elements only. The whole-rock data are supplemented by new strontium isotope data, which show that the systematics of the $^{87}Sr/^{86}Sr$ variations in the Main Zone are not as chaotic as Hamilton's (1977) data might suggest.

5.2 Major Element Variations

Whole-rock major element data are presented in Appendix 5, with total Fe represented as Fe_2O_3. These original data, recalculated to an assumed Fe_2O_3/FeO ratio of 0.1 and normalized to 100%, are presented with C.I.P.W. norms in Table 3. Variations in major element composition of the rocks within the Main Zone succession at Union Section are graphically illustrated by means of Harker-type diagrams, in which MgO is used as a simple index of fractionation (Fig. 20, 21), and also by means of plots against stratigraphic height (Fig. 22). There are no significant trends in the variation of SiO_2 in the succession under study, and it has therefore been omitted from the discussion. P_2O_5 is present in the rocks of the Main Zone in such low concentrations that it is of little petrological significance, and it is thus not considered here.

5.2.1 Fe_2O_3 and MgO

The plot of Fe_2O_3 vs. MgO (where total iron is represented as Fe_2O_3) suggests four groupings in the Main Zone (Fig. 20). In the discussion that follows, the groupings in Fig. 20 will be referred to as **groups**, which are not to be confused with the stratigraphically defined **units** referred to in the rest of this thesis.

The lowermost of the groups is group A (Fig. 20), which covers the stratigraphic interval from part-way up the Bastard Cyclic Unit (i.e from sample A346, at 18.2m), to the top of unit IV. Notably, the Bastard norite (sample A349) does not fit into group A, being

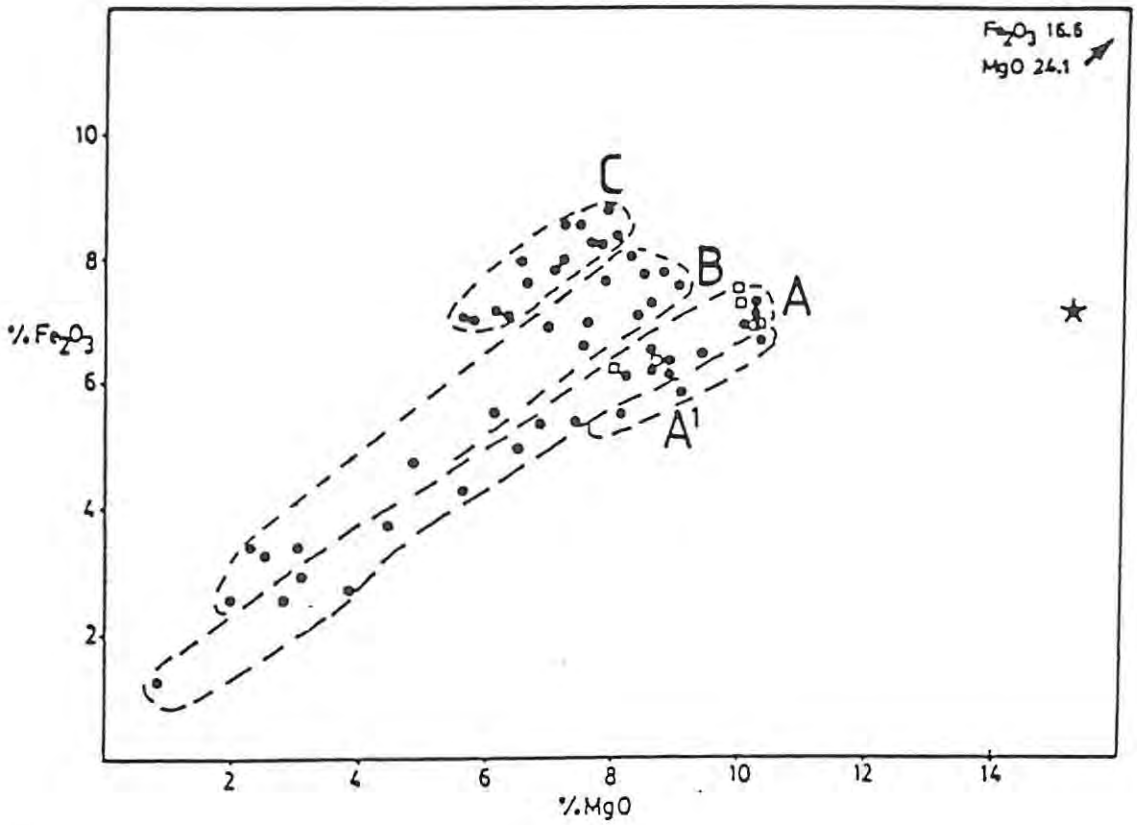

Fig. 20 : Harker-type diagram of Fe_2O_3 vs. MgO (total iron represented as Fe_2O_3). Group A covers the top of the Bastard Cyclic Unit and Main Zone units I, II, III and IV. Subgroup A' represents the Porphyritic Gabbro Marker in unit IV. Group B extends from 550m to 1600m in the Main Zone. Group C extends from 1600m to the Pyroxenite Marker (i.e. unit VIII of the Main Zone). Samples from above the Pyroxenite Marker are represented by unshaded squares, and the Bastard norite (sample A349) by the star ornamentation. The arrow indicates the composition of pyroxenite sample A297, in Main Zone unit III.

substantially more magnesian than the overlying rocks (Fig. 20). Group A displays the widest compositional range of the three groups, with MgO varying from less than one up to ten weight percent, and a corresponding variation in Fe_2O_3 of 1.22 to 7.64 weight percent. Sample A297, the pyroxenite at 275m in unit III, contains 16.6 weight percent Fe_2O_3 and 24.1 weight percent MgO, which means it forms a linear extension of group A, and therefore conforms to the pattern (Fig. 20). Samples from the Porphyritic Gabbro Marker in unit IV (A284, A280 and A275) diverge slightly from the general group A trend, and are defined as a subgroup of group A, designated A' (Fig. 20). The samples of subgroup A' are slightly enriched in MgO relative to the main group A trend.

Group B in Fig. 20 covers units V, VI and VII (i.e. the Main Zone interval from 550m to 1600m. The samples at the low Mg, low Fe end of this trend represent the anorthosite samples of the Main Mottled Anorthosite (unit V). Above 1600m, the samples of Main Zone unit VIII form group C in Fig. 20. Above the Pyroxenite Marker, there is a return to more primitive compositions (unshaded squares in Fig. 20), and these samples fall within the same compositional field as the relatively Mg-rich rocks of group A.

The variations of whole-rock Fe and Mg with stratigraphic height in the Main Zone are illustrated in terms of the ratio $Mg/(Mg+Fe_t)$ in Fig. 22a (Fe_t is total elemental Fe, expressed in weight percent). For ease of reference, this ratio is referred to here as the MMF ratio. Sample A349 (the Bastard norite), near the base of Fig. 22a, has an MMF ratio of 0.643, which accords with ratios calculated from de Klerk's (1982) data for the Bastard Cyclic Unit). Sample A346, 18.2m above the Bastard Reef, has a relatively iron-rich MMF of 0.48 (Fig. 21a). From A346, the MMF ratio **increases** steadily upwards to 0.58 in sample A280, which is within the Porphyritic Gabbro Marker in unit IV. From sample A280, the MMF ratio decreases continuously up to the top of unit VIII, where the ratio is 0.42 in sample MZ1. This broadly defined trend is punctuated at intervals by slight inflections, usually associated with the occurrence of Fe-rich ultramafic pegmatite bodies within the cumulate succession. This is particularly evident within the Main Mottled Anorthosite (unit V), where the MMF ratio of some samples is less than 0.4 (Fig. 22a). Across the Pyroxenite Marker, the whole-rock MMF ratio increases sharply, from 0.42 in sample MZ1 to between 0.53

and 0.56 in samples above the Pyroxenite Marker. There is an upward increase in the MMF ratio from sample MZ2 (0.531) to MZ5 (0.559), after which the ratio decreases to 0.528 in sample MZ7.

5.2.2 MnO

Manganese is a minor constituent of the Main Zone cumulates, MnO generally making up less than 0.2 weight percent of the rock (although this increases to 0.28 weight percent in pyroxenite). Very little Mn enters plagioclase, and manganese displays a preference for orthopyroxene over clinopyroxene. Microprobe data show that, in broad terms, The MnO content of orthopyroxene in the Main Zone varies from 0.35 to 0.50 weight percent, whilst that of clinopyroxene ranges from 0.20 to 0.25. The proportion of orthopyroxene to clinopyroxene will therefore have a considerable effect on the modal mineralogy of the rock.

The plot of whole-rock MnO versus stratigraphic height illustrates graphically the effect of modal mineralogy on the Mn-content of the rocks (Fig. 22b). In leucogabbro and anorthosite, notably in the lowermost 325m of the Main Zone (units I, II and III), the Main Mottled Anorthosite (unit V), and at 1400m and 1900m, the whole-rock Mno content decreases to below 0.05 weight percent. The plot of MnO versus MgO (Fig. 21f) has a positive slope, although there is a fairly wide scatter of data points. The positive slope indicates the preference of MnO for pyroxene over plagioclase, whilst the scatter is attributed to varying relative proportions of clinopyroxene and orthopyroxene.

5.2.3 TiO_2

The concentration of TiO_2 in orthopyroxene is of the order of 0.2 weight percent in the Main Zone gabbro, whereas in clinopyroxene, TiO_2 is present in the range 0.3 to 0.5 weight percent. Plagioclase contains only small amounts of TiO_2. Spinel **(sensu lato)** is absent from the Main Zone assemblage as a cumulus phase, and is very scarce as an intercumulus phase. These factors all add up to low whole-rock TiO2 concentrations in the Main Zone.

Disregarding a certain amount of scatter, there is a trend of increasing TiO_2 concentration through units I, II, III, IV, V and part

of VI in the Main Zone. This trend starts in the Bastard Cyclic Unit, where sample A346 (18.2m above the Bastard Reef) contains 0.09 weight percent TiO_2, and culminates in a concentration of 0.19 weight percent TiO_2 in sample A208, 787m above the Bastard Reef (Fig. 22c). Approximately half way through unit VI, TiO_2 decreases sharply to 0.12 weight percent in sample A198, 845m above the Bastard Reef. Above sample A198, the whole-rock TiO_2 concentration is relatively constant, disregarding the effects of pegmatite bodies at 1400m and 1900m, up to the Pyroxenite Marker and beyond, there being no noteworthy change in concentration across the Pyroxenite Marker itself. The sharp change in TiO_2 concentration patterns at approximately 800m is also reflected, in a rather more muted form, in the plot of MnO versus stratigraphic height (Fig. 22b). There is no obvious reason for the change in MnO and TiO_2 concentrations at 800m, mineralogical or otherwise, and the changes do not manifest themselves in the concentration patterns of other major or trace elements.

5.2.4 Al_2O_3, Na_2O and CaO

The variations of Al and Na in the Main Zone are influenced predominantly by plagioclase. This means that Al_2O_3 and Na_2O can be used more or less directly as indicators of the proportion of modal plagioclase in a rock. Ca is an important component, not only of plagioclase, but also of augite and pigeonite, which means that its behaviour is somewhat more complex than that of Al and Na.

At 1.14 weight percent Na_2O, sample A349 (the Bastard norite, 5.7m above the Bastard Reef) has a Na_2O content slightly higher than that of the noritic rocks in the UG1, UG2, Pseudo and Merensky cyclic units of the Upper Critical Zone (de Klerk, 1982). Above the Bastard norite, sample A346, still in the Bastard Cyclic Unit at 18.2m above the Bastard Reef, contains 2.21 weight percent Na_2O. From sample A346, the Na_2O content of the rocks decreases progressively upwards through units I, II, III and IV, barring localized fluctuations, to 1.6 weight percent in sample A254, near the top of unit IV (Fig. 22f).

Some of the more anorthositic layers in unit V (the Main Mottled Anorthosite) contain over 2.5 weight percent Na_2O. Disregarding these plagioclase-rich lithologies, however, there is a general trend of progressive increase in the whole-rock Na_2O content in the Main Zone

cumulates to 2.76 weight percent in sample MZ1, at the top of unit VIII. Across the Pyroxenite Marker, whole-rock Na_2O decreases sharply to 1.93 weight percent in sample MZ2. This is followed by a progressive decrease in Na_2O to 1.42% in sample MZ5, 280m above the Pyroxenite Marker, and a subsequent increase to 1.70 weight percent in sample MZ7, 440m above the Pyroxenite Marker. Notably, the pattern of Na_2O variation in the cumulates above the Pyroxenite Marker is a mirror image of the pattern of whole-rock MMF ratio variation in the same interval (Fig. 22, a and f).

The plot of Na_2O versus MgO (Fig. 21d) illustrates the strong modal influence of plagioclase, as expressed in a negative linear trend. The points enclosed within the dashed line in Fig. 21d represent Main Zone unit VIII (i.e. 1600m to 2250m above the Bastard Reef). Reference to the plot of modal plagioclase versus stratigraphic height (Fig. 12) indicates no increase in the proportion of modal plagioclase in the cumulates in this interval. The increase in whole-rock Na_2O must therefore be ascribed to an increase in the albite content of plagioclase above 1600m. Reference to microprobe data on plagioclase in unit VIII (Fig. 18) proves this assessment to be valid. The Bastard norite (sample A349, represented in Fig. 21d by a star) has a relatively low Na_2O content (1.14 weight percent), reflecting not only its relatively low modal plagioclase content (49.5%), but also the relatively An-rich nature of plagioclase in the Bastard Cyclic Unit (Kruger, 1982).

The influence of plagioclase on the Al_2O_3 content of the Main Zone cumulates is evident from a comparison of the plot of Al_2O_3 versus stratigraphic height (Fig. 22e) with the plot of modal plagioclase versus stratigraphic height (Fig. 12). In the Bastard norite (sample A349), the whole-rock Al_2O_3 content is 16.44 weight percent. In sample A346, 18.2m above the Bastard Reef, Al_2O_3 is sharply higher at 27.5 weight percent. There is a steady upward decrease in Al_2O_3 through the rest of the Bastard Cyclic Unit and Main Zone units I, II, III and the lower part of IV. Sample A275, near the top of the Porphyritic Gabbro Marker in unit IV, represents the culmination of the trend of upward decrease in Al_2O_3, at 17.24 weight percent. Above sample A275 (399m above the Bastard Reef), the whole-rock Al_2O_3 is variable, but generally between 17.5 and 18.7 weight percent, up to the top of unit IV. The exception is sample A257, a melagabbro in which a low modal

proportion of plagioclase dictates a whole-rock Al_2O_3 concentration of 13.8 weight percent. Modal control is also evident in sample A297, a pyroxenite with 2.29 weight percent Al_2O_3, and sample A299, a leuconorite with 27.4 weight percent Al_2O_3 (both the latter samples are in unit III).

In unit V (the Main Mottled Anorthosite), the whole-rock Al_2O_3 concentration is usually, although not always, above 25 weight percent (Fig. 22e), reflecting the modal mineralogy. There is very little variation in Al_2O_3 in units VI, VII and VIII, except for minor local modally-controlled increases in plagioclase-rich intervals (e.g. at 1400m). There is very little change in whole-rock Al_2O_3 across the Pyroxenite Marker, but the rocks above the Marker display a fairly steady decrease in Al_2O_3, from 18.85% in sample MZ2 to 16.33 weight percent in sample MZ7. On the plot of Al_2O_3 versus MgO (Fig. 21e), the negative slope indicates strong modal control by plagioclase.

The scatter of points on the plot of CaO versus MgO (Fig. 21c) reflects the modal influences of plagioclase and augite in different proportions. The general range of CaO concentrations in the Main Zone is approximately 10 to 15 weight percent, although it decreases to 3.3 weight percent in the pyroxenite layer at 275m (sample A297). In the plot of CaO versus stratigraphic height (Fig. 22d), the leucocratic intervals display higher CaO concentrations, reflecting the relatively low proportion of modal orthopyroxene in these rocks. There is an increase in the concentration of CaO in the rocks above the Pyroxenite Marker . One contribution to this increase is an increase in the modal clinopyroxene content of these gabbronorites (Fig. 12). Although there is a decrease in the proportion of modal plagioclase in the rocks above the Pyroxenite Marker, this is counteracted by an increase in the anorthite content of the plagioclase (Fig. 18).

5.2.5 $\underline{K_2O}$

Whole-rock K_2O in the Main Zone varies between 0.1 and 0.4 weight percent in gabbroic and anorthositic rocks, but decreases to 0.02 weight percent in pyroxenite (Fig. 22g). Microprobe and mineral separate analyses indicate concentrations of between 0.20 and 0.35 weight percent K_2O in plagioclase. The pyroxenes do not normally accept potassium into their lattices. Biotite and amphibole, on the

other hand, can accomodate substantial amounts of K_2O.

The gabbroic rocks of the Main Zone generally have K_2O concentrations somewhat less than 0.25 weight percent, and it is only in the anorthositic layers, which are generally associated with ultramafic pegmatite, that K_2O attains higher concentrations. This is especially true of the Main Mottled Anorthosite (unit V), where the K_2O content of plagioclase is generally below 0.2 weight percent. The high whole-rock K_2O contents encountered in this part of the succession are ascribed to the presence of secondary biotite, which is probably related to the same process which gave rise to the ultramafic pegmatite bodies in unit V.

5.2.6 Summary of Major Element Chemistry

Unfortunately, sample coverage of the lower units of the Main Zone is not as dense as might have been hoped. The plot of whole-rock MMF against stratigraphic height (Fig. 22a) is a case in point, where the complex variations exposed by closely-spaced microprobe analyses of orthopyroxene (Fig. 14) are lost because of low sample density. The high-Fe samples in unit V (Fig. 22a), for example, are exposed by the orthopyroxene MMF plot (Fig. 14) as being the culmination of an iron-enrichment trend which starts in unit IV. In a general sense, the whole-rock MMF ratio increases with stratigraphic height up to the Porphyritic Gabbro Marker, above which there is a trend of progressive iron-enrichment up to the top of unit VIII. Across the Pyroxenite Marker, there is a sharp increase in the MMF ratio.

The Main Zone may be divided into four separate groups of samples on the basis of the plot of Fe_2O_3 versus MgO (Fig. 20). The first of these is a relatively Mg-rich group, representing units I, II, III and IV of the Main Zone (i.e. up to 550m above the Bastard Reef). A subgroup of group A, designated A', is made up of samples from the Porphyritic Gabbro Marker. These latter samples are slightly more Mg-rich than the main lineage of A-group samples (Fig. 20). Group B in Fig. 20 covers the interval from the base of unit V to the top of unit VII (550m to 1600m above the Bastard Reef). Group C, which is made up of samples from Main Zone unit VIII, is the most iron-rich. Above the Pyroxenite Marker, there is a return to the relatively Mg-rich compositions of group A.

Whereas the MMF ratio traces the evolution of the mafic minerals (the pyroxenes) in the Main Zone, Na_2O and Al_2O_3 trace the fractionation of plagioclase, albeit only in broad terms. Both Na_2O and Al_2O_3 decrease more or less progressively upwards through units I, II, III and part of IV in the Main Zone, suggesting that plagioclase becomes more anorthitic upwards in this part of the succession. For the rest of the Main Zone up to the top of unit VIII, both Na_2O and Al_2O_3 increase progressively upwards, suggesting normal fractionation of plagioclase to more albitic compositions.

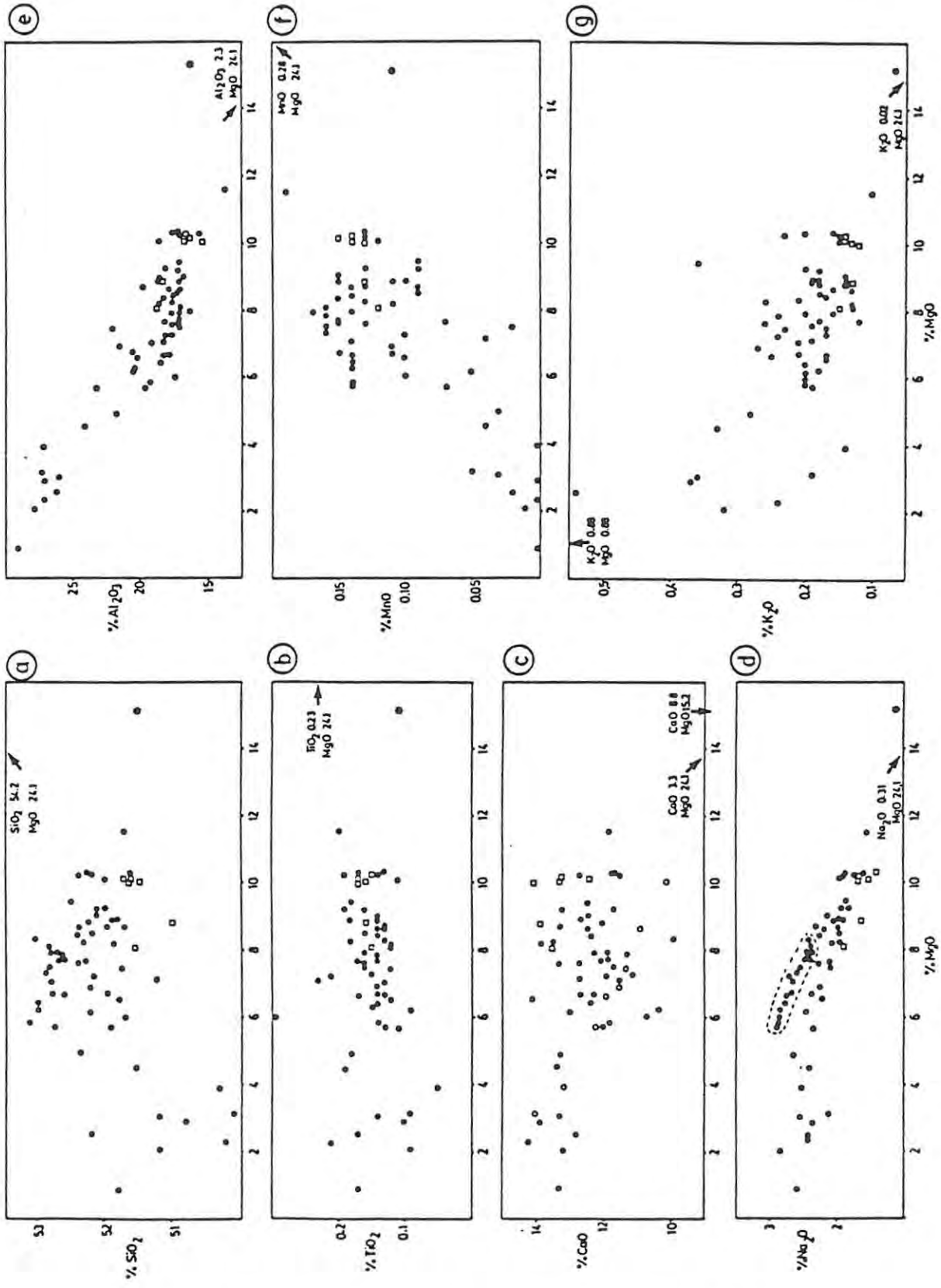

Fig. 21 . Harker-type binary diagrams of major elements vs. MgO

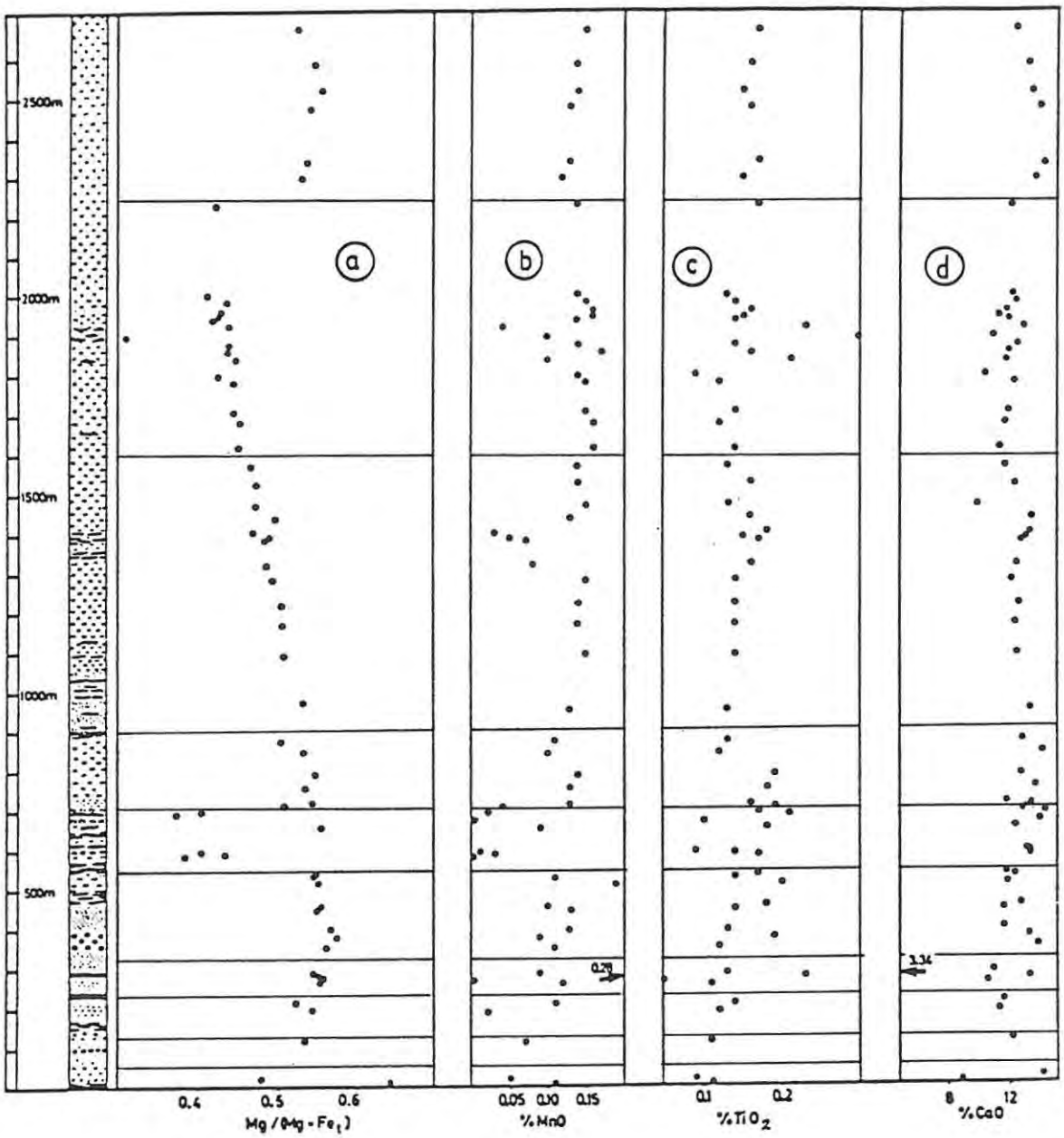

Fig. 22 . Variations in major element concentration in borehole SK2. Stratigraphic height in metres above the Bastard Reef.

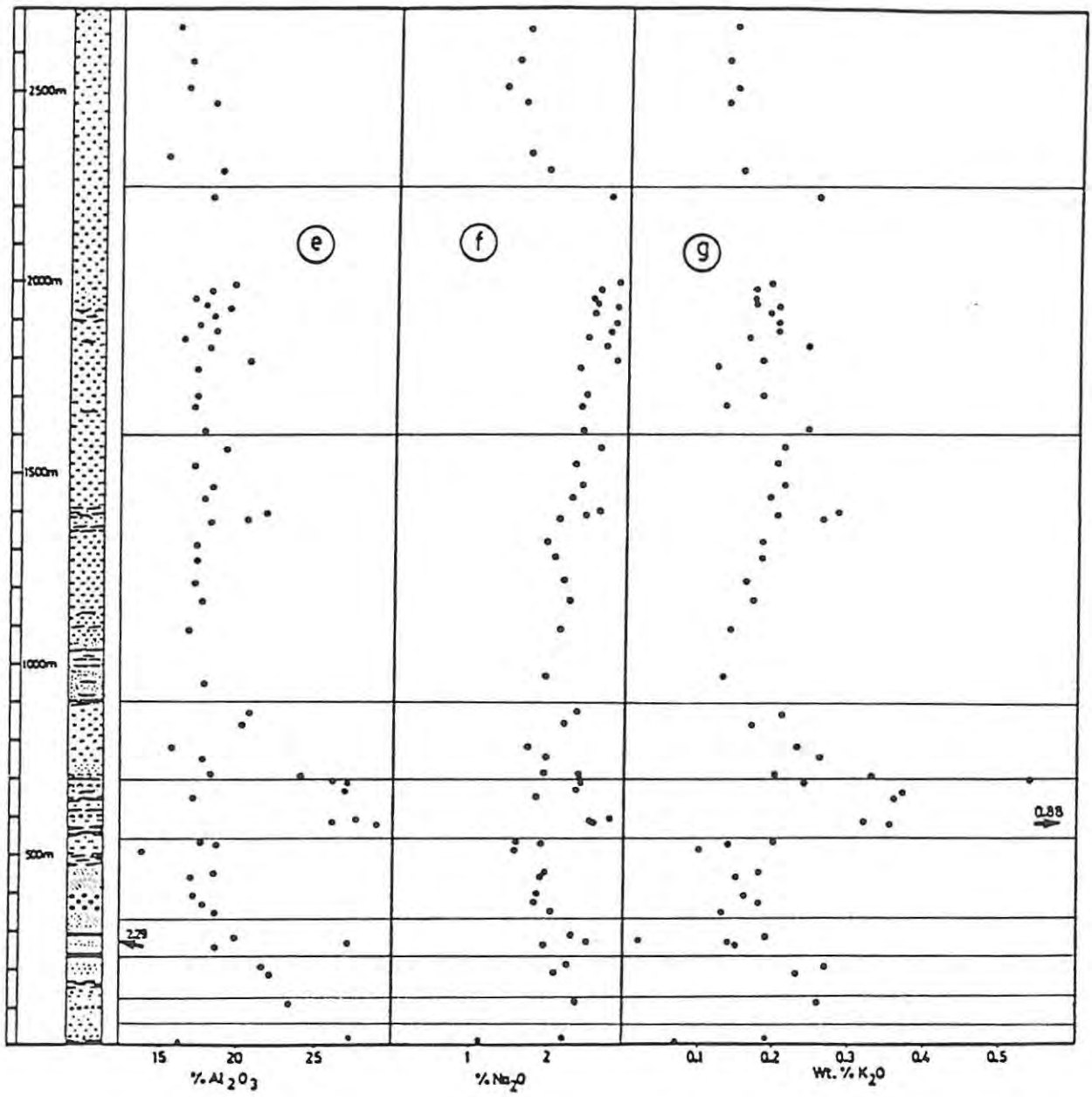

Fig. 22 . (continued)

TABLE 3
MAJOR ELEMENT ANALYSES AND WEIGHT % C.I.P.W. NORMS (ASSUMING AN OXIDATION RATIO CALCULATED AS $Fe_2O_3/FeO = 0.1$)

	A1	A5	A10	A13	A15	A18	A22	A25	A27	A29	A35	A38	A48	A52
SiO_2	52.83	52.80	52.78	52.88	53.13	51.28	51.77	53.00	52.73	52.18	53.01	52.71	52.58	52.85
TiO_2	0.13	0.14	0.16	0.15	0.14	0.23	0.30	0.14	0.16	0.21	0.09	0.12	0.14	0.12
Al_2O	19.61	18.16	17.04	17.78	19.43	18.59	17.48	18.50	16.44	18.05	20.56	17.23	17.23	17.03
Fe_2O_3	0.59	0.63	0.72	0.71	0.58	0.64	0.96	0.58	0.73	0.67	0.60	0.68	0.68	0.70
FeO	5.85	6.28	7.16	7.05	5.86	6.44	9.51	5.83	7.26	6.60	5.95	6.80	6.84	6.96
MnO	0.14	0.15	0.16	0.16	0.14	0.04	0.10	0.14	0.17	0.10	0.14	0.15	0.15	0.16
MgO	5.73	6.73	7.52	7.33	5.82	7.23	6.00	6.42	7.99	7.24	6.21	7.71	7.81	8.12
CaO	12.03	12.31	11.73	11.15	11.82	12.70	10.73	12.40	11.89	11.96	10.39	12.10	11.89	11.52
Na_2O	2.89	2.63	2.55	2.60	2.86	2.66	2.84	2.78	2.46	2.74	2.86	2.36	2.49	2.40
K_2O	0.19	0.17	0.17	0.17	0.20	0.19	0.20	0.20	0.16	0.24	0.18	0.12	0.18	0.13
P_2O_5	0.01	0.00	0.01	0.02	0.02	0.00	0.11	0.01	0.01	0.01	0.01	0.02	0.01	0.01
TOTAL	100.00	100.00	100.00	100.00	100.00	100.00	100.00	100.00	100.00	100.00	100.00	100.00	100.00	100.00
ap	0.02	0.00	0.02	0.05	0.05	0.00	0.26	0.02	0.02	0.02	0.02	0.05	0.02	0.02
il	0.25	0.27	0.31	0.29	0.27	0.44	0.58	0.27	0.31	0.40	0.17	0.23	0.27	0.23
or	1.12	1.00	1.00	1.00	1.18	1.12	1.18	1.18	0.95	1.42	1.06	0.71	1.06	0.77
ab	24.45	22.25	21.58	22.00	24.20	22.51	24.03	23.52	20.81	23.18	24.20	19.97	21.07	20.31
an	39.98	37.25	34.55	36.35	39.59	38.23	34.36	37.41	33.35	36.25	42.73	3.07	35.31	35.31
mt	0.86	0.91	1.04	1.03	0.84	0.93	1.39	0.84	1.06	0.97	0.87	0.99	0.99	1.01
dien	4.57	5.72	5.63	4.48	4.43	6.11	3.57	5.83	6.20	5.61	2.08	5.83	5.79	5.37
difs	3.30	3.78	3.78	3.05	3.15	3.73	3.91	3.74	3.98	3.55	1.42	3.64	3.58	3.27
diwo	8.20	9.95	9.85	7.87	7.90	10.35	7.58	10.04	10.68	9.61	3.65	9.95	9.86	9.09
hyen	9.70	11.04	13.10	13.77	10.06	6.03	10.15	10.16	13.70	9.49	13.39	13.37	13.52	14.85
hyfs	7.00	7.28	8.80	9.36	7.16	3.68	11.11	6.52	8.80	6.00	9.14	8.36	8.36	9.03
q	0.54	0.55	0.35	0.76	1.16	0.00	0.00	0.47	0.15	0.00	1.27	0.84	0.00	0.73
fo	0.00	0.00	0.00	0.00	0.00	4.12	0.86	0.00	0.00	2.05	0.00	0.00	0.10	0.00
fa	0.00	0.00	0.00	0.00	0.00	2.77	1.03	0.00	0.00	1.43	0.00	0.00	0.07	0.00

ap = apatite il = ilmenite mt = magnetite dien = diopside/enstatite hyen = hypersthene/enstatite
ab = albite an = anorthite or = orthoclase difs = diopside/ferrosilite hyfs = hypersthene/ferrosilite
q = quartz fo = forsterite fa = fayalite diwo = diopside/wollastonite

TABLE 3
MAJOR ELEMENT ANALYSES AND WEIGHT % C.I.P.W. NORMS (ASSUMING AN OXIDATION RATIO CALCULATED AS $Fe_2O_3/FeO = 0.1$)

	A63	A72	A79	A91	A100	A106	A108	A110	A117	A122	A133	A146	A155	A168
SiO_2	52.63	52.82	52.81	53.07	52.37	52.38	52.28	52.31	52.21	52.27	52.43	52.45	52.16	51.76
TiO_2	0.14	0.13	0.16	0.13	0.16	0.18	0.15	0.17	0.16	0.14	0.14	0.14	0.14	0.13
Al_2O_3	17.69	19.14	17.09	18.39	17.86	21.83	20.61	18.32	17.30	17.22	17.16	17.59	16.90	17.94
Fe_2O_3	0.68	0.57	0.63	0.67	0.55	0.40	0.46	0.58	0.64	0.65	0.60	0.58	0.63	0.54
FeO	6.81	5.71	6.32	6.64	5.46	3.98	4.59	5.80	6.41	6.48	6.01	5.83	6.26	5.39
MnO	0.16	0.14	0.14	0.15	0.13	0.03	0.05	0.07	0.08	0.15	0.14	0.15	0.15	0.13
MgO	7.92	7.05	7.96	8.34	7.59	4.96	6.18	7.64	8.55	8.81	8.63	8.41	9.03	8.66
CaO	11.29	11.56	12.30	9.95	13.31	13.29	12.99	12.73	12.48	12.02	12.53	12.40	12.45	13.33
Na_2O	2.44	2.66	2.38	2.44	2.38	2.66	2.48	2.11	1.98	2.08	2.20	2.28	2.14	1.99
K_2O	0.23	0.21	0.20	0.21	0.19	0.28	0.20	0.26	0.18	0.18	0.16	0.17	0.14	0.13
P_2O_5	0.01	0.01	0.01	0.01	0.00	0.01	0.01	0.01	0.01	0.00	0.00	0.00	0.00	0.00
TOTAL	100.00	100.00	100.00	100.00	100.00	100.00	100.00	100.00	100.00	100.00	100.00	100.00	100.00	100.00
ap	0.02	0.02	0.02	0.02	0.00	0.02	0.02	0.02	0.02	0.00	0.00	0.00	0.00	0.00
il	0.27	0.25	0.31	0.25	0.31	0.35	0.29	0.33	0.31	0.27	0.27	0.27	0.27	0.25
or	1.36	1.24	1.18	1.24	1.12	1.65	1.18	1.54	1.06	1.06	0.95	1.00	0.83	0.77
ab	20.64	22.51	20.14	20.64	20.14	22.51	20.98	17.85	16.75	17.60	18.61	19.29	18.11	16.84
an	36.64	39.67	35.36	38.61	37.49	46.80	44.52	39.75	37.79	37.12	36.48	37.26	36.10	39.64
mt	0.99	0.83	0.91	0.97	0.80	0.58	0.67	0.84	0.93	0.93	0.87	0.84	0.91	0.78
dien	4.76	4.43	6.48	2.70	7.44	4.86	5.15	6.01	6.21	5.82	6.75	6.38	6.75	7.17
difs	2.90	2.54	3.62	1.52	3.75	2.65	2.65	3.17	3.25	3.03	3.32	3.12	3.31	3.15
diwo	8.06	7.36	10.69	4.46	11.92	7.96	8.29	9.74	10.05	9.40	10.72	10.13	10.72	11.06
hyen	14.96	13.13	13.34	18.07	10.95	7.49	10.24	13.02	15.08	16.12	14.75	14.57	14.65	13.45
hyfs	9.11	7.52	7.44	10.18	5.52	4.08	5.26	6.87	7.88	8.37	7.25	7.13	7.18	5.91
q	0.29	0.52	0.50	1.33	0.00	1.04	0.76	0.87	0.68	0.26	0.04	0.00	0.00	0.00
fo	0.00	0.00	0.00	0.00	0.36	0.00	0.00	0.00	0.00	0.00	0.00	0.00	0.76	0.66
fa	0.00	0.00	0.00	0.00	0.20	0.00	0.00	0.00	0.00	0.00	0.00	0.00	0.41	0.32

TABLE 3

MAJOR ELEMENT ANALYSES AND WEIGHT % C.I.P.W. NORMS (ASSUMING AN OXIDATION RATIO CALCULATED AS $Fe_2O_3/FeO = 0.1$)

	A193	A198	A208	A213	A221	A222	A224	A226	A230	A233	A241	A243	A246	A254
SiO_2	51.95	51.82	52.40	52.35	52.16	51.58	52.22	50.25	50.80	52.53	51.23	51.23	51.85	51.63
TiO_2	0.13	0.12	0.19	0.18	0.16	0.19	0.17	0.21	0.10	0.18	0.09	0.14	0.17	0.17
Al_2O_3	20.62	20.32	15.72	17.74	18.29	24.15	26.21	27.15	27.11	17.21	27.94	26.16	29.15	17.59
Fe_2O_3	0.47	0.41	0.60	0.51	0.56	0.31	0.27	0.28	0.21	0.53	0.21	0.28	0.10	0.60
FeO	4.70	4.14	6.00	5.10	5.56	3.11	2.71	2.82	2.13	5.33	2.12	2.81	1.00	6.03
MnO	0.11	0.10	0.14	0.13	0.12	0.04	0.02	0.00	0.00	0.09	0.01	0.03	0.00	0.11
MgO	6.71	6.59	10.22	8.23	9.25	4.52	2.58	2.34	2.91	9.43	2.04	3.04	0.88	10.32
CaO	12.72	14.10	12.73	13.54	11.76	13.35	12.83	14.25	13.97	12.45	13.20	13.36	13.36	11.74
Na_2O	2.37	2.22	1.75	1.95	1.94	2.41	2.43	2.44	2.39	1.87	2.84	2.57	2.60	1.60
K_2O	0.21	0.17	0.23	0.26	0.20	0.33	0.54	0.24	0.37	0.36	0.32	0.36	0.88	0.20
P_2O_5	0.01	0.01	0.02	0.01	0.00	0.01	0.02	0.02	0.01	0.02	0.00	0.02	0.01	0.01
TOTAL	100.00	100.00	100.00	100.00	100.00	100.00	100.00	100.00	100.00	100.00	100.00	100.00	100.00	100.00
ap	0.02	0.02	0.05	0.02	0.00	0.02	0.05	0.05	0.02	0.05	0.00	0.05	0.02	0.02
il	0.25	0.23	0.37	0.35	0.31	0.37	0.33	0.40	0.19	0.35	0.17	0.27	0.33	0.33
or	1.24	1.00	1.36	1.54	1.18	1.95	3.19	1.42	2.19	2.13	1.89	2.13	5.20	1.18
ab	20.05	18.78	14.81	16.50	16.41	20.39	20.56	20.64	20.22	15.82	24.03	21.74	22.00	13.54
an	45.01	44.98	34.36	38.89	40.61	54.11	58.99	62.42	62.13	37.48	62.55	58.79	65.30	40.23
mt	0.68	0.59	0.87	0.74	0.81	0.45	0.39	0.41	0.30	0.77	0.30	0.41	0.14	0.87
dien	4.73	6.73	7.88	7.66	4.84	3.22	1.07	1.84	1.87	6.70	0.69	1.80	0.22	4.94
difs	2.33	2.97	3.24	3.32	2.04	1.49	0.74	1.45	0.92	2.63	0.49	1.13	0.15	2.02
diwo	7.53	10.40	11.97	11.78	7.40	5.03	1.89	3.40	2.97	10.07	1.23	3.08	0.38	7.50
hyen	11.98	9.68	17.57	12.83	18.19	8.04	5.36	3.99	5.38	16.78	4.39	5.77	1.97	20.76
hyfs	5.90	4.27	7.23	5.55	7.68	3.71	3.73	3.14	2.65	6.59	3.10	3.61	1.33	8.48
q	0.29	0.33	0.31	0.82	0.52	1.22	3.68	0.84	1.15	0.63	1.16	1.23	2.98	0.13
fo	0.00	0.00	0.00	0.00	0.00	0.00	0.00	0.00	0.00	0.00	0.00	0.00	0.00	0.00
fa	0.00	0.00	0.00	0.00	0.00	0.00	0.00	0.00	0.00	0.00	0.00	0.00	0.00	0.00

TABLE 3
MAJOR ELEMENT ANALYSES AND WEIGHT % C.I.P.W. NORMS (ASSUMING AN OXIDATION RATIO CALCULATED AS $Fe_2O_3/FeO = 0.1$)

	A255	A257	A264	A266	A275	A280	A284	A295	A297	A299	A301	A312	A315	A327
SiO_2	51.92	51.76	51.84	52.24	52.30	51.88	51.89	51.99	54.16	50.34	52.11	52.24	51.80	51.93
TiO_2	0.14	0.20	0.18	0.14	0.13	0.19	0.12	0.13	0.23	0.05	0.11	0.14	0.12	0.11
Al_2O_3	18.68	13.81	18.52	17.04	17.24	17.90	18.60	19.94	2.29	27.37	18.60	21.61	22.04	23.42
Fe_2O_3	0.53	0.81	0.51	0.60	0.56	0.48	0.46	0.52	1.39	0.22	0.58	0.45	0.45	0.35
FeO	5.25	8.11	5.09	5.96	5.58	4.81	4.57	5.15	13.91	2.22	5.79	4.47	4.48	3.53
MnO	0.11	0.19	0.10	0.13	0.13	0.09	0.11	0.09	0.28	0.00	0.12	0.11	0.02	0.07
MgO	8.91	11.56	8.93	10.21	10.36	9.19	8.20	8.68	24.07	3.94	10.07	6.90	7.45	5.68
CaO	12.40	11.89	12.66	11.61	11.65	13.47	13.84	10.98	3.34	13.19	10.50	11.53	11.31	12.29
Na_2O	1.92	1.57	1.98	1.92	1.89	1.81	2.08	2.32	0.31	2.52	1.97	2.27	2.10	2.36
K_2O	0.14	0.10	0.18	0.15	0.16	0.18	0.13	0.19	0.02	0.14	0.15	0.27	0.23	0.26
P_2O_5	0.00	0.00	0.01	0.00	0.00	0.00	0.00	0.01	0.00	0.01	0.00	0.01	0.00	0.00
TOTAL	100.00	100.00	100.00	100.00	100.00	100.00	100.00	100.00	100.00	100.00	100.00	100.00	100.00	100.00
ap	0.00	0.00	0.02	0.00	0.00	0.00	0.00	0.02	0.00	0.02	0.00	0.02	0.00	0.00
il	0.27	0.38	0.35	0.27	0.25	0.37	0.23	0.25	0.44	0.10	0.21	0.27	0.23	0.21
or	0.83	0.59	1.06	0.89	0.95	1.06	0.77	1.12	0.12	0.83	0.89	1.60	1.36	1.54
ab	16.24	13.28	16.75	16.24	15.99	15.31	17.60	19.63	2.62	21.32	16.67	19.21	17.77	19.97
an	41.94	30.34	41.12	37.41	38.09	40.19	41.03	43.44	4.80	62.96	41.47	47.98	50.04	52.55
mt	0.77	1.17	0.74	0.86	0.81	0.70	0.67	0.75	2.02	0.32	0.83	0.64	0.65	0.51
dien	5.37	7.52	6.00	5.55	5.51	7.54	7.68	3.01	3.24	0.67	2.93	2.45	1.67	2.29
difs	2.22	3.71	2.38	2.28	2.10	2.73	3.01	1.25	1.33	0.26	1.19	1.12	0.69	0.99
diwo	8.17	11.96	9.03	8.43	8.23	11.12	11.54	4.58	4.92	1.01	4.44	3.82	2.54	3.52
hyen	16.82	19.46	15.94	19.88	20.29	15.35	12.07	17.62	56.70	8.68	22.15	14.73	16.89	11.86
hyfs	6.95	9.60	6.32	8.17	7.73	5.56	4.73	7.32	23.21	3.37	9.01	6.70	6.99	5.13
q	0.41	0.00	0.00	0.00	0.07	0.08	0.00	0.00	0.62	0.00	0.22	1.46	1.18	1.44
fo	0.00	1.27	0.21	0.00	0.00	0.00	0.47	0.69	0.00	0.32	0.00	0.00	0.00	0.00
fa	0.00	0.69	0.09	0.00	0.00	0.00	0.20	0.32	0.00	0.14	0.00	0.00	0.00	0.00

TABLE 3

MAJOR ELEMENT ANALYSES AND WEIGHT % C.I.P.W. NORMS (ASSUMING AN OXIDATION RATIO CALCULATED AS $Fe_2O_3/FeO = 0.1$)

	A346	A349	C1	C19	C47	C60	MZ1	MZ2	MZ3	MZ4	MZ5	MZ6	MZ7
SiO_2	50.11	51.57	50.86	52.48	51.48	49.04	52.63	51.62	51.69	51.01	51.68	51.51	51.76
TiO_2	0.09	0.11	0.10	0.19	0.20	0.07	0.17	0.15	0.17	0.16	0.15	0.16	0.17
Al_2O_3	27.48	16.44	21.41	20.94	21.02	29.28	18.24	18.83	15.34	18.35	16.56	16.74	16.33
Fe_2O_3	0.24	0.60	0.45	0.47	0.52	0.16	0.65	0.50	0.61	0.53	0.58	0.59	0.64
FeO	2.42	5.99	4.45	4.74	5.24	1.57	6.49	5.07	6.09	5.29	5.75	5.90	6.47
MnO	0.05	0.11	0.07	0.07	0.07	0.00	0.14	0.12	0.13	0.13	0.14	0.14	0.15
MgO	3.18	15.17	8.93	7.32	7.69	2.93	6.63	8.07	9.99	8.81	10.24	10.07	10.16
CaO	14.03	8.80	11.21	11.01	11.27	14.44	12.01	13.56	14.12	13.91	13.33	13.18	12.46
Na_2O	2.21	1.14	2.35	2.43	2.14	2.32	2.77	1.92	1.72	1.66	1.42	1.56	1.70
K_2O	0.19	0.07	0.17	0.35	0.34	0.19	0.25	0.15	0.12	0.13	0.14	0.13	0.14
P_2O_5	0.00	0.00	0.00	0.00	0.03	0.00	0.02	0.01	0.02	0.02	0.01	0.02	0.02
TOTAL	100.00	100.00	100.00	100.00	100.00	100.00	100.00	100.00	100.00	100.00	100.00	100.00	100.00
ap	0.00	0.00	0.00	0.00	0.07	0.00	0.05	0.02	0.05	0.05	0.02	0.05	0.05
il	0.17	0.21	0.19	0.37	0.38	0.13	0.33	0.29	0.33	0.31	0.29	0.31	0.33
or	1.12	0.41	1.00	2.07	2.01	1.12	1.48	0.89	0.71	0.77	0.83	0.77	0.83
ab	18.70	9.65	19.88	20.56	18.11	19.63	23.44	16.24	14.55	14.05	12.01	13.20	14.38
an	64.51	39.54	47.40	45.20	46.75	68.92	36.60	42.32	33.78	42.24	38.40	38.29	36.52
mt	0.35	0.87	0.65	0.68	0.75	0.23	0.94	0.72	0.88	0.77	0.84	0.86	0.93
dien	1.31	1.23	2.34	2.54	2.39	0.77	5.41	6.72	9.83	7.27	7.67	7.41	6.77
difs	0.69	0.34	0.82	1.13	1.12	0.28	3.73	2.97	4.21	3.07	3.04	3.05	3.04
diwo	2.13	1.72	3.43	3.93	3.74	1.13	9.54	10.39	15.09	11.12	11.55	11.26	10.51
hyen	6.61	34.62	13.14	15.69	16.77	3.63	10.56	13.37	12.77	13.42	17.83	17.31	18.07
hyfs	3.50	9.65	4.60	6.98	7.86	1.31	7.28	5.90	5.47	5.67	7.06	7.14	8.11
q	0.92	0.00	0.00	0.84	0.05	0.00	0.00	0.16	0.00	0.00	0.47	0.00	0.00
fo	0.00	1.35	4.74	0.00	0.00	2.03	0.38	0.00	1.60	0.88	0.00	0.26	0.32
fa	0.00	0.41	1.83	0.00	0.00	0.81	0.29	0.00	0.75	0.41	0.00	0.12	0.16

5.3 Trace Element Chemistry

Non-normalized trace element data are presented in table 4, and represented graphically in plots of concentration versus stratigraphic height and binary plots against MgO(Fig. 23, 24)

5.3.1 Chromium

In the absence of a spinel phase, Cr distributes strongly into the pyroxenes, particularly clinopyroxene, whilst being almost totally rejected by plagioclase. Distribution coefficients suggested by Cox et al. (1979) are: D_{Cr} into clinopyroxene = 10; D_{Cr} into plagioclase = 0.01. This implies that the proportion of modal pyroxene in the rock will have a strong influence on Cr concentration. The effect of modal mineralogy will, however, be modified by strong fractionation effects due to the high distribution coefficients for Cr, particularly into clinopyroxene.

The variation of whole-rock Cr concentration with stratigraphic height is shown diagrammatically in Fig. 23a. The Bastard norite (sample A349) has a Cr-content of 1774ppm, which is substantially higher than any Main Zone rock, including pyroxenite. Above the Bastard norite, the Cr concentration decreases sharply to 240ppm in sample A346, a leuconorite 18.2m above the Bastard Reef. From sample A346 through the rest of the Bastard Cyclic Unit and Main Zone unit I, Cr fluctuates widely in the range 126ppm to 447ppm (Fig. 23a).

There are not enough data for any significant conclusions to be drawn regarding unit II. Unit III, by contrast, has been relatively comprehensively sampled. Even excluding the pyroxenite samples (A297 and A298), the range of Cr concentrations in unit III is fairly wide, with a range from 188ppm to 493ppm Cr. In the pyroxenite layer at 272.6m, Cr exceeds 800ppm. No whole-rock analysis is available for the pyroxenite at the base of unit III (i.e. at 223.5m), but Cr concentrations should be similar to samples A297 and A298, judging by microprobe analyses of orthopyroxene.

At the base of unit IV, sample A288 has a Cr content of 517ppm, which constitutes a noticeable increase from the maximum of 493ppm for the noritic rocks of unit III (Fig. 23a). The Cr concentration increases

further in the first 20m of unit IV, reaching 568ppm in sample A285, which is within the Porphyritic Gabbro Marker. Disregarding local aberrations (e.g. samples A265 and A266, with concentrations of 578ppm and 591ppm Cr, respectively), there is a trend of rapidly decreasing Cr concentration above sample A285. This trend transcends the boundary between units IV and V, and culminates in a concentration of 39ppm Cr in sample A224, near the top of unit V.

Sample A223, near the base of unit VI, has a concentration of 97ppm Cr. Upwards in the succession, Cr increases to 159ppm in sample A208 (787.2m above the Bastard Reef), before decreasing again to 55ppm in sample A191 (886.3m), near the top of unit VI. In the overlying unit VII, whole-rock Cr rarely exceeds 80ppm, except at approximately 1250m, where sample A126 has a concentration of 106ppm Cr (Fig. 23a).

The base of unit VIII, at 1600m, is marked by a locally anomalously high Cr content of 160ppm in sample A65. Whole-rock Cr decreases sharply above this, however, to 56ppm in sample A63. The balance of unit VIII is characterized by a more or less steady upward decrease in Cr concentration, culminating in a concentration of 9ppm Cr in sample MZ1, at the top of the unit.

Above the Pyroxenite Marker, there is a sharp increase in whole-rock Cr, and sample SP11 contains 337ppm Cr (Fig. 23a). Upwards from sample SP11, Cr continues to increase, reaching 612 ppm in sample MZ5, 280m above the Pyroxenite Marker, before decreasing again to 39ppm in sample MZ7, 440m above the Marker.

In the plot of Cr versus MgO (Fig. 24e), the Main Zone cumulates may be subdivided into a series of groupings, each corresonding to a definite stratigraphic interval. Notably, the Bastard norite (sample A349) is highly enriched in Cr relative to the Main Zone (1776ppm Cr, see arrow in Fig. 24e). The samples from above the Pyroxenite Marker (unshaded squares in Fig. 24e) do not correspond specifically to any of the sub-Pyroxenite Marker groups of samples.

The samples represented by the shaded circles above line A-B in Fig. 24e represent the stratigraphic interval including units I, II, III and part of IV. The pyroxenite layer at 272.6m in unit III is represented on Fig. 24e by an arrow (806ppm Cr; 24.1 weight percent MgO). Samples

A254, A255 and A257, which plot within the dashed line below line A-B in Fig. 24e, represent the uppermost 50m of unit IV, and are distinctly depleted in Cr relative to the underlying rocks. The shaded circles above line C-D in Fig. 24e represent samples from A246 to A193, covering units V and VI. The samples which plot below line C-D are the very low-Cr samples of units VII and VIII.

5.3.2 Vanadium

Vanadium distributes preferentially into clinopyroxene, for which Frey et al. (1978) quote a D_V of 1.5, whilst D_V for orthopyroxene is substantially lower, at 0.3. Vanadium is almost completely excluded by plagioclase, but distributes extremely strongly into any magnetite present in the rock. In the plot of V versus MgO (Fig. 24d), there is a gross positive relationship between the two parameters, although there is a good deal of scatter of data points, particularly between 5.5 and 8 weight percent MgO. In very broad terms, the samples from above 1600m (i.e. those of unit VIII) have relatively high V-contents, although this is by no means clear-cut. Rocks from above the Pyroxenite Marker have relatively low V-contents, akin to samples from the lowermost 500 metres of the Main Zone (unshaded squares in Fig. 24d). Relative to its high MgO content, the V-content of the Bastard norite (sample A349) is low (shaded star in Fig. 24d).

The variation of vanadium with stratigraphic height (Fig. 23b) defines fairly tightly constrained trends in units I, II, III and IV of the Main Zone, but the trends tend to become more diffuse in the upper four units of the Main Zone. The vanadium content of the noritic rocks of units I, II and III is invariably below 100ppm, except in the pyroxenite layers in unit III, where the concentration of vanadium exceeds 200ppm. The trend through units I, II and III including, incidentally, the Bastard norite (sample A349) is of almost constant V-content (Fig. 23b). In sample A288, at the base of unit IV, the vanadium content of the rocks increases sharply to 126ppm. Throughout unit IV, vanadium ranges in concentration between 110ppm and 140ppm, samples A260 (181ppm) and A257 (84ppm), near the top of unit IV, being notable exceptions.

In units V, VI, VII and VIII, the proximity of Fe-rich ultramafic pegmatite is likely to be the prime cause of scatter in V-concentration

data. The intervals affected by pegmatite bodies are generally anorthositic in character, and in these parts of the succession, rocks with anomalously high V contents are often spatially associated with rocks with equally anomalous low V concentrations (e.g. in unit V, and near the top of unit VI). The rapid alternation from high to low V concentrations may be construed as support for the contention, by Viljoen and Burvenich (1983), that the anorthosites are the source-beds from which the ultramafic pegmatite bodies segregated.

In very broad terms, there is a slow general increase in V concentration from the base of unit V (where V is of the order of 50 to 100ppm) to the top of unit VIII (where sample MZ1 has a V-content of 179ppm. Above the Pyroxenite Marker, V decreases sharply to 61ppm in sample SP11. This is followed by a progressive increase to 133ppm V in MZ3, approximately 100m above the Pyroxenite Marker. Vanadium concentration decreases to 101ppm in sample MZ4, 240m above the Pyroxenite Marker, followed by a muted increase to 114ppm in sample MZ7, 440m above the Pyroxenite Marker.

5.3.3 Cobalt

Frey et al. (1978) recommend distribution coefficients of 1.2 and 2 for cobalt into clinopyroxene and orthopyroxene, respectively, whilst the data of Paster et al. (1974) show D_{Co} for plagioclase to be approximately 0.03. The sense of variation of Co relative to MgO (Fig. 24b) is very similar to that of vanadium. The trend is more or less linear between the end-points of 6ppm Co at 0.9 weight percent MgO in an anorthosite (sample A246), and 113ppm Co at 24.1 weight percent MgO in an orthopyroxenite (sample A297). Within the range 5 to 10 weight percent MgO, there is a fairly wide scatter of Co concentrations in the approximate range 40 to 70ppm.

Although broadly similar to that of vanadium, the trend of cobalt variation with stratigraphic height is noticeably different in certain respects, mainly in the lower portions of the Main Zone and at the Pyroxenite Marker. The cobalt concentration of the Bastard norite (57ppm in sample A349) is noticeably higher than in the overlying Main Zone rocks. Above sample A349, sample A346 contains 24ppm Co. Barring minor localized digressions, whole-rock Co increases steadily from A346 to the top of unit V, where Co concentrations are of the order of 50ppm

to 65ppm. Co concentrations in the pyroxenite layer at 272.6m in unit III (113ppm to 117ppm) are marginally higher than cobalt concentrations recorded by de Klerk (1982) for pyroxenite in the Merensky and Bastard Cyclic Units.

In units V and VI, cobalt concentrations are generally well below 50ppm, particularly in the more anorthositic rock types. Exceptions, as in the case of vanadium, are those cumulate rocks in close proximity to ultramafic pegmatite bodies, in which cases Co may exceed 75ppm (e.g. samples A238, A208 and A182).

In the basal part of unit VII, anorthositic rocks of the Upper Mottled Anorthosite have Co concentrations below 40ppm. From approximately 1200m above the Bastard Reef, Co concentrations are generally above 50ppm, and often above 60ppm, reflecting the somewhat more melanocratic nature of the upper part of unit VII and unit VIII. There is no apparent change in Co concentrations across the Pyroxenite Marker, and the rocks above this horizon average 49ppm Co.

5.3.4 Nickel

The data of Frey et al. (1978) suggest that nickel partitions very strongly into both clinopyroxene and orthopyroxene, with D_{Ni} of the order of 4 for both minerals. Nickel is almost completely rejected by plagioclase. These considerations mean that Ni should vary in a positive and linear way with respect to MgO. There is a linear relationship in the plot of Ni versus MgO (Fig. 24a). From a low of 19ppm Ni and 0.9 weight percent MgO in anorthosite sample A246, there is an increase to 690ppm Ni and 24.1 weight percent MgO in orthopyroxenite sample A297. The group of slightly low-Ni samples between 7 and eight weight percent MgO (Fig. 24a) represent the interval between approximately 1800m and 2000m above the Bastard Reef (i.e. in the middle of unit VIII).

Although there are similarities in the trends of V, Co and Ni variation with stratigraphic height, the distinguishing feature of Ni variation is that it displays a trend of progressive depletion in the Main Zone, from just above the Porphyritic Gabbro Marker to the top of unit VIII (Fig. 23d). V and Co, on the other hand, display a trend of more or less constant concentration in this interval (i.e. from ±400m to the

Pyroxenite Marker), discounting minor local inflections.

In the lower part of the Main Zone, the behaviour of Ni follows a very similar pattern to that of Co, increasing from between 100ppm and 150ppm at the base of unit I to 302ppm at the top of unit IV. Within this interval, there is an inflection in unit III, where the pyroxenite layer at 272.6m contains 690ppm Ni. This is due to the high modal proportion of orthopyroxene in the rock.

Between 574m and approximately 1100m, there is wide scatter in the Ni data, in the range 11ppm to 220ppm, with particularly low concentrations at 592m (11ppm) and 932m (19ppm). The interval from 574m to 1100m corresponds to the Main and Upper Mottled Anorthosites and the intervening gabbronorite. The scatter in the Ni concentrations in this interval is attributed to variations in modal mineralogy, possibly exacerbated by the presence of ultramafic pegmatite bodies over much of the succession.

Above 1100m, where the Ni concentration is of the order of 190ppm, the overall trend is one of steady decrease in Ni concentration up to 2010m, where sample A1 contains 92ppm Ni. No data are available for the interval from 2010m to the top of unit VIII, but sample MZ1, at the top of unit VIII, has a Ni concentration of 159ppm, suggesting a general decrease in Ni in the top part of unit VIII (Fig. 23d). If sample MZ2, with a concentration of 159ppm Ni, is excluded, the samples above the Pyroxenite Marker are consistently higher in Ni than those of unit VIII of the Main Zone.

5.3.5 Scandium

Scandium in the Main Zone cumulates varies from 5ppm to 40ppm, the variation being due primarily to variations in modal mineralogy. Frey et al. (1978) recommend values of D_{Sc} = 3.1 for clinopyroxene, and 1.1 for orthopyroxene. This means that Sc partitions preferentially into pyroxene, particularly clinopyroxene. Data from Paster et al. (1974) suggest an extremely low D_{Sc} of 0.008 for plagioclase, implying almost total rejection of Sc by this mineral.

On the plot of Sc versus MgO (Fig. 24f), data points below the line A - B represent the noritic rocks of units I, II and III, as well as the

upper parts of the Bastard Cyclic Unit. Data points enclosed in the dashed line in Fig. 24f represent unit IV. All other points on the diagram represent samples from units V to VIII, as well as those from above the Pyroxenite Marker (the latter represented in Fig. 24f by unshaded squares).

The pattern of behaviour of Sc with stratigraphic height (Fig. 23e) is similar in almost all respects to that of vanadium. In the noritic rocks of units I, II and III, Sc concentrations are generally less than 15ppm, and invariably less than 20ppm, except in the pyroxenite layer at 272.6m (samples A297, A298), where the Sc concentration is 37ppm. There is a marked increase in the concentration of Sc in sample A288, at the base of unit IV, to 22.4ppm (Fig. 23e). Concentrations of Sc in excess of 20ppm are maintained throughout unit IV, attaining maxima of 30ppm and 32ppm in samples A257 and A260.

In unit V, the Main Mottled Anorthosite, Sc is generally less than 20ppm in the plagioclase-rich rocks, but certain samples exceed these concentrations. Sample A238 is notable in this regard, with an anomalously high concentration of 66ppm, probably due to the proximity of Fe-rich ultramafic pegmatite. In units VI, VII and VIII, Sc is usually between 20ppm and 35ppm, except in occasional leucocratic layers, or parts of the succession affected by pegmatite. Above the Pyroxenite Marker, there is a fairly wide range of Sc concentrations, between 20ppm and 39ppm, but there is no apparent inflection across the Pyroxenite Marker itself.

5.3.6 Zinc

Although there is little quantitative information available regarding the behaviour of zinc, its behaviour is similar in most respects to that of the compatible elements V, Co, Ni and Sc in the Main Zone (Fig. 23, Fig. 24). Paster et al. (1974) used distribution coefficients of 0.49 for Zn into pyroxene (combined orthopyroxene and clinopyroxene) and 0.13 for Zn into plagioclase. In the plot of Zn versus MgO, Zn varies from slightly more than 10ppm in anorthosite to approximately 60ppm in more melanocratic (±12 weight percent MgO) gabbro, and 120ppm in pyroxenite. The plot of Zn versus stratigraphic height (Fig. 23f) resembles in many respects the equivalent plot for Sc (Fig. 23e), although the Zn data display a slightly wider spread of concentrations.

The concentration of Zn is 47ppm in the Bastard norite (sample A349), but decreases rapidly to 19ppm in sample A346, 18m above the Bastard Reef. The concentration of Zn increases in a progressive but somewhat haphazard way through units I, II, III and IV, concentrations of 60ppm Zn being common at the top of unit IV. In the leucocratic rocks of the Main Mottled Anorthosite (unit V), Zn varies between 8ppm and 71ppm (Fig. 23f). As is the case with other transition metals, high Zn concentrations are often associated with proximity to ultramafic pegmatite bodies. Units VI, VII and VIII are characterized by Zn concentrations in the range 40ppm to 60ppm, except in particularly plagioclase-rich rocks, or those affected by pegmatite. There is no inflection in the general trend of Zn concentrations across the Pyroxenite Marker, although sample SP11, approximately 20m above the Pyroxenite Marker, has an anomalously high Zn content of 71ppm.

5.3.7 Copper

The distribution coefficients of Cu into plagioclase and the pyroxenes are extremely low. Paster et al. (1974) recommend D_{Cu} values of less than 0.1 for both plagioclase and pyroxene, whilst Frey et al. (1978) arbitrarily set the bulk distribution coefficient for Cu to between 0.00 and 0.01 in basaltic systems. The implication of this is that Cu is incompatible in the silicate mineral assemblage, and will remain incompatible except in the presence of a sulphide liquid. Campbell's (1977) work on the Jimberlana intrusion suggests that cumulate rocks in which the concentration of Cu is greater than 10ppm contain sulphides.

The general range of Cu concentrations in the Main Zone in borehole SK2 is between 10ppm and 30ppm. Lower concentrations than this occur occasionally in the succession, and substantially higher concentrations are encountered when the cumulates are in close proximity to ultramafic pegmatites. Although the data produce a fairly wide scatter in the plot of Cu versus stratigraphic height (Fig. 23g), a series of broadly defined trends is identifiable.

Cu concentrations in the Bastard Cyclic Unit are generally of the order of 25ppm, except in sample A346, which has a Cu-concentration of 13ppm. Sample A337, at the base of Main Zone unit I, has a relatively high Cu-content of 30ppm. At the top of unit I, sample A327 contains 19ppm

Cu. Only two samples were taken from unit II, where the extensive development of ultramafic pegmatite makes sampling difficult. At the base of unit III, sample A308 marks the beginning of a somewhat more clearly defined trend of increasing Cu concentrations, from 13ppm in A308 to 33ppm in sample A254, at the top of unit IV. The pyroxenite at 272.6m diverges from the general trend, with a Cu-content of 134ppm.

The pattern of Cu variation is rather scattered from the base of unit V up to, and beyond, the Pyroxenite Marker. Notably, the scatter of concentrations is most pronounced in the Main and Upper Mottled Anorthosites. Sample A191 (886m above the Bastard Reef) contains 1219ppm Cu. As is usual in the case of anomalous chemistry in the SK2 Main Zone cumulates, sample A191 is close to an ultramafic pegmatite.

5.3.8 Yttrium

The concentration of yttrium in the Main Zone cumulates is generally less than 10ppm, although slightly higher concentrations occur in isolated cases. The distribution coefficient of Y into plagioclase is substantially less than 0.1 (Drake and Weill, 1975; Pearce and Norry, 1979). The work of Frey et al. (1978) suggests that the distribution coefficient of Y into orthopyroxene is also extremely low (0.009), whilst for clinopyroxene, the distribution coefficient is of the order of 0.2. The implications of these data are that Y will only be accepted into late-crystallizing clinopyroxene, and will otherwise remain in the interstitial liquid.

Although the data are scattered, the plot of Y versus MgO (Fig. 24ℓ) suggests a muted positive slope, which is presumably related to the proportion of intercumulus clinopyroxene in the rock. Rocks with relatively high Y-concentrations (i.e. above 10ppm) are usually anorthosite or leucogabbro, and are almost invariably found in close proximity to ultramafic pegmatites. The high Y-content of these rocks is attributed to above-average amounts of trapped interstitial liquid.

In the plot of Y versus stratigraphic height (Fig. 23h), data are scattered in units I and II. Units III and IV are characterized by a broadly-defined trend of upward increase in Y, from approximately 3ppm at the base of unit III to 10.5ppm in sample A257, near the top of unit IV. Above sample A257, the uppermost two samples in unit IV (A254 and

A255) have sharply lower Y-contents (5.3ppm and 8.3ppm, respectively. The pyroxenite at 272.6m (in unit III) has a relatively high Y-content of 9ppm (Fig. 23h).

Upwards from the base of unit V to above the Pyroxenite Marker, there is a wide spread of Y concentrations, with no definable trends. The scatter is particularly noticeable in unit V (the Main Mottled Anorthosite), where Y ranges from 2.8ppm to 12.2ppm.

5.3.9 Strontium

The importance of Sr is that it reflects, almost directly, the modal proportion of plagioclase in the Main Zone cumulates. The inverse linear relationship between Sr and MgO (Fig. 24j) is evidence of this relationship. The experimental studies of Drake and Weill (1975) indicate that the distribution coefficient of Sr into plagioclase is somewhat greater than unity. This accords with distribution coefficient determinations on natural systems by Griffin and Murthy (1969) and Philpotts and Schnetzler (1970), which suggest that D_{Sr} for plagioclase is of the order of 1.3 in tholeiitic melts. The pyroxenes, by contrast, have low distribution coefficients for Sr, and Frey et al. (1978) quote values of $D_{Sr} = 0.165$ into clinopyroxene, and $D_{Sr} = 0.016$ into orthopyroxene.

In Fig. 24j, the trend of Sr versus MgO displays a change to a slightly lower negative slope at MgO concentrations lower than approximately 5 weight percent. These low-MgO samples represent anorthositic and leuconoritic rocks, and appear to have slightly low Sr-concentrations, relative to their modal mineralogy.

In the plot of Sr versus stratigraphic height (Fig. 23i), the Bastard norite (sample A349) has a strontium content of 201ppm. Above this, there is a sharp increase in Sr, to 344ppm in sample A346. From the top of the Bastard Cyclic Unit, there is an almost continuous decrease in Sr concentrations through units I, II, III and IV of the Main Zone, with samples at the top of unit IV containing between 177 and 225ppm Sr. The only notable deviations from this trend are the pyroxenite at 272.6m (16ppm Sr) and its immediate footwall anorthosite (356ppm Sr). These deviations are primarily modal effects.

5.3.10 Barium

Barium has distribution coefficients substantially less than one for the pyroxenes, and Paster et al. (1974) estimated D_{Ba} for plagioclase to be of the order of 0.7 in the Skaergaard cumulates. Although there is not a clear trend in the plot of Ba versus MgO (Fig. 24g), the overall impression is one of a negative slope, reflecting the influence of plagioclase on Ba concentration. Although plagioclase accepts Ba far more readily than do the pyroxenes, D_{Ba} for plagioclase is still less than one, and barium is essentially an incompatible element. The scatter in the plot of Ba versus MgO is ascribed to the concentration of Ba in varying proportions of intercumulus fluid in the cumulus rocks.

The similarity between Ba and Sr, in their affinity for plagioclase, is evident from a comparison of the plots of the two elements versus stratigraphic height (Fig. 23). Samples A349 and A346, both in the Bastard Cyclic Unit, return Ba concentrations of 39ppm and 88ppm, respectively. In sample A343, the pigeonite-bearing norite at 29.4m above the Bastard Reef, Ba increases sharply to 128ppm. Sample A340, near the top of the Bastard Cyclic Unit, contains 115ppm Ba. At the base of Main Zone unit I, sample A337 contains 115ppm Ba. From sample A337, there is a trend of progressively decreasing Ba concentration through units I, II, III and IV. In the pyroxenite at 272.6m in unit III, the Ba concentration is expectedly low (16 to 22ppm).

Unit V, the Main Mottled Anorthosite, is typified by relatively high levels of Ba (Fig. 23j), generally in the range 100ppm to 200ppm. Through units VI, VII, VIII and across the Pyroxenite Marker, there is a trend of slowly decreasing Ba concentration. This trend is not well defined, and there are several marked deviations from the general trend (Fig. 23j).

5.3.11 Zirconium

Pearce and Norry (1979) calculated distribution coefficients of 0.01 for Zr into plagioclase and orthopyroxene, and 0.1 into clinopyroxene, in basic assemblages. Hornblende, which occurs as a secondary mineral in parts of the Main Mottled Anorthosite, is assigned a distribution coefficient of 0.5 for Zr by Pearce and Norry (op. cit.). The

incompatible nature of Zr is apparent in the plot of Zr versus MgO (Fig. 24i), in which data are completely scattered. In general, Zr concentrations range from 0 to 10ppm, although a number of samples have higher concentrations, the maximum being 35.4ppm.

Zirconium displays very similar patterns of behaviour with stratigraphic height to the elements Ba and Rb (Fig. 23, j, k, ℓ), except for minor details. In units I, II and III of the Main Zone, Zr concentrations vary quite substantially, from below detection limit (sample A300) to 26.5ppm (sample A337), but no definite trends are discernible. A definite trend of upward increase in Zr begins at the base of unit IV (Fig. 23k), starting at 5.6ppm in sample A288, and rising to 15.5ppm in sample A262. Above sample A262, there is a rapid decrease in Zr, to 6.1ppm in sample A255. The point of inflection in the trend from increasing to decreasing Zr concentrations occurs in the vicinity of a substantial development of ultramafic pegmatite bodies, just below 500m (Fig. 23k). The concentration of Zr in sample A287 (15.7ppm) is anomalously high relative to its position near the base of unit IV, but no valid explanation can be found for this.

Unit V and the lower part of unit VI, up to 787m, are characterized by Zr concentrations which are widely variable, but are often in excess of 15ppm. Sample A246, an altered leucogabbro, displays the highest Zr concentration recorded in the SK2 succession (35.5ppm). Above 787m, Zr concentrations are almost invariably less than 10ppm, up to the top of unit VIII. There is a noticeable decrease in Zr across the Pyroxenite Marker, from 10.8ppm in sample MZ1 to 3.6ppm in sample SP11. This is followed, in the first 100m above the Pyroxenite Marker, by a steady increase to 9.8ppm Zr in sample MZ3. Above sample MZ3, Zr remains relatively constant between 8 and 10ppm up to 2690m.

5.3.12 Rubidium

Rubidium is present in the Main Zone cumulates in very low concentrations (generally less than 10ppm, and often below detection limit). From the work of Griffin and Murthy (1969), the distribution coefficient of Rb into plagioclase is of the order of 0.05, whilst distribution coefficients into the pyroxenes are substantially lower than this. The implication of the distribution coefficient data is that Rb is a highly incompatible element, but may in some situations be

accepted into late-crystallizing plagioclase. In general terms, however, Rb is expected to concentrate in the residual liquid.

The plot of Rb versus stratigraphic height (Fig. 23ℓ) illustrates the very low concentrations of Rb in the Main Zone rocks. Many of the samples analyzed, including all those above the Pyroxenite Marker, have Rb concentrations which are lower than the detection limit. There is a marked increase in Rb concentration in unit V (the Main Mottled Anorthosite), rising to a maximum of 35.4ppm in sample A246. Many of the anorthositic layers in this unit have undergone deuteric alteration, and the high Rb concentrations are ascribed to the presence of secondary biotite.

5.3.13 Summary of Trace Element Chemistry

As a broad generalization, the trace elements may be regarded as belonging to two groups, those that are compatible in the gabbroic mineral assemblage, and those that are incompatible. The behaviour of the compatible elements is governed by the mineralogy of the rocks, and can therefore be equated to some extent to the behaviour of the major elements. The incompatible elements, on the other hand, trace the behaviour of the interstitial liquid in cumulate rocks.

Binary plots of the trace elements against MgO (Fig. 24) give an indication of the behaviour of the trace elements. The transition elements Ni, Co, V, Zn and Sc all bear a positive relationship to MgO, demonstrating their affinity for the mafic minerals, in this case the pyroxenes. Cr is a somewhat more complex case than the other transition metals. What appears at first to be a scatter of points on the Cr versus MgO diagram can be resolved into a series of discrete trends, each relating to a separate stratigraphic interval within the Main Zone (Fig. 24e).

Strontium, and to a lesser extent barium, have an affinity for plagioclase. This is evident from the negative relationship between these two elements and MgO (Fig. 24, g and j). The concentrations of the incompatible elements (Y, Zr, Cu, Rb) are controlled by the amount of intercumulus liquid in the rock, and have no direct relationship to the modal mineralogy. Unit V (the Main Mottled Anorthosite), in particular, is notable for its high incompatible element concentrations

(Fig. 23).

Plots of the trace elements versus stratigraphic height (Fig. 23) vindicate to a large degree the demarcation of the successive units in the Main Zone, as used in this work. In the plot of Cr versus stratigraphic height (Fig. 23a), units I, II and III have Cr concentrations in the general range 190ppm to 490ppm. Near the base of unit IV, however, Cr increases to concentrations which are generally in excess of 500ppm. In sample A285, in the Porphyritic Gabbro Marker, Cr reaches a local maximum of 568ppm. From this point upwards, Cr concentration decreases steadily through units IV, V and VI. Units VII and VIII are characterized by Cr concentrations somewhat less than 80ppm, decreasing to 9ppm at the top of unit VIII. Above the Pyroxenite Marker , sharply higher Cr concentrations are encountered, in the range 340ppm to 610ppm.

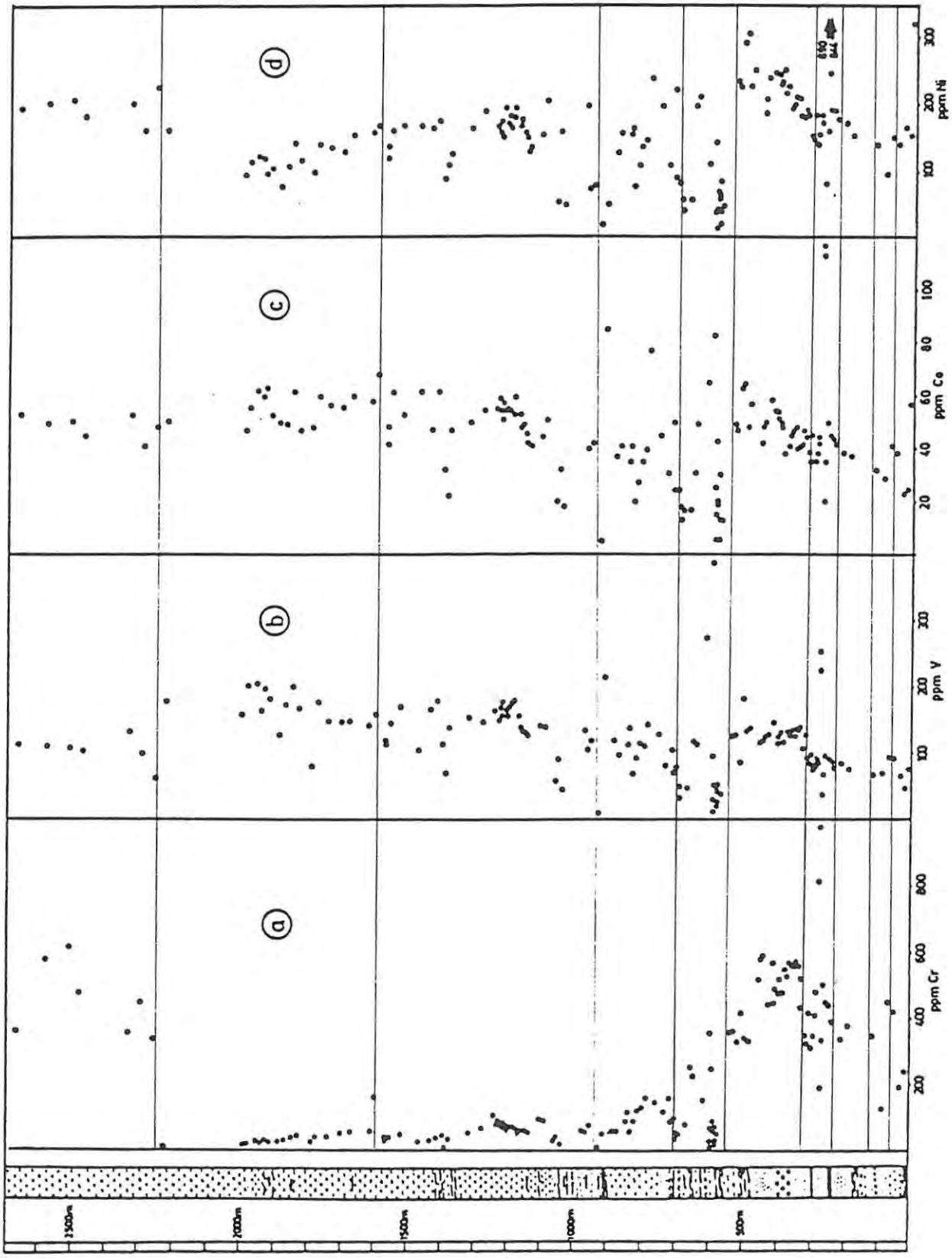

Fig. 23 . Trace element variations vs. stratigraphic height above the Bastard Reef in borehole SK2.

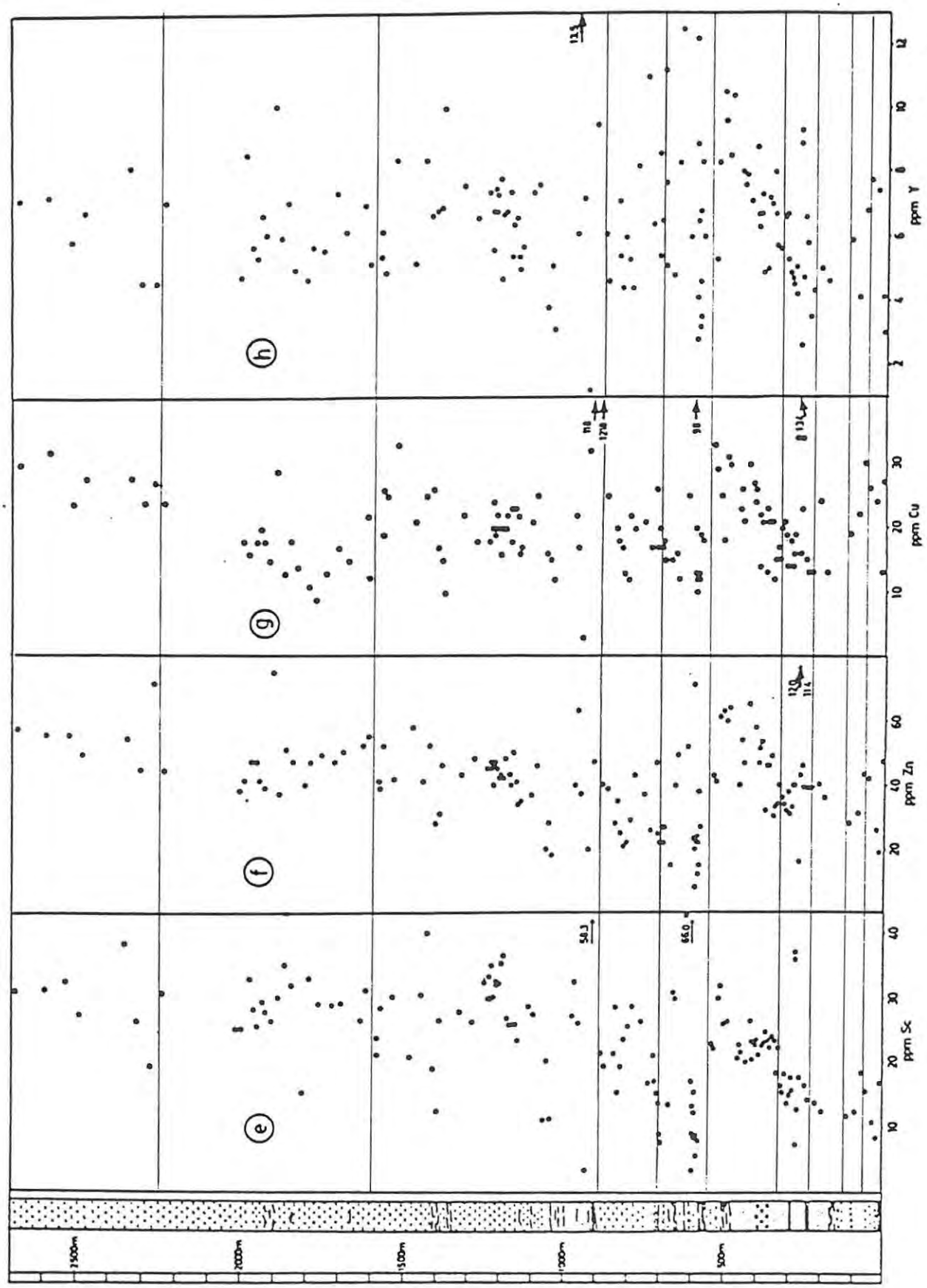

Fig. 23 . (continued)

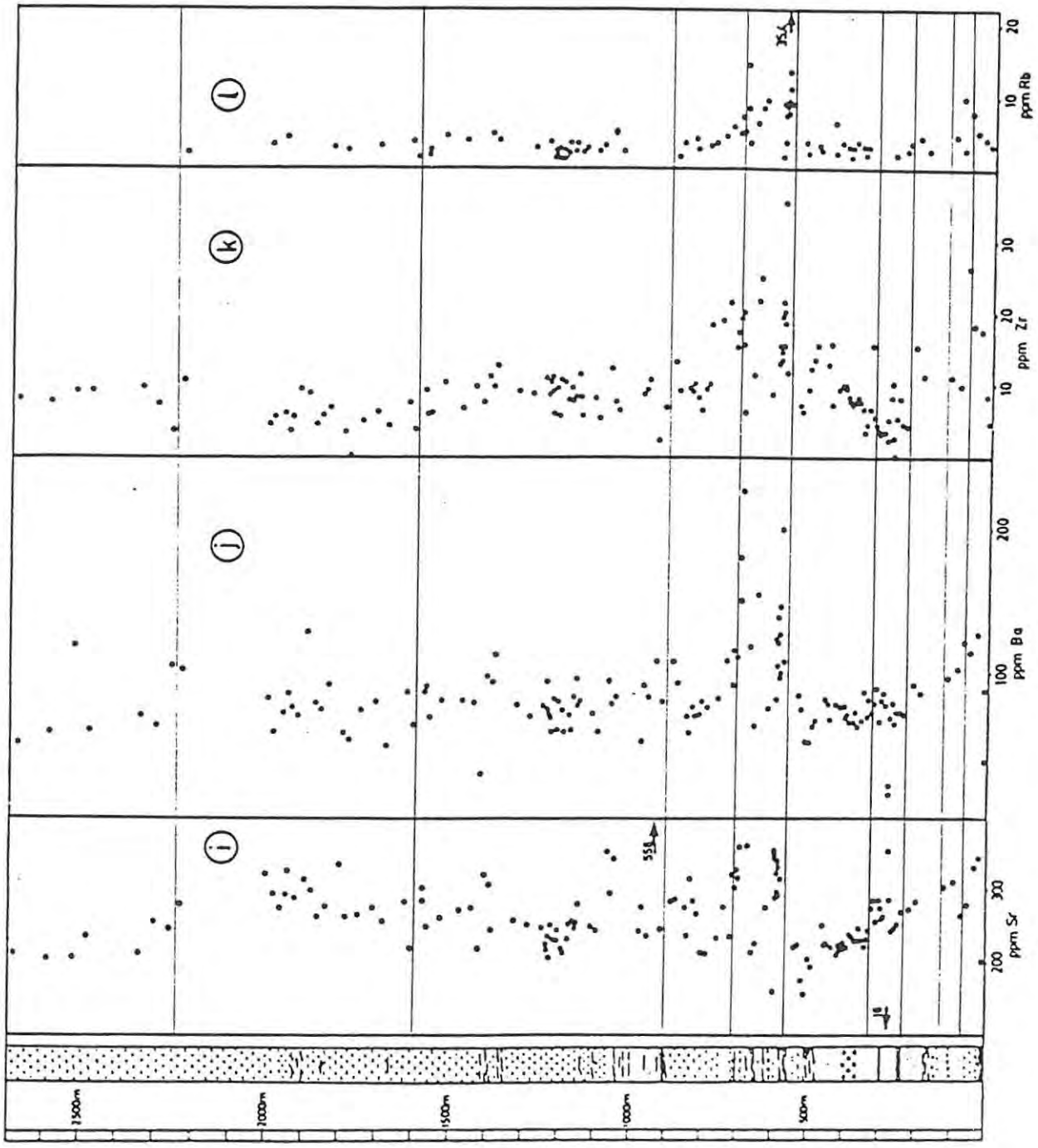

Fig. 23 . (continued)

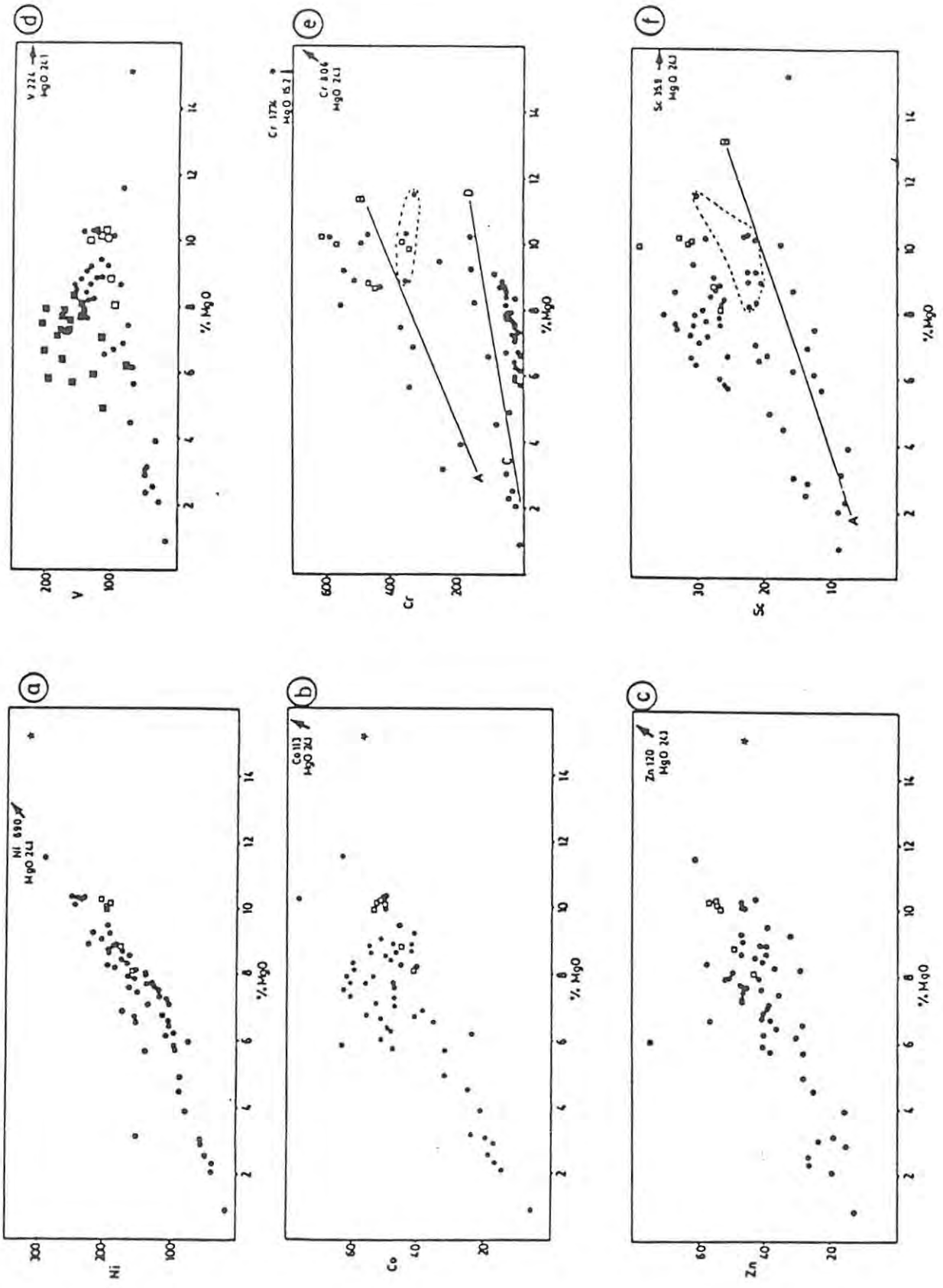

Fig. 24 : Binary plots of trace elements vs. MgO. Open squares represent samples from above the Pyroxenite Marker; star represents sample A349, from the Bastard Cyclic Unit; arrow indicates the composition of the pyroxenitic sample A297. Other markings are as described in the text.

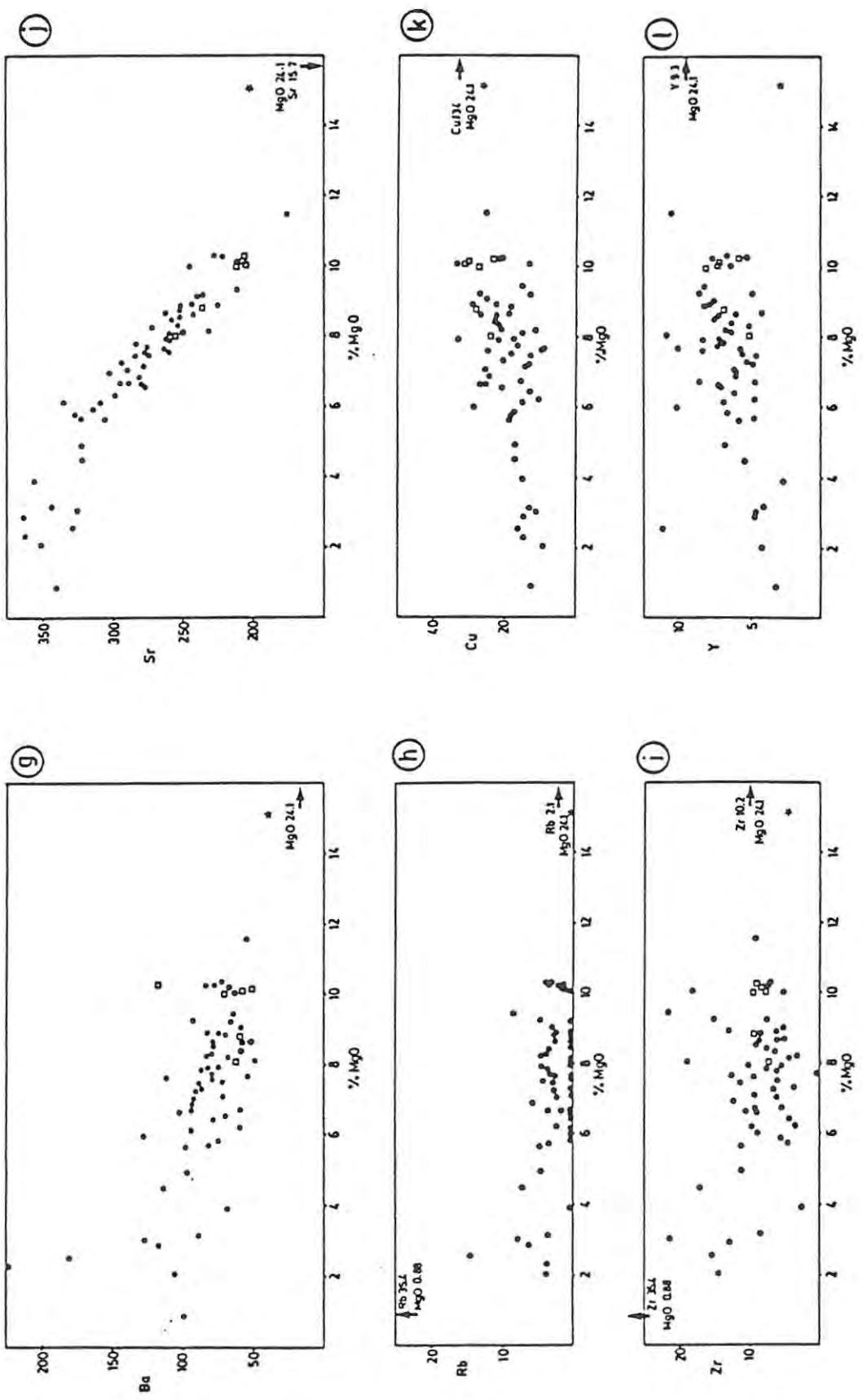

Fig. 24 . (continued)

TABLE 4

TRACE ELEMENT ANALYSES: BOREHOLE SK2

	A1	A5	A10	A13	A15	A18	A22	A25	A27	A29	A35	A38	A43	A48	A52	A63	A65	A71	A72	A74	A79	A91	A100	A103	A106
Co	47	56	62	60	63	53	50	49	62	47	48	60	57	56	60	58	68	48	47	62	53	59	47	59	32
Cr	14	17	21	17	29	22	23	29	38	40	22	38	38	50	53	56	160	34	28	37	45	24	26	37	42
V	159	201	205	164	198	182	129	172	200	169	80	175	148	148	147	141	158	119	115	145	170	103	166	179	113
Zn	38	41	47	47	41	39	74	37	51	47	40	47	49	47	50	52	55	41	39	52	42	58	41	52	28
Cu	18	16	18	20	18	15	29	13	18	14	11	9	13	17	15	22	12	19	26	25	33	21	25	26	17
Ni	92	111	119	117	94	102	73	105	140	114	97	139	132	128	152	156	167	119	134	159	166	166	162	176	87
Zr	4.8	5.6	6.0	3.9	5.7	9.6	9.0	4.6	5.8	6.9	3.7	nd	5.0	6.1	4.2	7.8	3.9	9.3	6.0	6.2	10.4	6.7	9.8	7.6	11.1
Y	4.8	8.6	5.7	5.4	6.7	6.1	10.1	6.0	7.1	5.0	4.7	5.7	5.6	7.4	6.2	7.0	5.2	5.4	6.2	4.9	8.4	5.2	8.4	6.7	6.8
Nb	nd	nd	nd	nd	nd	nd	nd	nd	nd	nd	nd	nd	nd	nd	nd	nd	nd	nd	nd	nd	nd	nd	nd	nd	nd
Rb	3.2	nd	4.2	nd	nd	nd	nd	nd	nd	2.9	2.4	nd	nd	3.1	nd	3.6	1.4	1.9	2.4	nd	4.5	3.9	nd	nd	4.7
Sr	322	295	276	293	328	290	315	300	262	278	336	264	266	276	259	284	220	286	303	250	261	273	277	220	322
Ba	81	58	71	85	75	70	129	78	74	91	58	53	74	80	48	86	63	86	90	69	80	80	79	29	98
Sc	25.5	25.5	33.1	28.5	26.0	29.8	26.9	30.2	35.2	32.2	15.6	33.4	29.4	29.0	29.4	26.9	31.4	24.0	21.4	28.8	30.4	21.0	30.9	40.1	19.2

	A108	A110	A117	A122	A126	A128	A129	A131b	A132	A133	A139	A140	A141	A142	A143	A145	A146	A147	A134	A148	A149	A135	A155	A137	A159
Co	23	47	50	54	55	54	57	51	57	54	54	55	54	53	59	53	48	49	46	42	41	44	51	20	32
Cr	5	32	51	62	106	75	87	76	80	66	74	71	60	68	67	61	50	54	54	58	51	91	87	24	38
V	69	137	152	147	166	150	168	154	178	156	165	154	170	175	176	156	138	134	131	126	116	140	139	54	90
Zn	31	46	43	48	45	45	47	40	46	47	45	42	43	42	48	43	40	50	41	34	35	37	46	20	28
Cu	15	10	22	18	18	20	24	19	20	27	20	16	20	20	22	18	23	23	22	16	17	21	25	16	15
Ni	108	123	161	188	167	157	172	150	171	192	170	180	162	177	191	166	174	157	149	128	134	152	201	50	107
Zr	9.9	12.9	9.1	8.8	11.0	8.9	10.3	11.2	9.3	6.0	9.6	5.8	10.8	10.2	8.0	9.8	7.9	8.3	11.6	8.2	5.7	8.1	5.4	12.1	7.8
Y	6.9	10.0	7.6	6.6	8.4	5.6	6.8	7.5	6.8	7.3	7.8	4.7	6.7	6.8	7.4	5.4	6.4	6.6	5.4	5.0	5.7	7.4	7.6	3.8	5.1
Nb	nd	nd	nd	nd	1.6	nd	nd	nd	nd	nd	nd	nd	1.3	nd	nd	nd	nd	nd	nd	nd	nd	nd	nd	1.6	nd
Rb	nd	3.9	nd	2.8	3.6	1.4	1.3	2.4	1.8	2.7	1.1	1.2	2.1	2.0	3.5	2.2	3.4	nd	2.1	nd	2.9	2.1	3.0	5.6	nd
Sr	309	247	258	252	249	226	218	237	208	252	231	230	245	220	213	232	254	258	248	253	280	250	244	353	298
Ba	93	112	77	69	76	94	74	70	69	58	81	60	80	74	58	70	60	83	96	77	80	72	58	94	78
Sc	12.7	26.8	28.0	26.5	32.7	30.1	33.5	30.1	35.1	30.2	32.9	32.3	32.4	35.4	36.8	27.0	26.0	26.0	26.0	26.0	23.6	28.8	27.7	11.2	20.2

nd = not detected

All concentrations in parts per million (p.p.m.)

TABLE 4

TRACE ELEMENT ANALYSES: BOREHOLE SK2

	A159	A161	A168	A138	A171	A176	A182	A191	A193	A198	A199	A200	A203	A204	A206	A208	A213	A217	A221	A222	A223	A224	A225	A226	A230
Co	32	18	46	40	42	5	86	37	41	35	41	20	27	35	39	77	45	31	50	24	24	18	13	17	17
Cr	38	15	59	59	73	5	43	55	54	85	112	57	86	117	124	159	141	116	158	85	97	39	50	46	76
V	90	44	133	105	118	8	214	118	97	112	136	67	91	114	110	141	128	80	105	70	78	36	31	49	46
Zn	28	18	40	63	37	20	57	40	39	28	35	25	21	22	29	43	37	26	47	25	22	27	22	27	15
Cu	15	12	22	17	3	32	118	1218	25	20	18	17	13	12	22	20	21	17	26	17	20	17	18	15	15
Ni	107	46	193	70	75	19	49	125	154	151	161	75	107	134	145	237	195	109	220	88	80	50	55	39	55
Zr	7.8	6.3	8.8	9.3	10.7	2.2	6.8	13.1	9.4	9.1	9.0	10.0	8.1	6.4	8.4	18.3	19.0	21.4	15.1	17.4	19.4	15.8	20.0	6.1	11.5
Y	5.1	3.1	6.1	13.5	7.2	1.2	9.5	6.1	4.6	7.1	5.4	4.4	6.0	5.3	4.4	8.2	11.0	6.4	8.6	5.4	6.5	11.2	7.7	5.1	4.8
Nb	nd	nd	nd	1.6	nd	nd	nd	nd	nd	nd	nd	nd	nd	nd	nd	nd	nd	2.3	nd	nd	nd	nd	1.9	nd	nd
Rb	nd	2.3	nd	nd	nd	nd	nd	1.7	3.6	nd	4.1	2.8	nd	nd	3.1	3.6	4.7	6.0	5.0	7.1	5.1	14.6	8.5	3.7	6.2
Sr	298	345	243	279	238.	556	247	285	289	277	238	317	288	269	214	211	231	278	236	321	304	329	318	363	364
Ba	78	83	52	92	83	108	79	108	94	70	59	76	70	71	80	76	82	109	92	115	111	180	150	226	118
Sc	20.1	11.2	27.2	32.8	26.1	3.3	58.3	21.6	19.6	21.5	28.9	15.4	19.5	23.7	24.9	28.8	26.5	17.0	21.1	17.1	15.3	13.9	9.0	7.6	13.6

	A233	A235	A236	A238	A240	A241	A242	A244	A245	A243	A246	A247	A248	A249	A254	A255	A257	A260	A261	A262	A264	A265	A266	A269	A271
Co	46	49	65	83	26	15	6	43	19	20	6	13	30	13	49	47	63	64	48	57	42	48	50	58	54
Cr	250	223	147	351	62	23	4	244	85	57	19	28	67	46	356	355	329	412	337	330	517	578	591	440	564
V	117	111	274	388	95	29	10	52	52	48	19	24	40	37	125	126	84	181	133	137	117	118	123	106	144
Zn	40	49	52	71	23	20	8	22	22	24	12	15	38	27	43	41	61	63	60	64	40	54	47	65	60
Cu	16	12	25	98	20	10	13	12	13	12	13	13	19	18	33	29	25	18	31	30	23	26	21	30	27
Ni	194	208	109	141	36	39	11	66	61	56	19	37	82	46	233	225	290	302	227	250	185	205	239	246	243
Zr	21.8	25.0	8.8	13.0	15.3	14.7	13.4	19.7	15.5	21.5	35.5	20.1	18.7	11.9	7.1	6.1	9.4	12.3	13.6	15.5	13.0	15.8	7.4	9.4	10.1
Y	8.3	12.5	8.0	12.2	8.9	4.1	2.8	6.5	6.8	4.6	3.2	3.5	8.3	6.0	5.3	8.3	10.5	9.6	8.5	10.4	8.0	7.6	7.9	7.1	8.8
Nb	nd	nd	nd	nd	nd	nd	1.8	1.3	nd	nd	nd	1.6	nd	1.7	nd	nd	nd	nd	nd	nd	nd	nd	nd	nd	nd
Rb	8.5	9.7	nd	1.8	9.2	3.9	7.8	8.7	9.6	7.9	35.4	13.6	11.3	9.1	3.9	2.3	nd	nd	3.2	2.7	nd	6.6	2.1	3.8	3.1
Sr	213	229	277	160	345	351	356	290	298	325	341	332	293	318	222	225	177	158	205	197	251	227	228	222	211
Ba	64	155	75	81	124	105	122	138	98	127	100	146	200	109	83	75	52	52	63	67	81	77	67	77	76
Sc	31	30	43	66	17.1	9.0	3.3	13.2	12.3	15.5	8.7	5.5	8.9	8.0	22.9	22.2	30	32	26.0	26.3	20.8	22.8	21.7	20.2	26.4

TABLE 4

TRACE ELEMENT ANALYSES: BOREHOLE SK2

	A273	A274	A275	A276	A278	A280	A281	A282	A283	A284	A285	A286	A287	A288	A289	A290	A291	A292	A293	A294	A295	A297	A298	A299	A300
Co	54	51	50	48	38	41	45	47	48	40	41	42	47	44	38	35	45	35	38	44	42	113	117	20	35
Cr	442	482	471	517	473	546	527	564	548	559	568	559	429	517	343	321	411	306	342	403	438	806	974	188	331
V	114	124	130	126	117	131	127	133	126	137	135	137	105	126	91	84	98	72	78	89	86	224	252	34	66
Zn	60	58	47	51	53	32	46	46	49	30	33	34	40	36	34	32	38	31	33	40	40	120	114	16	43
Cu	24	26	14	22	21	13	23	21	21	12	15	17	15	20	21	19	14	18	14	16	19	34	134	16	23
Ni	229	231	250	215	225	192	198	209	206	182	182	178	189	182	150	147	181	140	154	181	172	690	644	80	159
Zr	10.0	9.8	8.5	7.9	7.8	7.9	8.3	7.9	6.9	3.6	4.8	6.7	15.7	5.6	4.3	3.8	3.1	3.6	5.0	2.6	5.1	10.2	8.5	2.9	nd
Y	6.7	6.3	6.7	7.3	4.9	5.0	7.2	7.0	8.0	6.7	5.7	5.6	16.8	6.6	6.7	5.3	4.9	4.7	4.5	5.2	4.2	9.3	8.9	2.6	4.7
Nb	nd	nd	nd	nd	nd	nd	nd	nd	1.5	nd	nd	nd	nd	nd	nd	nd	nd	nd	nd	nd	nd	nd	nd	nd	nd
Rb	2.1	1.8	3.0	3.9	3.8	nd	3.3	2.1	3.1	nd	nd	nd	nd	nd	nd	nd	nd	nd	nd	nd	nd	2.1	nd	nd	nd
Sr	224	217	228	220	222	239	237	231	231	249	231	222	233	245	275	287	258	289	276	262	263	16	16	356	289
Ba	76	76	68	71	66	65	73	63	66	67	87	69	81	72	79	90	66	81	87	82	78	16	22	68	79
Sc	20.5	23.1	22.7	23.6	21.2	22.7	23.0	24.9	23.5	22.3	24.0	23.2	18.3	22.4	16.3	15.4	18.2	13.9	15.0	17.6	15.8	36	37	7.2	12.8

	A301	A303	A305	A308	A312	A315	A327	A334	A337	A340	A343	A346	A349	A350	A351	A352
Co	50	44	43	42	38	37	32	28	41	38	23	24	57	31	63	101
Cr	493	443	437	383	335	372	345	126	447	419	191	240	1774	755	1821	3074
V	96	90	86	76	84	75	67	69	94	91	63	46	73	42	87	138
Zn	46	39	39	39	40	36	28	31	43	42	26	19	47	25	66	98
Cu	34	15	13	13	24	13	19	22	30	26	24	13	27	67	136	319
Ni	246	189	187	175	170	150	138	94	149	139	63	151	319	221	559	1166
Zr	5.3	8.1	4.7	4.2	16.2	11.3	11.3	10.0	26.5	18.6	17.8	8.6	4.9	4.9	3.9	7.9
Y	6.5	5.8	3.5	4.3	5.0	4.6	5.9	4.1	6.8	7.7	7.4	4.1	3.0	3.0	5.0	6.2
Nb	nd	nd	nd	nd	nd	nd	nd	nd	nd	nd	nd	nd	nd	nd	nd	nd
Rb	nd	nd	2.7	3.8	4.5	2.7	5.0	3.0	8.1	5.5	4.4	3.5	nd	4.0	nd	nd
Sr	245	248	251	271	275	284	306	311	267	280	332	344	201	326	205	77
Ba	65	74	74	73	93	87	97	104	122	115	128	88	39	74	54	40
Sc	17.6	16.6	16.4	14.1	13.7	12.3	11.7	12.2	18.2	15.4	10.8	8.2	16.6	10.8	20.0	30.2

TABLE 4

TRACE ELEMENT ANALYSES: 11 Level 6[e] Crosscut

	C1	C8	C12	C19	C24	C25	C30	C37	C41	C47	C50	C51	C53	C55	C57	C60	C62	C64	C66	C67	C68	C69	C70	C71	C73
Co	37	33	53	33	33	19	52	18	36	37	23	19	16	16	16	10	9	45	54	73	75	86	86	56	6
Cr	425	367	652	370	411	211	562	199	449	466	152	142	190	182	151	126	99	1143	1848	2677	2901	2846	2921	3323	49
V	74	76	91	79	93	37	102	62	88	92	59	59	36	37	36	24	15	79	68	90	92	119	118	124	12
Zn	36	50	62	33	50	27	59	34	62	41	42	38	30	27	28	23	21	57	56	73	72	94	95	58	16
Cu	20	27	27	22	36	21	31	27	37	29	27	27	22	18	18	19	20	57	26	31	31	110	145	382	56
Ni	166	163	260	141	149	81	205	68	204	143	79	62	66	61	59	47	42	223	339	463	483	694	774	906	73
Zr	4.8	18.1	7.3	28.8	23.6	5.4	21.1	31.1	30.2	24.7	22.7	25.0	7.1	5.5	2.5	9.5	10.9	16.8	2.0	3.8	4.1	19.2	14.3	13.2	4.3
Y	2.6	5.3	4.4	5.5	7.0	2.0	7.5	8.1	7.1	7.3	6.4	5.8	2.1	2.1	8.1	3.0	2.1	5.9	1.4	2.8	3.2	6.4	6.2	4.4	2.4
Nb	nd	nd	nd	nd	nd	nd	2.3	nd	nd	nd	nd	nd	nd	nd	nd	nd	nd	nd	nd	nd	nd	nd	nd	nd	nd
Rb	nd	4.1	nd	9.9	2.8	2.3	5.0	13.4	10.6	7.9	7.9	10.2	2.9	nd	2.5	2.5	3.7	5.0	nd	nd	nd	5.3	3.3	3.8	nd
Sr	265	279	214	264	252	344	231	322	229	267	307	317	326	330	339	347	359	219	180	114	102	55	52	13	390

TRACE ELEMENT ANALYSES: Borehole SK4

	B1	B5	B12	B43	B58	B65	B70	B86	B97	B100
Co	26	53	50	54	29	29	50	30	36	47
Cr	30	66	65	274	124	238	498	299	314	618
V	62	101	117	136	59	59	135	76	82	106
Zn	36	55	35	31	33	24	43	30	36	52
Cu	25	26	11	21	21	11	15	21	21	19
Ni	87	186	178	243	117	117	218	119	141	229
Zr	15.9	16.5	3.8	30.4	28.5	15.2	22.0	23.8	28.6	13.7
Y	5.3	7.6	5.8	9.0	7.5	5.9	7.1	7.8	6.6	5.9
Nb	nd	nd	nd	nd	nd	nd	nd	nd	nd	nd
Rb	11.3	4.8	nd	7.6	10.7	10.5	7.4	8.1	5.6	8.6
Sr	364	275	244	241	359	403	244	318	300	267
Ba	121	87	62	56	127	135	74	106	71	94
Sc			29.3	33.2	14.0	13.8	25.3	15.2	17.9	

TRACE ELEMENT ANALYSES: Spitzkop 410 KQ

	SP1	SP3	SP5	SPK2	SPK6	MZ1	SP11	MZ2	MZ3	MZ4	MZ5	MZ6	MZ7	UZ1	UZ2
Co	38	30	44	51	54	51	48	41	53	45	51	50	53	94	38
Cr	349	153	239	27	28	9	337	443	348	472	612	578	359	192	31
V	94	63	117	90	86	179	61	99	133	101	109	110	114	297	72
Zn	52	40	55	60	67	44	71	44	54	49	55	55	57	120	54
Cu	31	21	27	31	24	24	27	24	28	28	24	32	30	38	26
Ni	171	135	199	153	130	159	221	159	198	179	204	198	188	167	56
Zr	27.9	18.9	24.5	3.4	4.4	10.8	3.6	7.5	9.8	9.5	9.2	7.9	8.1	5.5	nd
Y	8.7	5.6	9.0	6.1	3.8	7.1	4.6	5.2	8.2	6.8	5.9	7.3	7.2	11.7	3.9
Nb	nd	nd	nd	nd	nd	nd	nd	nd	nd	nd	nd	nd	nd	nd	nd
Rb	10.7	9.2	8.6	2.7	3.9	2.0	nd	nd	nd	nd	nd	nd	nd	nd	nd
Sr	254	274	232	290	312	280	246	256	211	235	206	206	207	161	409
Ba	169	146	132	100	92	101	104	62	70	60	118	59	50	106	131
Sc	20.5														

5.4 Interelement Ratios

5.4.1 Introduction

From the preceding sections of this discussion, it is apparent that there are strong modal controls on the behaviour of individual elements in the Main Zone. The use of appropriate interelement ratios largely eliminates these modal effects, and the behaviour of the ratios may therefore be regarded as more process-related. The interelement ratios discussed here are Cr/Sc, V/Cr, Ni/Co, Sr/Al_2O_3 and Ba/Sr (Fig. 25). In addition, the relationship between vanadium and chromium is discussed by reference to an interelement plot of V versus Cr.

5.4.2 The Cr/Sc Ratio

In the absence of a spinel phase, as is the case in the Main Zone, Cr and Sc both preferentially enter the clinopyroxene crystal structure. D_{Cr} for clinopyroxene is of the order of 10 (Cox et al., 1979), whereas D_{Sc} for clinopyroxene is of the order of 3 (Frey et al., 1978) This bears out the assertion by Irvine and Smith (1967) that Cr is an extremely good indicator of fractionation, particularly in the presence of clinopyroxene. In a magma crystallizing clinopyroxene, the residual liquid will be progressively depleted in Cr at a greater rate than it is depleted in Sc. The Cr/Sc ratio would therefore decrease with increasing fractionation.

In the plot of the Cr/Sc ratio versus stratigraphic height (Fig. 25a), the Bastard norite (sample A349) has a Cr/Sc ratio of 107. Cr/Sc decreases sharply to less than 30 in sample A346, 18.2m above the Bastard Reef. In Main Zone units I and II, the Cr/Sc ratio varies between 10 and 30, according to the relatively sparse available data.

Main Zone unit III can effectively be divided into two sub-units on the basis of the Cr/Sc ratio. The lower sub-unit, from the base of unit III to the base of the pyroxenite at 272.6m, is characterized by ratios between 25.8 and 28. The upper sub-unit, from pyroxenite sample A297 to sample A289, at the top of unit III, is characterized by ratios between 21 and 23, apart from sample A295 (283m above the Bastard Reef), where the ratio is 27.7.

In unit IV, the data may be grouped into three sub-units. The first of these is a loosely-defined trend of decreasing Cr/Sc ratio, ranging from 25 to 21, and extending from sample A288, at the base of unit IV, to sample A269, at 428.8m. This trend incorporates the Porphyritic Gabbro Marker. The second group of data covers the interval from 442m to 455m, incorporating samples A266, A265 and A264. These samples have Cr/Sc ratios between 25 and 27. The uppermost group of samples in unit IV covers the interval from approximately 487m to the top of the unit. This group of samples is marked by a sharp decrease in the Cr/Sc ratio, to values between 10.9 and 15.9

The Main Mottled Anorthosite, unit V, is characterized by Cr/Sc ratios which, with one exception, do not exceed 8, and reach a low of 1.18 The exception is sample A244 (at 588m), which has a Cr/Sc ratio of 18.55 There is no apparent explanation for this anomalously high Cr/Sc ratio (which incidentally corresponds with a high V/Cr ratio), except for the close proximity of an ultramafic pegmatite body. Above the Main Mottled Anorthosite, unit VI represents an extremely well-defined trend of decreasing Cr/Sc ratios. This trend extends from 7.5 in sample A221 (at the base of the unit) to 2.54 in sample A191 (at the top of the unit.

In unit VII, although the Cr/Sc ratio is consistently less than 3.5, there is a well-developed saw-tooth pattern. Notable high points in this pattern are sample A155 (Cr/Sc = 3.14) and sample A126 (Cr/Sc = 3.22). The base of unit VIII, at 1600m, is characterized by a locally very high Cr/Sc ratio of 5.1 (sample A65), but the ratio decreases sharply to 2.08 in sample A63. Above A63, there is a progressive decrease in the ratio to 0.30 in sample MZ1, at the top of unit VIII. No clear pattern is developed in the samples above the Pyroxenite Marker. They are, however, characterized by ratios which, in the range 8.95 to 18.59, are substantially higher than in the rocks of the underlying unit VIII.

5.4.3 The V/Cr Ratio

Vanadium is somewhat similar to scandium in its geochemical behaviour, being compatible in clinopyroxene, with a distribution coefficient of 1.5 (Frey et al., 1978). The V/Cr ratio is therefore complementary to the Cr/Sc ratio in representing the behaviour of the pyroxenes, and of

clinopyroxene in particular, although they are effectively the reverse of one another. In units I, II, III and IV of the Main Zone, the V/Cr ratio is invariably less than 0.35, with the exception of the aberrant ratio of 0.55 in sample A334 (at 86m). At these low ratios, variations are difficult to evaluate (Fig. 25b).

Unit V (the Main Mottled Anorthosite) may effectively be regarded as two sub-units in terms of the V/Cr ratio. The first of these sub-units covers the 45m interval from 574m to 619m, and represents a very broadly-defined trend of upward increase in the V/Cr ratio. The range of the ratio in this trend is from 0.6 or less to ratios approaching 2. The second part of unit V covers samples from 646m to 712m. From a ratio of less than 0.50 at 646m, V/Cr increases progressively upwards to between 0.80 and 0.90 at 700m.

At the base of unit VI, the V/Cr ratio decreases to 0.66 in sample A221. From the low ratios at the base of the unit, there is a virtually unbroken exponential increase in V/Cr to 4.97 in sample A182 (at the base of unit VII). Patterns of variation in V/Cr in unit VII are rather more complex than in the underlying and overlying units. Unit VII appears to consist of at least three, and possibly four, constituent cycles. These cycles form a sawtooth pattern which is, in essence, a mirror image of the pattern of Cr/Sc variation for the same interval. One sample in unit VII (A108, at 1396.6m), has an extremely high V/Cr ratio close to 13.

At the base of unit VIII, sample A65 has a relatively low V/Cr ratio of 0.99 (Fig. 25b), which is mirrored by a relatively high Cr/Sc ratio (5.1). Within a stratigraphic interval of 16 metres, the V/Cr ratio increases to 2.52, in sample A63. From here, there is a steady exponential increase in V/Cr, culminating at the top of unit VIII with a ratio of 19.4 (sample MZ1). Above the Pyroxenite Marker, the V/Cr ratio is consistently less than 0.4

5.4.4 The V/Sc Ratio

By comparison with the Cr/Sc and V/Cr ratios, the V/Sc ratio (Fig. 25c) displays less spectacular variations with stratigraphic height. the most obvious geochemical break displayed by the V/Sc ratio is at the Pyroxenite Marker, across which the ratio decreases sharply, from 5.78

in sample MZ1 to 3.04 in sample SP11. In parts of the succession where Fe-rich ultramafic pegmatites aboound, particularly in the Main Mottled Anorthosite and at the base of unit VII, the V/Sc ratio is most variable, with a bias towards low ratios. Another geochemical break occurs at the boundary between units III and IV, where the V/Sc ratio decrease from 6.14 in sample A312 to 5.36 in sample A308.

5.4.5 The Ni/Co Ratio

Nickel distribution coefficients are high for both clinopyroxene and orthopyroxene, ranging from 2 to 4 and from 3 to 5, respectively (Frey et al., 1978). Cobalt distribution coefficients are relatively low, D_{Co} being between 1 and 2 for clinopyroxene, and 2 for orthopyroxene (Frey et al., op. cit.). On this basis, the Ni/Co ratio would be expected to decrease as crystallization of pyroxene proceeds. This is the case in Main Zone units VI, VII and VIII. In the Main Zone units below the Main Mottled Anorthosite, however, Ni/Co increases upwards , suggesting the operation of a mechanism other than simple fractionation.

As with the V/Sc ratio, the Ni/Co ratio is apparently affected by the proximity of Fe-rich ultramafic pegmatite bodies. This is reflected in the low Ni/Co ratios in unit V and at the base of unit VII (Fig. 25d). Apart from these two zones, the plot of the Ni/Co ratio versus stratigraphic height may effectively be divided into three sectors.

The first of these sectors incorporates units I, II, III and IV of the Main Zone, and is characterized by a subdued general upward increase in the Ni/Co ratio, although data are somewhat scattered (Fig.25d). The pyroxenite layer at 272.6m in unit III displays high Ni/Co ratios (5.5 to 6.1). An anomalously high Ni/Co ratio of 5.53 is encountered in sample A278, near the top of the Porphyritic Gabbro Marker. Unit V (the Main Mottled Anorthosite) is characterized by such anomalously low Ni/Co ratios that it looks out of place in that part of the Main Zone (Fig. 25d). From the base of unit VI, where the ratio is somewhat over 4, Ni/Co decreases progressively through units VI, VII and VIII to a ratio of the order of sample MZ1. In the 440m interval above the Pyroxenite Marker, Ni/Co varies between 3.71 and 4.02.

5.4.6 The Ni/Sc Ratio

In most respects, the plot of the Ni/Sc ratio against stratigraphic height (Fig. 25e) is similar to the equivalent plot of the Ni/Co ratio. There is a noticeable difference between the two plots in units I, II, III and IV, however, where the Ni/Sc ratio displays more clearly-defined patterns than does the Ni/Co ratio. Near the base of the Bastard Cyclic Unit, samples A349 and A346 have Ni/Sc ratios between 18 and 19. Higher up in the Bastard Cyclic Unit, samples A343 and A340 have Ni/Sc ratios of 5.8 and 9, respectively. In Main Zone unit I, Ni/Sc varies between 7.7 and 11.8, but the data are too sparse for any trends to be identified. Only two samples were analyzed from unit II, both near the top of the unit. These two samples have Ni/Sc ratios between 12.2 and 12.4 The Ni/Sc ratio is 12.4 in sample A308, near the base of unit III.

There is a strongly defined trend of upward decrease in the Ni/Sc ratio through unit III, culminating in a ratio of 9.2 in sample A289. With a Ni/Sc ratio of between 17.3 and 19.2, the pyroxenite at 272.6m is a notable exception to the general trend (Fig. 25e). In the lower part of unit IV, the ratio is of the order of 8, but in sample A278 (378.5m), the ratio increases to above ten. From the base of unit V up to the top of unit VIII, the Ni/Sc ratio is consistently less than ten, and is particularly low in the Main and Upper Mottled Anorthosites. Across the Pyroxenite Marker, there is a marked increase in the Ni/Sc ratio, from 3.46 in sample MZ1 to 11.1 in sample SP11. The ratio decreases rapidly above SP11, however, and maintains an average of 6 for the rest of the succession up to 2690m.

5.4.7 The Ba/Sr Ratio

Barium and strontium are both influenced by plagioclase. Cox et al. (1979) recommend $D_{Sr} = 2.2$ and $D_{Ba} = 0.2$ for plagioclase. These distribution coefficients are in approximate accord with the experimental data of Drake and Weill (1975) for the normal range of magmatic temperatures. The latter authors demonstrated, however, that the distribution coefficients vary with changing temperature.

Unit V (the Main Mottled Anorthosite) is particularly noticeable on the plot of the Ba/Sr ratio versus stratigraphic height (Fig. 25f), because

plot of the Ba/Sr ratio versus stratigraphic height (Fig. 25f), because of the high ratios which characterize many of the samples within this unit. The Ba/Sr ratio varies from 0.25 to almost 0.7 in the Main Mottled Anorthosite. In the pyroxenite at 272.6m, the Ba/Sr ratio is an extremely high 1.36 in sample A298, presumably reflecting the intercumulus nature of the plagioclase.

5.4.8 The Sr/Al_2O_3 Ratio

Drake and Weill (1975) showed that Sr is concentrated in plagioclase relative to igneous liquids at all reasonable temperatures, and that the feldspar/liquid partition coefficient is essentially unaffected by the concentration of Sr. Orthopyroxene contains approximately 0.7 weight percent Al_2O_3, and clinopyroxene between 1.0 and 1.5 weight percent Al_2O_3. Plagioclase, however, is the major aluminous mineral in the Main Zone, containing of the order of 30 weight percent Al_2O_3, depending on composition. The Sr/Al_2O_3 ratio is therefore almost exclusively an indicator of plagioclase behaviour.

From 12.3×10^{-4} near the base of the Bastard Cyclic Unit, the Sr/Al_2O_3 ratio increases more or less continuously to 455m (sample A264), where the ratio is 13.64×10^{-4}. The only notable exception to this trend is the pyroxenite at 272.6m in unit III (sample A297), which has a ratio of 6.96×10^{-4}. In the topmost 20m of unit IV, samples A254, A255 and A257 have ratios between 12.13×10^{-4} and 12.90×10^{-4}, which are noticeably lower than those in the lower part of unit IV. The Sr/Al_2O_3 ratios of samples A254, A255 and A257 appear, in fact, to presage the low Sr/Al_2O_3 ratios of the lower part of the overlying unit V (the Main Mottled Anorthosite).

From the base of unit V, where the ratio reaches a low of 11.70×10^{-4} in sample A246, Sr/Al_2O_3 increases in a general way throughout units V, VI, VII and VIII (Fig. 25g). Locally low ratios are invariably associated with the close proximity of ultramafic pegmatite bodies. Across the Pyroxenite Marker, Sr/Al_2O_3 decreases from 15.26×10^{-4} in sample MZ1 to 13.41×10^{-4} in sample MZ2. From MZ2, there is a steady decrease in the ratio to 12.14×10^{-4} in MZ6, followed by a slight increase to 12.44×10^{-4} in sample MZ7.

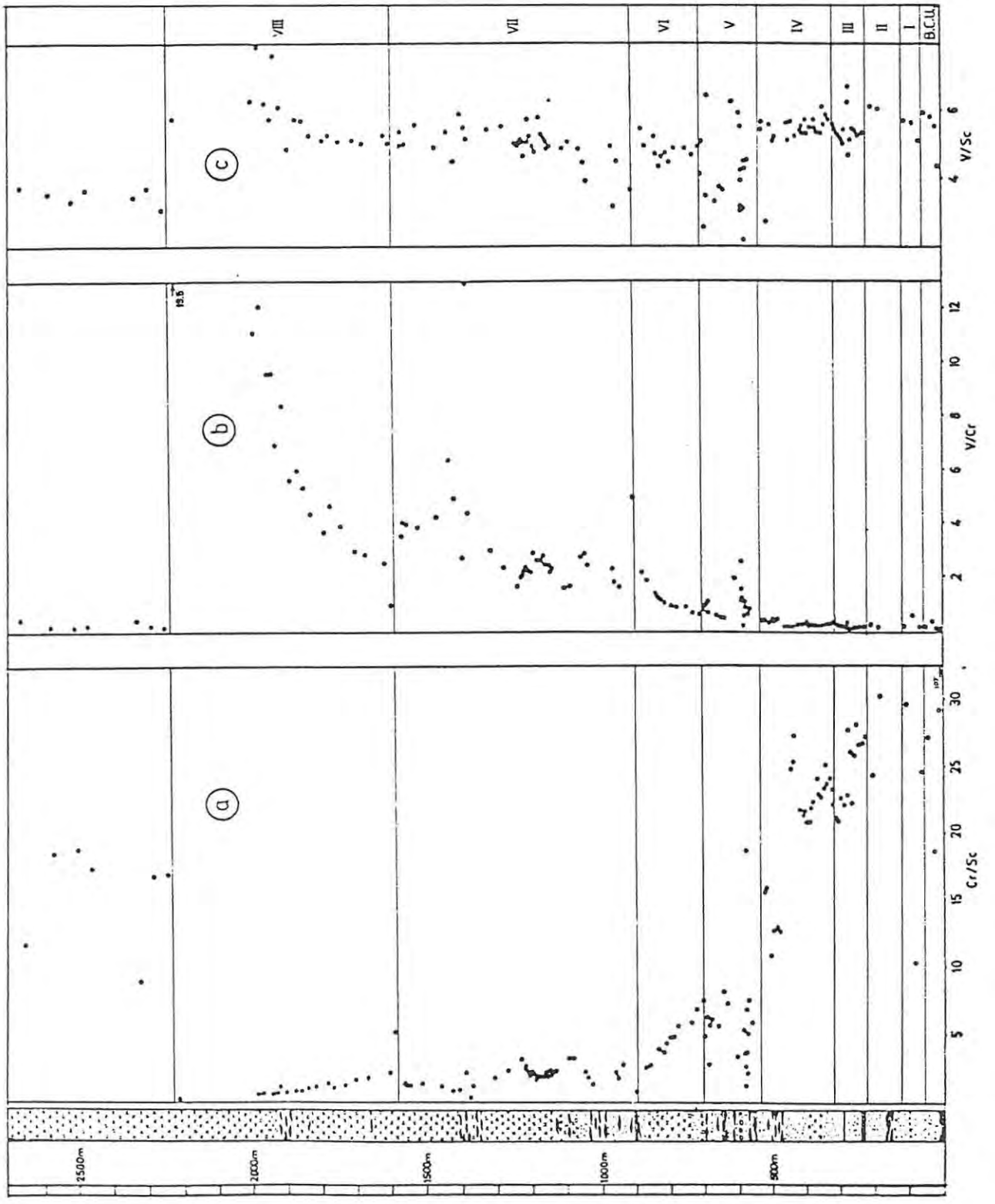

Fig. 25: Plots of whole-rock interelement ratios versus stratigraphic height

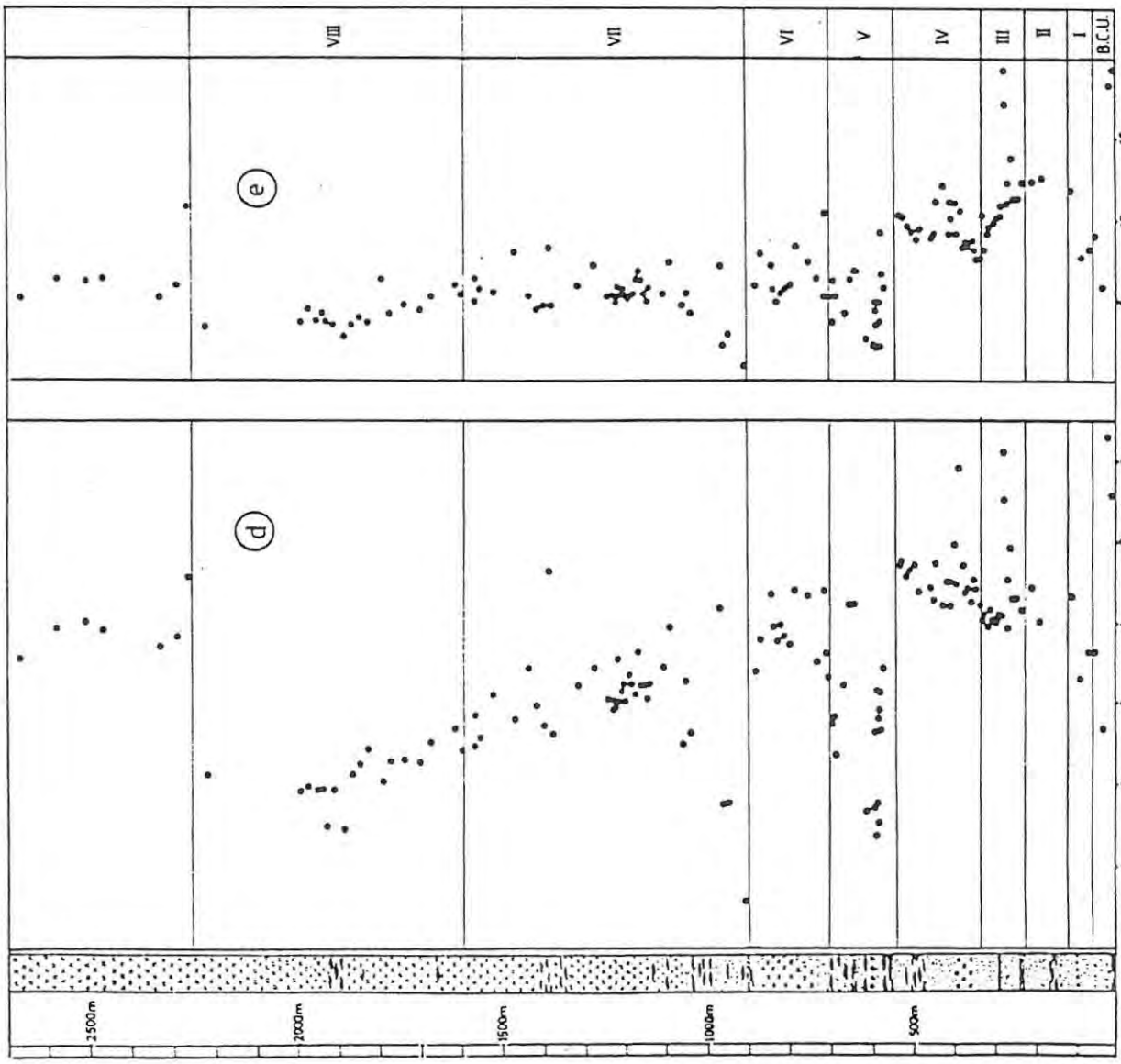

Fig. 25: Plots of whole-rock interelement ratios versus stratigraphic height.

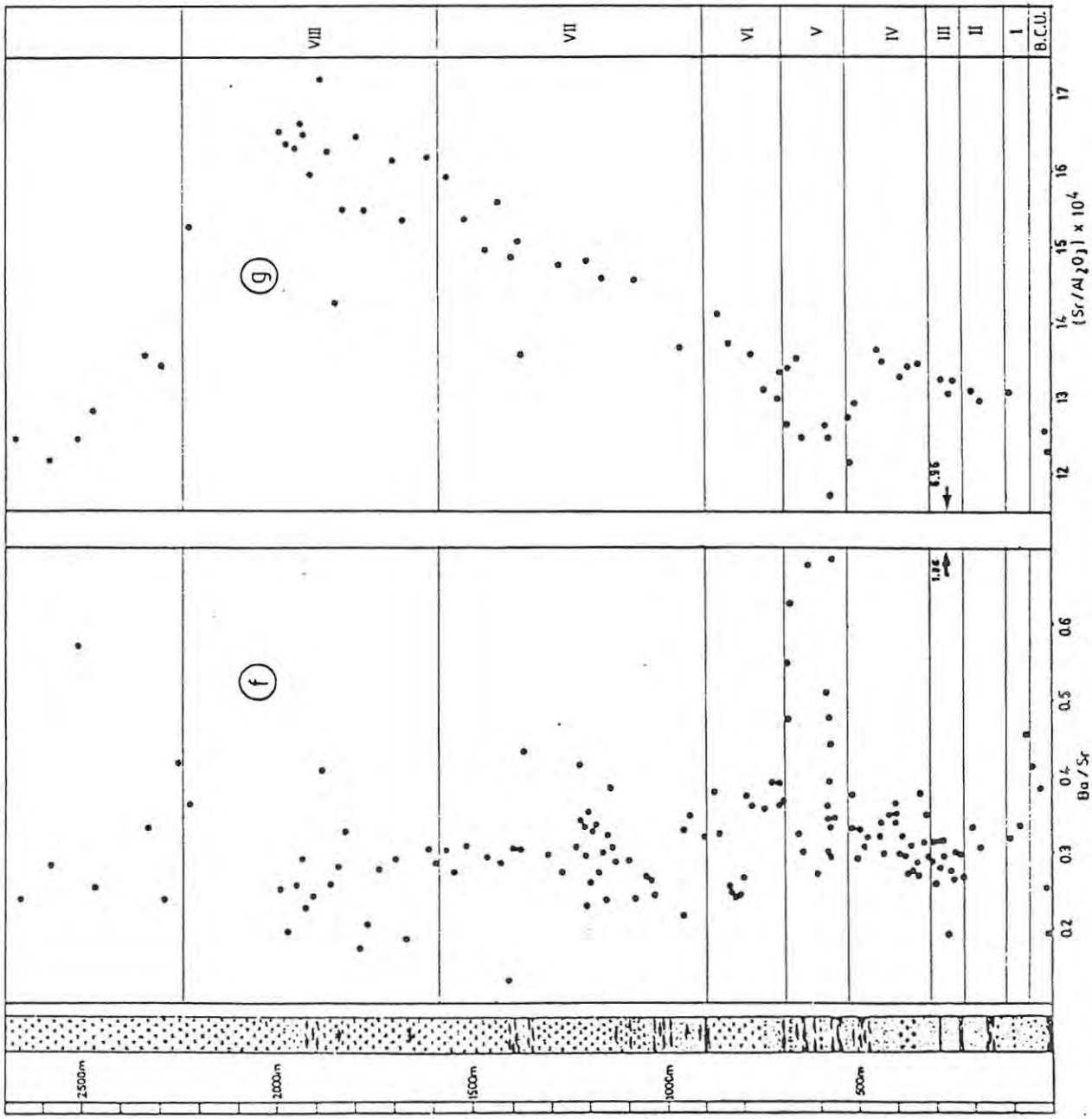

Fig. 25 : Plots of whole-rock interelement ratios versus stratigraphic height.

5.4.7 The Cr - V Plot

The interelement plot of Cr versus V (Fig. 26) can be resolved into a series of separate, more or less linear trends, generally radiating from the origin. Each trend represents a different stratigraphic interval in the Main Zone. The individual trends are essentially mixing lines between plagioclase (at the origin) and pyroxene (both orthopyroxene and clinopyroxene). Plagioclase is at the origin of the diagram because it accepts neither Cr nor V into its crystal lattice. Chromium is compatible in both clinopyroxene and orthopyroxene, although more so in clinopyroxene. Vanadium behaves similarly to Cr, having distribution coefficients of 1.5 into clinopyroxene and 0.3 into orthopyroxene.

In the Bastard and Merensky Cyclic Units, whole-rock Cr concentrations are relatively high (sample A349 has a whole-rock Cr content of 1774ppm, reflecting concentrations of the order of 0.5% Cr_2O_3 in orthopyroxene (appendix 7), and correspondingly high concentrations in clinopyroxene). The steepest of the trends in Fig. 26 represents samples from the upper part of the Bastard Cyclic Unit and Main Zone units I, II and III. The samples in unit IV form two distinct groups in Fig. 26. The lower part of unit IV, up to 455m, has relatively high Cr concentrations, in excess of 400ppm, and represents the Porphyritic Gabbro Marker and its immediate hanging- and footwall. Between 455m and the top of unit IV, smples A262 to A254 are notably enriched in vanadium relative to samples from below 455m. The upper part of unit IV is also characterized by anomalous iron enrichment of the pyroxenes (Fig. 14, Fig. 34). It is reasonable to conclude that the enrichment in both iron and vanadium in this interval is related to a common process, possibly related to the development of Fe-rich ultramafic pegmatite in unit V.

Above unit IV, Cr concentrations are almost invariably less than 300ppm, the notable exception being A238. In this latter sample, relatively high Cr (351ppm) is complemented by high V (388ppm), which relates to a higher than average proportion of mafic minerals (pyroxene) in the rock. Although there is a gross pattern of progressive decrease in Cr through units V, Vi, VII and VIII, there is substantial overlap between them (Fig. 26). This is also reflected in

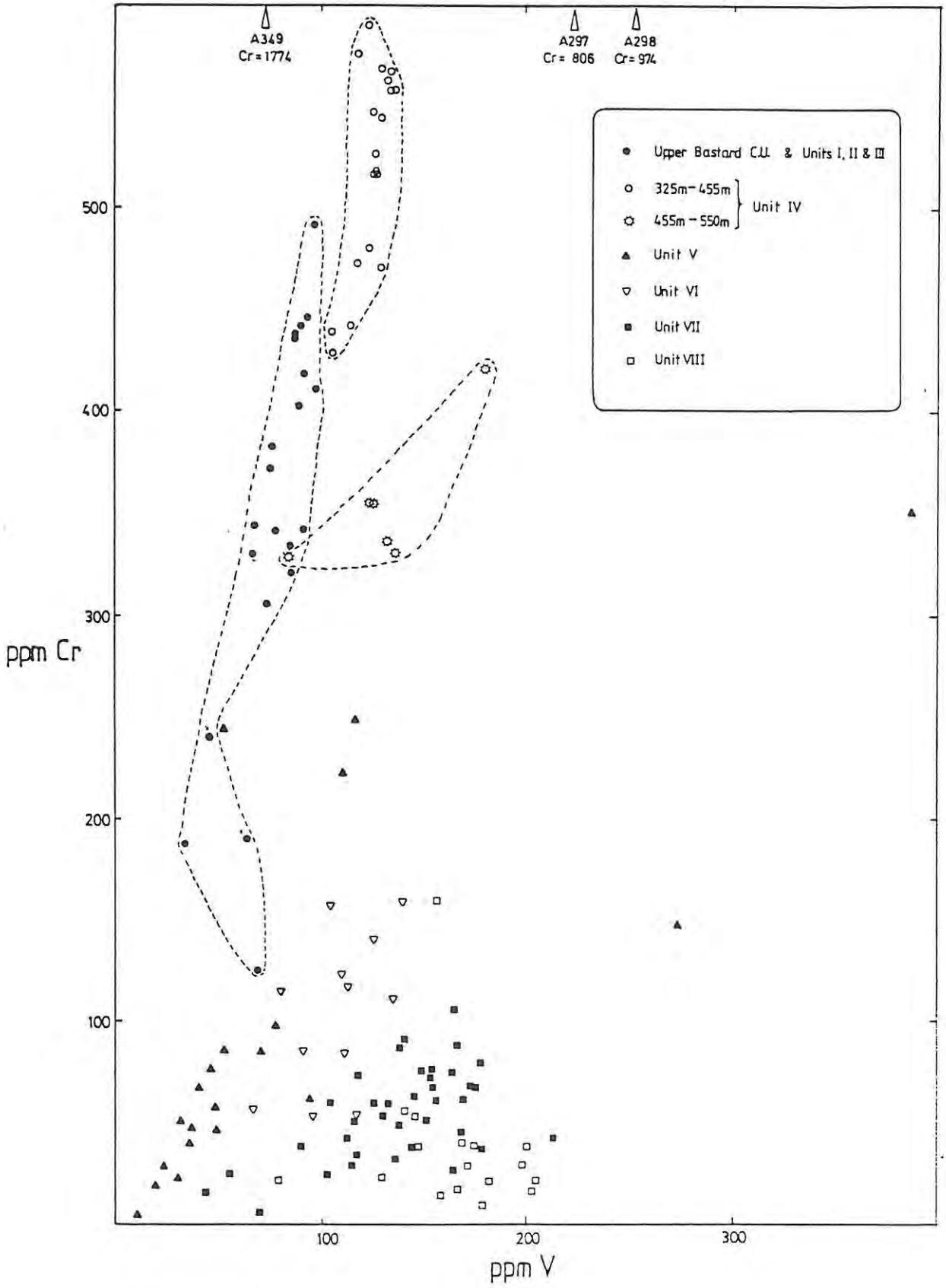

Fig. 26: Plot of Cr versus V

the highly variable V/Cr ratios in these units (Fig. 25b). Samples from above the Pyroxenite Marker are not plotted on Fig. 26, but they would fall within the same range as the samples from below 455m. Once again, this is reflected in the plot of the V/Cr ratio versus stratigraphic height (Fig. 25b)

5.4.10 Summary of Interelement Ratio Data

The various interelement ratios demarcate the boundaries between the units of the Main Zone rather more clearly than do plots of single elements against stratigraphic height. This is particularly true of the Cr/Sc and V/Cr ratios (Fig. 25 a & b). The most distinct change in the ratios is at the Pyroxenite Marker, affecting all except the Ba/Sr ratio.

There is an inflection in the Sr/Al_2O_3 ratio at 455m, in the upper part of unit IV. A change at this stratigraphic level is also strongly evident in the plot of Cr versus V (Fig. 26). It is at approximately 455m that the trend of anomalous iron-enrichment of the pyroxenes begins (Fig. 14, Fig. 34). It is suggested that all these patterns are related to the same phenomenon, and that they may be linked in some way to the development of Fe-rich ultramafic pegmatite. Unit V (the Main Mottled Anorthosite) is notable for its highly variable chemistry, particularly in terms of the V/Sc, Ni/Co, Ba/Sr and Sr/Al_2O_3 ratios.

5.5 Strontium Isotopes

On the basis of available whole-rock and microprobe data, thirty-six Main Zone samples were selected for strontium isotope analysis. The analyses were performed by F.J. Kruger, at the Bernard Price Institute for Geophysical Research, University of the Witwatersrand. The data are presented in Table 5.

It may be regarded as axiomatic that variations in the Sr isotope ratio in a magma body are the result of processes other than fractional crystallization or partial melting of isotopically homogeneous source materials. This implies that variations in isotope systematics through a magma chamber are the result of either mixing of isotopically different source magmas, or of varying degrees of contamination by isotopically different materials, generally of crustal origin.

Hamilton's (1977) study of the $^{87}Sr/^{86}Sr$ systematics of the mafic phase of the Bushveld Complex suggested that the sequence is characterized by abrupt changes in the strontium isotope initial ratio upward in the sequence. Each successive change was related by Hamilton to irregularities in cryptic variation. This in turn was related to emplacement of the Bushveld mafic phase as a series of magmatic influxes. Hamilton's sample material was drawn from both the western and the eastern lobes of the Bushveld, but his suite of Main Zone samples covers only the eastern lobe. The age of the Bushveld Complex, according to Hamilton, is 2095 ± 24 m.y. This age, however, was calculated using a decay constant for ^{87}Rb of $1.39 \times 10^{-11} yr^{-1}$. Use of the more modern decay constant of $1.42 \times 10^{-11} yr^{-1}$ returns an age of 2050 m.y.

Hamilton's (op. cit.) work has been supplemented by a detailed Sr isotope study of the Merensky Cyclic Unit and its immediate footwall and hangingwall by Kruger and Marsh (1982). Kruger and Marsh's data confirm Hamilton's findings for this stratigraphic interval, and show a dramatic increase in the initial Sr isotope ratio through the Merensky Cyclic Unit. The initial ratio (R_o) increases from ca. 0.7063 at the top of the Merensky footwall unit to 0.7075 at the base of the Bastard Cyclic Unit (Kruger and Marsh, 1982).

As a broadly-based reference study of the isotope systematics of the

Bushveld Complex, Hamilton's (1977) work has recently been superseded by Sharpe's (1985) study of the geochemistry and strontium isotope systematics of the eastern Bushveld Complex. An interval of particular interest in Sharpe's (1985) study is that between the Merensky Reef and the Pyroxenite Marker. This interval, according to Sharpe's data, is an anomalous package of high-R_o (A-type) magma, sandwiched within a relatively low-R_o column of U-dominant A+U hybrid magmas. (The A and U magmas are anorthositic and ultramafic in composition, respectively, and are discussed in detail by Irvine et al. (1983). Sharpe (1985) interpreted the high-R_o interval as a massive influx of magma, intruded into a density-stratified magma pile near the base of the chamber. Magma mixing over a 200 metre interval at the base of the fresh magma batch was instrumental in the formation of the Merensky Reef. At the top of the high-R_o magma column, the Pyroxenite Marker marks the position of a diffusive interface between new magma and the elevated pre-Merensky residuum. Data presented in this work suggest that the Sr-isotope systematics of the Main Zone are more complex than Sharpe's work would suggest, at least in the western Bushveld.

The variation in the Sr isotope initial ratio (R_o) with stratigraphic height at Union Section is illustrated in Fig. 27. At the base of the Bastard Cyclic Unit, the star in Fig. 27 represents an R_o of 0.70749, determined by Kruger and Marsh (1982) for the Rustenburg succession. Although data points are relatively sparsely distributed, the impression is one of a virtually linear increase in R_o from the base of the Bastard Cyclic Unit to the top of Main Zone unit II. At the top of unit II, sample A312 has an initial ratio of 0.70854 (Fig. 27).

At the base of unit III, R_o is sharply higher, at 0.70882, than in the underlying units. If sample A299 is discounted, the initial ratio decreases progressively to 0.70871 in sample A289, at the top of unit III. Sample A299 is a leuconorite which contains blebs of pegmatitic material. Possibly significantly, A299 forms the footwall to the Pyroxenite layer at 272.6m. Sample A299 may be interpreted as the top of a cyclic unit, in which a component of trapped pre-Merensky Reef material contributes to the relatively low initial ratio (Fig. 27).

Across the boundary between units III and IV, the initial ratio increases sharply, and is between 0.70879 and 0.70890 for the first 26m of unit IV. Samples A287 and A284 have particularly high initial

ratios, in the vicinity of 0.70890, whilst the R_o of sample A286 (0.70879) is somewhat lower. The initial ratio decreases upwards through unit IV to 0.70864 in sample A260. Above A260, R_o decreases somewhat more sharply, to 0.70841 in sample A254, near the top of unit IV.

Unit V (The Main Mottled Anorthosite) displays an extremely wide range of initial ratios, from 0.70737 to 0.70902. The lowest initial ratio (0.70737) is in sample A236, which is an anomalously fine-grained gabbro. Sample A236 is also notable for an anomalously high V/Cr ratio (1.86). Sample A243, near the base of unit V, displays the highest R_o recorded in the Main Zone at Union Section (0.70902).

Only one sample (A193) is available for unit VI, so no assessment can be made of this unit. The base of the overlying unit VII is marked by a 130mm thick fine-grained pyroxenite, above which the leucocratic rocks of the Upper Mottled Anorthosite are developed. Sample A182 is a leucogabbro within the Upper Mottled Anorthosite. Sample A182 contains blebs of ultramafic pegmatite material, in a similar manner to sample A299 in unit III. The strontium isotope initial ratio in sample A182 is particularly low (0.70765), as is the case in sample A299. The rest of unit VII (i.e. above the Upper Mottled Anorthosite) is characterized by initial ratios which vary quite noticeably in a relatively narrow range from 0.70801 to 0.70850. The lower part of unit VII, from 966m to 1147m, is characterized by a progressive increase in R_o, from 0.70826 in sample A138 to 0.70846 in sample A149. From sample A149, there is a sharp inflection to a lower ratio of 0.70822 in sample A146. Near the top of unit VII, sample A74 displays a relatively low initial ratio (0.70801).

In unit VIII, R_o varies from 0.70816 to 0.70838. There are only four data points in this unit, and for this reason detailed trends in R_o are impossible to assess in unit VIII. Across the Pyroxenite Marker, there is a sharp decrease in R_o, from 0.70829 in sample MZ1 to 0.70768 in sample SP11. From SP11, there is a decrease in R_o to 0.70731 in sample MZ6.

The strontium isotope ratios encountered in the Main Zone are high for mafic rocks, and require some interpretation. The high ratios must be ascribed either to some process which produces enrichment in the

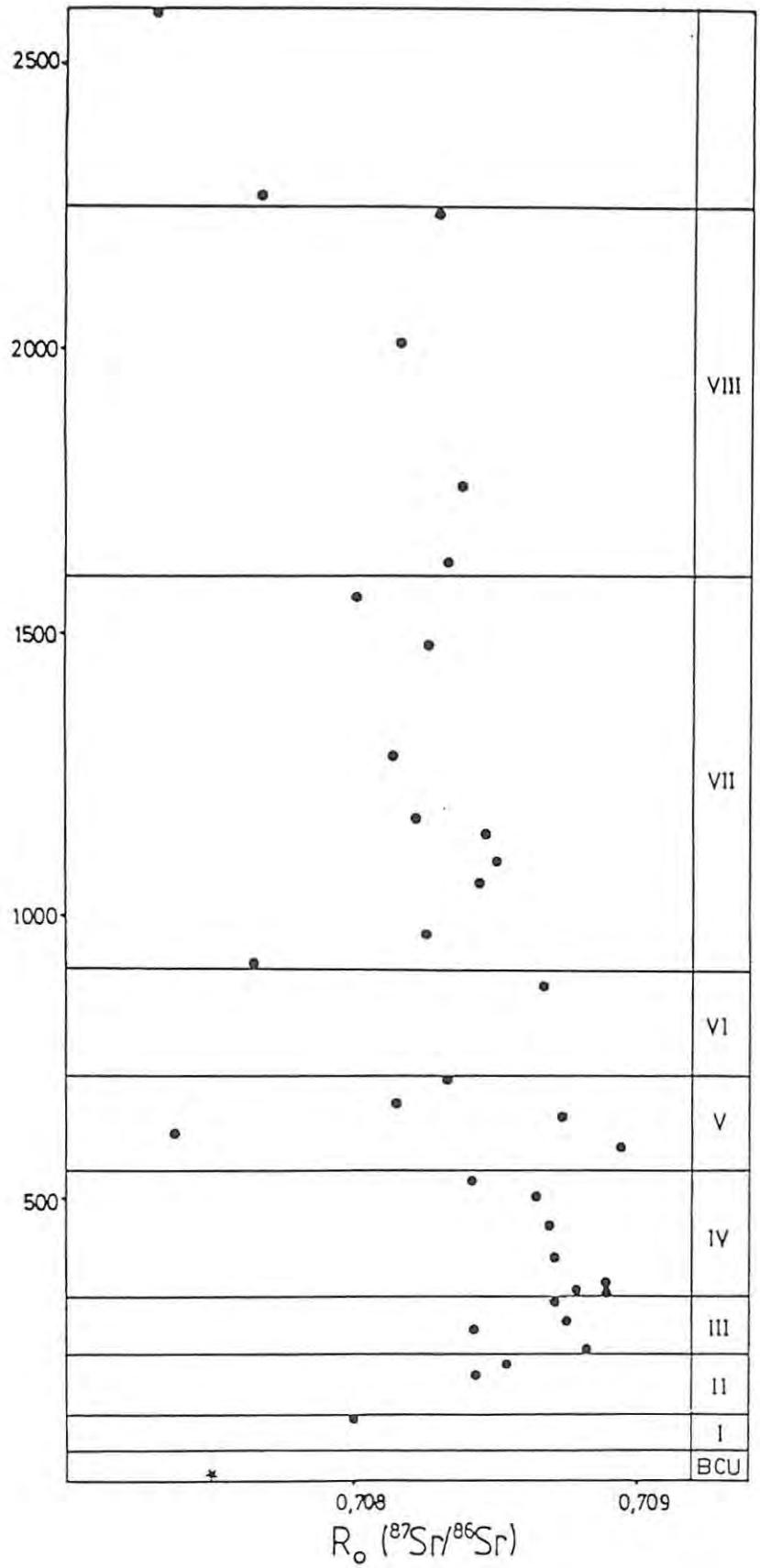

Fig. 27 : Plot of initial $^{87}Sr/^{86}Sr$ ratios versus stratigraphic height in the Main Zone. The star indicates the ratio of 0.70749, determined by Kruger and Marsh (1982) for the base of the Bastard Cyclic Unit at R.P.M. Rustenburg section.

Sample Number	Rb ppm	Sr ppm	$^{87}Sr/^{86}Sr$ (atomic)	$^{87}Sr/^{86}Sr$ (present)	R_o @ 2050 m.y.	Strat. Height
MZ-6a	1.5	209	0.0210	$0.70793^{\pm}3$	0.70731	2600m
SP-11	1.4	226	0.0183	$0.70822^{\pm}2$	0.70768	2270m
MZ-1	3.2	289	0.0317	$0.70923^{\pm}4$	0.70829	2240m
A-1	1.7	317	0.0150	$0.70860^{\pm}4$	0.70816	2010m
A-43b	1.7	257	0.0194	$0.70895^{\pm}3$	0.70838	1757m
A-63	3.2	271	0.0338	$0.70933^{\pm}3$	0.70833	1627m
A-74b	3.2	249	0.0376	$0.70912^{\pm}4$	0.70801	1565m
A-91b	2.8	268	0.0305	$0.70918^{\pm}2$	0.70826	1480m
A-122	3.1	240	0.0369	$0.70923^{\pm}3$	0.70814	1285m
A-146b	2.2	237	0.0271	$0.70902^{\pm}3$	0.70822	1172m
A-149	2.2	264	0.0241	$0.70917^{\pm}2$	0.70846	1147m
A-155	1.4	252	0.0157	$0.70896^{\pm}3$	0.70850	1098m
A-159	2.0	285	0.0203	$0.70904^{\pm}2$	0.70844	1058m
A-138	1.4	285	0.0145	$0.70869^{\pm}2$	0.70826	966m
A-182	0.85	259	0.0096	$0.70793^{\pm}3$	0.70765	916m
A-193	2.9	285	0.0298	$0.70955^{\pm}3$	0.70867	875m
A-222	6.3	299	0.0613	$0.71014^{\pm}5$	0.70833	712m
A-230a	7.1	342	0.0598	$0.70992^{\pm}3$	0.70815	670m
A-235	10.0	214	0.1349	$0.71271^{\pm}3$	0.70873	646m
A-236	0.84	258	0.0094	$0.70765^{\pm}2$	0.70737	619m
A-241	4.2	324	0.0372	$0.71004^{\pm}3$	0.70894	593m
A-243	7.4	315	0.0679	$0.71103^{\pm}3$	0.70902	584m
A-254	3.4	209	0.0478	$0.70982^{\pm}2$	0.70841	533m
A-260	0.95	136	0.0202	$0.70924^{\pm}3$	0.70864	503m
A-264	1.8	238	0.0222	$0.70935^{\pm}3$	0.70869	455m
A-275a	2.6	227	0.0335	$0.70970^{\pm}4$	0.70871	399m
A-284a	0.89	233	0.0111	$0.70923^{\pm}3$	0.70890	351m
A-286b	1.4	231	0.0172	$0.70930^{\pm}4$	0.70879	339m
A-287	1.9	247	0.0224	$0.70955^{\pm}3$	0.70889	332m
A-289	1.4	269	0.0149	$0.70915^{\pm}4$	0.70871	320m
A-295b	1.6	272	0.0169	$0.70925^{\pm}3$	0.70875	284m
A-299	1.1	340	0.0092	$0.70869^{\pm}5$	0.70842	270m
A-308	1.9	249	0.0224	$0.70948^{\pm}3$	0.70882	236m
A-312a	4.3	270	0.0462	$0.70990^{\pm}3$	0.70854	209m
A-315	3.4	271	0.0360	$0.70949^{\pm}3$	0.70843	189m
A-327	3.5	297	0.0344	$0.70902^{\pm}1$	0.70800	113m

Table 5 : Whole-rock strontium isotope data. Initial $^{87}Sr/^{86}Sr$ ratio (R_o) calculated using a decay constant of $1.42 \times 10^{-11} yr^{-1}$ for ^{87}Rb.
Analyses by F.J.Kruger, Bernard Price Institute, University of the Witwatersrand.

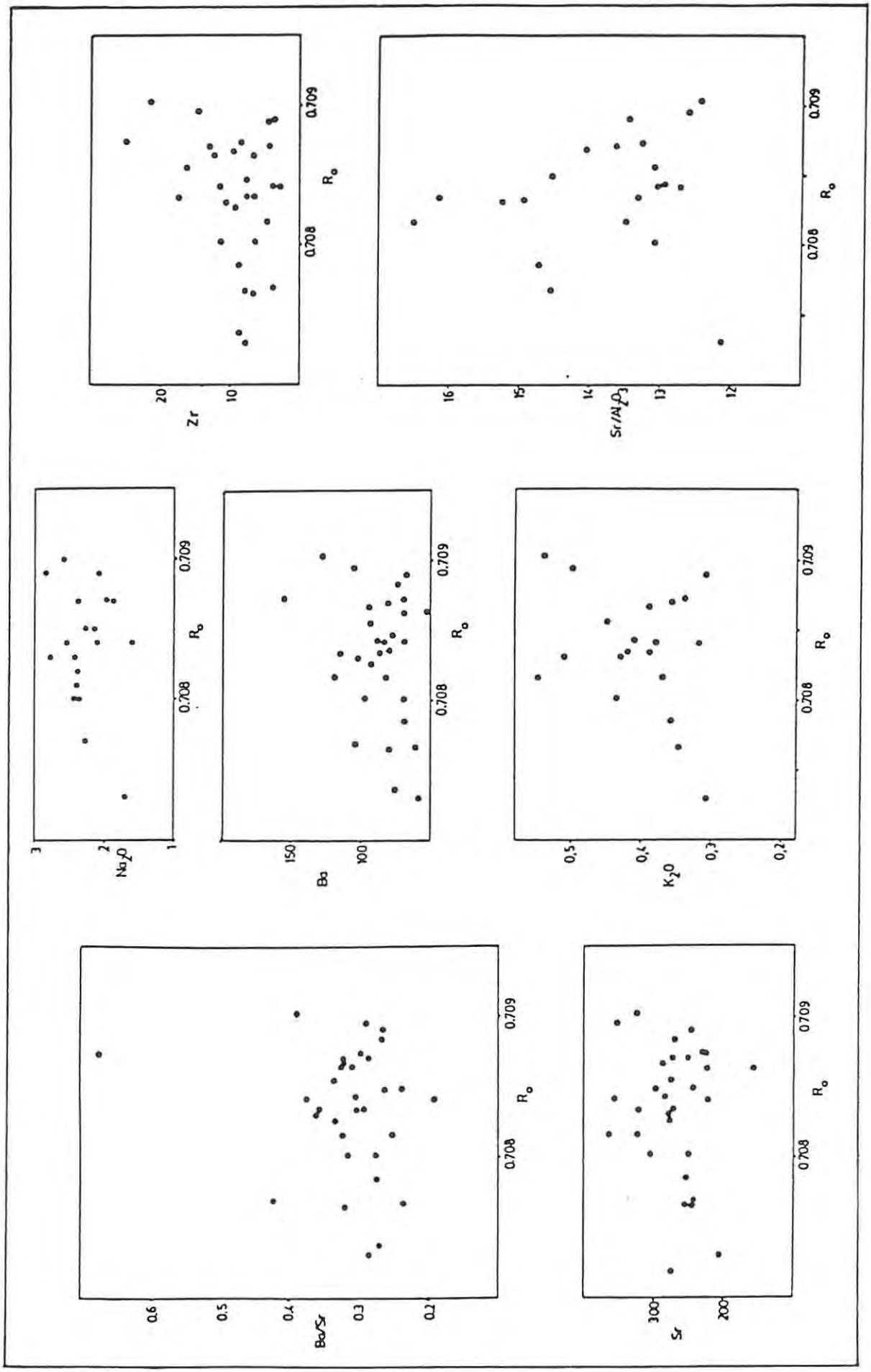

Fig. 28 : Binary plots with initial $^{87}Sr/^{86}Sr$ ratio (R_o) as the abscissa.

6. DISCORDANT BODIES OF IRON-RICH ULTRAMAFIC PEGMATITE

6.1 Introduction

In borehole SK2, the layered rocks of the Main Zone are transgressed by discordant bodies of iron-rich ultramafic pegmatite. The pegmatites, which are an integral part of the layered sequence of the Bushveld Complex, have been described in some detail by Cameron and Desborough (1964) and, more recently, by Scoon (1985) and Viljoen and Scoon (1985). In borehole SK2, the pegmatite bodies are small and irregular, and their occurrence appears to be stratigraphically controlled. The common association of pegmatite with the more leucocratic varieties of cumulate rock has been noted by a number of researchers into the Bushveld Complex (**inter alia** Wagner, 1929; Coertze, 1960; Cameron and Desborough, 1964; Viljoen and Scoon, 1985).

New analytical data presented here (Tables 6 - 10; Fig. 31) support the assertion by Viljoen and Scoon (1985) that the iron-rich ultramafic pegmatites become increasingly fractionated with stratigraphic height. Viljoen and Scoon relate the development of ultramafic pegmatite to the expulsion and concentration of residual iron-rich fluids in the latter stages of development of cyclic units. This implies a close link between the pegmatite bodies and their associated cumulate rocks.

6.2 Classification and Occurrence

In a comprehensive study of the different types of transgressive, postcumulus ultramafic rocks in the Bushveld Complex, Scoon (1985) recognized four varieties, as follows:

Group 1: Non-platiniferous magnesian dunite.
Group 2: Platiniferous ultramafic pegmatite bodies.
Group 3: Iron-rich ultramafic pegmatite.
Group 4: Other bodies, including orthopyroxenite pegmatite, anorthositic pegmatite, vermiculite pegmatite, amphibolite or shonkinite bodies, and the Vlakfontein nickel pipes.

The orthopyroxenite bodies of Group 4 occur in the Critical Zone in some of the platinum mines of the western Bushveld. Scoon (1985)

suggested that they may be reconstituted cumulates, and as such are unrelated to the ultramafic pegmatite suite. Anorthosite pegmatite bodies are common in the Upper Zone of the eastern Bushveld (Willemse, 1969; von Gruenewaldt, 1973). Scoon (1985) suggested that there may be a relationship between the anorthosite pegmatite and the Fe-rich ultramafic pegmatite suite. This possibility is enhanced by the association of small bodies of anorthositic pegmatite with the Fe-rich ultramafic pegmatite bodies in the SK2 Main Zone succession (see appendix 1 of this work).

Within Scoon's (1985) system of classification of the Bushveld postcumulus bodies, the overwhelming majority of the pegmatite bodies in the SK2 succession fall into Group 3 (Iron-rich ultramafic pegmatite). Scoon (op. cit.) distinguished two subgroups within Group 3. The first of these is the silicate-rich type, in which Fe-Ti oxides are subordinate to olivine and clinopyroxene, whilst the second subgroup is composed almost exclusively of Fe-Ti oxides. The pegmatite bodies in borehole SK2 are predominantly of the former, silicate-rich variety. The oxide-rich variety of pegmatite is predominantly developed in the Upper Zone, although oxide-rich pegmatite bodies do occur in the Main Zone, especially in the footwall of the Pyroxenite Marker.

Iron-rich ultramafic pegmatite bodies were first described in the eastern Bushveld by Wagner (1929), who recognized their strong association with anorthositic cumulates. This association has been confirmed by airborne aeromagnetic surveys of the southwestern Bushveld (Viljoen and Burvenich, 1983; Scoon, 1985). In the southwestern Bushveld, three linear magnetic anomalies have been recognized in the lower part of the Main Zone, parallel to strike. The first of these corresponds to the Giant Mottled Anorthosite at the top of the Bastard Cyclic Unit. The second linear anomaly occurs approximately 500 metres above the Merensky Reef, at a level corresponding to the Main Mottled Anorthosite, whilst the third anomaly is encountered 900 metres above the Merensky Reef, within the Upper Mottled Anorthosite.

In the SK2 succession, concentrations of ultramafic pegmatite occur slightly above the Giant Mottled Anorthosite, in the Main Mottled Anorthosite, in the Upper Mottled Anorthosite, and at approximately 1350m, 1600m and 1800m above the Bastard Reef (Fig. 31).

6.3 Mineralogy and Petrology

In hand specimen, the Fe-rich ultramafic pegmatite bodies in borehole SK2 are readily distinguished from their cumulate host rocks by their dark colour and coarse granular texture. The ultramafic pegmatite bodies are characterized by a fairly simple mineralogy in which clinopyroxene, Ti-magnetite and olivine are the major components. Plagioclase, which forms an important part of many of the Main Zone pegmatite bodies, is regarded by Scoon (1985) as being relict cumulus material. Base metal sulphides are common accessory minerals in the pegmatite bodies, and apatite occurs in the more fractionated varieties.

The modal proportions of the main constituent minerals vary substantially, not only from body to body, but also within individual bodies. This variation is complicated, not only by the relatively large grain size, but also by a tendency towards mineralogical zonation in the pegmatite bodies. These factors render modal analyses and, as a corollary, whole-rock geochemical analyses rather unreliable, at least in a local sense.

Clinopyroxene is an ubiquitous component of the pegmatites. It differs from cumulus clinopyroxene in the Main Zone in its composition (more Fe-rich) and in its microtextures. In the ultramafic pegmatite bodies, large grains of clinopyroxene exhibit distinctive fine exsolution lamellae of Ca-poor pyroxene parallel to (001). Smaller clinopyroxene grains tend to exhibit fairly coarse polysynthetic twinning, possibly as a result of deformation or annealing. In certain pegmatite bodies sampled in this study (A252 in particular), symplectic intergrowths of clinopyroxene and Fe-Ti oxide occur, after the fashion described by McSween (1980) and Zeck et al. (1982). In addition to the symplectites, some pegmatite bodies contain clinopyroxene grains which appear to have exsolved oriented platelets of an opaque phase (possibly ilmenite or magnetite, as suggested by Fleet et al., 1980, or Zeck et al., 1982). The pegmatitic clinopyroxene becomes increasingly fractionated with increasing stratigraphic height. The MMF ratio of clinopyroxene varies from 0.69 at a height of 157m (sample A320) to 0.33 at a height of 1913m (sample A20). The variation is a continuous progression between the two compositional extremes (Fig. 31).

Olivine was observed only in the Main Zone ultramafic pegmatites in samples A348 (which is within the Bastard Cyclic Unit), sample A252 (near the top of unit IV) and samples A107 and A115 (both approximately 1400m above the Bastard Reef). Olivine in sample A348 has a composition of Fa_{55-56}. That in samples A107 and A115, on the other hand, is more Fe-rich at Fa_{72-74}. Apart from the Fe-rich nature of the olivine, the evolved nature of the A107 and A115 pegmatite samples is reflected in the fact that they both contain apatite. The apatite occurs as relatively large, subhedral grains (up to 0.5mm), and its presence is reflected in the above average phosphorus content of these samples (Table 7).

Ilmenite and Ti-magnetite are invariably present in the pegmatite bodies. The textures and mineralogy of these opaque oxides are consistent with crystallization of Fe-Ti-enriched liquids at magmatic temperatures (Reynolds and Scoon, 1983). Base-metal sulphides are irregularly developed in the pegmatite bodies, and generally constitute less than 5 modal percent of the bodies. Pyrrhotite is the predominant sulphide phase, with subordinate amounts of cubanite, pentlandite and chalcopyrite.

Plagioclase makes up varying proportions of the pegmatite bodies, and occurs as large grains, generally in excess of 5mm in length. Notably, plagioclase is absent from the large pegmatite bodies in the Upper Critical Zone (Scoon, 1985), and plagioclase in the relatively small bodies in the SK2 succession is likely to be relict cumulus material. Orthopyroxene, which is present in small amounts in some of the bodies sampled, is probably similar to plagioclase in being relict cumulus material.

As an aid to the assessment of the available geochemical data for the pegmatite bodies (Tables 7 - 10), a brief description of the main petrographic features of each body analyzed in this work is given below. The stratigraphic positions of the samples are indicated in Fig. 31.

A348 Olivine (Fo_{55-56}) is the major component of sample A348, and occurs in grains up to 2mm in diameter. Triple junctions between grains are common. The olivine grains are fresh, and are often surrounded by interstitial magnetite. Augite occurs

in grains of various sizes, sometimes exceeding 5mm. Augite may be twinned, and is characterized by fine, acicular inclusions of ilmenite. The large areas of interstitial magnetite are characterized by robust ilmenite exsolution lamellae, and somewhat finer pleonaste lamellae, the pleonaste lamellae being surrounded by ulvospinel. Ulvospinel also forms a "cloth" texture in the groundmass of the magnetite. Polygonal ilmenite grains display triple junctions. Sample A348 is characterized by very strongly developed mineral zoning.

A320 Augite (En_{36-41}) predominates in sample A320. The augite grains are characterized by fine (diallage-type) polysynthetic twinning, and grains may be bent. The grain size of augite varies from less than 0.5mm to over 5mm. Orthopyroxene and plagioclase in the sample are probably of cumulus origin. Granular ilmenite is abundant, and interstitial magnetite tends to occur concentrated in layers within the pegmatite body. The magnetite is characterized by ilmenite exsolution lamellae.

A252 The dominant minerals in sample A252 are augite and magnetite. The predominant sulphide is pyrrhotite, with subordinate chalcopyrite. Augite, which occurs in grains up to 5mm in diameter, is often characterized by a vermicular intergrowth with magnetite (Fig. 29). Plagioclase, grains of which may reach more than 5mm in diameter, and smaller (0.5mm to 1mm) grains of orthopyroxene are probably of cumulus origin. Olivine is a minor constituent of sample A252, and is easily missed in thin section due to mineral zonation.

A237 Sample A237 consists primarily of augite ($En_{32.1-34.7}$), which displays typical diallage-type twinning. Ilmenite and magnetite together form up to 10% of the sample, with magnetite displaying ilmenite exsolution lamellae.

A227 Augite (En_{31}), the dominant mineral in sample A227, displays diallage twinning, and may be optically continuous over more than 20mm. Augite is peppered with tiny grains of pyrrhotite. Magnetite, which forms five modal percent or less of the pegmatite, contains exsolution lamellae of coarse ilmenite and fine pleonaste.

A172 Sample A172 is an intimate mixture of cumulus and pegmatite material, characterized by grains of diallage augite. Large plagioclase grains in the sample may reach 6mm in diameter. Magnetite, which contains ilmenite exsolution lamellae, is partially altered to chlorite.

A166 As with sample A172, A166 is a mixture of pegmatite and cumulus material. Diallage augite grains may be optically continuous over 20mm or more. Plagioclase grains often exceed 5mm in length.

A165 Sample A165 consists predominantly of cumulus gabbronorite, in which plagioclase grain boundaries are granulated. Relatively small (less than 5mm) grains of diallage augite occur scattered throughout the gabbronorite. Pegmatitic augite constitutes 10% to 20% of the rock, the balance being cumulus plagioclase and pyroxene.

A163 Sample A163 contains approximately eighty percent modal diallage augite (Fig. 30), the balance of the sample consisting of interstitial magnetite.

A152 Diallage grains (En_{27}) may be optically continuous over 20mm in sample A152. Interstitial magnetite forms 5% to 10% of the sample. Large grains of plagioclase, and smaller grains of orthopyroxene, are probably reconstituted cumulus material.

A115 Olivine ($Fa_{74.5}$) is modally dominant over augite ($En_{26.6}$) in the mineral assemblage of sample A115. Magnetite constitutes less than 5% by volume of the sample. Olivine grains are generally 1mm to 2mm in diameter. Apatite is a minor constituent of the sample, occurring in clusters of euhedral grains up to 0.5mm in diameter.

A107 Large olivine grains ($Fa_{71.6-72.3}$) are optically continuous over more than 10mm, as is diallage (En_{29-30}). Plagioclase grains are of a similarly large size. Apatite occurs in clusters of euhedral grains up to 2mm in diameter. The pegmatite body exhibits strong mineralogical zoning. Estimated mineral proportions are: olivine 65%; diallage 20%; magnetite 10%;

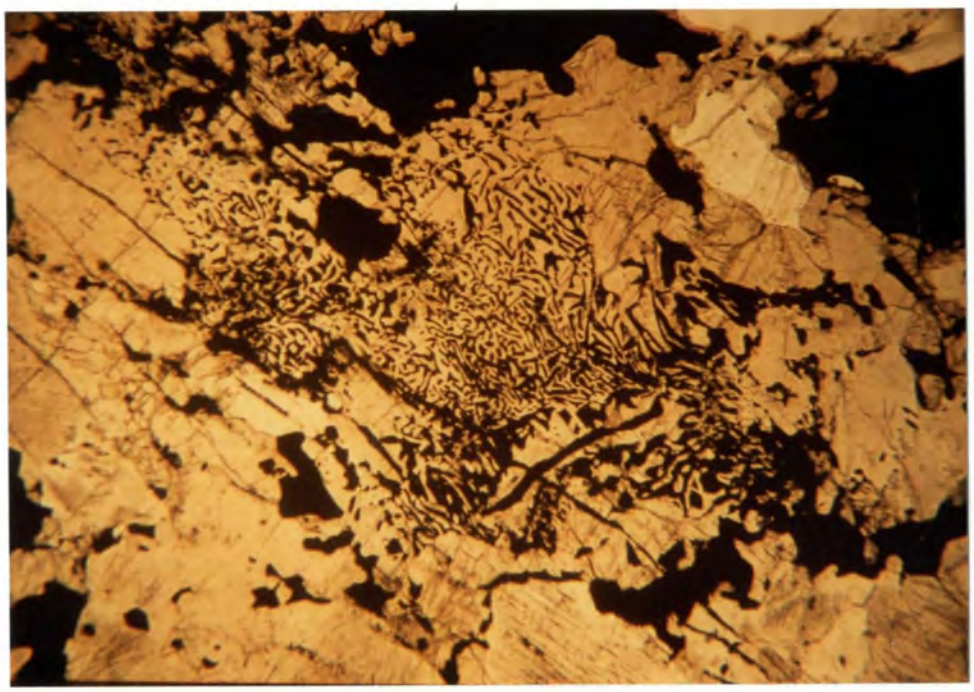

Fig. 29 : Vermicular intergrowth of augite (brown) and magnetite (black) in Fe-rich ultramafic pegmatite. Sample A252 (plane polarized light).

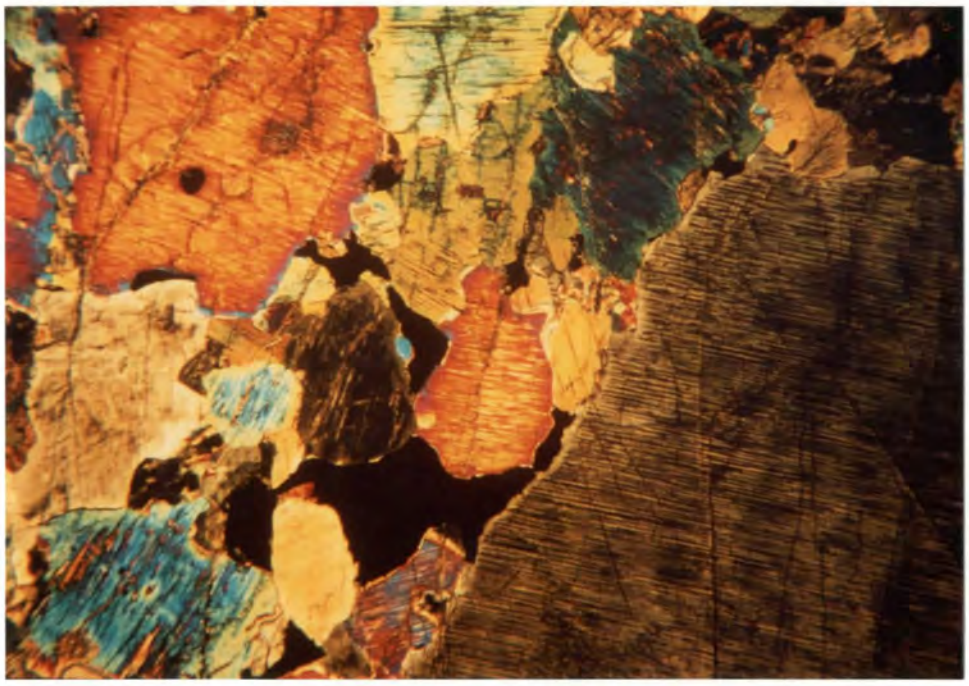

Fig. 30 : Diallage-type twinning in augite in Fe-rich ultramafic pegmatite. Sample A163 (crossed nicols).

apatite 5%.

A59 Sample A59 is notable for its high proportion of interstitial magnetite, which covers large areas of the sample. The magnetite has exsolved pleonaste, but very little ulvospinel, implying Ti-depletion. Large grains of diallage often exceed 6mm in diameter. There is a large proportion of cumulus material in the sample (up to 35%). The included cumulus orthopyroxene (En_{42}) is strongly enriched in iron relative to orthopyroxene from a similar stratigraphic level, but unaffected by pegmatite (cumulate samples A52 and A63, within 40m either side of A59, have orthopyroxene compositions of En_{63-64}).

A31 Diallage grains may be up to 15mm in diameter, but are generally less than 10mm. Magnetite, which forms 5% to 10% of the sample, displays a well-developed cloth texture of ilmenite after exsolved ulvospinel. The sample contains a fair amount of granular ilmenite. Plagioclase grains often exceed 10mm in length.

A20 The main constituent of A20 is diallage augite ($En_{20.7}$), grains of which may exceed 5mm, but are generally smaller. Platelets in the diallage appear to be exsolved rutile.

6.4 Geochemistry

Whole-rock chemical analyses of a representative suite of Fe-rich ultramafic pegmatite samples are presented in Table 7. The coarse grain size and variable modal mineralogy within individual pegmatite bodies means that the whole-rock geochemical data are not fully representative. In Fig. 31, some aspects of the chemistry of the pegmatites are presented diagrammatically. In this diagram, shaded circles represent the pegmatites, whilst the Main Zone cumulates are represented by unshaded symbols.

The whole-rock MMF ratios of the pegmatites range from 0.1 to 0.38, which is more iron-rich than any Main Zone cumulates in SK2 except for some in the Main Mottled Anorthosite (550m to 715m), and an isolated sample near the top of unit VIII (sample A22). In each case,

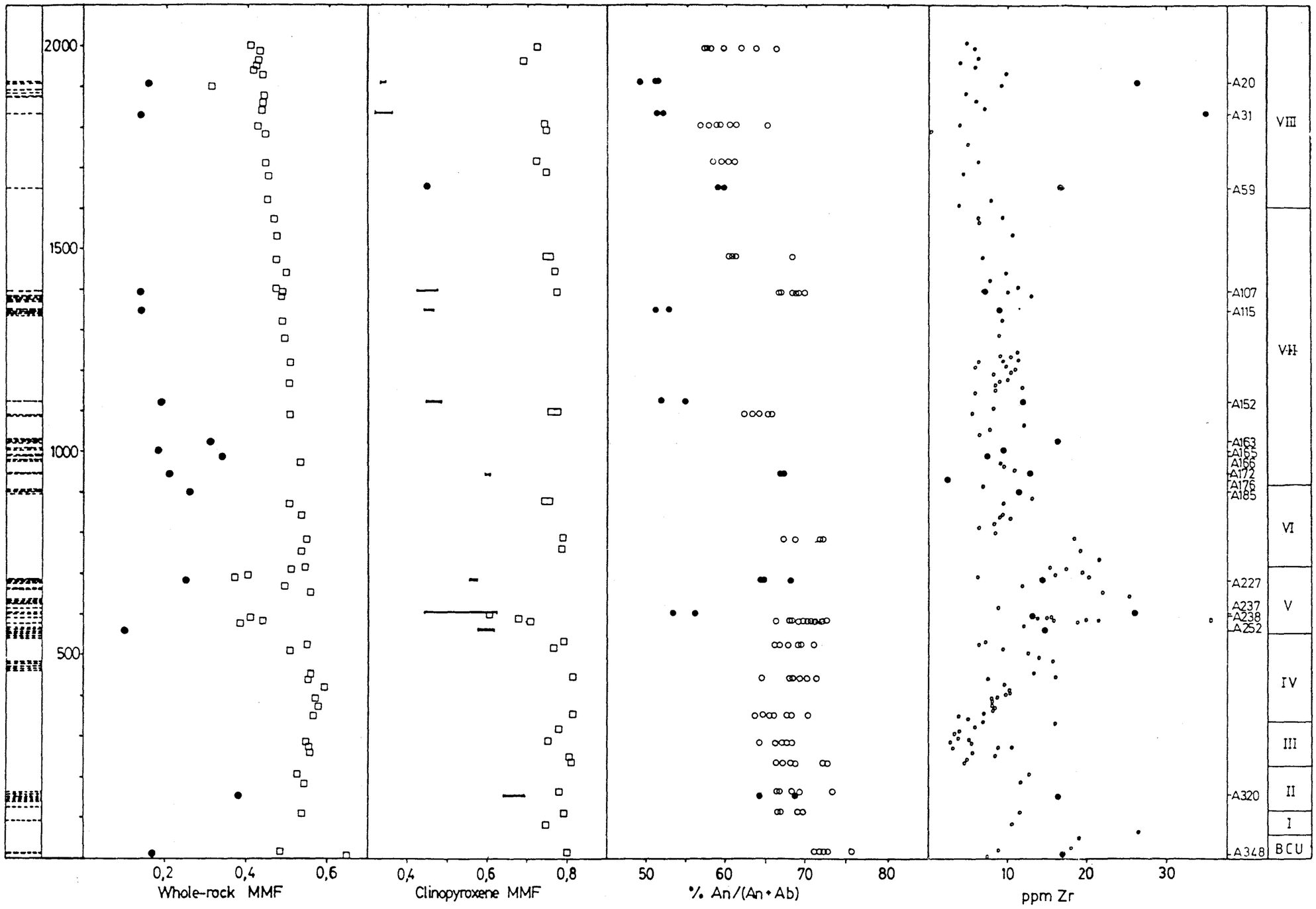

Fig. 31 : Plots of selected geochemical parameters versus stratigraphic height in borehole SK2. Pegmatite occurrences are indicated in the simplified borehole log along the lefthand margin by dashed lines. Pegmatite samples are represented by shaded circles or, in the case of the clinopyroxene MMF ratio, by solid lines representing the within-sample range of compositions. Cumulate rock samples are represented by unshaded circles or squares.

the Bastard and Merensky Cyclic Units, intercumulus clinopyroxene is substantially more iron-rich than the pyroxene in the associated mottles. If equilibrium conditions of crystallization are assumed to have obtained, then crystallization of intercumulus clinopyroxene would rapidly enrich the residual intercumulus liquid in iron. This iron-rich residual liquid may be trapped, either by commencement of crystallization of a new cyclic unit, or by a new influx of magma. In response to filter-pressing and/or annealing processes, the intercumulus residual liquid will migrate. In the Muskox intrusion, Irvine (1980a) invoked upward migration of intercumulus liquid into overlying cyclic units to explain the non-convergence of geochemical trends with lithologically-defined cyclic units. This process, which Irvine (op. cit.) termed "**infiltration metasomatism**", was assumed to be a response to compaction of the crystal pile. Late-stage veins in the Rhum intrusion, which are generally concordant with cumulus layering, were attributed by Butcher (1985) to a process which he termed "**channelled metasomatism**"

The formation of the Fe-rich ultramafic pegmatite bodies in the SK2 Main Zone succession is likely to be due to a process which combines aspects of both infiltration metasomatism and channelled metasomatism. Following Scoon's (1985) model, the parental liquid of the pegmatite bodies is the postcumulus liquid in mottled anorthosite layers. This implies that the pegmatitic liquid was in equilibrium with the host anorthosite cumulate. Migration of these liquids, and coalescence in structurally favourable sites, would lead to the formation of the pod-like ultramafic pegmatite bodies. In the formation of relatively small pegmatite bodies, of the type encountered in SK2, the pegmatite liquid is likely to **displace**, rather than replace, the host cumulate rocks. If the liquid migrates out of the cumulate rock in which it formed, a disequilibrium relationship will lead to partial **replacement** of the associated cumulate rocks. This may explain the dichotomy in plagioclase compositions of the SK2 pegmatite bodies (Fig. 31). Those bodies in which plagioclase is similar in composition to stratigraphically equivalent cumulates are likely to have formed more or less **in situ** in their host cumulates. Where plagioclase in the pegmatite is more sodic than in associated cumulates, however, disequilibrium conditions are indicated. In this latter situation, the pegmatite liquid is likely to have migrated away from its source rock.

TABLE 6
WHOLE-ROCK CHEMISTRY OF Fe-RICH ULTRAMAFIC PEGMATITES AND RELATED ROCKS.

	A20	A31	A59	A107	A115	A152	A163	A165	A166
SiO_2	47.29	42.15	-	39.45	41.22	49.51	46.57	42.65	50.99
TiO_2	0.98	3.17	-	0.67	1.65	0.58	1.35	2.23	0.39
Al_2O_3	11.56	6.72	-	11.79	12.12	15.51	2.27	12.32	19.34
Fe_2O_3	21.92	28.47	-	30.31	27.08	15.01	23.84	24.29	7.64
MnO	0.26	0.39	-	0.38	0.33	0.23	0.28	0.22	0.11
MgO	4.72	5.25	-	5.75	4.99	4.02	12.54	6.14	4.63
CaO	12.52	13.03	-	8.29	10.96	13.14	15.13	12.08	13.35
Na_2O	2.24	1.46	-	2.07	2.09	2.98	0.21	1.87	2.82
K_2O	0.22	0.13	-	0.22	0.18	0.21	0.00	0.12	0.29
P_2O_5	0.31	0.17	-	2.28	2.16	1.19	0.01	0.01	0.00
LOI	+1.09	+1.14	-	+1.23	+1.15	+0.29	+1.53	+1.61	0.20
H_2O-	0.38	0.03	-	0.04	0.03	0.07	0.01	0.00	0.05
TOTAL	101.31	99.83	-	100.02	101.66	102.16	100.68	100.32	99.81
Co	53	59	60	128	83	38	174	247	41
Cr	77	29	36	26	10	6	155	78	11
V	88	276	112	31	65	19	566	492	91
Zn	113	183	168	156	127	252	96	124	56
Cu	58	156	140	104	145	82	730	2009	75
Ni	58	189	184	52	39	55	250	563	60
Zr	26.2	34.8	16.5	6.9	8.8	11.7	16.2	9.3	7.2
Y	20.1	25.5	35.1	24.0	29.7	30.0	17.0	10.2	8.1
Nb	nd	nd	nd	nd	nd	nd	nd	nd	nd
Rb	nd	nd	nd	nd	nd	nd	nd	nd	4.9
Sr	250	139	274	301	308	368	19	207	334
Ba	123	90	101	129	122	151	19	61	86
Sc	91	162	62	15	43	73	119	65	45

TABLE 6
WHOLE-ROCK CHEMISTRY OF Fe-RICH ULTRAMAFIC PEGMATITES AND RELATED ROCKS.

	A172	A176	A185	A227	A237	A238	A252	A320	A348
SiO_2	41.68	–	46.26	46.62	–	–	24.47	47.96	26.29
TiO_2	3.26	–	1.62	1.87	–	–	6.61	1.16	7.94
Al_2O_3	11.74	–	13.41	13.59	–	–	3.03	4.35	1.99
Fe_2O_3	23.83	–	15.58	16.18	–	–	51.45	18.12	47.56
MnO	0.25	–	0.20	0.18	–	–	0.33	0.20	0.37
MgO	7.23	–	6.48	6.24	–	–	6.37	12.98	10.91
CaO	11.93	–	13.53	13.61	–	–	8.36	15.55	6.29
Na_2O	1.66	–	2.26	1.41	–	–	0.23	0.39	0.08
K_2O	0.10	–	0.13	0.23	–	–	0.01	0.03	0.00
P_2O_5	0.01	–	0.01	0.05	–	–	0.00	0.01	0.00
LOI	+0.68	–	+0.45	+0.53	–	–	+1.83	+0.62	+2.44
H_2O-	0.03	–	0.04	0.04	–	–	0.02	0.10	0.01
TOTAL	101.04	–	99.07	99.49	–	–	99.05	100.23	99.00
Co	132	5	91	90	124	83	482	117	285
Cr	61	5	242	67	291	351	502	703	1465
V	696	8	352	376	383	388	1285	1090	2076
Zn	10	20	89	97	83	71	314	496	294
Cu	36	32	187	151	140	98	9583	2842	643
Ni	13	19	110	65	103	141	1111	1369	548
Zr	17.6	2.2	11.5	14.3	26.0	13.0	14.4	16.3	16.9
Y	12.6	1.2	9.3	14.3	18.6	12.2	9.9	15.6	8.2
Nb	2.1	nd	nd	nd	nd	nd	nd	nd	nd
Rb	nd	nd	1.9	4.5	6.5	1.8	nd	nd	1.3
Sr	180	556	234	234	31	160	30	40	10
Ba	72	108	64	113	38	81	30	28	26
Sc	74	3.3	77	79	134	66	319	117	86

TABLE 7

Pyroxene Analyses by Electron Microprobe

	A20/1	A20/2	A20/3	A31/1	A31/2	A31/3	A59/1	A107/1	A107/2	A107/3	A115/1	A115/2	A152/1	A152/2	A152/3
SiO_2	49.23	49.68	49.29	49.37	49.35	49.77	50.34	50.58	49.98	50.59	50.40	50.45	50.70	50.61	50.68
TiO_2	0.42	0.36	0.49	0.41	0.42	0.42	0.16	0.54	0.54	0.54	0.50	0.51	0.48	0.50	0.49
Al_2O_3	1.34	1.29	1.49	0.67	1.49	1.35	0.54	1.40	1.14	1.63	1.60	1.60	1.29	1.34	1.51
FeO	24.26	23.79	23.04	35.84	23.46	23.69	31.59	21.38	24.52	19.24	19.95	18.61	17.42	18.56	20.11
MnO	0.66	0.66	0.67	0.65	0.66	0.66	0.88	0.46	0.46	0.47	0.47	0.47	0.47	0.47	0.47
MgO	6.77	6.82	6.93	9.44	7.39	7.52	14.43	10.16	10.01	9.81	8.89	9.14	9.28	9.22	9.16
CaO	17.46	17.93	18.44	4.57	17.45	17.31	2.62	16.22	13.77	18.27	18.60	20.33	21.11	20.25	18.20
Na_2O	0.17	0.11	0.19	0.18	0.16	0.16	0.00	0.15	0.15	0.14	0.13	0.13	0.12	0.13	0.13
Cr_2O_3	0.00	0.01	0.03	0.00	0.00	0.00	0.01	0.01	0.02	0.04	0.03	0.00	0.00	0.00	0.01
NiO	0.03	0.03	0.03	0.03	0.03	0.03	0.04	0.00	0.00	0.00	0.00	0.00	0.00	0.00	0.00
TOTAL	100.34	100.68	100.60	101.16	100.41	100.91	100.61	100.90	100.60	100.73	100.57	101.24	100.87	101.08	100.76
Recalculated as cations per 6 oxygens															
Si	1.952	1.959	1.944	1.972	1.948	1.954	1.969	1.953	1.953	1.949	1.953	1.941	1.950	1.949	1.958
Ti	0.013	0.011	0.015	0.012	0.012	0.012	0.005	0.016	0.016	0.016	0.015	0.014	0.014	0.014	0.015
Al	0.063	0.060	0.069	0.032	0.069	0.062	0.025	0.064	0.053	0.074	0.073	0.073	0.058	0.061	0.069
Fe	0.805	0.785	0.760	1.197	0.774	0.778	1.033	0.690	0.801	0.620	0.647	0.599	0.560	0.598	0.650
Mn	0.022	0.022	0.022	0.022	0.022	0.022	0.029	0.015	0.015	0.015	0.015	0.015	0.015	0.015	0.015
Mg	0.400	0.401	0.407	0.562	0.435	0.440	0.841	0.585	0.583	0.563	0.514	0.524	0.532	0.529	0.528
Ca	0.742	0.758	0.779	0.196	0.738	0.728	0.110	0.671	0.577	0.754	0.772	0.838	0.870	0.835	0.753
Na	0.013	0.008	0.015	0.014	0.012	0.012	0.000	0.011	0.011	0.010	0.010	0.010	0.009	0.010	0.010
Cr	0.000	0.000	0.001	0.000	0.000	0.000	0.000	0.000	0.001	0.001	0.001	0.000	0.000	0.000	0.000
Ni	0.001	0.001	0.001	0.001	0.001	0.001	0.001	0.000	0.000	0.000	0.000	0.000	0.000	0.000	0.000
At% En	20.56	20.63	20.93	28.75	22.33	22.61	42.39	30.05	29.73	29.08	26.57	26.73	27.11	26.97	27.32
Fs	41.33	40.38	39.04	61.24	39.77	39.97	52.07	35.47	40.87	32.00	33.46	30.54	28.56	30.46	33.66
Wo	38.11	38.99	40.03	10.01	37.90	37.42	5.53	34.48	29.40	38.92	39.97	42.74	44.38	42.57	39.02
Mg/F	0.332	0.338	0.349	0.319	0.360	0.361	0.449	0.459	0.421	0.476	0.443	0.467	0.487	0.470	0.448

TABLE 7

Pyroxene Analyses by Electron Microprobe

	A172/1	A172/2	A227/1	A227/2	A237/1	A237/2	A237/3	A237/4	A237/5	A252/1	A252/2	A252/3	A320/1	A320/2	A320/3	A320/4
SiO_2	51.68	51.58	50.85	51.50	51.58	50.82	50.85	50.07	51.06	49.05	49.26	51.52	51.87	51.73	51.28	51.26
TiO_2	0.43	0.43	0.43	0.43	0.44	0.43	0.43	0.20	0.44	0.69	0.69	0.69	0.43	0.44	0.44	0.43
Al_2O_3	1.77	1.61	1.55	1.45	2.10	1.64	1.49	0.64	2.27	2.00	1.84	1.42	1.56	1.60	2.51	2.14
FeO	14.80	14.32	15.55	14.73	12.49	17.49	16.35	31.99	12.98	14.40	14.10	13.17	14.18	10.50	12.72	13.93
MnO	0.47	0.47	0.47	0.47	0.47	0.47	0.47	0.64	0.47	0.37	0.37	0.37	0.47	0.47	0.47	0.47
MgO	12.38	12.38	10.73	10.98	11.66	11.29	11.03	14.32	11.96	10.93	11.46	11.90	14.27	13.27	12.72	14.06
CaO	19.90	19.57	21.34	21.68	22.13	18.55	19.66	1.72	21.16	21.23	20.92	21.62	17.69	22.18	21.99	18.68
Na_2O	0.17	0.17	0.18	0.17	0.17	0.18	0.18	0.00	0.17	0.28	0.28	0.27	0.17	0.17	0.17	0.17
Cr_2O_3	0.02	0.03	0.04	0.03	0.10	0.02	0.03	0.02	0.08	0.02	0.01	0.02	0.06	0.02	0.11	0.06
NiO	0.00	0.00	0.00	0.00	0.02	0.02	0.02	0.03	0.02	0.00	0.00	0.00	0.02	0.02	0.02	0.02
TOTAL	101.62	100.56	101.14	101.44	101.16	100.91	100.51	99.63	100.61	98.97	98.92	100.98	100.72	100.40	100.43	101.22
Recalculated as cations per 6 oxygens																
Si	1.940	1.951	1.936	1.947	1.937	1.941	1.946	1.975	1.929	1.907	1.911	1.943	1.947	1.941	1.925	1.920
Ti	0.012	0.012	0.012	0.012	0.012	0.012	0.012	0.006	0.013	0.020	0.020	0.020	0.012	0.012	0.012	0.012
Al	0.078	0.072	0.070	0.065	0.093	0.074	0.067	0.030	0.101	0.092	0.084	0.063	0.069	0.071	0.111	0.094
Fe	0.465	0.453	0.495	0.466	0.392	0.559	0.523	1.055	0.410	0.468	0.457	0.415	0.445	0.330	0.336	0.436
Mn	0.015	0.015	0.015	0.015	0.015	0.015	0.015	0.021	0.015	0.012	0.012	0.012	0.015	0.015	0.015	0.015
Mg	0.693	0.698	0.609	0.619	0.653	0.643	0.629	0.842	0.673	0.633	0.663	0.669	0.798	0.742	0.712	0.785
Ca	0.800	0.793	0.871	0.878	0.890	0.759	0.806	0.073	0.856	0.884	0.869	0.874	0.711	0.892	0.884	0.749
Na	0.012	0.012	0.013	0.012	0.012	0.013	0.013	0.000	0.012	0.021	0.021	0.020	0.012	0.012	0.012	0.012
Cr	0.001	0.001	0.001	0.001	0.003	0.001	0.001	0.001	0.001	0.001	0.000	0.001	0.002	0.001	0.003	0.002
Ni	0.000	0.000	0.000	0.000	0.001	0.001	0.001	0.001	0.002	0.000	0.000	0.000	0.000	0.001	0.001	0.001
TOTAL	4.015	4.007	4.023	4.014	4.009	4.017	4.014	4.004	4.013	4.038	4.038	4.016	4.012	4.017	4.011	4.026
At% En	35.38	35.90	30.84	31.53	33.72	32.78	32.12	42.74	34.71	31.89	33.31	34.17	40.84	37.80	36.83	39.83
Fs	23.73	23.30	25.08	23.73	20.27	28.50	26.72	53.57	21.14	23.58	22.99	21.22	22.77	16.78	17.41	22.14
Wo	40.88	40.80	44.09	44.74	46.01	38.72	41.16	3.69	44.15	44.53	43.70	44.61	36.39	45.42	45.76	38.03
MMF	0.599	0.606	0.552	0.571	0.625	0.535	0.546	0.444	0.622	0.575	0.592	0.617	0.642	0.693	0.679	0.643

TABLE 8

Plagioclase Analyses by Electron Microprobe

	A20/1	A20/2	A20/3	A31/1	A31/2	A59/1	A59/2	A59/3	A115/1	A115/2	A115/3
SiO_2	57.42	56.09	57.96	57.27	55.00	53.96	52.88	53.20	54.87	56.13	53.59
Al_2O_3	27.38	27.45	27.10	27.35	27.35	28.97	28.70	28.95	27.62	27.74	28.19
FeO	0.29	0.40	0.39	0.31	0.32	0.51	0.53	0.47	0.91	0.35	0.41
CaO	10.31	10.45	10.09	10.36	10.28	11.76	12.05	11.99	10.58	10.35	10.63
Na_2O	5.88	5.50	5.25	5.28	5.39	4.54	4.55	4.64	5.25	5.48	5.28
K_2O	0.53	0.32	0.57	0.62	0.64	0.34	0.38	0.38	0.56	0.42	0.43
TOTAL	101.81	100.21	101.35	101.19	98.98	100.08	99.09	99.63	99.79	100.46	98.53
Recalculated as cations per 8 oxygens											
Si	2.542	2.524	2.568	2.549	2.510	2.442	2.426	2.425	2.493	2.518	2.465
Al	1.433	1.456	1.418	1.435	1.471	1.545	1.549	1.554	1.478	1.468	1.524
Fe	0.010	0.015	0.014	0.012	0.012	0.019	0.020	0.018	0.034	0.013	0.015
Ca	0.489	0.504	0.479	0.494	0.503	0.570	0.593	0.585	0.515	0.498	0.524
Na	0.507	0.479	0.452	0.456	0.477	0.398	0.403	0.409	0.462	0.477	0.468
K	0.029	0.018	0.032	0.035	0.037	0.020	0.022	0.022	0.032	0.024	0.025
TOTAL	5.010	4.996	4.965	4.979	5.011	4.994	5.012	5.013	5.015	4.998	5.020
Mol% An	47.67	50.33	49.71	50.16	49.43	57.70	58.27	57.62	51.04	49.84	51.55
Ab	49.46	47.89	46.94	46.26	46.90	40.31	39.61	40.26	45.74	47.75	46.03
Or	2.87	1.78	3.35	3.57	3.66	1.99	2.13	2.12	3.22	2.41	2.42
Ab/(Ab+An)	50.92	48.76	48.57	47.98	48.69	41.13	40.47	41.13	47.26	48.93	47.17

	A152/1	A152/2	A172/1	A172/2	A227/1	A227/2	A227/3	A237/1	A237/2	A320/1	A320/2
SiO_2	56.93	56.33	52.08	53.16	53.93	53.33	54.43	56.65	56.98	51.77	53.13
Al_2O_3	28.08	27.26	30.34	30.11	30.26	30.63	29.49	28.81	28.47	31.35	30.57
FeO	0.41	0.48	0.19	0.14	0.39	0.33	0.43	0.35	0.29	0.32	0.19
CaO	11.25	10.60	14.40	13.99	13.55	13.82	13.28	11.83	11.16	14.54	13.59
Na_2O	5.07	5.45	3.84	3.81	4.06	3.54	4.05	5.08	5.34	3.68	4.20
K_2O	0.42	0.43	0.27	0.27	0.25	0.24	0.42	0.25	0.29	0.30	0.29
TOTAL	102.15	100.54	101.12	101.48	102.43	101.89	102.10	102.97	102.53	101.96	101.97
Recalculated as cations per 8 oxygens											
Si	2.513	2.529	2.349	2.380	2.390	2.374	2.419	2.482	2.504	2.317	2.368
Al	1.466	1.443	1.616	1.593	1.587	1.613	1.551	1.495	1.480	1.659	1.612
Fe	0.015	0.018	0.007	0.005	0.014	0.012	0.016	0.013	0.010	0.012	0.007
Ca	0.532	0.510	0.695	0.671	0.643	0.659	0.632	0.555	0.525	0.696	0.649
Na	0.437	0.475	0.337	0.332	0.352	0.308	0.351	0.436	0.458	0.321	0.364
K	0.023	0.025	0.016	0.015	0.014	0.014	0.023	0.013	0.015	0.017	0.016
TOTAL	4.985	4.999	5.020	4.996	4.999	4.980	4.992	4.995	4.993	5.022	5.016
Mol% An	53.61	50.51	66.36	65.92	63.75	67.22	62.80	55.29	52.58	67.42	63.05
Ab	44.06	47.04	32.15	32.62	34.90	31.38	34.88	43.37	45.88	30.98	35.40
Or	2.33	2.44	1.48	1.46	1.35	1.39	2.32	1.34	1.55	1.60	1.55
Ab/(Ab+An)	45.11	48.22	32.64	33.10	35.38	31.83	35.71	43.98	46.60	31.48	35.96

TABLE 9

Olivine Analyses by Electron Microprobe

	A107/1	A107/2	A107/3	A115/1	A115/2	A115/3	A348/1	A348/2
SiO_2	31.91	32.15	32.51	32.29	32.40	32.44	34.54	34.74
FeO	53.75	54.01	53.81	56.13	55.47	55.59	44.83	45.00
MnO	1.01	0.94	1.01	0.99	1.00	1.00	0.62	0.62
MgO	11.57	11.59	11.96	10.86	10.69	10.65	20.55	19.74
CaO	0.10	0.12	0.06	0.10	0.12	0.09	0.08	0.10
NiO	0.00	0.01	0.03	0.05	0.00	0.02	0.03	0.02
TOTAL	98.34	98.82	99.38	100.42	99.68	99.79	100.65	100.22
Recalculated as cations per 4 oxygens								
Si	1.005	1.007	1.010	1.004	1.012	1.012	1.002	1.013
Fe	1.416	1.415	1.398	1.459	1.449	1.450	1.088	1.097
Mn	0.027	0.025	0.027	0.026	0.026	0.026	0.015	0.015
Mg	0.540	0.541	0.554	0.503	0.498	0.495	0.889	0.858
Ca	0.003	0.004	0.002	0.003	0.004	0.003	0.002	0.003
Ni	0.000	0.000	0.001	0.001	0.000	0.001	0.001	0.000
TOTAL	2.995	2.993	2.990	2.996	2.988	2.988	2.998	2.987
Mol% Fo	27.73	27.67	28.37	25.64	25.57	25.45	44.96	43.88
Fa	72.27	72.33	71.63	74.36	74.43	74.55	55.04	56.12

TABLE 10

Fe-Ti Oxide Analyses by Electron Microprobe (Recalculated by the method of Stormer (1983))

	A31/1	A31/2	A31/3	A31/4	A31/5	A59/1	A59/2	A59/3	A59/4	A107/1	A107/2	A107/3	A172/1	A172/2	A227/1
TiO_2	50.89	20.31	51.03	12.78	17.00	48.40	48.33	6.89	6.07	50.66	13.26	50.94	50.78	12.23	49.29
Al_2O_3	0.21	3.01	0.27	2.09	3.57	0.26	0.29	1.76	2.69	0.23	4.07	0.22	0.23	2.46	0.26
FeO	43.95	49.21	44.04	42.55	46.46	40.94	41.14	34.95	36.52	43.70	42.39	43.57	44.38	41.59	42.75
Fe_2O_3	5.00	25.14	4.63	42.03	31.58	10.06	9.35	52.29	53.88	4.57	37.34	4.57	5.53	41.31	8.28
MnO	0.63	0.51	0.66	0.35	0.41	1.20	1.34	0.40	0.32	0.71	0.44	0.66	0.86	0.33	0.90
MgO	0.66	0.14	0.66	0.28	0.25	0.77	0.54	1.02	0.14	0.64	0.39	0.88	0.23	0.27	0.37
Cr_2O_3	0.00	0.04	0.02	0.09	0.05	0.01	0.00	0.04	0.09	0.02	0.04	0.00	0.04	0.20	0.05
Total	101.34	98.36	101.31	100.17	99.32	101.64	100.99	97.35	99.71	100.53	97.93	100.84	102.05	98.39	101.90
Ti	0.95	0.58	0.95	0.36	0.48	0.90	0.91	0.20	0.17	0.95	0.38	0.95	0.94	0.35	0.92
Al	0.00	0.13	0.00	0.09	0.16	0.00	0.00	0.08	0.12	0.00	0.18	0.00	0.00	0.11	0.00
Fe^{2+}	0.91	1.55	0.91	1.33	1.45	0.85	0.86	1.13	1.15	0.91	1.34	0.91	0.92	1.32	0.89
Fe^{3+}	0.09	0.71	0.09	1.18	0.89	0.19	0.18	1.52	1.53	0.09	1.06	0.09	0.10	1.18	0.15
Mn	0.01	0.02	0.01	0.01	0.01	0.03	0.03	0.01	0.01	0.02	0.01	0.01	0.02	0.01	0.02
Mg	0.02	0.01	0.02	0.02	0.01	0.03	0.02	0.06	0.01	0.02	0.02	0.03	0.01	0.02	0.01
Cr	0.00	0.00	0.00	0.00	0.00	0.00	0.00	0.00	0.00	0.00	0.00	0.00	0.00	0.01	0.00

	A237/1	A237/2	A237/3	A237/4	A252/1	A252/2	A252/3	A252/4	A252/5	A252/6	A348/1	A348/2	A348/3	A348/4
TiO_2	6.42	49.22	50.73	6.89	4.09	51.33	14.07	2.23	4.90	50.66	50.91	13.60	51.37	12.94
Al_2O_3	2.31	0.30	0.31	3.25	1.61	0.23	11.79	1.43	1.99	0.23	0.28	4.49	0.24	4.11
FeO	36.89	42.80	43.87	38.31	34.34	42.78	43.58	33.53	35.27	43.28	42.04	43.28	42.33	42.69
Fe_2O_3	54.03	8.57	5.28	52.32	58.85	4.10	31.19	64.15	57.34	4.90	5.74	38.12	5.18	39.63
MnO	0.27	0.91	1.41	0.23	0.16	1.14	0.47	0.08	0.15	1.23	0.56	0.25	0.60	0.33
MgO	0.37	0.30	0.18	0.05	0.34	1.25	2.09	0.24	0.42	0.58	1.78	0.93	1.83	0.79
Cr_2O_3	0.73	0.05	0.08	0.88	0.29	0.04	0.28	0.33	0.34	0.05	0.05	0.87	0.03	0.92
Total	101.02	102.16	101.86	101.93	99.68	100.87	103.47	101.99	100.41	100.93	101.36	101.54	101.58	101.41
Ti	0.18	0.92	0.95	0.19	0.12	0.96	0.36	0.06	0.09	0.95	0.94	0.37	0.95	0.35
Al	0.10	0.01	0.01	0.14	0.07	0.01	0.47	0.06	0.09	0.01	0.01	0.19	0.01	0.18
Fe^{2+}	1.15	0.89	0.91	1.18	1.09	0.89	1.24	1.05	1.11	0.90	0.87	1.31	0.87	1.30
Fe^{3+}	1.52	0.16	0.10	1.45	1.69	0.08	0.80	1.80	1.62	0.09	0.11	1.04	0.10	1.09
Mn	0.01	0.02	0.03	0.01	0.01	0.02	0.01	0.00	0.00	0.03	0.01	0.01	0.01	0.01
Mg	0.02	0.01	0.01	0.00	0.02	0.05	0.11	0.01	0.02	0.02	0.07	0.05	0.07	0.04
Cr	0.02	0.00	0.00	0.03	0.01	0.00	0.01	0.01	0.01	0.00	0.00	0.02	0.00	0.03

7. THE MAIN ZONE IN THE CONTEXT OF THE BUSHVELD COMPLEX

SACS (1980) regarded the Giant Mottled Anorthosite as the top of the Mathlagame Norite , thus including the Merensky and Bastard Cyclic Units in the Upper Critical Zone. (The Mathlagame Norite of the SACS terminology is the equivalent of the Upper Critical Zone.) Kruger and Marsh (1982) showed that there is a dramatic increase in the strontium isotope initial ratio across the Merensky Cyclic Unit, from ca. 0.7063 in the immediate footwall of the Merensky Reef to 0.7075 at the base of the Bastard Cyclic Unit. These data led Kruger and Marsh (1982) to suggest that the Merensky Reef represents a major event in the Bushveld magma chamber. On this basis, they regarded the Merensky Reef as the base of the Main Zone.

The decision by SACS (1980) to define the top of the Bastard Cyclic Unit as the top of the Upper Critical Zone has a sound basis in petrological observations. The Merensky and Bastard Cyclic Units are the uppermost two of a series of well-defined cyclic units, including the UG1 and UG2 and Pseudo Reefs, in the Upper Critical Zone (Fig. 31). These cyclic units are characterized by a cyclicity in which the succession chromitite - (harzburgite) - pyroxenite - norite - anorthosite repeats itself systematically. Perhaps the most important feature of the Upper Critical Zone is that all the cyclic units, up to and including the Bastard Cyclic Unit, contain cumulus chromite. The Main Zone rocks above the Giant Mottled Anorthosite, significantly, contain no cumulus chromite.

The term **"rhythmic layering"**, coined by Wager and Deer (1939), might aptly be used to describe the conspicuous, more or less systematic recurrence of layers, or sequences of layers, found in the Upper Critical Zone. The Main Zone, on the other hand, is characterized by what McBirney and Noyes (1979) termed **"intermittent layering"**, in which modally graded layers occur periodically, separated by substantial thicknesses of relatively uniform cumulate rock. Irvine (1982) objected to the use of the term intermittent layering on the semantic basis that, whereas the **layers** themselves may be intermittent, the **layering** is continuous. The term "intermittent layering" is appropriate here, however, because regardless of philological arguments, it adequately conveys an impression of the nature of the layering in the Main Zone.

Viewed in isolation, Kruger and Marsh's (1982) data suggest an instantaneous event at the level of the Merensky Reef. Data presented in section 5.5 of the present work suggest that there is a sustained increase in the strontium isotope initial ratio (R_o), from the base of the Merensky Reef all the way up to the top of Main Zone unit III. There may even be a justification, on these grounds, for suggesting that the Porphyritic Gabbro Marker is the real base of the Main Zone. Such a contention might be supported by modal mineralogical data. These data show that, whereas units I, II and III of the Main Zone have noritic tendencies, containing less than ten percent modal intercumulus clinopyroxene, the Porphyritic Gabbro Marker marks a sudden increase in the proportion of modal clinopyroxene (Fig. 34).

On balance, the disappearance of cumulus chromite above the Bastard Cyclic Unit is probably the most appropriate criterion for the demarcation of the base of the Main Zone, consistent with the recommendations of SACS (1980). It should be noted, however, that this is in conflict with the guidelines of Wager and Brown (1968), who defined new units on the possibly more acceptable criterion of the appearance of new minerals. Eales et al.(1986) have reinforced the petrological criteria for this demarcation with geochemical data. Their whole-rock Co/V and MgO/(MgO+FeO) ratios, and the orthopyroxene Cr/Al ratio in particular, define a sharp discontinuity at the top of the Bastard Cyclic Unit. Of the plots against stratigraphic height in Fig. 32 of this work, Zr defines a particularly interesting trend, with a marked increase in concentration at the top of the Giant Mottled Anorthosite. In a cumulate rock, an increase in the concentration of an incompatible element like Zr is probably indicative of an increase in residual porosity (Wager, 1963; Campbell, 1987). This implies a higher proportion of trapped intercumulus liquid in the rocks above the Giant Mottled Anorthosite. Crystallization of the trapped liquid will tend to produce orthocumulate textures, as are observed in units I and II of the Main Zone, in particular. The significance of the entrapment of intercumulus liquid is dealt with in section 9 of this work.

In classifying the Main Zone, SACS (op. cit.) employed Molyneux's (1970) threefold subdivision of the Main Zone into Subzones A, B and C, although they assigned local stratigraphic names to them. According to Molyneux's (1970) system, Subzone A extends from the base of the Main

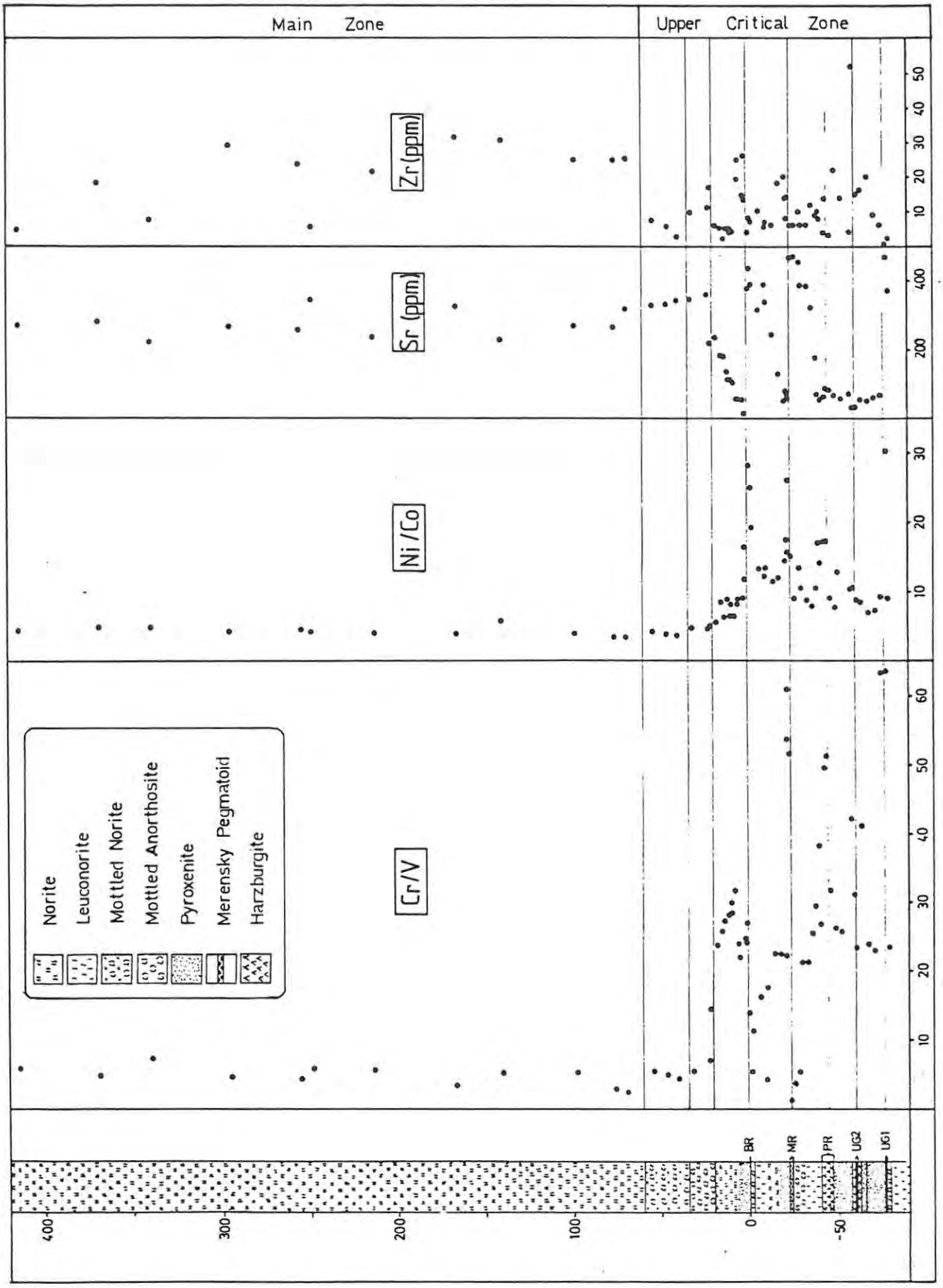

Fig. 32 : Diagram illustrating geochemical variations through the Upper Critical Zone and the lower part of the Main Zone at RPM Union Section. Stratigraphic heights are in metres above or below the Bastard Reef. The base of the Main Zone is at the top of the Giant Mottled Anorthosite, 53m above the Bastard Reef. (BR = Bastard Reef; MR = Merensky Reef; PR = Pseudo Reef.) Data from 11 6^S crosscut, Union Section (this study) and from de Klerk (1982).

Zone to the top of the Upper Mottled Anorthosite (i.e. up to the basal part of unit VII, as defined here). Subzone B extends from the top of Subzone A to the base of the Pyroxenite Marker. This separation of Subzone A from Subzone B is not justified, according to petrological and geochemical data presented in this thesis. If anything, the base of the Porphyritic Gabbro Marker (unit IV) is a more appropriate place for the boundary between major subzones of the Main Zone, assuming that such a subdivision is justified at all.

Molyneux placed the base of Main Zone subzone C at the Pyroxenite Marker. This horizon is apparently not characterized everywhere by the development of a pyroxenite layer, but sharp changes in petrologic and geochemical parameters suggest that it is a major lithological boundary. Subzone C extends to the base of the Upper Zone which, according to Willemse (1969), begins at the base of the Main Magnetite Layer. Molyneux (1970), adjusted the position of the base of the Upper Zone to the first appearance of cumulus magnetite, in a magnetite anorthosite some way below the Main Magnetite layer. Regardless of the favoured position of its exact base, the diagnostic feature of the Upper Zone, according to traditional doctrine, is the presence of cumulus magnetite in the rocks.

Sharpe (1985) demonstrated that the succession from the Merensky Reef to the Pyroxenite Marker is isotopically distinct from the rest of the Complex. He suggested that this interval constitutes an anomalous wedge of magma, genetically separate from the rest of the Complex. The compositionally anomalous magma, according to Sharpe, intruded at approximately the level of the Merensky Reef, uplifting the supernatant residual liquid in the magma chamber in the process. The implication of this is that the Upper Critical and Upper Zones are consanguineous, whilst the Main Zone gabbronorites between the Merensky Reef and the Pyroxenite Marker are the crystallization products of a later influx of magma.

According to Kruger et al.(1986; in press), samples from the entire succession above the Pyroxenite Marker fall on a single Rb-Sr isochron, and hence have a common Sr-isotope initial ratio of 0.7073[1. Kruger et al. suggest that the rocks above the Pyroxenite Marker crystallized from a <u>new</u> influx of magma (R_o ca. 0.7067), which was blended with the liquid residue of the pre-Pyroxenite Marker magma. The model precludes

the addition of further significant quantities of magma, except in the unlikely case that they were isotopically equivalent to the blended magma. It is submitted, therefore, that the Pyroxenite Marker represents the last major addition of magma to the system. On these grounds, it is not unreasonable to suggest that the Pyroxenite Marker forms the base of the Upper Zone.

In the "gap" areas of the northwestern Bushveld, major transgressions of Upper Zone material across the Main and Critical Zones occur at the level of the Main Magnetite layer (Fig. 7). Coertze (1974) regarded these transgressions as strong evidence for the intrusion of a new magma. The isotopic evidence produced by Kruger et al. (in press) would, however, tend to preclude such a major influx of new magma, because this would be likely to alter the strontium isotope systematics. In addition, the new magma, or the resulting hybrid liquid, would have had to have an unusual composition to be able to precipitate copious quantities of magnetite so soon after intrusion. The transgressions might equally well be explained by tectonic adjustments in the floor rocks of the magma chamber, which Vermaak (1976), for example, appeals to as an explanation for erosional features elsewhere within the layered succession.

In summary, the petrological, geochemical and isotopic evidence favour the demarcation of the interval between the top of the Bastard Cyclic Unit and the Pyroxenite Marker as a genetically distinct zone within the layered succession. It is therefore recommended that Subzone C be removed from the Main Zone, and included as the basal subzone of the Upper Zone, as suggested by Kruger et al.(in press), and that only the interval from the top of the Bastard Cyclic Unit to the base of the Pyroxenite Marker be included in the Main Zone.

The criteria for the subdivision of the Main Zone into the various units in this work are presented in tabulated form in Table 6. Some of these subdivisions (that between Units I and II, for example) may not be primary genetic features, and may quite conceivably be related to postcumulus processes, possibly linked to the formation of the ultramafic pegmatite bodies. Such boundaries are likely to be of only local extent, and therefore not an integral part of the Main Zone stratigraphy. Other boundaries, on the other hand (particularly those between Units II and III, and between Units III and IV), are almost

certainly primary features, probably linked to magma influxes (see section 9 of this work), and are likely to be laterally continuous.

TABLE 11

CRITERIA USED IN THE SUBDIVISION OF THE MAIN ZONE OF THE BUSHVELD COMPLEX

Units	Petrographic evidence	Mineral chemical evidence	Whole-rock geochemistry
I-II	-	Opx. changes from En_{74} to En_{64} across boundary between units I & II.	Increase in TiO_2, Co, Ni & Zn; decrease in Al_2O_3, Y, Sr, Ba across the boundary between units I & II.
II-III	Coarse feldspathic pyroxenite at the base of unit III.	Change in opx. from $En_{69.1}$ to $En_{72.3}$ across boundary.	Decrease in Ba & Zr concentrations and V/Sc ratio across boundary.
III-IV	Abrupt increase in modal cpx., decrease in modal plagioclase.	Opx. changes from $En_{68.9}$ to En_{71} across boundary.	Sr R_o increases from 0.70871 to 0.70889 across boundary. Unit IV characterized by trend of progressive decrease in R_o.
IV-V	High modal proportion of plag. in unit V.	Opx. anomalously enriched in Fe in unit V.	Sharp increase in Sr R_o across boundary.
V-VI	Decrease in modal plag. across boundary.	-	Unit VI dominated by strong fractionation of V/Cr ratio.
VI-VII	Fine-grained orthopyroxenite at base of unit VII. Plag. is the only primocryst phase in unit VII. Inverted pigeonite appears with hypersthene in unit VII	-	Sharp decrease in Sr R_o, decrease in V/Sc ratio, decrease in Zr.
VII-VIII	Pigeonite completely supplants hypersthene at base of unit VIII. Pigeonite cumulus.	-	Unit VIII dominated by strong fractionation of V/Cr ratio.
VIII-UZ	Hypersthene supplants pigeonite at Pyroxenite Marker.	Opx. changes from $En_{58.5}$ to $En_{69.1}$ across boundary. Plag. changes from $An_{58.7}$ to $An_{71.5}$ across boundary.	Decrease in R_o, V/Cr ratio, increase in Cr/Sc across boundary.

8. CRYSTALLIZATION PROCESSES IN MAGMA CHAMBERS

The most conspicuous feature of the Bushveld and other layered complexes is the laterally persistent layering of the cumulate rocks. In their investigation of the Skaergaard intrusion, Wager and Deer (1939) defined two types of layering. The first of these, rhythmic layering, is the most obvious form of layering, and is manifest in the conspicuous variations in the proportions of the chief minerals in the rock. Intermittent layering (McBirney and Noyes, 1979) is a variation on the theme of rhythmic layering which, although not quite as conspicuous, can nevertheless be observed in the field. Cryptic layering, by comparison, is the inconspicuous, and for the most part gradual, change in the composition of the constituent minerals of successive layers in a layered complex. This latter form of layering is not readily appreciated in the field, but is none the less of paramount importance in petrogenetic modelling. McBirney and Noyes (1979) and Irvine (1982) have both reviewed the terminology of layered intrusions in some detail (see additional commentary in chapter 7 of this work), and a detailed review would not be appropriate here.

Any theoretical model to account for the layering, both rhythmic and cryptic, in the Bushveld Complex must also be able to account for its extreme lateral persistence. In other words, any process invoked must have been effective more or less instantaneously over virtually the entire complex. In the broadest terms, theories to account for layering involve either the generation of separate magmas at depth, by processes such as partial melting or differentiation, or differentiation **in situ**, or a combination of the two.

In its most extreme form, the concept of multiple intrusion takes the form of Coertze's (1960, 1974) belief that each separate rock type, from dunite through to anorthosite, is emplaced as a discrete, sill-like influx of magma. Coertze's hypothesis of new intrusions for each discrete lithology would be favoured by the presence of disconformable contacts between layers, and presumably also by erosional features. Coertze (1960) believed he had evidence for cross-cutting relationships between an anorthosite layer and the general layering of the Main Zone to the south of Pilanesberg. Cousins (1960) disputed Coertze's interpretation, submitting that the anorthosite layer in question, and others like it in the Main Zone, are

laterally continuous along strike, and are conformable with the gross layering of the complex. A host of subsequent studies of the Main Zone (Meyer, 1969; Von Gruenewaldt, 1973; Molyneux, 1974; Viljoen and Burvenich, 1983; this study) have vindicated Cousins's interpretation of the conformable relationship between the anorthosite layers and the Main Zone gabbro in general. From the present study, it is evident that the Main and Upper Mottled Anorthosite layers are not only laterally persistent, but generally have gradational upper and lower contacts (the thin feldspathic pyroxenite at the base of the Upper Mottled Anorthosite in SK2 being a notable exception). Gradational contacts of this sort are certainly not to be anticipated in the case of sill-like intrusions.

The diametrically opposed viewpoint to Coertze's, espoused by Hall (1932), Willemse (1959, 1969) and Cameron (1978), is that the complex differentiated **in situ** from a single large body of magma. Strontium isotope data presented by Sharpe (1986) for the layered succession of the Bushveld Complex as a whole indicate sudden, marked changes in the initial ratio (R_o) at various points within the succession, notably at the Lower Critical Zone/Upper Critical Zone boundary, at the base of the Merensky Reef, and at the Pyroxenite Marker. These changes are accompanied, in each case, by abrupt changes in whole-rock and mineral chemical parameters. On a similar but smaller scale, abrupt changes in strontium R_o and other geochemical parameters, notably the MMF ratio, are present in the Main Zone succession in SK2, particularly at the bases of Units III and IV (Fig. 34). Such sharp changes, especially in isotope systematics, are irreconcilable with the fractionation of a single, large batch of magma.

The views of most recent workers occupy the middle ground between the above two extremes, and involve the successive emplacement of a series of batches of grossly similar magma. Many researchers regard these magma batches as having had tholeiitic affinities, although a number of more recent workers (Vermaak, 1976; Hamilton, 1977; von Gruenewaldt, 1979; Cawthorn et al., 1979; McCarthy and Cawthorn, 1980; Irvine et al., 1983; Sharpe, 1981; 1985) believe that early influxes into the magma chamber were more mafic, high-Mg magmas.

Cameron (1978) found it difficult to believe that the Lower Zone, with its overwhelmingly dominant pyroxenites and only minor peridotitic

rocks, could be derived from a magma as mafic as a high-Mg basalt. There is, however, a body of evidence to suggest that the early magma of the Bushveld Complex was of bonninitic affinities, with high MgO (in excess of 14%), and high SiO_2 (over 56%). The existence of mantle-derived bonninitic melt compositions has been documented by Cameron et al. (1979), Crawford et al. (1981) and Hickey and Frey (1982), amongst others. Irvine and Sharpe (1982) and Irvine et al. (1983) proposed that the early, ultramafic (U) magma lineage in the Bushveld and Stillwater Complexes was bonninitic. In the Irvine model, the U magma was succeeded by a more anorthositic (A) magma. The Lower and Lower Critical Zones were believed to have crystallized from the U magma lineage, and the Upper Critical and Main Zones essentially from the A lineage (Sharpe and Irvine, 1983). "Finger-type" mixing of the two magmas within a stratified magma chamber is the theoretical mechanism whereby layering, particularly the pronounced cyclic layering of the Upper Critical Zone, was thought to have been produced.

On the basis of new geochemical, REE and Sr-isotopic data on the marginal rocks of the eastern Bushveld, Sharpe (1986) has recently modified the original Irvine and Sharpe (op. cit.) model, incorporating a third (B-type) magma. The B-type magma is an iron-rich tholeiite, intruded periodically during the accumulation of the Critical Zone. As such, it is not of direct concern to this study. The first appearance of the original A liquid, according to Sharpe's (op. cit.) modified model, is at the Merensky Reef. Although Sharpe (1986) was unable to find marginal rocks compatible with the postulated A-type liquid, he suggested that it was an aluminous tholeiite, with MgO of the order of six weight percent, total iron (expressed as FeO) in the region of eight weight percent, low K_2O, and Sr R_o ±0.709. The Main Zone is believed by Sharpe to have crystallized essentially from the A liquid, although (B+U±A) liquid forms a small component of the lowermost layers of the Main Zone. Sharpe believed the Upper Zone (above the Pyroxenite Marker) to have crystallized from the uplifted U+B supernatant residual liquid of the Critical Zone, possibly mixed with a small amount of Main Zone A-type liquid.

Objections raised by Kruger et al. (in press) to Sharpe's (1985) model concern thermal and density considerations. Sharpe's model requires that the A-type (Main Zone) magma intrude the U (or U+A or U+B) magma at a level commensurate with its density. The A magma underflows the

U-dominant mixture, presumably on the grounds that the A liquid is relatively Fe-rich and Si-poor. The fact that the A-liquid has intruded at its density level implies that the density difference between the two magmas will be critically balanced. The U-lineage liquid, being of more primitive (Mg-rich) composition, will be hotter than the underlying A liquid. In this situation, there must be downward transfer of heat across the boundary between the A and U liquids. It is highly likely, in this situation, that the cooled upper (U-type) layer will become more dense than the underlying A-type liquid. This is the classic situation for the formation of an unstable finger-type interface at the level of the Pyroxenite Marker, rather than the stable diffusive-type interface suggested by Sharpe. There should therefore have been substantial mixing across the interface at a very early stage, rather than at the late stage required by Sharpe's model.

Assuming that a stable interface were possible at the Pyroxenite Marker, the crystallization of substantial quantities of plagioclase in the Main Zone would make the successive residual liquids of the A liquid progressively more dense. This would serve only to make the putative diffusive interface ever more stable, thus prohibiting the late-stage mixing of the two liquids, as suggested by Sharpe (1985).

The alternative model, presented by Kruger et al., is that the entire lithological succession from the Pyroxenite Marker to the roof of the complex is attributable to a major influx of new magma. The new magma (R_o ca. 0.7067) blended thoroughly with the residue of the Main Zone magma, in the ratio 7:3, giving a resultant R_o of ±0.7073. Minor additions of the new magma below the Pyroxenite Marker are not discounted, and are in fact advocated by Kruger et al. (1986). Such minor magma additions in the upper reaches of the Main Zone were also suggested by Marais (1976), on geochemical grounds.

The data of this thesis support the Kruger et al. model of a major influx of new magma at the Pyroxenite Marker. Furthermore, there is evidence that a relatively low-R_o magma was intruded into the Main Zone at the base of Unit VII, where sample A182 has a particularly low R_o in terms of its position in the Main Zone (Fig. 34). The trend of progressive increase in R_o upwards in unit VII from sample A182 suggests that the new, relatively low-R_o magma underflowed the residue

of the high-R_o magma in the chamber (Fig. 34). The initial crystallization of orthopyroxene from the new magma (resulting in the formation of the feldspathic pyroxenite at 900m in SK2) produced a relatively low-density, low-R_o residual liquid, which mixed upwards with the overlying high-R_o supernatant liquid to produce the observed trend in unit VII. The relatively low R_o of the uppermost two samples in unit V (Fig. 34) may be an indication that the Upper Zone-type magma had even began to intrude as low down as the Main Mottled Anorthosite.

In terms of parental magma compositions, Sharpe's (1986) theoretical A_o magma is a likely candidate for at least for the lower few hundred metres of the Main Zone. Most importantly, this magma must have had a strontium isotope R_o of 0.709 or more. Apart from this, a magma that may loosely defined as an aluminous tholeiite (Irvine and Sharpe, 1983; Sharpe, 1986) has the appropriate composition to produce the plagioclase-dominant mineralogy of the lower Main Zone cumulates.

The magma that began to enter the magma chamber at the base of unit VII, or even as low as unit V, had a relatively lower R_o, and was probably genetically equivalent to the magma from which the Upper Zone crystallized. Kruger et al. (in press) favour a magma of composition similar to Sharpe's B-type magma as the parental magma of the Upper Zone. The B-type magma (Sharpe, 1986) has slightly lower SiO_2 (48-50 wt%) than the A-type magma, low K_2O and Rb, vanadium concentration of the order of 200-350ppm,and a strontium isotope initial ratio in the range 0.7065-0.7075. This Upper Zone-type magma may best be described as an iron-rich tholeiite.

The anomalously fine-grained sample A236 in Unit V (Fig. 13a) may plausibly be considered a chilled sample of the Upper Zone-type magma, intruded some time after crystallization of the surrounding cumulates. Sample A236 has a strontium isotope R_o of 0.70737, which is virtually equivalent to the R_o of 0.7073 of the Upper Zone cumulates, but slightly higher than the estimated initial ratio of 0.7067 for the unmixed Upper Zone magma (Kruger et al., in press). The relatively iron-rich composition of the orthopyroxene in A236 (En_{56}) attests to its having crystallized from a relatively iron-rich magma. The relatively high whole-rock vanadium content of A236 (274ppm) is within the ratio quoted by Sharpe (1986) for the B-type magma, whilst the chromium content is relatively low (147 ppm).

The physical mechanism of crystallization within a magma chamber must have a profound effect on the composition and appearance of layered cumulates. Until fairly recently, most crystallization models relied principally on processes of magmatic sedimentation, or crystal settling, as a mechanism for crystal fractionation from the magma (Wager and Brown, 1968). Since the late seventies, however, mechanisms involving **in situ** bottom crystallization as a dominant process have received a good deal of attention (**inter alia** McBirney and Noyes, 1979).

In its simplest form, magmatic sedimentation was thought by Buddington (1936) to have produced layering by simple gravity sorting (gravity stratification) according to the specific gravity of different minerals. Wager and Deer (1939) required that gravity stratification be further modified by some additional process, to explain the fissility, or parallelism, of platy minerals within rhythmic layers. Wager and Brown (1968) ascribed this parallelism, known as igneous lamination, to the action of currents within the magma chamber. Working on Main Zone rocks, Ferguson and Botha (1963) similarly concluded that igneous lamination is the result of current activity in the magma chamber. These latter authors extended the model by incorporating a process whereby plagioclase crystals are winnowed out of the crystal assemblage and kept afloat in the magma, thus allowing the deposition of bands of mafic minerals. This last point has a bearing on the density of various minerals relative to the parent magma, which has been an important factor in the rejection of the original crystal settling models of cumulus crystallization (McBirney and Noyes, 1979; Irvine, 1982).

Of particular importance in the rejection of the classical cumulus theory is the case of plagioclase, which is less dense than any magma that might reasonably be expected to have been parental to the Bushveld Complex, or part thereof. Crystal **flotation** should, on these grounds, be given as much consideration as crystal **settling.** The positive buoyancy of plagioclase within basaltic melts has, furthermore, been demonstrated experimentally (Campbell et al., 1978). Vermaak (1976) invoked the process of flotation of successive batches of plagioclase in the Upper Critical Zone of the Bushveld Complex, principally to explain apparent inversed fractionation trends in certain parts of the

succession. The flotation of early-formed (and therefore relatively calcic) plagioclase would result in the residual liquid in the basal layers of a cyclic unit evolving to progressively more sodic compositions. The effect would therefore be that, although pyroxene may define an upward iron-enrichment trend, as expected, plagioclase would display an apparently anomalous trend of upward calcium enrichment. This decoupling of the trends of cryptic variation of plagioclase and pyroxene is evident in unit VI of the Main Zone (Fig. 34), and has also been documented in the Upper Critical Zone by Cameron (1982), de Klerk (1982) and Kruger (1982). The conclusion to be drawn from these data is that neither crystal settling nor **in situ** bottom growth mechanisms can fully explain the observed trends of cryptic variation. The most plausible mechanism is bottom growth, modified to a greater or lesser extent by flotation of plagioclase.

Whilst Irvine (1980b) did not subscribe entirely to the concept of magmatic sedimentation, he believed there were certain aspects of the layering of the Skaergaard intrusion, in particular, which could not be explained by **in situ** bottom crystallization alone. Irvine's (1980b) model incorporated deposition from density currents to account for graded layers, and bottom crystallization in association with double-diffusive convection to account for thinly layered or uniform sequences of rock.

The concept of double-diffusive convection in magma chambers has received a good deal of attention since the work of Turner and Gustafson (1978). Turner and Gustafson introduced the concept of double-diffusive convection, already documented in studies of stratification in saline water, to the study of magmatic processes in magma chambers. McBirney and Noyes (1979) suggested that the striking layering in the Upper Zone of the Skaergaard intrusion may have formed in the fluid state by processes of double-diffusive convection. In terms of the McBirney and Noyes model, gravity stratification of the magma chamber takes place due to diffusivity differences between heat and chemical components. Crystallization takes place in a stagnant boundary layer, with mineralogy and mineral composition controlled by diffusion at the cooling surface of the solidifying magma.

The concept of crystallization in a stagnant boundary layer, isolated from the rest of the magma chamber, was used by Jackson (1961) to

explain the layering in the Stillwater Complex. Donaldson (1977) believed that "comb layers", i.e. layers with vectorially oriented crystals, formed under quiet conditions, due to **in situ** crystallization on the base and walls of the magma chamber. Donaldson believed that crystallization under these conditions is a response, not only to the thermal gradient, but also to a diffusion-controlled composition gradient. Experimental work by Jaupart et al. (1984) and Jaupart and Brandeis (1986), on the other hand, emphasises thermal, rather than compositional effects on crystallization in stagnant boundary layers. Jaupart and his co-workers simulated convection in a magma chamber using viscous oils. They found that cooling through the base of a liquid layer produces a stagnant boundary layer, which is not penetrated by convected plumes descending from the top of the layer. The liquid layer therefore consists of a lower stagnant boundary layer, and an upper convecting layer, with the stagnant boundary layer effectively isolated from the overlying convecting part of the liquid layer.

The theoretical mechanism of **lateral accretion** was introduced by Irvine (1981) to explain the layering in the Muskox intrusion. By this process, cumulate layers form simultaneously from a series of liquid layers undergoing double-diffusive convection. The conceptual advantage of the lateral accretion model is that it allows the simultaneous crystallization of several liquid layers. This is primarily because the different compositions of successive layers result in different crystallization temperatures for each. The lateral accretion model is discussed extensively by Irvine et al. (1983). These authors discuss the application of the model to both the Stillwater and the Bushveld complexes. Critical material evidence for the lateral accretion model would be the gradual down-dip elimination of successive rock layers from the succession. Whilst it would be extremely difficult to find direct evidence to refute the model, especially in an intrusion the size of the Bushveld, the circumstantial evidence weighs against it, in that there is no direct field evidence of the elimination of rock layers at the depth to which mining has so far proceeded in the Bushveld Complex.

Wilson and Larsen (1985) tentatively applied the lateral accretion model to parts of the Fongen-Hyllingen intrusion in Norway, but noted some of its shortcomings. The lateral accretion model involves

down-dip solidification along a lateral accretion front, each rock layer crystallizing from its parent liquid layer. Near the crystallization front, residual buoyant liquid will rise from the zone of crystallization to the top of the liquid layer. Depending on its density, the residual liquid will either convect within its parent layer, or rise along the accretion front to join the overlying liquid layer. The upward loss of liquid by a crystallizing layer is apparently compensated for by gain of liquid from the underlying layer. The exception is the lowermost liquid layer, in which upward losses of residual liquid are not compensated for by gains from below. This leads to the gradual thinning, and eventual elimination, of successive basal liquid layers. As pointed out by Wilson and Larsen (op. cit.), a process critical to the lateral accretion mechanism is the upward transfer of residual liquid from one layer to the next across double-diffusive interfaces. This is contrary to the experimentally determined principles of double-diffusive convection (Turner and Gustafson, 1978; Huppert and Sparks, 1984), by which there can be no large-scale transfer of material between two liquid layers until there is a complete breakdown of the diffusive interface, leading inevitably to the merging and complete homogenization of the two pre-existing liquid layers. Even if lateral accretion were a viable mechanism, its applicability to the Bushveld Complex is negated by the isotopically distinct nature of the Footwall, Merensky and Bastard Cyclic Units (Kruger and Marsh, 1982; Sharpe, 1986).

Replenishment of a crystallizing magma chamber with fresh magma is the central theme of numerous models of the evolution of layered complexes (Irvine, 1977a & b; Dunham and Wadsworth, 1978; Loney and Himmelberg, 1983). The physics of replenishment of a magma chamber by an influx of hotter, more dense primitive magma is addressed by Huppert and Sparks (1980). These authors suggested that there will initially be no mixing between the resident magma in the chamber and the new influx. When the two magmas reach thermal equilibrium, they may either mix or remain separate layers, depending on the stage of fractionation, and therefore the density, of the lower layer of magma. The case of a hot, dense magma underlying a cooler, less dense magma is a prerequisite for the **diffusive** case of double-diffusive convection which, as pointed out by Irvine et al. (1983), results in a persistent, and even self-perpetuating, interface between the liquid layers. The alternative, **finger** case of double-diffusive convection arises when the

upper of two liquid layers is less dense only because it is hotter than the underlying layer. Finger-type double-diffusive convection is, by its very nature, only a transitory phenomenon.

As discussed earlier in this chapter, discontinuties in geochemical parameters, specifically the strontium isotope R_o and the orthopyroxene Mg/(Mg+Fe) ratio, in the SK2 succession (Fig. 34) are concrete evidence of new magma influxes during crystallization of the Main Zone. The fact that discrete geochemical trends are maintained in the rock record (e.g. in units III and IV of the Main Zone) means that liquid layers within the chamber maintained their integrity during crystallization. This is strong evidence for the operation of double-diffusive processes in the Main Zone.

9 THE MAIN ZONE AS PART OF AN EVOLVING MAGMA CHAMBER

By their very nature, Sr isotope ratios are not affected by fractional crystallization processes. Any variations in the strontium isotope initial ratio (R_o) must therefore be ascribed either to the mixing of isotopically different magma sources, or to contamination of the magma (generally by crustal material). Being unaffected by fractionation processes, strontium isotope data form a sound platform on which to base a discussion of the evolution of the Main Zone.

Sharpe (1985) suggested, on the basis of strontium isotope data, that the interval between the Merensky Reef and the Pyroxenite Marker in the eastern Bushveld is a "fossilized 2-3km thick layer of gabbroic magma ... differentiated **in situ** with relatively minor mixing between the under- and overlying magma". Strontium isotope data presented here (Figs. 27 and 34) for the Main Zone in the northwestern Bushveld indicate a somewhat more complicated pattern of variation than is suggested by Sharpe's data. The prime reason for this may be the somewhat larger database employed here.

Given that R_o variations in the Main Zone cannot be ascribed to fractionation, they must be related either to **in situ** contamination or to magma mixing of two isotopically different source magmas. **In situ** contamination would require that the existing magma be contaminated by more radiogenic Sr, presumably derived from partial melting of the roof and/or walls of the intrusion. Selective intake of Sr from the wallrocks, without significant changes in the bulk chemistry of the magma, was a mechanism suggested by Pankhurst (1969). This is, however, an intuitively simplistic model, and one would expect to see the effects of bulk contamination in the chemistry and mineralogy of the Main Zone rocks.

The maximum strontium isotope R_o of the Main Zone rocks analyzed in this work is 0.709, which is significantly higher than the R_o of 0.7064 in the Merensky footwall rocks (Kruger and Marsh, 1982). Using a D_{Sr} of 1.8 (Henderson, 1982), and an average content of 478ppm Sr in plagioclase separates from below the Merensky Reef (Kruger, 1982), the calculated Sr content of the pre-Main Zone magma is 266ppm. A similar calculation using the average Sr content of plagioclase separates from

the Main Zone (411ppm; this study) returns a noticeably lower strontium content of 228ppm in the Main Zone magma.

This implies that any potential contaminant must have had a relatively low Sr content, allied to a strontium isotopic initial ratio in excess of 0.709. The Rooiberg felsites and Rashoop granophyre that form the roof of the Complex both have relatively low Sr contents (180-190ppm in the felsites; Twist, 1985; 10-100ppm in the granophyre; Walraven, 1985). Sharpe (1985) quoted unpublished data which suggest that the Sr R_o of the Rooiberg felsites might be 0.708 or less. Walraven (1985) was unable to obtain a satisfactory isochron age on the granophyre, but estimated that the Sr R_{2050} should be of the order of 0.72±1. Although Sharpe's (1985) R_o data effectively exclude the Rooiberg felsites as a potential contaminant, Walraven's (1985) data indicate that the granophyre might have produced the observed changes in R_o and absolute Sr content in the Main Zone cumulates. Another possible source of **in situ** contamination is the Pretoria Group shales, which have Sr contents in the range 77-265ppm (Hunter and Hamilton, 1978). Calculations using data from Hunter and Hamilton (op. cit.) suggest that the R_{2050} of these shales is between 0.708 and 0.723.

Using the simple computer program in appendix eight, mixing exercises were performed using data from Kruger and Marsh (1982) and Kruger (1982) for the R_o and absolute Sr concentration in the original, unmixed magma. The exercise was performed assuming that the Bushveld granophyre is the contaminant, and that the maximum Sr content of 100ppm measured by Walraven (1985) is close to the true maximum Sr content of the granophyre. The results of the exercise (Table 12a) indicate that 35% to 40% contamination of the magma would be required to produce compositions approaching the estimated composition of the liquid from which the Main Zone crystallized. A similar calculation, using the median values of Hunter and Hamilton's (1978) data for the Pretoria Group shale (i.e. Sr R_o=0.7160; Sr=171ppm), also indicates of the order of 40% contamination of the magma (Table 12b).

Assuming that the composition of the pre-Merensky Reef magma was similar to that of Sharpe's (1985) U_1 liquid, and using the results of the isotope mixing exercise, the results of mixing 40% granophyre and shale, respectively, with the U_1 liquid were calculated. The results,

f	R_o(mix)	Sr(mix)
0.40	0.7113	166.4
0.45	0.7107	174.7
0.50	0.7101	183.0
0.55	0.7096	191.3
0.60	0.7091	199.6
0.65	0.7087	207.9
0.70	0.7083	216.2
0.75	0.7079	224.5

TABLE 12(a) : Calculations of variations in R_o and Sr concentration with changing proportions of magma and granophyre:
f=magma/(magma+granophyre).
Starting compositions are:
Magma: R_o=0.7064; Sr=266ppm
Granophyre: R_o=0.7200; Sr=100ppm

f	R_o(mix)	Sr(mix)
0.40	0.7111	209.0
0.45	0.7106	213.8
0.50	0.7102	218.5
0.55	0.7097	223.3
0.60	0.7093	228.0
0.65	0.7089	232.8
0.70	0.7085	237.5
0.75	0.7081	242.3

TABLE 12(b) Calculations of variations in R_o and Sr concentrations with changing proportions of magma and Pretoria Group shale:
f=magma/(magma+shale).
Starting compositions are:
Magma: R_o=0.7064; Sr=266ppm
Shale: R_o=0.7160; Sr=171ppm

displayed in Table 13, suggest that mixing of either shale or granophyre with the U liquid would produce a liquid composition most notable for its high silica and potassium concentrations, and low calcium content. Essentially, the resultant liquid would be quartz- and K-feldspar normative, and would crystallize relatively sodic plagioclase and very little clinopyroxene. In short, neither contaminated liquid in Table 13 approaches a composition, of the nature of Sharpe's (op. cit.) A liquid, that is capable of crystallizing Main Zone-type cumulates.

As indicated by Kruger and Marsh (1982), if contamination did, in fact, occur at the roof of the intrusion, transport of the contaminating Sr to the crystallization front at the base of the magma column implies whole-magma convection. The evidence in this study (Fig. 34) is that there are well-defined cyclic units in the Main Zone. Whether these cyclic units are the product of density- stratification of the magma, or of successive magma influxes, they are evidence against whole-magma convection on the required scale. Given these constraints, only the uppermost layer of the Rustenburg Layered Suite ought to have suffered significant contamination.

If Sharpe's (1985) model of the late-stage intrusion of the Main Zone magma into a density-stratified magma chamber is to be believed, there appears to be no mechanism, in any event, whereby the Main Zone magma could have been contaminated by the roof rocks without affecting the intervening Upper Zone liquid. Even if, as suggested by Kruger et al. (1986, in press), the Upper Zone does not represent an uplifted supernatant residual liquid, but was intruded as a new magma in its own right, one would expect to see evidence of contamination in the Upper Zone as well as the Main Zone. Kruger et al. present data which show that the entire Upper Zone has a remarkably consistent Sr R_o of the order of 0.7074, even to within a few metres of the roof rocks, where one would have anticipated the most extensive contamination. Apart from showing no direct signs of contamination, the Upper Zone cumulates have R_o substantially lower than the Main Zone. It appears strange that **in situ** contamination should selectively affect only the succession between the Merensky Reef and the Pyroxenite Marker, rather than the whole complex.

	U_1	A_1	Granophyre	Shale	Gran./U_1	Shale/U_1
SiO_2	55.48	49.92	74.09	59.90	62.92	58.63
TiO_2	0.28	0.35	0.39	0.60	.32	.42
Al_2O_3	10.48	16.37	11.64	17.30	10.94	13.61
Fe_2O_3	-	-	1.65	5.00	-	-
FeO	9.25	9.36	2.02	3.00	6.95	8.72
MnO	0.17	0.19	0.14	0.20	0.16	0.19
MgO	15.42	8.22	0.06	3.90	9.28	10.90
CaO	6.10	13.17	0.80	0.50	3.98	3.87
Na_2O	1.73	1.74	3.05	0.50	2.26	1.25
K_2O	0.76	0.11	5.07	3.90	2.48	2.11
P_2O_5	0.05	0.01	nd	0.14	0.03	0.09
LOI	-	-	0.81	5.48	-	-
TOTAL	99.72	99.44	99.72	100.42	99.32	99.79

TABLE 13

Compositional data for hypothetical U1 and A1 Bushveld parental magmas (Sharpe, 1985), and representative analyses of the Bushveld granophyre (Von Gruenewaldt, 1972) and the Pretoria Group shale (Visser, 1964). Analyses labeled Gran./U_1 and Shale/U_1 represent 60% mixtures of U1 with granophyre and shale, respectively.

On the basis of the available data, it seems unlikely that the high and variable Sr R_o in the Main Zone could have arisen from **in situ** contamination of the magma by the wallrocks. Instead, it appears likely that the different isotope ratios of successive magmas were generated at source, and that the complex R_o patterns observed in the Main Zone resulted mainly by periodic intrusion and mixing of parental magmas with different R_o.

Kruger and Marsh (1982) showed that the Sr R_o increases from 0.7064 in the footwall of the Merensky Reef to 0.7075 at the base of the Bastard Cyclic Unit at RPM Rustenburg Section. Data presented here indicate that R_o continues to increase in a more or less linear fashion to the top of Main Zone unit II, where sample A312 has an R_o of 0.70854 (Fig. 34). Kruger and Marsh suggested that the strontium R_o profile across the Merensky Cyclic Unit is due to infiltration metasomatism of the crystallization products of a high-R_o hybrid liquid by low-R_o postcumulus liquids from below. It seems unlikely, however, that infiltration metasomatism could have affected 200m to 300m of cumulus material. Data presented by Eales et al.(1986) show that, in the Upper Critical Zone of the Bushveld, each successive cyclic unit exhibits different narrow ranges of Sr/Al_2O_3 ratios, suggesting that each cycle is the product of a separate injection of magma. These data further suggest that infiltration of residual liquid residua from the top of one cyclic unit into the base of the next is not apparent in the geochemistry beyond approximately three metres. This evidence applies to the bases of the Merensky and Bastard Cyclic Units as well as the underlying cyclic units of the Upper Critical Zone. If the observed Sr R_o increase from the base of the Merensky Cyclic Unit to the top of Main Zone unit II (Fig. 34) were to be ascribed to one continuous infiltration metasomatism process, the decoupling of the Sr isotopic from the whole-rock geochemical data would have to be explained.

It is possible that the progressive increase in R_o from the Merensky Reef to the top of Main Zone unit II represents a process of continuous change in the magma at source. Each successive magma generated at source could have had a slightly higher R_o. Corresponding to the change in R_o, there would be a steady change in the bulk chemistry of the magma, from a composition typical of the Upper Critical Zone (possibly the U-type magma (Sharpe, 1985)), to a composition more

typical of the Main Zone (Sharpe's A-type magma). In this way, the gradation in geochemical and isotopic parameters in the lower part of the Main Zone would have been built up by successive influxes of progressively more plagioclase-rich, higher-R_o magmas. Density considerations would dictate that each successively more felsic magma would enter the chamber above its predecessor.

If, on the other hand, the entire succession from the Merensky Reef to the top of unit II is to be ascribed to a single influx of new, high-R_o magma, some mechanism other than infiltration metasomatism must be considered to explain the upward increase in R_o. Expanding on the work of Sparks et al. (1980) concerning the mixing of magmas of different densities, Campbell et al. (1983) related the fluid dynamics, and therefore mixing characteristics, of magmas in a magma chamber to density considerations. Campbell et al. pointed out that fractionation of the relatively dense ferromagnesian minerals (pyroxene and olivine) gives rise to successively lighter residual liquids. Fractionation of plagioclase, on the other hand, has the opposite effect, producing successively denser residual liquids. Sparks and Huppert (1984) coined the term "fractionation density" as a measure of the density of magmatic residua due to fractionation of different mineral species.

According to Campbell et al. (op. cit.), if new magma entering a magma chamber is lighter than the fractionated residual liquid in the chamber, the new magma will ascend as a turbulent plume, entraining host liquid as it rises. Entrainment within the plume results in the development of a hybrid layer where the plume begins to spread out at the top of the magma chamber. An important effect in the model proposed by Campbell et al. (1983) is that the larger the plume of new magma, the less efficient the mixing process, with the result that successively lighter magma reaches the top of the magma chamber. Light magma collecting at the top of the chamber rolls sideways, displacing heavier magma in its path. As a consequence, the chamber becomes stratified, with light, hot liquid overlying cooler, denser liquid.

Assuming that the new, high-R_o, Main Zone magma is lighter than the fractionated residual liquid in the chamber, the potential exists for pluming of the new magma. This will lead ultimately to stratification of the magma chamber, with each hybrid liquid layer having a

successively higher R_o. Crystallization from the stratified liquid column would then presumably give the R_o profile observed in the Merensky and Bastard Cyclic Units and lower part of the Main Zone (Fig. 34). The fundamental premise of this model is, of course, that the supernatant residual liquid in the chamber is denser than the new influx of magma. This is highly unlikely in terms of fractionation density of an Upper Critical Zone magma that has been crystallizing olivine, pyroxene, and even chromite. Even in the unlikely event that the new magma were, in fact, lighter than the residual liquid, this would probably only be so because the new magma would be relatively hot. The stratification of the liquid in the chamber after the postulated pluming event would therefore be highly unstable, and susceptible to convective overturn (Campbell et al., 1983).

A modification of the pluming model applies when intrusion occurs into a density-stratified magma chamber (Campbell et al., op. cit.). In this case, the new influx will rise to a level commensurate with neutral buoyancy in the stratified liquid column, and will then spread out laterally. This scenario is favoured by Eales et al. (1986) for the interval between the Merensky footwall and the Porphyritic Gabbro Marker. The high-R_o Main Zone magma, rising to its level of neutral buoyancy in the supernatant residual liquid in the chamber, would spread out at the approximate level of the Porphyritic Gabbro Marker. The new magma is likely to have been lighter than the underlying liquid only because it was hotter - ideal conditions for finger-type double-diffusive convection. The mixing of the residual liquid with the intromittent new magma would give rise to the Sr isotope and geochemical gradient observed between the base of the Main Zone and the Porphyritic Gabbro Marker. The breakdown of the existing liquid stratification of the magma chamber is a cornerstone of this latter model. In the pluming model, the preservation of the inherently unstable stratification of the liquid, due specifically to pluming, is vital to the interpretation of the observed geochemistry of the lower part of the Main Zone. The model of post-intrusive mixing, favoured by Eales et al. (op. cit.), is also preferred here.

There are distinct chemical differences between the Merensky and Bastard Cyclic Units, on one hand, and the lower part of the Main Zone on the other (Eales et al., 1986), which discount the likelihood that

the former units crystallized from the Main Zone magma or magmas, or hybridized equivalents thereof. Eales et al. overcame this problem by suggesting that the Merensky and Bastard Cyclic Units are the crystallization products of small influxes of hot, dense, relatively low-R_o mafic magma, intruded at the crystal/liquid interface after the intrusion and hybridization of the Main Zone magma. Decreasing fractionation density, due to crystallization of pyroxene and olivine from these mafic magmas, led ultimately to mixing with the overlying, relatively high-R_o hybrid liquid, giving the Sr R_o profiles observed by Kruger and Marsh (1982).

Above the Bastard Cyclic Unit, the rocks are predominantly norites and gabbronorites, in which plagioclase is the major cumulus phase. For this reason, the liquid would have become more dense with fractionation (Campbell et al., 1983), leading to stagnation (Morse, 1986). Crystallization from a stagnant liquid layer should yield predominantly orthocumulate rocks with a relatively high residual porosity (Campbell, 1987). Although the concentrations of incompatible components (K_2O, Zr, Rb, Ba) are slightly elevated in units I and II of the Main Zone (Fig. 23), the effect is not as marked as would be anticipated. This implies the operation of some secondary process or processes. Campbell (1987), in a review of the possible processes responsible for secondary adcumulus growth, pointed out that annealing, unlike filter-pressing (Irvine, 1980), or compositional convection in intercumulus liquid (Tait et al., 1984), operates independently of gravity, and can therefore explain low porosity in plagioclase-dominant cumulates. The process referred to by Campbell (op. cit.) as annealing, probably more appropriately termed sintering, has been appealed to by Kruger and Marsh (1985) to explain the expulsion of interstitial liquid from cumulates in the Upper Critical Zone. Circumstantial evidence for the late-stage expulsion of intercumulus liquid is the presence of discordant bodies of Fe-rich ultramafic pegmatite throughout the SK2 succession.

Within unit II of the Main Zone, the orthopyroxene Mg/(Mg+Fe) ratio <u>increases</u> from the base to the top of the unit (Fig. 34). Although data are somewhat sparse, there is no indication of a similar reversal of the apparent trend of fractionation in plagioclase compositions over this interval. There is a major concentration of Fe-rich ultramafic

pegmatite bodies in the lower part of unit II (Fig. 34). Sample A320 is a representative sample of one of these pegmatite bodies. The modal mineralogy of A320 is dominated by augite, with subordinate granular ilmenite and interstitial magnetite. Plagioclase and orthopyroxene within the sample are regarded as being of cumulus origin. Two microprobe analyses of plagioclase in A320 return compositions of $A_{64.5}$ and $An_{68.5}$, not sensibly different from the range in plagioclase compositions in the overlying cumulate sample A319 (Fig. 34). A comparison of the augite analyses from the respective samples, however, shows a range of MMF ratios between 0.642 and 0.693 in A320, whilst in A319 (the cumulate sample) the clinopyroxene MMF ratio ranges from 0.768 to 0.786. The implication is that the liquid from which the pegmatites crystallized was in chemical equilibrium with the cumulus plagioclase with which it came into contact, but was highly enriched in iron. Cumulus pyroxene with which the late-stage liquids came into contact would therefore re-equilibrate to more iron-rich compositions. Evidence of subsolidus compositional re-equilibration is the wide range in orthopyroxene compositions (MMF 0.654-0.681) displayed by cumulate sample A319 (Fig. 34). It is therefore suggested that the apparent reversed fractionation trend is, in fact, a secondary phenomenon, due to the subsolidus re-equilibration of the cumulates with iron-rich late-stage liquids in the lower reaches of the unit.

Across the boundary from unit II to unit III, there is a sharp increase in R_o, from 0.70854 in sample A312 to 0.70882 in sample A308. The orthopyroxene MMF and whole-rock Cr/Sc ratios, in particular, display discrete, well-defined trends in both units III and IV. Another particularly notable feature at the base of unit III is that there is a sharp change in the whole-rock Zr/Y ratio. In the Upper Critical Zone, from the UG1 up to the Bastard Reef, the Zr/Y ratio is more or less consistently of the order of 2 (Eales et al., 1986). Zr/Y ratios of the order of 2 continue into Main Zone units I and II, but there is a sharp change, to ratios generally less than 1.5, at the base of unit III. The decrease in the Zr/Y ratio is directly relatable to a sharp decrease in the concentration of Zr at the base of unit III (Fig. 23).

In contrast to the steady upward increase in Sr R_o through units I and II, units III and IV exhibit separate, distinct trends of upward decrease in R_o. The exception is sample A299 in unit III (Fig. 34),

which has an anomalously low R_o. The strontium initial ratio is particularly high (in excess of 0.7088) at the bases of both units III and IV, and the trend of upward decrease in R_o through both these units implies progressive mixing with an overlying low-R_o component. The upward decrease in such parameters as the orthopyroxene Mg/(Mg+Fe) ratio and the whole-rock Cr/Sc ratio (Fig. 34), on face value apparently fractionation effects, may also be explained by progressive mixing of a new magma with a relatively evolved superincumbent residual liquid.

In terms of the model proposed by Eales et al. (1986), the steady increase in R_o through units I and II is due to the hybridization of low-R_o residual liquid in the magma chamber with a new influx of high-R_o magma of the Main Zone lineage. This hybridization would have taken place by mixing through a finger-type convective system, after emplacement of the new magma at a level commensurate with neutral buoyancy in the liquid column. In an extension of the model proposed by Eales et al., it is postulated here that units III and IV represent relatively small influxes of high-R_o magma at the crystal-liquid interface, subsequent to partial crystallization of the hybrid liquid. Undercooling through the substantive crystalline floor of the magma chamber resulted in the preservation of the high R_o of the new magma in the initial products of crystallization, possibly in a stagnant boundary layer (Jaupart and Brandeis, 1986). Undercooling through the floor of the chamber is likely to have been only a transitory phenomenon, rapidly terminated by the "stove" effect of upwelling new, hot magma (Campbell, 1987). Unlike the closed system modelled by Jaupart and Brandeis, however, the upper, convecting layer of the new magma was open to the overlying supernatant residual liquid. Progressive mixing with the mixed R_o hybrid liquid at the upper surface produced the R_o profiles observed in units III and IV.

At the base of unit IV, there is a sharp change in virtually all geochemical and petrological parameters (Fig. 34). Notably, there is a sharp change to more magnesian orthopyroxene compositions, as well as an increase in the whole-rock Cr/Sc ratio. These changes are accompanied by sharply higher strontium isotope initial ratios, and a sudden increase in the proportion of augite in the rocks, as well as an increase in the clinopyroxene/(clinopyroxene+orthopyroxene) ratio.

There is also a distinct decrease in the proportion of modal plagioclase at the base of unit IV.

Unit IV is similar in many respects to the underlying unit III. The Sr R_o profile, for example, is similar in displaying a trend of upward decrease. There is also an overall upward decrease in the orthopyroxene Mg/(Mg+Fe) and whole-rock Cr/Sc ratios (Fig. 34). Closer inspection reveals that these latter two ratios do not display simple trends, however. The Cr/Sc ratio, for example, increases sharply from less than 22 below 430m, to 25 or more above. Above approximately 455m, the Cr/Sc ratio decreases dramatically to less than 16 in the upper reaches of unit IV. Below 430m, the orthopyroxene Mg/(Mg+Fe) ratio is relatively constant, in the region of 0.740, but there is a pronounced trend of upward iron enrichment in orthopyroxene above 430m in unit IV (Fig. 34). The iron-enrichment trend stops before the top of unit IV, and sample A255, near the top of the unit, contains orthopyroxene of significantly more magnesian composition than do the cumulates immediately below it (Fig. 34). Although microprobe data are not available for the overlying sample A254 (the uppermost sample in unit IV), the whole-rock chemical data suggest that A254 and A255 behave in a coherent fashion. It is therefore reasonable to assume that the orthopyroxene in sample A254 is similar to that in A255 in being enriched in magnesium.

The sharp changes in whole-rock and mineral compositions at the top of unit IV are associated with a decrease in the Sr isotope R_o of sample A254 (Fig. 34). Some significant parallels may be drawn between sample A254 and sample A299 (in the middle of unit III), both of which exhibit relatively low R_o. It is noticeable that samples A254 and A255, in common with A299, are relatively plagioclase-rich (Fig. 34), and that both samples also have relatively primitive whole-rock MMF and Cr/Sc ratios.

Both samples A254 and A255 and sample A299 may reflect crystallization of what Morse (1986) referred to as light rejected solute (LRS), in other words the relatively light residual liquid after crystallization of mafic minerals (specifically in the Upper Critical Zone), which is removed from the cumulate interface by convection currents. Such rejected solute will be rich in plagioclase, and should also contain a

small proportion of mafic components, the latter displaying fairly primitive MMF ratios if separated from early cumulates. If the light rejected solute does not mix readily with the liquid above the cumulate interface, but forms discrete layers or pods within it, crystallization of these layers would produce plagioclase-rich cumulates with relatively high MMF and Cr/Sc ratios, as observed in sample A299 and samples A254 and A255 (Fig. 34). In addition, if these layers of LRS are derivatives of pre-Merensky cumulates, they will have relatively low strontium initial ratios, also observed in samples A299 and A254. A problem with this concept is that small, discrete layers are unlikely to survive in any convecting magma.

The mechanism of flotation of buoyant early-crystallized plagioclase from the crystallization front (Eales et al., 1986), although differing in detail from the process outlined by Morse (op. cit.), would ultimately produce similar results. It is reasonable to assume that the floated plagioclase schlieren would entrap a certain proportion of relatively primitive mafic intercumulus liquid, with effects similar to those described above for the case of removal and subsequent crystallization of LRS. The advantage of the mechanism proposed by Eales et al. (op. cit.) is that partially solid schlieren are more likely to survive intact in a convecting magma than are bodies of liquid.

The early removal of plagioclase components from the crystallization front, either in the liquid state as light rejected solute (Morse, 1986), or in the crystalline state (Vermaak, 1976; Eales et al., 1986), can potentially explain the decoupling of plagioclase and orthopyroxene compositional trends through unit IV (Fig. 34). The early-formed plagioclase, removed to the top of the liquid layer either by convection or flotation, will be Ca-rich. Successively later-crystallizing generations of plagioclase reaching the top of the liquid layer will be increasingly albitic. In this way, the fractionation trend of plagioclase will be built up from the top of the liquid layer down, whilst fractionation of pyroxene will progress from the bottom up.

An adjunct to the model of upward flotation of early-formed plagioclase (Eales et al., 1986) is that successive influxes of new magma intruded

at the crystal/liquid interface will add continually to the population of plagioclase in the supernatant residual liquid. The implication is that the supernatant residual liquid will eventually crystallize anorthositic lithologies containing plagioclase of mixed parentage. If the original parent magmas had different isotopic signatures, this would be reflected in highly variable isotope ratios in the resultant anorthosites. This is the case in unit V (the Main Mottled Anorthosite), in which the strontium initial ratio is extremely variable (Fig. 34), the highest R_o being 0.70902, in sample A243. Sample A236, which has an exceptionally low R_o of 0.70737, is believed not to be a cumulate. Its extremely fine grain size (Fig. 13a) suggests that it could be a later sill- or dyke-like intrusive into the cumulates. If so, it may be regarded as an intrusive representative of the low-R_o magma intruded at the Pyroxenite Marker (Kruger et al., in press).

Above the Main Mottled Anorthosite, unit VI displays a striking trend of exponential increase in the V/Cr ratio (Fig. 34). This is accompanied by a progressive decrease in the Cr/Sc ratio. Although only three pyroxene analyses are available, the indications are that there is a progressive decrease in the orthopyroxene Mg/(Mg+Fe) ratio upwards through the unit. These trends all indicate uninterrupted Rayleigh fractionation through unit VI. No significant trends are apparent in the other parameters illustrated in Fig. 34. The V/Cr and Cr/Sc trends are notable in that they both appear to transgress the boundary between units VI and VII, on the evidence of the high V/Cr and low Cr/Sc ratios of sample A182, near the base of unit VII. The boundary between these two units is considered a real one, on the basis that the lower contact of unit VII is marked by a feldspathic pyroxenite layer (Fig. 34). From petrographic studies, sample A182 is clearly not a simple cumulate, as it contains coarse-grained diallage augite, as well as magnetite, suggesting a component of ultramafic pegmatite. The Sr R_o of A182 is anomalously low (Fig. 34), which further suggests that it is not a normal cumulate.

The anomalous chemistry and low R_o of sample A182 might be largely a function of the pegmatite component in the rock. There is a possibility that the ultramafic pegmatite bodies in SK2 may generally exhibit low strontium isotope initial ratios relative to their host

cumulates. This conjecture is still to be tested by Sr isotope analysis of a representative suite of pegmatite samples. The implication, however, is that the pegmatite liquids were not generated **in situ**, but migrated to their sites of crystallization from elsewhere in the cumulate succession. The Sr R_o data might be taken as an indication that the original source of at least some of the Main Zone ultramafic pegmatites may be in the low-R_o cumulates of the Critical Zone.

A completely different interpretation of the geochemical data for unit VII, and the one favoured here, is that there was a small influx of low-R_o, Upper Zone-type (Kruger et al., in press) magma at the base of the unit. The low R_o of sample A182, and the profile of upward increase in R_o through the basal part of unit VII, are taken to indicate the influx of a relatively dense, Fe-rich, low-R_o magma. Mixing at the upper surface of this magma batch with the high-R_o liquid in the chamber produced the observed R_o profile. The pegmatites are taken to represent the migration and accumulation of dense, Fe-rich rejected solute from this new batch of magma. Being relatively dense, this rejected solute will not rise, but rather sink, as crystallization progresses, explaining the concentration of pegmatites at the base of the unit. This model is more plausible than the one described earlier, in that it does not require migration of pegmatite liquids over vast distances.

Main Zone unit VII is characterized by numerous reversals in the pattern of variation of the V/Cr ratio (Fig. 34). The variation of the Cr/Sc ratio is effectively the reverse of the V/Cr trend, due largely to the fact that Cr, with its high bulk distribution coefficient, is the numerator in one ratio, and the denominator in the other. These variations could be ascribed to any one of a number of processes. One possibility to be considered is fractional crystallization within a stratified magma chamber, each reversal representing the base of a new liquid layer. The same effect could be produced by fractionation of successive influxes of new magma. Crystallization from a stratified liquid column, or from successive influxes of new magma, would be expected to produce a definite sawtooth pattern, with sharp reversals at the base of each liquid layer. A careful examination of the V/Cr and Cr/Sc variations in unit VII (Fig. 34), by contrast, reveals

smooth, sinuous trends, rather than the anticipated sharp, sawtooth pattern. The trends in these ratios are accompanied by variations in the concentration of incompatible elements, notably Zr, Rb and Ba (Fig. 23).

If the chemical variations in unit VII are not to be attributed to new influxes of magma, some internal mechanism must be found to account for them. Variations in the proportion of trapped intercumulus liquid in the rocks can produce chemical variations of the magnitude observed (Barnes, 1986). Apart from chemical effects, specifically in this case variations in iron-enrichment in pyroxenes, and in incompatible element concentrations, the proportion of intercumulus minerals such as clinopyroxene is an indication of the proportion of trapped intercumulus liquid in the rock.

Campbell (1987) suggested that the initial porosity of a rock is governed by a balance between nucleation and crystal growth at the crystal/liquid interface. High initial porosities develop when new crystals nucleate at the top of the crystal pile before a significant proportion of the intercumulus liquid has been expelled. If adjacent crystals at the top of the cumulate pile are able to continue growing , expelling intercumulus liquid in the process, low initial porosities, and therefore adcumulate textures, result. The development of adcumulate textures is aided by low melt viscosity, a low thermal gradient in the zone of crystallization, and vigorous convection in the magma chamber. Such secondary processes as expulsion of intercumulus liquid by compaction of the crystal pile (Irvine, 1980a) are regarded as unlikely by Campbell (1987) and by Morse (1986). Morse (op. cit.) and Sparks et al. (1985) emphasized the effects of convection in the formation of adcumulate textures.

Large variations in thermal gradient or melt viscosity are considered unlikely in the absence of new influxes of magma, but variable rates of magma convection during the solidification of unit VII might well have affected the proportion of trapped liquid in the rocks. Whatever the governing mechanism, variations in trapped liquid proportions offer a satisfactory solution to the problem of rapid compositional changes from primary hypersthene to inverted pigeonite over short distances, particularly in the lower parts of unit VII.

Where inverted pigeonite exists in close proximity to primary hypersthene, it occurs as small grains, often surrounded or partially surrounded by augite. The coexisting hypersthene occurs as larger grains with an intercumulus texture. Von Gruenewaldt and Weber-Diefenbach (1976) believed the pigeonite to have been a primocryst phase, which somehow managed to coexist with a more magnesian liquid. Subsequent to crystallization of the pigeonite primocrysts, reaction took place with the high-Mg liquid, resulting in an inversion to primary hypersthene. The small grains of pigeonite present in the rocks were regarded by von Gruenewaldt and Weber-Diefenbach as relict grains, which had somehow escaped the postulated reaction process. Subsolidus reaction of primary hypersthene with trapped dense, iron-rich intercumulus liquid offers a more plausible alternative to the model proposed by von Gruenewaldt and Weber-Diefenbach. The variability in the amount of trapped intercumulus liquid accounts for variations in the amount of inverted pigeonite in the rock.

One of the most conspicuous geochemical features of Main Zone unit VIII is the pronounced increase in the V/Cr ratio through the unit (Fig. 34), suggesting continuous Rayleigh fractionation. The strontium isotope initial ratio is remarkably constant in unit VIII, especially by comparison with the underlying unit VII, which suggests that the magma was well homogenized during crystallization of this unit. It is very likely, in fact, that unit VIII is simply a continuation of unit VII, the only difference between the two units being that the liquid was effectively homogenized by the beginning of unit VIII. Homogenization of the magma (or magma mixture) suggests vigorous convection. Convection, in its turn, is an aid to adcumulate growth (Sparks et al., 1985; Morse, 1986; Campbell, 1987), which is a process facilitating Rayleigh fractionation.

The fractionation of the magma in unit VIII was terminated by a major influx of low-R_o magma at the level of the Pyroxenite Marker (Kruger et al., in press). There is abundant evidence for this influx in Fig. 34, where virtually all petrological and geochemical indicators show a sudden reversion to markedly more primitive compositions. Sharpe (1985) regarded the succession above the Pyroxenite Marker as the uplifted residual liquid of the Upper Critical Zone, displaced by the emplacement of the large wedge of high-R_o magma from which the Main

Zone crystallized. The evidence of this study is that Sharpe's model is something of an oversimplification, and that the major new magma influx proposed by Kruger et al. provides a more satisfactory explanation of the evidence to hand. The differences between Sharpe's model and that proposed by Kruger et al. have been discussed in detail in chapter eight of the present work, and will not be repeated here.

An attempt has been made to model the V/Cr ratio variations through the Main Zone (Fig. 34) in terms of magma influxes, mixing and crystallization, using the computer program in appendix 9. The program models successive influxes of magma using Rayleigh fractionation, equilibrium crystallization or orthocumulate fractionation equations. Details of the formulae used are given in appendix 9, together with the input and output data from a series of experimental runs using the program. Distribution coefficient data are from Frey et al. (1978) and Cox et al. (1979), and the compositional data are loosely based on Sharpe's (1985) data for the A_1-type parental magma. These data have been used to plot the theoretical fractionation curves (dashed lines) in Fig. 33. In this diagram, F (the fraction of liquid remaining in the magma chamber)is equated to stratigraphic height, and analytical data have been included for comparison with the theoretical curves.

In Fig. 33, the succession from the top of the Bastard Reef to the postulated major influx of Main Zone (MZ) type magma (at approximately 300m) was modelled using Campbell's (1987) equation for orthocumulate fractionation, assuming 30% trapped intercumulus liquid. The succeeding interval, from 300 metres to 900 metres, was modelled by Rayleigh fractionation of a mixture of new magma with the residue of the pre-300 metre magma (Fig. 33). The initial impression is of a fairly good fit between the observed and theoretical curves in this interval. The change in the theoretical V/Cr ratio is, however, noticeably more gradual than that of the observed data in the uppermost part of the interval. This discrepancy may be ascribed to variable bulk distribution coefficients for Cr and V, particularly in the latter stages of fractionation. Alternatively, the proportion of trapped intercumulus liquid may increase as the magma becomes more viscous in the latter stages of fractionation (Campbell, 1987). Although data are presented for the interval above 900m (units VII and VIII), they are not considered representative, and it has not been possible to fit a

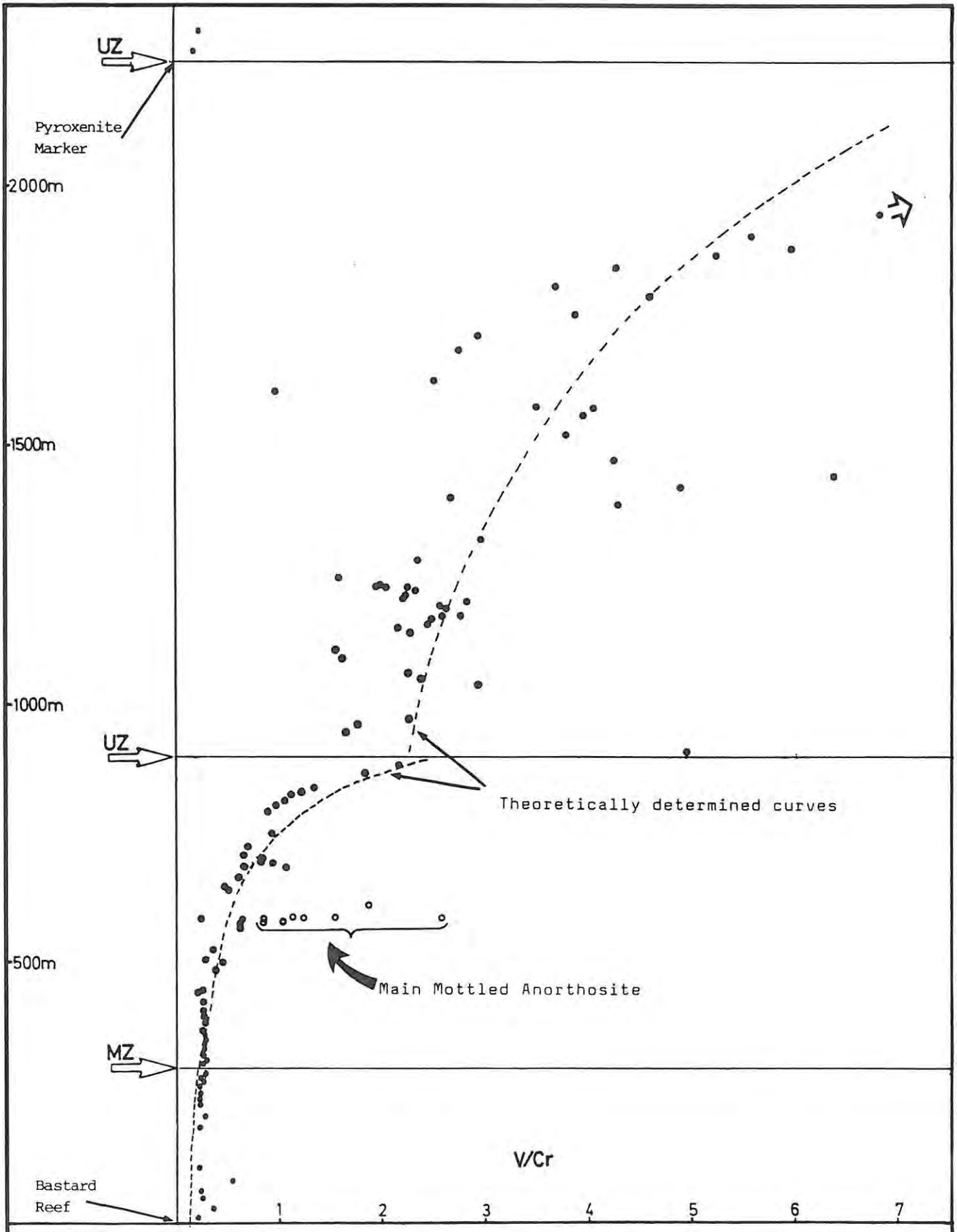

Fig. 33 : Diagram illustrating theoretical fractionation curves, calculated for the V/Cr ratio using the program MULTIFRACT. Observed V/Cr data are plotted for comparison. Arrows along the lefthand margin indicate postulated major magma influxes (MZ = Main Zone-type; UZ = Upper Zone-type).

satisfactory fractionation model to this part of the succession.

The overall impression from the fractional crystallization modelling exercise is that although Rayleigh fractionation may be an appropriate mechanism in parts of the Main Zone (notably unit VI), it is modified to varying degrees by other effects. In particular, the crystallization, with or without significant migration, of trapped late-stage intercumulus fluids is likely to be an important influence.

10. SUMMARY AND CONCLUSIONS

In this work, the Main Zone succession at RPM Union Section has been described primarily by reference to the deep surface exploration borehole SK2. Whilst borehole core has the advantage of providing a (hopefully) continuous stratigraphic section, it is limited in that the lateral continuity provided, for example, by surface outcrop, is not available. This limitation is a particularly significant factor in the case of SK2, in which there is an inordinately high concentration of Fe-rich ultramafic pegmatite bodies. This does not diminish the value of the study, however, because it is becoming increasingly apparent that the pegmatites are an integral, if late stage, part of the so-called Rustenburg Layered Suite. The limitation imposed is that SK2 cannot be regarded as a representative stratigraphic intersection of the Main Zone at Union Section.

Although Molyneux's (1970) threefold subdivision of the Main Zone, into subzones A, B and C, has become entrenched in the literature, it is submitted that this system is no longer valid. As discussed in chapter 7 of this thesis, subzones A and B are separated from one another on very tenuous grounds. Subzone C, on the other hand, is so distinct from subzones A and B, particularly in terms of its strontium isotopic signature, that it should not even be considered part of the same zone. It is proposed here that the Main Zone be redefined as the interval from the top of the Bastard Cyclic unit to the base of the Pyroxenite Marker. This means that the former subzone C of the Main Zone now becomes the lowermost subzone of the Upper Zone, with which it has strong isotopic affinities.

Rather than being divided into subzones A and B, as before, the interval defined in this work as the Main Zone has been subdivided into eight units. The geochemical attributes of at least some of these eight units may be attributable, at least in part, to the operation of (late-stage) processes peculiar to the SK2 succession. It is believed, however, that they form a basis from which further work on the Main Zone can proceed.

The lower two units of the Main Zone are characterized by a continuous upward increase in the strontium isotope initial ratio (Fig. 34). This is ascribed to the progressive mixing of the residual liquid of the

Upper Critical Zone with an overlying batch of relatively high-R_o, Main Zone-type magma (Eales et al., 1986). Alternatively, the Sr R_o gradient was produced by an ongoing process of influx and crystallization, with minor mixing, of successively higher-R_o magma throughout units I and II.

Units III and IV represent the influx and fractionation of successive batches of high-R_o magma, modified at their upper contacts by partial hybridization with the uplifted, relatively low-R_o residual liquid of earlier magmas. The base of unit IV, which contains the distinctive "Porphyritic Gabbro Marker", is marked by a significant increase in the modal proportion of clinopyroxene, accompanied by a decrease in modal plagioclase (Fig. 34).

Main Zone unit V is the interlayered sequence of gabbronorite and anorthosite that Molyneux (1970) named the Main Mottled Anorthosite. This unit is enigmatic, not only in respect of the Sr R_o data, but also in terms of its highly variable whole-rock and mineral chemistry (Fig. 34). This chemical variability is explained in terms of the model proposed by Eales et al. (1986), whereby the supernatant residual liquid in the magma chamber represents a hybrid of successive different magma influxes. By virtue of buoyancy considerations, this hybrid residual liquid will be charged with plagioclase crystals of different parentages. The crystallization of such a hybrid mixture of liquid and crystals could conceivably produce the geochemical variety found in the Main Mottled Anorthosite.

Within unit V, sample A236 is especially anomalous, being fine-grained, enriched in iron, and having a particularly low R_o (Fig. 34). These various attributes are ascribed to the rock being a later sill-like intrusion into the already solidified cumulates. If this assessment is correct, sample A236 may well be an intrusive equivalent of the low-R_o magma intruded in large quantities at the level of the Pyroxenite Marker (Kruger et al., 1986, in press).

Unit VI is notable for nothing so much as its striking trend of exponential increase in the V/Cr ratio(Fig. 34). An attempt has been made to model this trend by Rayleigh fractionation (Fig. 33). Although the fit between the observed and calculated curves is fairly good, the observed V/Cr ratio increases more rapidly than can be accounted for by

simple Rayleigh fractionation. A possible explanation for this is that as crystallization progresses, the magma becomes more viscous. As a result, increasing amounts of (relatively V-rich) intercumulus liquid are trapped in the cumulus network (Campbell, 1987).

The Sr R_o is particularly low in sample A182, at the base of unit VII, and increases progressively upwards through the lower part of the unit (Fig. 34). It is believed that this trend is due to a small influx of low-R_o magma with an Fe-rich tholeiite composition, similar to Sharpe's (1986) proposed B-type Bushveld parental magma. This is not a new concept, as Marais (1977) suggested that geochemical variations in the Main Zone below the Pyroxenite Marker represent the gradual addition of small amounts of new magma. The influx at the base of unit VII, which is regarded as a precursor to the massive influx of Fe-rich magma at the level of the Pyroxenite Marker, mixed progressively with the overlying, relatively high-R_o residual liquid to produce the observed Sr R_o trend (Fig. 34). The trend was enhanced by the sinking of relatively dense, Fe-rich, low-R_o intercumulus liquid (Morse, 1986) from the new magma, some of which ultimately accumulated to form the ultramafic pegmatite bodies that are concentrated at the base of unit VII. Attempts to model units VII and, in particular, unit VIII, as a body undergoing fractional crystallization were unsuccessful (Fig. 33). As in the case of unit VI, this does not necessarily mean that the model is inapplicable, but rather that the effects of fractionation were masked and modified by other effects, particularly variations in the proportion of trapped intercumulus liquid, and possibly also minor new influxes of magma.

Above unit VIII, the Pyroxenite Marker marks a major addition of relatively low-R_o, Fe-rich magma (Kruger et al., 1986, in press). The effects of this major influx of magma are evident in virtually all mineralogical and whole-rock geochemical parameters, including the strontium isotope initial ratio (Fig. 34). In concurrence with Kruger et al. (op. cit.), the Pyroxenite Marker is taken here to represent the base of the Upper Zone. Coertze (1974) regarded the major transgressions of the northern and southern "gap" areas that flank Union Section (Fig. 7) as evidence of a major influx of magma just below the stratigraphic level of the Main Magnetite Layer (i.e. at the base of the Upper Zone, as originally defined). These transgressions could, however, equally well be due to a tectonic adjustment in the

magma chamber, not necessarily associated with a magma influx.

The SK2 borehole succession is characterized in various places by concentrations of Fe-rich ultramafic pegmatite. As noted by Viljoen and Burvenich (1983) and Viljoen and Scoon (1985), the pegmatite bodies are very often associated with relatively anorthositic cumulates. The rejected solute from the crystallization of the anorthosite is likely to be relatively dense (Morse, 1986), and will therefore tend to pond near the base of the anorthositic source cumulates, possibly with some local migration and into structurally favourable sites, leading ultimately to the formation of the pegmatite bodies.

The present work, supported by evidence from the recent work of Sharp (1985, 1986) and Kruger et al. (1986, in press), suggests that the currently accepted threefold subdivision of the Main Zone (Molyneux, 1970, 1974; Von Gruenewaldt, 1971, 1973; SACS, 1980) is no longer tenable. In the first instance, the uppermost of the currently recognized subzones of the Main Zone (Subzone C) should be included in the Upper Zone, on isotopic grounds. The subdivision of what remains of the Main Zone into subzones A and B is also not supported by geochemical and isotopic data presented here.

The Main Zone, as recognized in this work, extends from the top of the Bastard Cyclic Unit to the base of the Pyroxenite Marker. This interval has been subdivided here into eight units, using various criteria (Table 6). These eight units should not be regarded as the definitive subdivision of the Main Zone, particularly since borehole SK2 is characterized by an unusual preponderance of late-stage, Fe-rich ultramafic pegmatite bodies. Detailed geochemical studies of the Main Zone in other parts of the Bushveld, preferably including areas undisturbed by pegmatite, are required for correlation and comparison with the present work.

The pegmatite bodies, which must be regarded as an integral, if late-stage, part of the overall cumulate succession, require some detailed study. Isotopic data on these bodies would be particularly useful, as these would facilitate genetic correlation of the pegmatites with their associated cumulate rocks.

APPENDIX I

Borehole log of surface exploration borehole S.K.2, Rustenburg Platinum Mines, Union Section.

BOREHOLE LOG OF SURFACE EXPLORATION BOREHOLE S.K.2, SPITZKOP 410 KQ

Height above Bastard Reef (metres)	Description of core	Sample Numbers
2010.15 - 1958.62	Medium - grained, foliated gabbronorite	A1 - A13
1958.62 - 1958.45	Two fesic bands within the gabbronorite	
1958.45 - 1914.35	Medium - grained gabbronorite, intruded by dolerite at 1920 and 1919m.	
1914.35 - 1906.24	Intimate mixture of mafic pegmatite and gabbronorite	A20, A21
1906.24 - 1896.69	Gabbronorite, intruded by a minor mafic pegmatite at 1903m. Gabbronorite becomes increasingly fractured and more leucocratic approaching the pegmatite at 1896.69m.	A22
1896.69 - 1892.31	Mafic Pegmatite	A23
1892.31 - 1889.51	Gabbronorite	A24
1889.51 - 1884.23	Intimate mixture of gabbronorite and mafic pegmatite	
1884.23 - 1875.65	Medium - grained gabbronorite, containing blebs of mafic pegmatite at 1878m. Gabbronorite becomes more leucocratic towards pegmatite at 1875.65m.	A25
1875.65 - 1875.20	Mafic pegmatite.	
1875.20 - 1851.61	Medium - grained, weakly foliated gabbronorite, sheared at intervals with associated minor alteration. Blebs of pegmatite occur at 1875.65m.	A26 - A28
1851.61 - 1851.35	Intrusive dolerite dyke.	
1851.35 - 1838.17	Medium -grained leucogabbronorite with sheared fragments of mafic pegmatite throughout.	A29
1838.17 - 1827.58	Sheared gabbronorite, intruded by four bodies of mafic pegmatite. (Sample A31 represents the pegmatite, A30 the gabbronorite.)	A30, A31
1827.58 - 1651.18	Weakly foliated, medium - grained gabbronorite with high - angle fractures throughout. Igneous lamination is apparent at 1795m. Below 1662m, plagioclase takes on a distinctive, pink colour. Gabbronorite becomes finer-grained approaching the pegmatite at 1651.18m.	A32 - A58
1651.18 - 1650.88	Mafic pegmatite. True thickness is only 80mm, but the pegmatite is in a steeply dipping (70°) shear zone.	A59
1650.88 - 1517.35	Medium-grained gabbronorite. Altered plagioclase gives the rock a white speckled appearance. Pegmatite (mafic) in high-angle shear zone at 1522.35m. High-angle fractures are present throughout.	A60 - A81
1517.35 - 1511.99	Fine-grained gabbronorite	A82
1511.99 - 1500.14	Medium-grained leucogabbronorite with high-angle fractures	A83, A84
1500.14 - 1498.48	Intrusive dolerite	A85, A86
1498.48 - 1496.94	Medium-grained gabbronorite.	
1496.94 - 1494.45	Intrusive Kimberlite	A87, A88
1494.45 - 1467.31	Medium-grained leucogabbronorite.	A89 - A93
1467.31 - 1466.39	Dolerite intrusive, preceded by three stringers in the hangingwall	A94
1466.39 - 1400.68	Medium-grained gabbro, with altered plagioclase giving a speckled appearance.	A95 - A106
1400.68 - 1398.80	Mafic Pegmatite.	A107
1398.80 - 1387.15	Medium-grained leucogabbronorite.	A108 - A110
1387.15 - 1368.95	Mafic pegmatite, intrusive as a series of bodies into gabbronorite. Sample A112 represents gabbronorite, A111 represents pegmatite.	A111, A112
1368.95 - 1354.73	Medium-grained gabbronorite	A113, A114
1354.73 - 1335.60	Mafic pegmatite. Gradational lower contact with gabbronorite.	A115
1335.60 - 1126.59	Medium-grained gabbronorite with felspathic banding 1236m to 1228m.	A116 - A151
1126.59 - 1125.86	Mafic pegmatite.	A152
1125.86 - 1092.15	Medium-grained gabbronorite, sheared and altered 1123 to 1116m.	A153 - A155
1092.15 - 1087.87	Mafic pegmatite.	A156

BOREHOLE LOG OF S.K.2 (contd.)

Height above Bastard Reef (metres)	Description of core	Sample Numbers
1087.87 - 1063.20	Medium-grained, foliated gabbronorite.	A157a - A158
1063.20 - 1061.45	Spotted leucogabbronorite with sheared upper and lower contacts. Alteration is extreme in the vicinity of the upper shear zone.	A159a
1061.45 - 1051.35	Medium-grained gabbronorite, fractured and altered in lower reaches.	A159
1051.35 - 1033.39	Spotted leucogabbronorite.	A160 - A162
1033.39 - 1021.89	Highly sheared mafic pegmatite with minor disseminated sulphides.	A163
1021.89 - 1010.88	Spotted leucogabbro, with plagioclase-rich zone at 1018m.	A164
1010.88 - 1010.77	Mafic pegmatite.	
1010.77 - 1006.10	Spotted leucogabbronorite, with minor mafic pegmatites at 1008 to 1009m.	
1006.10 - 1001.66	Mafic pegmatite, highly sheared and altered. Oxide and sulphide mineralisation concentrated at lower contact.	A165
1001.66 - 996.09	Sheared melagabbronorite with disseminated sulphides 1001.66 to 1001.00m.	
996.09 - 994.25	Sheared, spotted anorthosite, with a band of almost monomineralic anorthosite at 994.6m.	
994.25 - 992.05	Porphyritic gabbronorite, sheared at contact with underlying pegmatite.	
992.05 - 988.66	Mafic pegmatite, containing a large proportion of included gabbroic material. Interstitial magnetite abounds, and clinopyroxene crystals reach 50mm in length. Disseminated sulphide is a minor component.	A166
988.66 - 982.66	Medium-grained, porphyritic gabbronorite, increasingly melanic approaching underlying pegmatite.	A167
982.66 - 976.95	Brecciated mafic pegmatite/gabbronorite mixture with minor sulphides.	
976.95 - 950.62	Medium-grained, porphyritic gabbronorite with zone of pyroxene enrichment at 967.71m.	A168 - A171b
950.62 - 945.35	Mafic pegmatite, highly sheared, and interspersed with brecciated gabbro.	A172, A173
945.35 - 930.82	Leucogabbronorite with blebs of mafic pegmatite.	A174 - A176
930.82 - 924.63	Fine-grained gabbronorite, occasionally spotted with cumulus orthopyroxene.	A177 - A179
924.63 - 917.24	Spotted leucogabbronorite.	A180
917.24 - 914.35	Medium-grained gabbronorite with occasional interstitial magnetite. Lower contact sheared.	A181, A182
914.35 - 911.69	Medium to fine-grained leucogabbronorite.	A183
911.69 - 900.00	Mafic pegmatite with gabbroic inclusions.	A184 - A186
900.00 - 898.24	Leucogabbronorite with spots of pyroxene up to 20mm diameter.	A187
898.24 - 897.85	Intimate mixture of mafic pegmatite and leucogabbronorite.	
897.85 - 897.72	Fine-grained pyroxenite.	
897.72 - 897.20	Spotted leucogabbronorite, coarsening downward.	
897.20 - 896.79	Medium-grained gabbronorite.	
896.79 - 891.20	Highly sheared mixture of pegmatite and gabbronorite.	A188, A189
891.20 - 731.55	Medium-grained gabbronorite with pink feldspars.	A190 - A218
731.55 - 687.41	Spotted to mottled leucogabbronorite.	A219 - A226
687.41 - 678.25	Mafic pegmatite with large clinopyroxene crystals, especially near the sheared upper contact with leucogabbronorite. The pegmatite is itself intruded by dolerite between 678.82 and 678.52.	A227, A228
678.25 - 677.76	Medium-grained gabbronorite, increasingly fractured towards contact with the underlying pegmatite.	
677.76 - 677.35	Mafic pegmatite with highly sheared upper contact.	
677.35 - 677.06	Intrusive dolerite.	A229
677.06 - 670.04	Sheared and serpentinised gabbronorite containing minor pegmatites.	
670.04 - 667.60	Mottled anorthosite, with proportion of mottles decreasing downward.	A230, A231

BOREHOLE LOG OF S.K.2 (contd.)

Height above Bastard Reef (metres)	Description of core	Sample Numbers
667.60 - 666.39	Altered medium-grained gabbronorite with mafic pegmatite infilling in gash vein.	
666.39 - 662.73	Mafic pegmatite with inclusions of gabbronorite.	A232
662.73 - 640.55	Medium-grained leucogabbronorite with occasional felsic gash veins and minor pegmatites (mafic).	A233 - A235
640.55 - 625.64	Mafic pegmatite. Sulphides occur associated with shear zones	
625.64 - 616.92	Fine-grained, greyish gabbronorite, with shears and minor pegmatites at intervals.	A236
616.92 - 616.35	Mafic pegmatite.	
616.35 - 607.75	Fine-grained gabbronorite, with minor pegmatites in upper reaches.	
607.75 - 599.72	Mafic pegmatite with fairly substantial magnetite and minor sulphides. Inclusions of gabbronorite occur near the top of the body.	A237
599.72 - 596.60	Medium to coarse-grained, speckled leucogabbronorite	A238
596.60 - 591.03	Mottled leucogabbro, with monomineralic anorthosite 592.67 to 591.71m	A239 - A242
591.03 - 590.73	Magnetite-rich mafic pegmatite.	
590.73 - 578.66	Mottled leucogabbronorite, with size of mottles decreasing downwards. Alteration and brecciation of the leucogabbronorite occurs below the pegmatite at 590.73m.	A243 A248
578.66 - 577.35	Mafic pegmatite with sharp upper contact, sheared lower contact.	
577.35 - 567.96	Mottled leucogabbronorite, disturbed and altered under the influence of adjacent pegmatites. Contains minor disseminated sulphides, and blebs of pegmatite (mafic).	A249, A250
567.96 - 566.63	Mafic pegmatite, with inclusion of leucogabbronorite	
566.63 - 563.35	Spotted leucogabbronorite, altered at both pegmatite contacts. Sulphide stringers are present at the contact with the overlying pegmatite.	A251
563.35 - 557.05	Mafic pegmatite with sulphide and magnetite mineralisation. Sharp upper contact, gradational lower contact.	A252
557.05 - 540.07	Intimate mixture of mafic pegmatite and highly altered gabbronorite	
540.07 - 535.35	Felsic pegmatite with graphic texture and inclusions of amphibole. Both contacts are gradational.	A253
535.35 - 483.22	Medium-grained gabbronorite and leucogabbronorite, displaying igneous lamination.	A254 - A262
483.22 - 460.65	Mixture of mafic pegmatite, felsic pegmatite and gabbroic material.	A263
460.65 - 406.85	Medium-grained, unfoliated leucogabbronorite.	A264 A272
406.85 - 344.97	"Porphyritic norite marker", with large phenocrysts of bronzite in a gabbroic matrix. Grades into leucogabbronorite above and below.	A273 - A285
344.97 - 282.74	Medium grained, unfoliated leucogabbronorite.	A286 - A295
282.74 - 272.60	Pyroxenite with sheared upper contact.	A296 - A298
272.60 - 229.15	Pink tinted, medium-grained leucogabbronorite, grading upwards into a pure anorthosite, which does, however, contain large (10cm) blebs of pyroxenite.	A299 - A308
229.15 - 223.55	Coarse-grained pyroxenite, with sharp upper and lower contacts.	A309
223.55 - 162.85	Medium-grained leucogabbronorite, spotted below 198m. Minor mafic pegmatites at 197.5m and 176.3m.	A310 - A319
162.85 - 138.05	Fractured and altered mafic pegmatite. Lower contact gradational, upper contact sharp.	A320
138.05 - 129.52	Medium-grained porphyritic norite, grading downwards into a thin band of melanorite.	A321 - A324
129.52 - 125.45	Speckled norite	A325

BOREHOLE LOG OF S.K.2 (contd.)

Height above Bastard Reef (metres)	Description of core	Sample Numbers
125.45 - 124.55	Mafic pegmatite. Gradational upper contact.	
124.55 - 108.70	Medium-grained gabbronorite, but altered and highly variable near contact with overlying pegmatite, blebs of which are to be found in the gabbronorite.	A326 - A328
108.70 - 92.80	Speckled leuconorite, grading into mottled anorthosite closer to underlying pegmatite.	A329 - A333
92.80 - 92.45	Magnetite-rich pegmatite.	
92.45 - 49.70	Medium-grained, speckled leuconorite, grading upwards into mottled anorthosite closer to the overlying pegmatite.	A334 - A340
49.70 - 22.90	Coarse-grained, mottled leuconorite.	A341 - A344
22.90 - 13.60	Mottled anorthosite, grading into spotted/mottled anorthosite after 19.5m	A345 - A347
13.60 - 9.80	Magnetite-rich mafic pegmatite with minor sulphides. Sheared upper and lower contacts.	A348
9.80 - 0.00	Fine-grained, felspathic pyroxenite, becoming increasingly felspathic upwards. Very thin chromitite seam in broken core represents the base of the Bastard Reef.	A349
0.00 - -0.86	Mafic pegmatite with disseminated sulphides replaces the mottled anorthosite footwall of the Bastard Reef.	
-0.86 - -5.33	Spotted anorthosite, becoming increasingly pyroxenitic downwards.	
-5.33 - -6.17	Porphyritic felspathic pyroxenite, highly altered in lowermost 4cm.	
-6.17 - -6.21	Fine-grained chromitite with disseminated sulphides. Represents the base of the Pothole Merensky Reef.	
-6.21 - -7.32	Pegmatoidal felspathic pyroxenite with highly altered remnant olivines. Disseminated sulphides and magnetite stringers throughout. (Coarse Pseudo Reef?)	
-7.32 - -12.37	Porphyritic felspathic pyroxenite.	
-12.37 - -12.61	Brecciated remnant of U.G.2 chromitite in serpentinized pyroxenite.	

APPENDIX 2

List of all samples analyzed

Borehole SK2 : List of all samples analysed, including rock type and height above the Bastard Reef.

SAMPLE No.	Height	Rock Type
A1	2009.9m	Pigeonite gabbro
A5	1996.2m	Pigeonite gabbro
A10	1970.9m	Pigeonite gabbro
A13	1958.6m	Pigeonite gabbro
A15	1947.4m	Pigeonite gabbro
A18	1932.1m	Pigeonite gabbro
A20	1912.9m	Fe-rich ultramafic pegmatite
A22	1902.2m	Pigeonite gabbro
A25	1882.1m	Pigeonite gabbro
A27	1864.7m	Pigeonite gabbro
A29	1844.7m	Pigeonite gabbro
A31	1835.4m	Fe-rich ultramafic pegmatite
A35	1804.2m	Pigeonite gabbro
A38	1789.3m	Pigeonite gabbro
A43	1757.2m	Pigeonite gabbro
A48	1716.1m	Pigeonite gabbro
A52	1688.0m	Pigeonite gabbro
A59	1651.2m	Fe-rich ultramafic pegmatite
A63	1626.9m	Pigeonite gabbro
A65	1610.6m	Pigeonite gabbro
A71	1579.7m	Pigeonite gabbro
A72	1578.5m	Pigeonite gabbro
A74	1564.9m	Pigeonite gabbro
A79	1533.3m	Hypersthene gabbro
A91	1479.7m	Hypersthene gabbro
A100	1441.4m	Pigeonite gabbro
A103	1422.2m	Pigeonite gabbro
A106	1404.3m	Pigeonite gabbro
A107	1399.4m	Fe-rich ultramafic pegmatite
A108	1396.6m	Pigeonite gabbro (altered)
A110	1388.3m	Pigeonite gabbro with pegmatite blebs
A115	1349.5m	Fe-rich ultramafic pegmatite
A117	1323.9m	Hypersthene gabbro (altered)
A122	1284.9m	Hypersthene gabbro

SAMPLE No.	Height	Rock Type
A126	1248.7m	Hypersthene gabbro
A128	1238.5m	Hypersthene gabbro
A129	1235.5m	Pigeonite gabbro
A131b	1229.7m	Pigeonite leucogabbro
A132	1227.5m	Hypersthene gabbro
A133	1222.1m	Hypersthene gabbro
A139	1216.8m	Pigeonite gabbro
A140	1211.0m	Pigeonite gabbro
A141	1204.5m	Pigeonite gabbro
A142	1198.9m	Pigeonite gabbro
A143	1192.7m	Hypersthene gabbro
A145	1179.7m	Hypersthene leucogabbro
A146	1172.3m	Hypersthene gabbro
A147	1166.3m	Hypersthene gabbro
A134	1159.6m	Hypersthene gabbro
A148	1153.5m	Hypersthene gabbro
A149	1147.1m	Hypersthene gabbro
A152	1126.4m	Fe-rich ultramafic pegmatite
A135	1110.5m	Hypersthene gabbro (altered)
A155	1098.1m	Hypersthene gabbro
A137	1062.8m	Spotted pigeonite leuconorite
A159	1057.8m	Pigeonite gabbro
A161	1044.1m	Pigeonite gabbro
A163	1029.1m	Fe-rich ultramafic pegmatite
A165	1001.7m	Fe-rich ultramafic pegmatite
A166	991.3m	Fe-rich ultramafic pegmatite
A168	972.1m	Hypersthene gabbro
A138	966.4m	Hypersthene gabbro
A171	955.9m	Hypersthene gabbro
A172	948.1m	Fe-rich ultramafic pegmatite
A176	932.0m	Anorthosite with pegmatite blebs
A182	915.6m	Hypersthene gabbro with pegmatite blebs
A185	904.4m	Fe-rich ultramafic pegmatite
A191	886.3m	Hypersthene gabbro
A193	875.0m	Hypersthene gabbro
A198	845.5m	Hypersthene gabbro

SAMPLE No.	Height	Rock Type
A199	840.0m	Hypersthene gabbro
A200	833.1m	Hypersthene leucogabbro
A203	821.2m	Hypersthene gabbro
A204	812.5m	Hypersthene gabbro
A206	800.4m	Hypersthene gabbro
A208	787.2m	Hypersthene gabbro
A213	758.6m	Hypersthene gabbro
A217	735.8m	Hypersthene leucogabbro
A221	717.1m	Hypersthene gabbro
A222	712.1m	Hypersthene gabbro
A223	703.3m	Hypersthene gabbro
A224	699.5m	Hypersthene leucogabbro (altered)
A225	694.4m	Hypersthene leucogabbro (altered)
A226	691.5m	Hypersthene leucogabbro with biotite & mt.
A227	686.4m	Fe-rich ultramafic pegmatite
A230	669.5m	Leucogabbro with interstitial augite
A233	656.9m	Hypersthene gabbro
A235	646.1m	Hypersthene gabbro
A236	618.6m	Fine-grained hypersthene gabbro
A237	601.0m	Fe-rich ultramafic pegmatite
A238	598.1m	Pigeonite gabbro
A240	595.7m	Anorthosite with minor interstitial augite
A241	592.9m	Anorthosite with minor interstitial augite
A242	592.1m	Anorthosite with minor interstitial augite
A244	588.1m	Anorthosite with interstitial augite & biot
A245	584.6m	Leucogabbro (altered)
A243	584.2m	Leucogabbro (altered)
A246	581.3m	Leucogabbro (altered)
A247	580.9m	Hypersthene gabbro with minor biotite
A248	580.1m	Hypersthene gabbro with minor biotite
A249	574.2m	Anorthosite with minor interstitial augite
A252	562.5m	Fe-rich ultramafic pegmatite
A254	533.1m	Hypersthene gabbro
A255	528.1m	Hypersthene gabbro
A257	514.1m	Hypersthene melagabbro
A260	503.1m	Hypersthene gabbro
A261	495.3m	Hypersthene gabbro

SAMPLE No.	Height	Rock Type
A262	487.4m	Hypersthene gabbro
A264	454.7m	Hypersthene gabbro
A265	448.7m	Hypersthene gabbro
A266	442.2m	Hypersthene gabbro
A269	428.8m	Hypersthene gabbro
A271	413.6m	Hypersthene gabbro
A273	406.7m	Hypersthene gabbro
A274	405.9m	Spotted hypersthene leucogabbro with biotite
A275	398.6m	Porphyritic Gabbro Marker
A276	394.1m	Porphyritic Gabbro Marker
A278	387.5m	Porphyritic Gabbro Marker
A280	375.1m	Porphyritic Gabbro Marker
A281	370.1m	Porphyritic Gabbro Marker
A282	363.9m	Porphyritic Gabbro Marker
A283	357.8m	Porphyritic Gabbro Marker
A284	350.5m	Porphyritic Gabbro Marker
A285	345.8m	Porphyritic Gabbro Marker
A286	338.9m	Porphyritic Gabbro Marker
A287	332.3m	Hypersthene norite
A288	326.0m	Hypersthene norite
A289	319.6m	Hypersthene norite
A290	312.9m	Porphyritic hypersthene norite
A291	305.6m	Hypersthene norite
A292	299.2m	Hypersthene norite
A293	292.9m	Hypersthene norite
A294	285.8m	Hypersthene norite
A295	283.5m	Hypersthene norite
A297	275.8m	Hypersthenite
A298	274.1m	Hypersthenite
A299	270.4m	Porphyritic hypersthene norite
A300	266.7m	Porphyritic norite
A301	260.1m	Porphyritic norite
A303	252.9m	Hypersthene norite
A305	242.4m	Hypersthene norite
A308	235.5m	Hypersthene norite
A309	228.8m	Hypersthenite
A312	208.5m	Hypersthene norite

SAMPLE No.	Height	Rock Type
A315	188.5m	Hypersthene norite
A317	178.4m	Hypersthene norite
A319	165.5m	Hypersthene norite
A320	157.4m	Fe-rich ultramafic pegmatite
A322	134.2m	Pigeonite gabbro
A327	112.6m	Hypersthene norite
A334	86.0m	Hypersthene norite
A337	64.2m	Porphyritic leuconorite with biotite
A340	50.5m	Hypersthene norite
A343	29.4m	Pigeonite leuconorite
A346	18.2m	Leuconorite
A348	12.7m	Fe-rich ultramafic pegmatite
A349	5.7m	Hypersthene norite
A350	-2.5m	Porphyritic hypersthene leuconorite
A351	-4.3m	Porphyritic hypersthene leuconorite
A352	-5.6m	Felspathic pyroxenite

LIST OF ALL SAMPLES ANALYSED, INCLUDING ROCK TYPE AND HEIGHT ABOVE BASTARD REEF.

Borehole SK 4

Sample Number	*Height above Bastard Reef	Rock Type
B1	1234.5m	Hypersthene gabbronorite. Minor biotite & spinel.
B5	1226.8m	Hypersthene gabbronorite. Minor biotite & spinel.
B12	1209.2m	Pigeonite gabbronorite. Fine-grained.
B43	937.5m	Hypersthene gabbronorite.
B58	789.9m	Hypersthene leuconorite with large patches of augite.
B65	689.2m	Hypersthene gabbronorite. Deuterically altered.
B70	607.0m	Porphyritic hypersthene gabbronorite.
B86	445.0m	Porphyritic hypersthene leucogabbronorite.
B97	291.0m	Porphyritic hypersthene gabbronorite.
B100	201.9m	Highly altered gabbronorite.

Spitzkop 410 KQ

Sample Number	Height above Bastard Reef	Rock Type
SP1	930m	Coarse-grained hypersthene gabbronorite.
SP3	1060m	Coarse-grained porphyritic hypersthene gabbronorite.
SP5	1180m	Hypersthen gabbronorite.
SPK2	1910m	Pigeonite gabbronorite. Polygonised.
SPK6	1980m	Pigeonite gabbronorite. Polygonised.
MZ1	2240m	Pigeonite gabbronorite.
SP11	2270m	Pigeonite gabbronorite.
MZ2	2310m	Hypersthene gabbronorite.
MZ3	2350m	Hypersthene gabbronorite.
MZ4	2490m	Hypersthene gabbronorite.
MZ5	2530m	Hypersthene gabbronorite.
MZ6	2600m	Hypersthene gabbronorite.
MZ7	2690m	Hypersthene gabbronorite.

LIST OF ALL SAMPLES ANALYSED

11 Level 6[s] Crosscut

Sample Number	*Height above Bastard Reef	Rock Type
C1	415.30m	Hypersthene gabbronorite.
C8	369.00m	Hypersthene norite. Late intercumulus augite. Alterec
C12	339.50m	Hypersthene norite. Late intercumulus augite.
C19	294.55m	Coarse-grained hypersthene gabbronorite.
C24	255.73m	Coarse hypersthene gabbronorite. Hypersthene altered.
C25	248.72m	Hypersthene spotted leuconorite. Minor augite.
C30	212.70m	Hypersthene gabbronorite. Minor biotite.
C37	165.71m	Coarse porphyritic hypersthene leuconorite.
C41	139.41m	Coarse hypersthene gabbronorite.
C47	97.37m	Coarse hypersthene gabbronorite.
C50	75.45m	Hypersthene/pigeonite leucogabbronorite.Late augite.
C51	68.47m	Coarse porphyritic hypersthene leuconorite.
C53	53.25m	Coarse porphyritic hypersthene leuconorite.
C55	44.91m	Porphyritic hypersthene leuconorite.
C57	39.43m	Porphyritic hypersthene leuconorite.
C60	30.68m	Porphyritic hypersthene leuconorite.
C62	21.89m	Porphyritic hypersthene leuconorite.
C64	21.27m	Hypersthene norite. 5% spinel. Late-stage augite.
C66	12.72m	Hypersthene norite.
C67	9.06m	Hypersthene norite. Late-stage intercumulus augite.
C68	7.70m	Hypersthene melanorite.
C69	4.79m	Coarse hypersthene melanorite. 5% spinel.
C70	1.03m	Coarse hypersthenite. Minor interstitial augite.
C71	0.00m	Highly altered hypersthenite on sheared Bastard conta
C73	-10.30m	Anorthosite. Slightly sericitised.

* Heights above the Bastard Reef for Spitzkop and 11 Level samples are calculated assuming an average regional dip of 20°.

APPENDIX 3

X-RAY FLUORESCENCE ANALYSIS OF WHOLE-ROCK SAMPLES

Major and trace element analyses of whole-rock samples was done on a Philips PW1410 semi-automatic X-ray fluorescence spectrometer, employing the batch-processing system in general use at Rhodes University (Marsh, 1979). The machine was calibrated using a variety of international and internal (Rhodes) standards.

Major elements, excluding Na, were analysed on fusion discs, prepared by the method of Norrish and Hutton (1969). Sodium was analyzed separately on pressed powder bricquettes, as were all the trace elements.

Full corrections were made for instrumental drift, dead-time, background, tube and spectral line interferences. Mass absorption coefficients (MACs) were calculated from major element data using Heinrich's (1966) values. Where major element data were not available, MACs were calculated by the Mo-Compton method (Reynolds, 1967; Nesbitt et al., 1976). Typical L.L.D. (lower limit of detection) and C.E (counting error) data for Main Zone cumulus rocks are listed below. These values are based on counting statistics, and often differ substantially from those qouted, particularly in the case of Fe-rich ultramafic pegmatite samples. Typical running conditions for the XRF are listed in Table A (overleaf).

Element	L.L.D.	C.E.
Ba	13.0	4.6
Rb	0.8	0.2
Sr	0.6	0.3
Nb	0.6	0.2
Y	0.6	0.2
Zr	0.5	0.2
Co	2.4	0.6
Cr	2.5	0.9
V	3.5	1.0
Sc	1.1	0.3
Zn	0.5	0.4
Cu	0.5	0.2
Ni	0.8	0.4

TABLE A : X-RAY FLUORESCENCE ANALYTICAL CONDITIONS

Element	Emission line	Tube	kV	mA	Crystal	Time (secs)	Counter	Collimator	Specimen
Si	Kα	Cr	55	40	PET	40	flow	coarse	fusion disc
Ti	Kα	Cr	55	40	LiF(200)	10	flow	fine	fusion disc
Al	Kα	Cr	55	40	PET	40	flow	coarse	fusion disc
Fe	Kα	Cr	55	40	LiF(200)	20	flow	fine	fusion disc
Mn	Kα	Cr	55	40	LiF(200)	20	flow	coarse	fusion disc
Mg	Kα	Cr	55	40	TLAP	200	flow	fine	fusion disc
Ca	Kα	Cr	55	40	LiF(200)	10	flow	fine	fusion disc
Na	Kα	Cr	55	40	TLAP	100	flow	fine	powder pellet
K	Kα	Cr	55	40	LiF(200)	10	flow	fine	fusion disc
P	Kα	Cr	55	40	Ge	20	flow	coarse	fusion disc
Sr	Kα	W	55	40	LiF(220)	200	scint.	fine	powder pellet
Rb	Kα	W	55	40	LiF(220)	200	scint.	fine	powder pellet
Zr	Kα	W	55	40	LiF(220)	200	scint.	fine	powder pellet
Y	Kα	W	55	40	LiF(220)	200	scint.	fine	powder pellet
Nb	Kα	W	55	40	LiF(220)	200	scint.	fine	powder pellet
Co	Kα	W	55	40	LiF(220)	200	flow	fine	powder pellet
Cr	Kα	W	55	40	LiF(220)	200	flow	fine	powder pellet
V	Kα	W	55	40	LiF(220)	200	flow	fine	powder pellet
Zn	Kα	Mo	55	40	LiF(220)	200	flow+scint.	fine	powder pellet
Cu	Kα	Mo	55	40	LiF(220)	200	flow+scint.	fine	powder pellet
Ni	Kα	Mo	55	40	LiF(220)	200	flow+scint.	fine	powder pellet

APPENDIX 4

Major element analyses, inclusive of LOI and H_2O^-

SAMPLE	SiO2	TiO2	Al2O3	Fe2O3	MnO	MgO	CaO	Na2O	K2O	P2O5	LOI	H2O-	TOTAL
A-1	52.87	0.13	19.63	7.10	0.14	5.74	12.04	2.89	0.19	0.01	0.06	0.05	100.85
A-5	52.30	0.14	17.99	7.54	0.15	6.67	12.19	2.61	0.17	0.00	0.07	0.05	99.88
A-10	52.89	0.16	17.07	8.69	0.16	7.53	11.75	2.55	0.17	0.01	0.10	0.04	101.12
A-13	52.89	0.15	17.78	8.54	0.16	7.33	11.15	2.60	0.17	0.02	0.05	0.06	100.90
A-15	52.74	0.14	19.29	7.05	0.14	5.78	11.74	2.84	0.20	0.02	0.12	0.04	100.10
A-18	50.57	0.23	18.34	7.69	0.04	7.13	12.53	2.62	0.19	0.00	0.06	0.04	99.44
A-20	47.29	0.98	11.56	21.92	0.26	4.72	12.52	2.24	0.22	0.31	+1.09	0.38	101.31
A-22	50.87	0.29	17.18	11.33	0.10	5.90	10.54	2.79	0.20	0.11	0.21	0.60	100.12
A-25	53.01	0.14	18.50	7.06	0.14	6.42	12.40	2.78	0.20	0.01	0.07	0.03	100.76
A-27	52.74	0.16	16.44	8.80	0.17	7.99	11.89	2.46	0.16	0.01	0.16	0.04	101.02
A-29	51.76	0.21	17.91	7.94	0.10	7.18	11.87	2.72	0.24	0.01	0.08	0.03	100.05
A-31	42.15	3.17	6.72	28.47	0.39	5.25	13.03	1.46	0.13	0.17	+1.14	0.03	99.83
A-35	53.02	0.09	20.56	7.22	0.14	6.21	10.39	2.86	0.18	0.01	0.12	0.02	100.82
A-38	52.79	0.12	17.26	8.25	0.15	7.72	12.12	2.36	0.12	0.02	0.08	0.03	101.02
A-48	52.21	0.14	17.11	8.21	0.15	7.76	11.81	2.47	0.18	0.01	0.03	0.06	100.14
A-52	52.86	0.12	17.03	8.43	0.16	8.12	11.52	2.40	0.13	0.01	0.05	0.05	100.88
A-63	51.57	0.14	17.33	8.08	0.16	7.76	11.06	2.39	0.23	0.01	0.16	0.07	98.96
A-72	52.82	0.13	19.14	6.92	0.14	7.05	11.56	2.66	0.21	0.01	0.06	0.03	100.73
A-79	52.03	0.16	16.84	7.53	0.14	7.84	12.12	2.34	0.20	0.01	0.04	0.03	99.28
A-91	52.62	0.13	18.24	7.97	0.15	8.27	9.87	2.42	0.21	0.01	0.12	0.04	100.05
A-100	52.55	0.16	17.92	6.63	0.13	7.62	13.36	2.39	0.19	0.00	0.11	0.04	101.10
A-106	52.39	0.18	21.83	4.82	0.03	4.96	13.29	2.66	0.28	0.01	0.08	0.02	100.55
A-107	39.45	0.67	11.79	30.31	0.38	5.75	8.29	2.07	0.22	2.28	+1.23	0.04	100.02
A-108	51.96	0.15	20.48	5.53	0.05	6.14	12.91	2.46	0.20	0.01	0.13	0.04	100.06
A-110	51.71	0.17	18.11	6.95	0.07	7.55	12.58	2.09	0.26	0.01	0.18	0.05	99.73
A-115	41.22	1.65	12.12	27.08	0.33	4.99	10.96	2.09	0.18	2.16	+1.15	0.03	101.66
A-117	52.22	0.16	17.30	7.76	0.08	8.55	12.48	1.98	0.18	0.01	0.20	0.03	100.95
A-122	51.06	0.14	16.82	7.65	0.15	8.61	11.74	2.03	0.18	0.00	0.06	0.04	98.48
A-133	52.15	0.14	17.07	7.24	0.14	8.58	12.46	2.19	0.16	0.00	0.06	0.04	100.23
A-146	51.61	0.14	17.31	6.95	0.14	8.27	12.20	2.24	0.17	0.00	0.10	0.03	99.16

SAMPLE	SiO2	TiO2	Al2O3	Fe2O3	MnO	MgO	CaO	Na2O	K2O	P2O5	LOI	H2O-	TOTAL
A-152	49.51	0.58	15.51	15.01	0.23	4.02	13.14	2.98	0.21	1.19	+0.29	0.07	102.16
A-155	51.46	0.14	16.68	7.49	0.15	8.91	12.29	2.11	0.14	0.00	0.07	0.02	99.46
A-163	46.57	1.35	2.27	23.84	0.28	12.54	15.13	0.21	0.00	0.01	+1.53	0.01	100.68
A-165	42.65	2.23	12.32	24.29	0.22	6.14	12.08	1.87	0.12	0.01	+1.61	0.00	100.32
A-166	50.99	0.39	19.34	7.64	0.11	4.63	13.35	2.82	0.29	0.00	0.20	0.05	99.81
A-168	51.83	0.13	17.97	6.54	0.13	8.67	13.35	1.99	0.13	0.00	0.10	0.05	100.89
A-172	41.68	3.26	11.74	23.83	0.25	7.23	11.93	1.66	0.10	0.01	+0.68	0.03	101.04
A-185	46.26	1.62	13.41	15.58	0.20	6.48	13.53	2.26	0.13	0.01	+0.45	0.04	99.07
A-193	51.97	0.13	20.62	5.69	0.11	6.71	12.72	2.37	0.21	0.01	0.02	0.06	100.62
A-198	50.78	0.12	19.91	4.90	0.10	6.46	13.82	2.18	0.17	0.01	0.01	0.04	98.50
A-208	52.48	0.19	15.74	7.28	0.14	10.24	12.75	1.75	0.23	0.02	0.05	0.03	100.90
A-213	53.04	0.18	17.97	6.25	0.13	8.34	13.72	1.98	0.26	0.01	0.10	0.03	102.01
A-221	51.42	0.16	18.03	6.64	0.13	9.12	11.59	1.91	0.20	0.00	0.12	0.02	99.34
A-222	51.21	0.19	23.98	3.73	0.04	4.49	13.26	2.39	0.33	0.01	0.06	0.04	99.73
A-224	51.76	0.17	25.97	3.23	0.02	2.56	12.72	2.41	0.54	0.02	0.11	0.04	99.55
A-226	49.56	0.21	26.78	3.35	0.00	2.31	14.05	2.41	0.24	0.02	0.18	0.05	99.16
A-227	46.62	1.87	13.59	16.18	0.18	6.24	13.61	1.41	0.23	0.05	+0.53	0.04	99.49
A-230	50.35	0.10	26.86	2.55	0.00	2.88	13.85	2.37	0.37	0.01	0.12	0.03	99.49
A-233	52.19	0.18	17.09	6.42	0.09	9.37	12.36	1.86	0.36	0.02	0.09	0.03	100.06
A-241	51.24	0.09	27.94	2.57	0.01	2.04	13.20	2.84	0.32	0.00	0.07	0.02	100.34
A-243	51.56	0.14	26.33	3.42	0.03	3.06	13.45	2.59	0.36	0.02	0.08	0.04	101.08
A-246	52.13	0.17	29.31	1.22	0.00	0.88	13.43	2.61	0.88	0.01	0.13	0.04	100.81
A-252	24.47	6.61	3.03	51.45	0.33	6.37	8.36	0.23	0.01	0.00	+1.83	0.02	99.05
A-254	51.22	0.17	17.45	7.24	0.11	10.24	11.65	1.59	0.20	0.01	0.03	0.03	99.94
A-255	51.92	0.14	18.68	6.36	0.11	8.91	12.40	1.92	0.14	0.00	0.08	0.03	100.69
A-257	50.62	0.20	13.51	9.58	0.19	11.31	11.63	1.54	0.10	0.00	0.05	0.04	98.77
A-264	51.25	0.18	18.31	6.09	0.10	8.83	12.52	1.96	0.18	0.01	0.07	0.04	99.54
A-266	51.86	0.14	16.91	7.16	0.13	10.14	11.53	1.91	0.15	0.00	0.06	0.05	100.04
A-275	52.41	0.13	17.28	6.78	0.13	10.38	11.67	1.89	0.16	0.00	0.04	0.03	100.90
A-280	51.04	0.19	17.61	5.73	0.09	9.04	13.25	1.78	0.18	0.00	0.04	0.04	98.99

SAMPLE	SiO2	TiO2	Al2O3	Fe2O3	MnO	MgO	CaO	Na2O	K2O	P2O5	LOI	H2O-	TOTAL
A-284	51.09	0.12	18.31	5.44	0.11	8.07	13.63	2.05	0.13	0.00	0.05	0.02	99.02
A-295	52.17	0.13	20.01	6.26	0.09	8.71	11.02	2.33	0.19	0.01	0.08	0.02	101.02
A-297	54.16	0.23	2.29	16.85	0.28	24.07	3.34	0.31	0.02	0.00	0.07	0.03	101.65
A-299	50.34	0.05	27.37	2.69	0.00	3.94	13.19	2.52	0.14	0.01	0.10	0.01	100.36
A-301	51.68	0.11	18.45	6.95	0.12	9.99	10.41	1.95	0.15	0.00	0.09	0.03	99.93
A-312	51.69	0.14	21.38	5.35	0.11	6.83	11.41	2.25	0.27	0.01	0.09	0.02	99.55
A-315	51.79	0.12	22.04	5.41	0.02	7.45	11.31	2.10	0.23	0.00	0.12	0.02	100.61
A-320	47.96	1.16	4.35	18.12	0.20	12.98	15.55	0.39	0.03	0.01	+0.62	0.10	100.23
A-327	51.75	0.11	23.34	4.25	0.07	5.66	12.25	2.35	0.26	0.00	0.07	0.02	100.13
A-346	50.11	0.09	27.48	2.93	0.05	3.18	14.03	2.21	0.19	0.00	0.11	0.01	100.39
A-348	26.29	7.94	1.99	47.56	0.37	10.91	6.29	0.08	0.00	0.00	+2.44	0.01	99.00
A-349	51.58	0.11	16.44	7.25	0.11	15.17	8.80	1.14	0.07	0.00	0.13	0.01	100.81
C-1	50.87	0.10	21.42	5.40	0.07	8.93	11.21	2.35	0.17	0.00	0.14	0.01	100.67
C-19	53.28	0.19	21.26	5.81	0.07	7.43	11.18	2.47	0.36	0.00	0.10	0.02	102.17
C-47	51.34	0.20	20.96	6.32	0.07	7.67	11.24	2.13	0.34	0.03	0.10	0.02	100.42
C-60	48.85	0.07	29.17	1.89	0.00	2.92	14.38	2.31	0.19	0.00	0.17	0.02	99.97
MZ-1	52.91	0.17	18.34	7.91	0.14	6.67	12.07	2.78	0.25	0.02	0.07	0.00	101.33
MZ-2	52.29	0.15	19.07	6.23	0.12	8.17	13.74	1.95	0.15	0.01	0.05	0.29	102.22
MZ-3	52.41	0.17	15.55	7.48	0.13	10.13	14.31	1.74	0.12	0.02	0.05	0.06	102.17
MZ-4	51.83	0.16	18.64	6.52	0.13	8.95	14.13	1.69	0.13	0.02	0.05	0.26	102.51
MZ-5	51.76	0.15	16.58	6.98	0.14	10.26	13.35	1.42	0.14	0.01	0.07	0.91	101.77
MZ-6	52.11	0.16	16.94	7.23	0.14	10.19	13.33	1.58	0.13	0.02	0.05	0.20	102.08
MZ-7	52.26	0.17	16.49	7.91	0.15	10.26	12.58	1.72	0.14	0.02	0.04	0.13	101.87
A-35plag	53.33	0.04	29.55	0.63	0.00	0.24	12.17	3.81	0.29	0.00	0.18	0.00	100.24
A-108plag	52.74	0.04	30.54	0.39	0.00	0.29	12.64	3.73	0.32	0.00	0.23	0.04	100.96
A-155plag	51.43	0.12	30.72	0.32	0.00	0.28	13.30	3.59	0.28	0.00	0.12	0.04	100.20
A-280plag	51.71	0.04	30.98	0.52	0.00	0.52	13.96	3.21	0.29	0.00	0.17	0.04	101.44
A-312plag	51.38	0.03	30.96	0.35	0.00	0.20	13.42	3.38	0.31	0.00	0.07	0.02	100.12
C-1plag	50.09	0.04	30.84	0.43	0.00	0.26	13.62	3.04	0.29	0.01	0.20	0.00	98.82

APPENDIX 5

Modal Analyses

Modal analyses were done using a Swift automatic point counter and electro-mechanical stage. Mineral proportions are calculated as percentages, and each analyis is based on between 600 and 800 points.

MODAL MINERALOGY

Sample No.	Plag	Opx	Cpx	Spinel	Other
MZ7	52.7	32.1	15.2	0.0	0.0
MZ5	52.1	29.4	18.3	0.0	0.3
MZ3	49.7	27.1	23.2	0.0	0.0
SP11	59.0	36.4	3.4	0.3	0.8
MZ1	60.4	24.9	14.7	0.0	0.0
A1	65.4	24.4	10.2	0.0	0.0
A13	65.2	27.4	7.4	0.0	0.0
A27	59.5	30.6	9.9	0.0	0.0
A35	70.7	27.5	1.9	0.0	0.0
A38	57.5	28.6	13.9	0.0	0.0
A48	58.2	30.2	11.7	0.0	0.0
A52	60.9	30.5	8.6	0.0	0.0
A63	54.7	33.9	10.8	0.0	0.6
A79	54.1	23.1	21.9	0.0	0.9
A91	56.7	39.2	3.9	0.0	0.2
A106	69.6	9.4	19.6	0.0	1.5
A117	59.6	24.8	13.6	0.0	1.9
A133	56.1	25.5	18.2	0.0	0.2
A146	56.0	32.1	11.8	0.0	0.2
A149	64.4	24.2	10.7	0.0	0.7
A155	53.7	26.6	19.7	0.0	0.0
A137	80.2	7.0	11.8	0.0	1.0
A159	74.8	12.7	11.8	0.4	0.2
A161	77.5	5.4	14.0	0.0	3.0
A168	54.2	25.7	20.0	0.0	0.2
A171	61.6	21.8	13.4	0.0	3.2
A191	65.9	28.5	5.4	0.0	0.2
A193	75.1	6.5	17.9	0.0	0.5
A198	69.4	19.5	11.1	0.0	0.0
A199	54.6	21.0	24.4	0.0	0.0
A200	82.7	3.2	14.1	0.0	0.0
A203	68.1	6.0	25.7	0.0	0.2
A204	73.9	11.2	14.7	0.0	0.2
A206	66.3	15.7	17.8	0.0	0.2
A208	48.6	27.3	23.7	0.0	0.4
A213	55.0	18.6	26.2	0.0	0.2

Sample No.	Plag	Opx	Cpx	Spinel	Other
A217	72.8	15.7	10.2	0.0	1.3
A221	50.7	36.7	12.5	0.0	0.2
A226	93.5	2.9	2.2	0.2	1.2
A230	89.0	4.8	2.5	0.0	3.7
A236	47.9	32.9	19.0	0.3	0.0
A242	94.3	0.0	1.1	0.5	4.1
A245	77.1	6.6	13.9	0.0	2.4
A246	87.7	0.6	1.5	0.0	10.3
A248	84.7	11.4	1.7	0.0	2.2
A249	92.3	0.0	0.2	0.3	7.1
A254	54.6	28.3	15.6	0.0	1.5
A255	56.1	32.3	11.4	0.0	0.2
A257	36.6	42.2	21.1	0.0	0.1
A260	46.0	37.0	16.7	0.3	0.0
A264	60.6	25.8	13.5	0.0	0.1
A266	56.7	23.8	18.7	0.0	0.8
A275	55.5	24.6	19.5	0.0	0.4
A280	59.0	28.1	8.9	0.0	4.0
A284	56.9	16.4	26.5	0.0	0.1
A285	62.3	20.8	16.9	0.0	0.0
A286	53.2	23.5	23.2	0.0	0.0
A287	55.3	34.0	10.7	0.0	0.0
A288	59.3	30.0	10.8	0.0	0.0
A289	69.4	23.1	7.3	0.0	0.2
A290	66.6	25.6	7.8	0.0	0.0
A291	64.6	26.8	8.4	0.0	0.1
A292	70.2	23.1	6.7	0.0	0.0
A295	66.0	27.4	6.4	0.0	0.0
A297	3.6	90.7	4.6	0.0	1.4
A300	68.6	22.7	8.3	0.0	0.4
A301	58.6	35.3	6.0	0.0	0.1
A303	68.6	25.8	5.4	0.0	0.2
A305	66.3	29.1	4.3	0.0	0.3
A308	71.9	23.8	4.3	0.0	0.0
A309	12.8	84.7	2.3	0.2	0.0
A312	67.1	20.2	11.1	0.1	1.5
A315	74.3	23.8	1.6	0.0	0.3
A327	74.4	18.0	7.1	0.0	0.6

Sample No.	Plag	Opx	Cpx	Spinel	Other
A334	79.2	13.6	6.7	0.2	0.3
A337	63.6	29.8	3.7	0.1	2.8
A340	67.2	21.7	9.4	0.0	1.6
A346	82.6	11.7	4.6	0.1	1.0
A349	49.5	46.1	3.9	0.2	0.3

APPENDIX 6

Electron Microprobe Analyses

Mineral analyses were executed on a Cambridge Instruments Microscan V Electron Microprobe utilizing wavelength-dispersive spectrometers. Data collection and reduction was done on an on-line microcomputer, using the Bence-Albee reduction routine (Bence and Albee, 1968). Specimen current was set at 30nA, and the accelerating potential at 20kV.

APPENDIX 7

Electron Probe Analyses of Minerals

ORTHOPYROXENE ANALYSES AND STRUCTURAL FORMULAE BASED ON SIX OXYGENS

	MZ7/1	MZ7/2	MZ4/1	MZ4/2	MZ4/3	MZ2/1	MZ2/2	MZ2/3	MZ2/4	MZ1/1	MZ1/2	A5/1	A5/2	A5/3	A5/4	A5/5	A5/6	A5/7	A13/1	A13/2	A13/3	A27/1	A27/2	A27/3
SiO_2	53.39	51.97	53.52	54.91	54.30	52.42	51.90	53.18	52.60	51.93	52.11	52.68	52.99	53.42	52.85	52.56	52.57	52.82	52.88	52.97	53.31	52.40	51.47	52.83
TiO_2	0.21	0.21	0.14	0.14	0.14	0.21	0.21	0.21	0.21	0.18	0.18	0.21	0.24	0.16	0.19	0.16	0.22	0.19	0.16	0.16	0.16	0.14	0.14	0.14
Al_2O_3	0.67	0.82	0.99	0.97	0.90	0.80	0.78	0.81	0.76	0.64	0.70	0.51	0.70	0.51	0.56	0.54	0.56	0.86	0.61	0.77	0.64	0.57	0.67	0.60
FeO	18.64	18.05	17.05	16.97	17.27	18.41	18.26	18.21	17.67	24.85	24.91	23.55	23.14	23.79	23.65	23.61	23.92	23.96	22.47	22.62	22.95	24.15	23.95	23.57
MnO	0.46	0.46	0.38	0.38	0.38	0.43	0.43	0.43	0.43	0.56	0.56	0.55	0.51	0.54	0.59	0.54	0.24	0.58	0.57	0.57	0.57	0.56	0.56	0.56
MgO	25.60	25.09	25.74	25.47	25.58	24.76	25.06	25.64	25.47	20.76	20.39	21.50	21.42	21.05	21.17	22.33	21.75	21.55	21.74	21.47	21.59	21.21	21.03	21.71
CaO	0.79	1.71	1.20	1.87	1.34	1.43	1.56	1.04	2.12	0.97	0.81	0.96	1.09	0.65	0.67	0.79	0.97	1.03	0.64	0.91	0.83	1.08	0.77	0.82
Na_2O	0.06	0.06	0.00	0.00	0.00	0.03	0.03	0.03	0.03	0.00	0.00	0.01	0.04	0.05	0.04	0.04	0.03	0.05	0.00	0.00	0.00	0.05	0.05	0.05
Cr_2O_3	0.11	0.08	0.12	0.10	0.12	0.14	0.09	0.10	0.12	0.05	0.01	0.02	0.00	0.03	0.02	0.00	0.02	0.02	0.01	0.00	0.01	0.02	0.05	0.02
NiO	0.05	0.05	0.08	0.08	0.08	0.05	0.02	0.10	0.05	0.03	0.03	0.01	0.04	0.03	0.05	0.03	0.05	0.01	0.06	0.07	0.06	0.06	0.06	0.06
TOTAL	99.98	98.50	99.21	100.89	100.11	98.68	98.34	99.75	99.46	99.96	99.65	100.00	100.17	100.23	99.79	100.60	100.33	101.07	99.14	99.54	100.11	100.23	98.75	100.36
Si	1.959	1.940	1.963	1.980	1.975	1.952	1.940	1.953	1.942	1.964	1.974	1.977	1.981	1.997	1.986	1.962	1.969	1.965	1.988	1.986	1.989	1.970	1.964	1.975
Ti	0.006	0.006	0.004	0.004	0.004	0.006	0.006	0.006	0.006	0.005	0.005	0.006	0.007	0.004	0.005	0.004	0.006	0.005	0.005	0.005	0.005	0.004	0.004	0.004
Al	0.029	0.036	0.043	0.042	0.039	0.035	0.035	0.036	0.033	0.029	0.031	0.023	0.031	0.022	0.025	0.024	0.025	0.038	0.027	0.034	0.028	0.025	0.030	0.026
Fe	0.572	0.564	0.524	0.511	0.525	0.574	0.572	0.560	0.546	0.786	0.789	0.739	0.723	0.744	0.743	0.737	0.749	0.745	0.707	0.710	0.716	0.759	0.765	0.737
Mn	0.015	0.015	0.012	0.012	0.012	0.014	0.014	0.014	0.014	0.018	0.018	0.017	0.016	0.017	0.019	0.017	0.008	0.018	0.018	0.018	0.018	0.018	0.018	0.018
Mg	1.400	1.399	1.409	1.367	1.387	1.377	1.400	1.404	1.403	1.171	1.152	1.203	1.193	1.173	1.186	1.243	1.214	1.195	1.220	1.201	1.200	1.188	1.198	1.209
Ca	0.031	0.068	0.048	0.073	0.053	0.057	0.063	0.041	0.084	0.040	0.033	0.039	0.044	0.026	0.027	0.032	0.039	0.041	0.026	0.037	0.034	0.043	0.032	0.033
Na	0.004	0.004	0.000	0.000	0.000	0.003	0.003	0.003	0.003	0.000	0.000	0.001	0.003	0.004	0.003	0.003	0.002	0.004	0.000	0.000	0.000	0.003	0.004	0.004
Cr	0.003	0.003	0.004	0.003	0.003	0.004	0.003	0.003	0.004	0.001	0.000	0.001	0.000	0.001	0.001	0.000	0.000	0.001	0.000	0.000	0.001	0.001	0.001	0.001
Ni	0.001	0.002	0.002	0.002	0.002	0.002	0.001	0.003	0.001	0.001	0.001	0.000	0.001	0.001	0.002	0.001	0.001	0.000	0.002	0.002	0.002	0.002	0.002	0.002
TOTAL	4.021	4.037	4.009	3.994	4.000	4.024	4.036	4.023	4.035	4.016	4.005	4.006	3.999	3.989	3.997	4.023	4.014	4.012	3.993	3.992	3.992	4.014	4.018	4.009
At% En	69.88	68.86	71.16	70.07	70.59	68.57	68.81	70.04	69.01	58.63	58.35	60.73	60.87	60.38	60.62	61.78	60.64	60.31	62.47	61.67	61.56	59.69	60.05	61.11
Fs	28.55	27.77	26.44	26.21	26.73	28.59	28.10	27.92	26.87	39.38	39.98	37.32	36.90	38.28	38.00	36.65	37.42	37.62	36.21	36.45	36.72	38.13	38.37	37.23
Wo	1.57	3.37	2.40	3.72	2.68	2.84	3.09	2.04	4.13	1.99	1.67	1.95	2.23	1.34	1.38	1.57	1.94	2.07	1.32	1.88	1.72	2.18	1.58	1.66
MMF	0.710	0.713	0.729	0.728	0.725	0.706	0.710	0.715	0.720	0.598	0.593	0.619	0.623	0.612	0.615	0.628	0.618	0.616	0.633	0.628	0.626	0.610	0.610	0.621
Al/Cr	9.22	13.58	11.47	14.61	11.30	7.95	11.78	11.11	9.44	19.08	104.3	38.01	-	25.34	41.74	-	41.74	64.10	90.93	-	47.70	28.33	33.29	44.72

ORTHOPYROXENE ANALYSES AND STRUCTURAL FORMULAE BASED ON SIX OXYGENS

	A35/1	A35/2	A35/3	A35/4	A35/5	A38/1	A38/2	A38/3	A38/4	A48/1	A48/2	A52/1	A52/2	A52/3	A63/1	A63/2	A63/3	A79/1	A79/2	A91/1	A91/2	A91/3	A100/1	A100/2
SiO_2	52.97	52.70	52.32	53.11	53.03	53.43	52.98	52.43	52.85	53.45	53.32	53.39	53.29	52.55	53.84	53.74	53.83	54.83	51.28	52.13	52.43	52.76	53.48	53.50
TiO_2	0.16	0.18	0.20	0.13	0.18	0.18	0.19	0.19	0.14	0.21	0.16	0.14	0.14	0.14	0.20	0.21	0.20	0.22	0.18	0.17	0.17	0.17	0.13	0.23
Al_2O_3	0.76	0.57	0.59	0.60	1.20	0.64	0.76	1.46	0.71	0.59	0.61	0.62	0.58	0.59	0.59	0.47	0.65	0.65	0.75	0.75	0.70	0.61	0.61	0.68
FeO	22.63	22.59	23.10	22.73	22.39	21.74	21.76	22.06	20.88	22.65	22.78	21.68	21.58	21.78	22.23	22.03	22.21	21.29	21.41	20.27	20.42	20.80	20.91	20.71
MnO	0.45	0.51	0.55	0.51	0.47	0.54	0.52	0.56	0.48	0.54	0.54	0.53	0.53	0.53	-	-	-	-	-	0.48	0.48	0.48	0.46	0.47
MgO	21.80	22.18	22.50	22.77	22.52	21.92	21.86	21.64	21.28	21.95	22.29	22.34	22.62	22.44	22.57	22.56	22.16	22.73	23.39	24.00	23.49	23.86	22.87	22.88
CaO	0.73	0.95	0.81	0.61	0.93	0.73	0.91	1.05	2.21	0.73	0.72	0.83	0.84	0.72	0.82	1.35	0.75	1.65	1.66	1.22	1.36	0.66	0.73	0.89
Na_2O	0.01	0.08	0.06	0.04	0.16	0.00	0.08	0.01	0.00	0.00	0.00	0.00	0.00	0.00	-	-	-	-	-	0.01	0.01	0.01	0.00	0.07
Cr_2O_3	0.05	0.02	0.00	0.01	0.02	0.02	0.02	0.01	0.01	0.02	0.02	0.02	0.02	0.00	0.03	0.00	0.01	0.02	0.00	0.03	0.02	0.03	0.01	0.02
NiO	0.04	0.08	0.05	0.07	0.04	0.04	0.03	0.04	0.03	0.07	0.08	0.05	0.05	0.05	-	-	-	-	-	0.06	0.06	0.06	0.06	0.06
TOTAL	99.60	99.85	100.18	100.58	100.94	99.24	99.10	99.45	98.59	100.21	100.52	99.60	99.65	98.80	100.28	100.36	99.81	101.39	98.67	99.12	99.14	99.44	99.26	99.51
Si	1.984	1.973	1.959	1.972	1.960	1.999	1.988	1.965	1.992	1.989	1.980	1.990	1.986	1.978	1.992	1.989	2.000	1.998	1.939	1.949	1.961	1.965	1.993	1.988
Ti	0.005	0.005	0.006	0.004	0.005	0.005	0.005	0.005	0.004	0.006	0.004	0.004	0.004	0.004	0.006	0.006	0.006	0.006	0.005	0.005	0.005	0.005	0.004	0.006
Al	0.034	0.025	0.026	0.026	0.052	0.028	0.034	0.064	0.032	0.026	0.027	0.027	0.025	0.027	0.026	0.021	0.028	0.028	0.033	0.034	0.031	0.027	0.027	0.030
Fe	0.709	0.707	0.723	0.706	0.692	0.680	0.683	0.691	0.658	0.705	0.708	0.676	0.673	0.686	0.688	0.682	0.690	0.649	0.677	0.634	0.639	0.648	0.652	0.644
Mn	0.014	0.016	0.017	0.016	0.015	0.017	0.017	0.018	0.015	0.017	0.017	0.017	0.017	0.017	-	-	-	-	-	0.015	0.016	0.015	0.015	0.015
Mg	1.217	1.238	1.255	1.260	1.241	1.222	1.223	1.209	1.196	1.217	1.234	1.242	1.257	1.261	1.245	1.244	1.227	1.235	1.318	1.339	1.310	1.325	1.270	1.267
Ca	0.029	0.038	0.032	0.024	0.037	0.029	0.037	0.042	0.089	0.029	0.029	0.034	0.034	0.029	0.033	0.054	0.030	0.064	0.067	0.049	0.055	0.026	0.029	0.035
Na	0.001	0.006	0.004	0.003	0.011	0.000	0.006	0.001	0.000	0.000	0.000	0.000	0.000	0.000	-	-	-	-	-	0.001	0.000	0.001	0.000	0.005
Cr	0.001	0.001	0.000	0.000	0.000	0.001	0.001	0.000	0.000	0.001	0.001	0.001	0.001	0.000	0.001	0.000	0.000	0.001	0.000	0.001	0.001	0.001	0.000	0.001
Ni	0.001	0.002	0.002	0.002	0.001	0.001	0.001	0.001	0.001	0.002	0.002	0.002	0.002	0.002	-	-	-	-	-	0.002	0.002	0.002	0.002	0.002
TOTAL	3.995	4.012	4.025	4.013	4.014	3.982	3.993	3.998	3.988	3.992	4.002	3.992	3.997	4.004	3.989	3.995	3.981	3.981	4.039	4.029	4.019	4.016	3.990	3.993
At% En	62.25	62.41	63.43	63.32	62.99	63.27	62.95	62.23	61.53	62.39	62.63	63.64	64.02	63.80	63.34	62.86	63.02	63.38	63.91	66.23	65.37	66.27	65.11	65.11
Fs	36.26	35.67	35.96	35.46	35.14	35.21	35.17	35.60	33.88	36.12	35.91	34.64	34.27	34.73	35.00	34.44	35.44	33.31	32.83	31.36	31.89	32.42	33.40	33.07
Wo	1.50	1.92	1.62	1.22	1.87	1.51	1.88	2.17	4.59	1.49	1.45	1.72	1.71	1.47	1.65	2.70	1.53	3.31	3.26	2.42	2.74	1.31	1.49	1.82
MMF	0.632	0.636	0.635	0.641	0.642	0.642	0.642	0.636	0.645	0.633	0.636	0.648	0.651	0.648	0.644	0.646	0.640	0.656	0.661	0.679	0.672	0.672	0.661	0.663
Al/Cr	22.66	42.48	-	-	-	47.70	56.65	-	-	43.98	45.47	30.81	43.23	-	29.32	-	-	48.45	-	37.76	52.92	30.81	-	50.68

ORTHOPYROXENE ANALYSES AND STRUCTURAL FORMULAE BASED ON SIX OXYGENS

	A108/1	A108/2	A108/3	A117/1	A117/2	A149/1	A149/2	A155/1	A155/2	A155/3	A155/4	A155/5	A155/6	A155/7	A155/8	A155/9	A159/1	A159/2	A159/3	A193/1	A193/2	A193/3	A193/4	A208/1
SiO_2	53.93	54.83	54.41	53.73	52.65	53.78	54.70	53.47	53.57	52.46	53.45	53.38	53.15	53.03	53.11	52.74	54.23	53.51	53.51	53.59	53.00	53.63	53.91	54.07
TiO_2	0.17	0.17	0.17	0.30	0.30	0.21	0.20	0.19	0.49	0.20	0.23	0.21	0.18	0.23	0.24	0.17	0.18	0.18	0.18	0.21	0.21	0.21	0.24	0.24
Al_2O_3	0.79	0.85	0.77	0.62	0.66	0.65	0.63	0.67	0.73	0.72	0.75	0.79	0.76	0.73	0.93	0.67	0.58	0.53	0.52	0.70	0.49	0.64	0.64	0.70
FeO	17.38	17.42	17.87	20.60	20.93	19.82	19.97	19.51	18.02	19.52	20.43	18.92	19.77	19.58	19.44	19.97	21.46	20.53	21.67	20.46	19.84	19.87	18.38	18.12
MnO	0.49	0.49	0.49	-	-	-	-	0.42	0.40	0.44	0.45	0.40	0.43	0.44	0.43	0.44	-	-	-	0.43	0.44	0.44	0.41	0.41
MgO	24.78	25.11	25.08	23.17	23.19	23.32	23.38	24.57	23.89	24.87	24.58	24.42	25.06	25.18	24.62	24.78	23.28	22.74	23.17	24.11	24.43	23.87	24.98	25.60
CaO	2.91	1.70	1.49	1.18	1.44	1.32	0.87	0.72	2.67	0.96	1.03	1.95	0.70	1.02	1.63	0.81	0.86	1.85	0.92	0.75	1.23	1.72	1.47	1.14
Na_2O	0.01	0.01	0.01	-	-	-	-	0.00	0.00	0.03	0.00	0.00	0.00	0.00	0.00	0.00	-	-	-	0.01	0.01	0.01	0.00	0.00
Cr_2O_3	0.03	0.02	0.03	0.00	0.00	0.01	0.04	0.02	0.02	0.02	0.03	0.02	0.02	0.02	0.02	0.03	0.02	0.01	0.05	0.01	0.04	0.03	0.02	0.06
NiO	0.06	0.06	0.06	-	-	-	-	0.03	0.08	0.07	0.05	0.07	0.04	0.06	0.08	0.08	-	-	-	0.08	0.08	0.08	0.11	0.11
TOTAL	100.54	100.66	100.37	99.60	99.17	99.11	99.79	99.62	99.87	99.29	100.99	100.16	100.11	100.29	100.50	99.69	100.61	99.35	100.02	100.35	99.77	100.48	100.16	100.42
Si	1.966	1.985	1.980	1.990	1.968	1.995	2.009	1.974	1.970	1.950	1.957	1.962	1.957	1.950	1.950	1.955	1.992	1.991	1.983	1.972	1.963	1.971	1.972	1.969
Ti	0.005	0.005	0.005	0.008	0.008	0.006	0.006	0.005	0.014	0.006	0.006	0.006	0.005	0.006	0.007	0.005	0.005	0.005	0.005	0.006	0.006	0.006	0.007	0.007
Al	0.034	0.037	0.033	0.027	0.029	0.028	0.027	0.029	0.032	0.032	0.032	0.034	0.033	0.032	0.040	0.029	0.025	0.023	0.023	0.031	0.021	0.028	0.028	0.030
Fe	0.530	0.527	0.544	0.638	0.654	0.615	0.613	0.602	0.554	0.607	0.626	0.582	0.609	0.602	0.597	0.619	0.659	0.639	0.672	0.629	0.614	0.611	0.562	0.552
Mn	0.015	0.015	0.015	-	-	-	-	0.013	0.012	0.014	0.014	0.012	0.013	0.014	0.013	0.014	-	-	-	0.014	0.014	0.014	0.013	0.013
Mg	1.345	1.353	1.360	1.279	1.292	1.289	1.280	1.352	1.309	1.378	1.342	1.338	1.375	1.380	1.348	1.369	1.275	1.261	1.280	1.321	1.348	1.307	1.362	1.389
Ca	0.114	0.066	0.058	0.047	0.058	0.052	0.034	0.028	0.105	0.038	0.040	0.077	0.028	0.040	0.064	0.032	0.034	0.074	0.037	0.030	0.049	0.068	0.058	0.045
Na	0.001	0.001	0.001	-	-	-	-	0.000	0.000	0.000	0.000	0.000	0.000	0.000	0.000	0.000	-	-	-	0.001	0.001	0.001	0.000	0.000
Cr	0.001	0.001	0.001	0.000	0.000	0.000	0.001	0.001	0.001	0.001	0.001	0.001	0.001	0.001	0.001	0.001	0.001	0.000	0.001	0.001	0.001	0.001	0.001	0.002
Ni	0.002	0.002	0.002	-	-	-	-	0.001	0.002	0.002	0.001	0.002	0.001	0.002	0.002	0.002	-	-	-	0.002	0.002	0.002	0.004	0.004
TOTAL	4.012	3.992	3.998	3.989	4.009	3.985	3.971	4.006	3.999	4.027	4.020	4.014	4.021	4.027	4.023	4.026	3.990	3.993	4.000	4.006	4.021	4.009	4.007	4.009
At % En	67.64	69.52	69.32	65.13	64.47	65.90	66.40	68.19	66.51	68.11	66.82	67.02	68.37	68.24	67.09	67.77	64.78	63.90	64.38	66.72	67.03	65.82	68.73	69.96
Fs	26.63	27.10	27.72	32.49	32.65	31.42	31.82	30.38	28.15	30.00	31.16	29.13	30.26	29.77	29.72	30.64	33.50	32.37	33.78	31.78	30.54	30.77	28.36	27.78
Wo	5.73	3.39	2.96	2.38	2.88	2.68	1.78	1.44	5.34	1.89	2.01	3.85	1.37	1.99	3.19	1.59	1.72	3.74	1.84	1.49	2.43	3.41	2.91	2.26
MMF	0.718	0.720	0.714	0.667	0.664	0.677	0.676	0.692	0.703	0.694	0.682	0.697	0.693	0.696	0.693	0.689	0.659	0.664	0.656	0.677	0.687	0.681	0.708	0.716
Al/Cr	29.44	42.73	38.76	-	-	-	23.48	49.93	54.41	53.67	37.27	58.88	56.65	54.41	69.32	33.29	43.23	-	15.50	52.92	18.26	23.85	32.30	17.39

ORTHOPYROXENE ANALYSES AND STRUCTURAL FORMULAE BASED ON SIX OXYGENS

	A213/1	A213/2	A213/3	A213/4	A226/1	A226/2	A235/1	A235/2	A236/1	A236/2	A238/1	A238/2	A247/1	A247/2	A255/1	A255/2	A257/1	A257/2	A262/1	A262/2	A262/3	A264/1	A264/2	A264/3
SiO_2	54.12	53.86	53.70	54.03	50.66	50.76	54.25	54.26	51.98	51.70	51.60	52.10	53.06	53.31	54.35	54.49	53.92	54.24	54.75	54.09	53.65	54.16	54.54	54.16
TiO_2	0.28	0.29	0.17	0.24	0.12	0.18	0.18	0.18	0.18	0.18	0.19	0.19	0.19	0.19	0.25	0.25	0.29	0.26	0.22	0.22	0.13	0.22	0.25	0.18
Al_2O_3	0.73	0.75	0.75	0.71	0.60	0.64	0.54	0.87	0.79	0.68	0.80	0.59	0.72	0.74	0.63	0.60	0.76	0.64	0.75	0.67	0.80	0.76	0.76	0.85
FeO	18.07	18.55	17.67	17.91	29.35	28.73	17.93	18.24	24.99	25.82	27.29	27.04	22.04	21.15	17.36	17.83	19.44	19.91	18.00	18.26	17.46	18.19	17.92	17.67
MnO	0.41	0.43	0.42	0.43	-	-	-	-	-	-	-	-	0.41	0.41	0.42	0.42	0.41	0.45	-	-	-	-	-	-
MgO	24.66	24.68	24.83	25.09	16.56	16.61	25.55	25.31	19.18	19.56	18.42	18.44	22.46	22.91	25.77	25.62	23.58	23.99	25.69	24.79	25.05	25.14	24.99	25.14
CaO	1.12	1.12	1.46	1.08	0.86	1.27	0.73	0.99	1.46	0.77	1.04	0.69	1.36	1.50	2.01	1.01	2.03	1.03	1.42	1.55	1.94	1.10	1.42	1.99
Na_2O	-	-	-	-	-	-	-	-	-	-	-	-	-	-	-	-	-	-	-	-	-	-	-	-
Cr_2O_3	0.03	0.02	0.04	0.03	0.02	0.01	0.00	0.05	0.03	0.04	0.02	0.03	0.08	0.07	0.09	0.10	0.05	0.08	0.06	0.08	0.10	0.12	0.14	0.12
NiO	0.07	0.04	0.07	0.05	-	-	-	-	-	-	-	-	0.08	0.08	0.11	0.11	0.06	0.07	-	-	-	-	-	-
TOTAL	99.49	99.74	99.11	99.57	98.17	98.20	99.18	99.90	98.61	98.75	99.36	99.08	100.40	100.36	100.99	100.42	100.54	100.67	100.89	99.66	99.13	99.69	100.02	100.11
Si	1.987	1.978	1.979	1.981	1.990	1.990	1.990	1.980	1.990	1.982	1.981	1.999	1.971	1.972	1.967	1.979	1.977	1.984	1.978	1.983	1.974	1.981	1.987	1.974
Ti	0.008	0.008	0.005	0.007	0.004	0.005	0.005	0.005	0.005	0.005	0.005	0.005	0.005	0.005	0.007	0.007	0.008	0.007	0.006	0.006	0.004	0.006	0.007	0.005
Al	0.032	0.032	0.033	0.031	0.028	0.030	0.023	0.037	0.036	0.031	0.036	0.027	0.032	0.033	0.027	0.026	0.033	0.028	0.032	0.029	0.035	0.033	0.033	0.037
Fe	0.555	0.570	0.545	0.549	0.964	0.942	0.550	0.557	0.800	0.828	0.876	0.868	0.684	0.654	0.525	0.541	0.596	0.609	0.544	0.560	0.537	0.557	0.546	0.539
Mn	0.013	0.013	0.013	0.013	-	-	-	-	-	-	-	-	0.013	0.013	0.013	0.013	0.013	0.014	-	-	-	-	-	-
Mg	1.349	1.351	1.364	1.371	0.970	0.970	1.397	1.377	1.095	1.118	1.054	1.054	1.243	1.263	1.388	1.386	1.289	1.308	1.383	1.355	1.374	1.371	1.357	1.366
Ca	0.044	0.044	0.058	0.042	0.036	0.053	0.029	0.039	0.060	0.032	0.043	0.028	0.054	0.059	0.078	0.039	0.080	0.040	0.055	0.061	0.076	0.043	0.055	0.078
Na	-	-	-	-	-	-	-	-	-	-	-	-	-	-	-	-	-	-	-	-	-	-	-	-
Cr	0.001	0.001	0.001	0.001	0.001	0.000	0.000	0.001	0.001	0.001	0.001	0.001	0.002	0.002	0.003	0.003	0.001	0.002	0.002	0.002	0.003	0.003	0.004	0.003
Ni	0.002	0.001	0.002	0.001	-	-	-	-	-	-	-	-	0.002	0.003	0.003	0.004	0.002	0.002	-	-	-	-	-	-
TOTAL	3.989	3.998	3.999	3.997	3.992	3.990	3.994	3.996	3.986	3.997	3.996	3.982	4.007	4.005	4.011	3.999	3.998	3.994	3.999	3.995	4.003	3.994	3.988	4.001
At %En	69.26	68.76	69.37	69.86	49.22	49.37	70.71	69.81	56.00	56.53	53.42	54.06	62.73	63.90	69.72	70.47	65.60	66.82	69.79	68.58	69.12	69.57	69.29	68.91
Fs	28.48	29.00	27.70	27.98	48.94	47.91	27.84	28.23	40.94	41.87	44.41	44.48	34.54	33.10	26.36	27.53	30.34	31.12	27.44	28.34	27.03	28.24	27.88	27.17
Wo	2.26	2.24	2.93	2.16	1.84	2.71	1.45	1.96	3.06	1.60	2.17	1.45	2.73	3.01	3.91	2.00	4.06	2.06	2.77	3.08	3.85	2.19	2.83	3.92
Mg#	0.709	0.703	0.715	0.714	0.501	0.507	0.717	0.712	0.578	0.574	0.546	0.549	0.645	0.659	0.726	0.719	0.684	0.682	0.718	0.708	0.719	0.711	0.713	0.717
Al/Cr	36.27	55.90	27.95	35.28	44.72	95.40	-	25.94	39.26	25.34	59.63	29.32	13.60	15.97	10.60	8.27	22.66	11.93	18.63	12.48	11.93	9.44	8.09	10.56

ORTHOPYROXENE ANALYSES AND STRUCTURAL FORMULAE BASED ON SIX OXYGENS

	A266/1	A266/2	A266/3	A271/1	A271/2	A271/3	A280/1	A280/2	A280/3	A280/4	A284/1	A284/2	A284/3	A284/4	A284/5	A284/6	A284/7	A287/1	A287/2	A290/1	A290/2	A290/3	A290/4	A290/5
SiO_2	54.50	54.76	54.27	54.41	53.62	53.53	53.70	54.48	54.54	53.66	54.36	54.80	54.00	54.33	53.84	54.45	54.58	53.63	54.91	55.08	54.81	54.92	54.51	55.75
TiO_2	0.21	0.20	0.22	0.18	0.17	0.22	0.16	0.20	0.14	0.18	0.14	0.19	0.16	0.19	0.17	0.19	0.22	0.21	0.18	0.46	0.55	0.48	0.53	0.62
Al_2O_3	0.70	0.79	0.72	0.81	0.98	0.81	0.76	0.77	0.73	0.79	0.97	0.77	0.75	0.80	0.83	0.84	0.78	0.79	0.86	0.67	0.75	0.76	0.65	0.72
FeO	17.40	17.38	17.65	16.00	16.47	16.59	16.57	16.49	15.88	16.09	15.84	16.25	16.71	16.57	16.34	16.48	16.45	16.55	16.60	17.20	17.98	17.94	16.71	17.00
MnO	0.40	0.39	0.39	-	-	-	-	-	-	-	0.35	0.38	0.36	0.36	0.38	0.37	0.36	-	-	0.34	0.36	0.39	0.38	0.29
MgO	25.60	25.28	25.56	25.80	25.72	25.95	26.45	25.51	25.73	26.02	26.82	27.10	26.98	27.62	26.70	26.33	26.79	25.81	25.78	24.55	24.47	24.59	23.89	24.08
CaO	0.84	1.44	1.16	1.91	2.05	1.39	1.10	1.30	1.83	1.89	1.62	0.69	0.76	1.13	1.82	1.89	1.32	1.60	1.68	1.40	1.12	1.40	2.44	2.08
Cr_2O_3	0.12	0.16	0.16	0.12	0.15	0.15	0.15	0.14	0.13	0.14	0.12	0.15	0.13	0.13	0.13	0.13	0.12	0.13	0.14	0.08	0.11	0.10	0.09	0.08
NiO	0.05	0.03	0.08	-	-	-	-	-	-	-	0.08	0.07	0.08	0.06	0.07	0.05	0.06	-	-	0.06	0.09	0.07	0.07	0.10
TOTAL	99.82	100.43	100.21	99.23	99.16	98.64	98.89	98.89	98.98	98.77	100.30	100.40	99.93	101.19	100.31	100.73	100.68	98.72	100.15	99.84	100.24	100.65	99.27	100.72
Si	1.986	1.985	1.976	1.984	1.965	1.970	1.969	1.993	1.990	1.967	1.964	1.974	1.963	1.951	1.954	1.965	1.967	1.972	1.986	2.004	1.993	1.990	1.999	2.009
Ti	0.006	0.005	0.006	0.005	0.005	0.006	0.004	0.006	0.004	0.005	0.004	0.005	0.004	0.005	0.005	0.005	0.006	0.006	0.005	0.013	0.015	0.013	0.015	0.017
Al	0.030	0.034	0.031	0.035	0.042	0.035	0.033	0.033	0.031	0.034	0.041	0.033	0.032	0.034	0.035	0.036	0.033	0.034	0.037	0.029	0.032	0.032	0.028	0.031
Fe	0.530	0.527	0.537	0.488	0.505	0.511	0.508	0.505	0.484	0.493	0.478	0.490	0.508	0.498	0.496	0.497	0.496	0.509	0.502	0.523	0.547	0.544	0.512	0.512
Mn	0.012	0.012	0.012	-	-	-	-	-	-	-	0.011	0.012	0.011	0.011	0.012	0.011	0.011	-	-	0.010	0.011	0.012	0.012	0.009
Mg	1.390	1.366	1.387	1.402	1.405	1.423	1.446	1.391	1.399	1.421	1.444	1.455	1.461	1.478	1.444	1.417	1.439	1.415	1.390	1.331	1.326	1.328	1.306	1.294
Ca	0.033	0.056	0.045	0.075	0.080	0.055	0.043	0.051	0.072	0.074	0.063	0.027	0.031	0.043	0.071	0.073	0.051	0.063	0.065	0.055	0.044	0.054	0.096	0.080
Cr	0.003	0.005	0.005	0.003	0.004	0.004	0.004	0.004	0.004	0.004	0.003	0.004	0.004	0.004	0.004	0.004	0.003	0.004	0.004	0.002	0.003	0.003	0.003	0.002
Ni	0.001	0.001	0.002	-	-	-	-	-	-	-	0.002	0.002	0.002	0.002	0.002	0.001	0.002	-	-	0.002	0.003	0.002	0.002	0.003
TOTAL	3.992	3.990	4.001	3.992	4.007	4.004	4.008	3.983	3.984	3.999	4.010	4.002	4.015	4.025	4.022	4.010	4.009	4.003	3.989	3.968	3.974	3.979	3.971	3.957
At %En	71.18	70.09	70.42	71.37	70.59	71.57	72.39	71.46	71.56	71.47	72.74	73.31	73.11	73.21	71.82	71.29	72.47	71.21	71.02	69.73	69.20	68.95	68.22	68.58
Fs	27.14	27.04	27.28	24.83	25.36	25.67	25.45	25.92	24.78	24.80	24.10	24.83	25.41	24.64	24.66	25.03	24.97	25.62	25.66	27.41	28.53	28.23	26.77	27.16
Wo	1.68	2.87	2.30	3.80	4.04	2.76	2.16	2.62	3.66	3.73	3.16	1.35	1.48	2.15	3.52	3.68	2.57	3.17	3.33	2.86	2.28	2.82	5.01	4.26
MMF	0.724	0.722	0.721	0.742	0.736	0.736	0.740	0.734	0.743	0.742	0.751	0.748	0.742	0.748	0.744	0.740	0.744	0.735	0.735	0.718	0.708	0.710	0.718	0.716
Al/Cr	8.70	7.36	6.71	10.06	9.74	8.05	7.55	8.20	8.37	8.41	12.05	7.65	8.60	9.17	9.52	9.63	9.69	9.06	9.16	12.48	10.16	11.33	10.77	13.42

ORTHOPYROXENE ANALYSES AND STRUCTURAL FORMULAE BASED ON SIX OXYGENS

	A295/1	A295/2	A295/3	A297/1	A297/2	A297/3	A305/1	A305/2	A305/3	A305/4	A299/1	A299/2	A299/3	A308/1	A308/2	A309/1	A309/2	A309/3	A312/1	A312/2	A312/3	A317/1	A317/2	A319/1
SiO_2	55.37	55.35	54.71	54.50	54.05	54.37	53.41	53.93	54.08	53.61	55.52	54.54	54.11	54.80	33.08	53.20	54.72	54.72	54.42	53.95	52.69	52.82	53.08	54.44
TiO_2	0.55	0.60	0.73	0.21	0.20	0.22	0.18	0.18	0.18	0.18	0.23	0.18	0.19	0.26	0.26	0.19	0.35	0.22	0.20	0.24	0.19	0.15	0.16	0.50
Al_2O_3	0.72	0.77	0.73	0.52	0.66	0.71	0.73	0.67	0.75	0.76	0.79	0.65	0.77	0.63	0.78	0.64	0.82	0.87	0.82	0.74	0.80	0.72	0.78	0.66
FeO	17.00	17.30	17.28	15.63	16.10	15.83	16.14	16.31	16.25	15.56	16.05	16.22	16.21	16.40	16.09	16.72	16.23	16.48	18.24	18.15	17.38	18.94	18.87	19.99
MnO	0.36	0.35	0.37	0.36	0.40	0.36	0.31	0.31	0.31	0.31	–	–	–	0.33	0.33	–	–	–	–	–	–	–	–	0.40
MgO	24.61	24.62	24.35	25.81	25.84	25.63	25.85	26.06	25.68	25.91	26.81	26.56	26.43	26.93	26.96	27.28	26.94	26.57	24.98	25.05	25.03	24.47	24.01	22.31
CaO	1.90	1.12	1.12	1.78	0.73	1.73	1.61	1.32	1.41	1.74	1.42	1.14	2.84	1.37	1.13	0.85	1.85	1.70	0.98	1.06	2.63	1.54	1.76	1.06
Cr_2O_3	0.13	0.09	0.11	0.10	0.08	0.12	0.14	0.14	0.13	0.15	0.12	0.11	0.12	0.14	0.13	0.08	0.14	0.14	0.12	0.16	0.14	0.09	0.12	0.06
NiO	0.09	0.09	0.10	0.09	0.07	0.10	0.05	0.05	0.05	0.05	–	–	–	0.07	0.07	–	–	–	–	–	–	–	–	–
TOTAL	100.73	100.29	99.51	99.00	98.13	99.07	98.42	98.97	98.84	98.27	100.94	99.40	100.67	100.93	100.83	98.96	101.05	100.70	99.76	99.35	98.86	98.73	98.78	99.42
Si	1.998	2.003	1.998	1.992	1.992	1.987	1.971	1.977	1.983	1.976	1.985	1.983	1.956	1.970	1.976	1.953	1.963	1.970	1.988	1.981	1.953	1.966	1.974	2.012
Ti	0.015	0.016	0.020	0.006	0.006	0.006	0.005	0.005	0.005	0.005	0.006	0.005	0.005	0.007	0.007	0.005	0.009	0.006	0.005	0.007	0.005	0.004	0.004	0.014
Al	0.031	0.033	0.032	0.022	0.029	0.031	0.032	0.029	0.032	0.033	0.033	0.028	0.033	0.027	0.033	0.028	0.035	0.037	0.035	0.032	0.035	0.032	0.034	0.029
Fe	0.513	0.524	0.528	0.478	0.496	0.484	0.498	0.500	0.498	0.480	0.480	0.493	0.490	0.493	0.483	0.513	0.487	0.496	0.557	0.557	0.539	0.590	0.587	0.618
Mn	0.011	0.011	0.011	0.011	0.012	0.011	0.010	0.010	0.010	0.010	–	–	–	0.010	0.010	–	–	–	–	–	–	–	–	0.013
Mg	1.323	1.328	1.325	1.406	1.419	1.396	1.422	1.424	1.404	1.423	1.429	1.440	1.424	1.441	1.439	1.492	1.440	1.426	1.360	1.371	1.383	1.357	1.331	1.229
Ca	0.073	0.043	0.044	0.070	0.029	0.068	0.064	0.052	0.055	0.069	0.054	0.044	0.110	0.053	0.044	0.033	0.071	0.066	0.038	0.042	0.104	0.061	0.070	0.042
Cr	0.004	0.003	0.003	0.003	0.002	0.003	0.004	0.004	0.004	0.004	0.003	0.003	0.003	0.004	0.004	0.002	0.004	0.004	0.003	0.005	0.004	0.003	0.004	0.002
Ni	0.003	0.003	0.003	0.003	0.002	0.003	0.001	0.001	0.001	0.001	–	–	–	0.003	0.002	–	–	–	–	–	–	–	–	–
TOTAL	3.970	3.963	3.964	3.990	3.987	3.990	4.006	4.002	3.993	4.001	3.991	3.996	4.021	4.008	3.998	4.027	4.009	4.004	3.987	3.994	4.023	4.013	4.003	3.958
At %En	69.30	70.08	69.87	71.98	73.00	71.68	71.68	72.07	71.71	72.19	72.78	72.81	70.36	72.52	73.22	73.19	72.08	71.74	69.55	69.59	68.25	67.59	66.95	65.07
Fs	26.86	27.63	27.82	24.42	25.52	24.84	25.11	25.31	25.46	24.32	24.45	24.95	24.21	24.81	24.55	25.17	24.36	24.96	28.49	28.29	26.59	29.35	29.52	32.71
Wo	3.85	2.29	2.31	3.57	1.48	3.48	3.21	2.62	2.83	3.48	2.77	2.25	5.43	2.67	2.23	1.64	3.56	3.30	1.96	2.12	5.16	3.06	3.53	2.22
MIF	0.721	0.717	0.715	0.746	0.741	0.743	0.741	0.740	0.738	0.748	0.749	0.745	0.744	0.745	0.749	0.744	0.747	0.742	0.709	0.711	0.720	0.697	0.694	0.665
Al/Cr	8.26	12.75	10.03	7.75	12.30	8.82	7.77	7.13	8.60	7.55	9.81	8.81	9.57	6.71	8.41	11.93	8.73	9.26	10.19	6.89	8.52	11.93	9.69	16.40

ORTHOPYROXENE ANALYSES AND STRUCTURAL FORMULAE BASED ON SIX OXYGENS

	A319/2	A319/3	A319/4	A322/1	A322/2	A327/1	A327/2	A327/3	A334/1	A334/2	A337/1	A337/2	A346/1	A346/2	A346/3	A346/4	A346/5	A349/1	A349/2	A349/3	C66/1	C66/2	C55/1	C55/2
SiO_2	54.61	54.90	54.14	53.56	53.57	55.55	55.83	55.55	52.88	52.99	55.17	55.06	54.54	55.06	54.85	55.18	54.72	55.50	55.77	53.59	54.25	55.40	55.67	53.16
TiO_2	0.88	0.57	0.28	0.28	0.28	0.49	0.54	0.40	0.18	0.18	0.17	0.17	0.70	0.46	0.44	0.48	0.41	0.18	0.18	0.17	0.15	0.15	0.18	0.18
Al_2O_3	0.72	0.79	0.89	0.68	0.67	0.72	0.83	0.75	0.73	0.84	0.82	0.69	0.71	0.70	0.61	0.69	0.64	1.22	1.16	1.19	1.25	1.17	0.76	0.80
FeO	20.40	19.12	18.81	22.24	21.67	16.61	16.59	15.61	21.04	20.66	19.39	19.41	19.62	20.50	20.53	20.38	19.78	12.33	12.42	12.16	11.55	11.60	18.79	18.35
MnO	0.38	0.36	0.32	-	-	0.32	0.36	0.33	0.42	0.42	-	-	0.35	0.37	0.38	0.40	0.32	-	-	-	-	-	-	-
MgO	21.59	22.50	22.53	22.36	21.96	24.55	24.78	25.27	23.45	23.67	24.93	24.85	23.27	23.63	23.43	24.08	23.73	28.68	29.34	28.37	29.68	29.75	25.37	24.62
CaO	1.55	1.57	1.76	1.23	2.16	0.78	1.21	1.74	0.80	0.72	1.90	1.24	1.63	0.74	0.79	0.76	0.65	1.79	1.35	2.09	0.93	0.79	1.40	1.39
Cr_2O_3	0.06	0.14	0.15	0.09	0.08	0.10	0.12	0.16	0.11	0.14	0.12	0.11	0.12	0.15	0.11	0.17	0.20	0.51	0.48	0.48	0.52	0.46	0.17	0.15
NiO	-	0.01	0.01	-	-	0.01	0.01	0.02	0.06	0.06	-	-	0.07	0.06	0.07	0.06	0.06	-	-	-	-	-	-	-
TOTAL	100.19	99.96	98.88	100.44	100.39	99.13	100.27	99.83	99.63	99.68	102.50	101.53	101.01	101.67	101.21	102.19	100.51	100.21	100.70	98.05	98.33	99.32	102.33	98.64
Si	2.009	2.012	2.006	1.983	1.984	2.022	2.012	2.007	1.967	1.967	1.975	1.986	1.987	1.993	1.996	1.987	1.998	1.970	1.968	1.951	1.956	1.972	1.986	1.972
Ti	0.024	0.016	0.008	0.008	0.008	0.013	0.015	0.011	0.005	0.004	0.005	0.005	0.019	0.013	0.012	0.013	0.011	0.005	0.005	0.005	0.004	0.004	0.005	0.005
Al	0.031	0.034	0.039	0.030	0.029	0.031	0.035	0.032	0.032	0.037	0.035	0.029	0.030	0.030	0.026	0.029	0.028	0.051	0.048	0.051	0.053	0.049	0.032	0.035
Fe	0.628	0.586	0.583	0.688	0.671	0.506	0.500	0.472	0.655	0.642	0.581	0.586	0.598	0.621	0.625	0.614	0.604	0.366	0.367	0.370	0.348	0.345	0.561	0.569
Mn	0.012	0.011	0.010	-	-	0.010	0.011	0.010	0.013	0.012	-	-	0.011	0.011	0.012	0.012	0.010	-	-	-	-	-	-	-
Mg	1.184	1.229	1.244	1.234	1.212	1.332	1.331	1.361	1.301	1.310	1.330	1.336	1.263	1.275	1.271	1.292	1.291	1.518	1.543	1.539	1.595	1.579	1.349	1.362
Ca	0.061	0.062	0.070	0.049	0.086	0.030	0.047	0.067	0.032	0.029	0.073	0.048	0.064	0.029	0.031	0.029	0.025	0.068	0.051	0.082	0.036	0.030	0.054	0.055
Cr	0.002	0.004	0.004	0.003	0.002	0.003	0.003	0.005	0.003	0.004	0.003	0.003	0.003	0.004	0.003	0.005	0.006	0.014	0.013	0.014	0.015	0.013	0.005	0.004
Ni	-	0.000	0.000	-	-	0.000	0.000	0.001	0.002	0.002	-	-	0.002	0.002	0.002	0.002	0.002	-	-	-	-	-	-	-
TOTAL	3.950	3.953	3.964	3.994	3.992	3.948	3.954	3.964	4.010	4.008	4.001	3.993	3.977	3.977	3.977	3.983	3.974	3.992	3.996	4.012	4.006	3.993	3.991	4.003
At %En	63.22	65.49	65.59	62.59	61.56	71.30	70.88	71.63	65.46	66.14	67.06	67.84	65.64	66.26	65.97	66.78	67.23	77.76	78.70	77.31	80.59	80.78	68.72	68.55
Fs	33.52	31.23	30.73	34.93	34.09	27.07	26.63	24.83	32.94	32.39	29.27	29.73	31.05	32.25	32.43	31.71	31.44	18.76	18.69	18.59	17.60	17.67	28.56	28.67
Wo	3.26	3.28	3.68	2.48	4.35	1.63	2.49	3.55	1.60	1.47	3.67	2.43	3.31	1.49	1.60	1.51	1.32	3.49	2.60	4.09	1.82	1.54	2.73	2.78
MMF	0.654	0.677	0.681	0.642	0.644	0.725	0.727	0.743	0.665	0.671	0.696	0.695	0.679	0.673	0.670	0.678	0.681	0.806	0.808	0.806	0.821	0.820	0.706	0.705
Al/Cr	17.89	8.41	9.48	11.26	12.48	10.73	10.31	6.99	9.89	8.94	10.19	9.35	8.82	6.96	8.27	6.05	4.77	3.57	3.60	3.70	3.58	3.79	6.66	7.95

CLINOPYROXENE ANALYSES AND STRUCTURAL FORMULAE BASED ON SIX OXYGENS

	MZ7/1	MZ7/2	MZ4/1	MZ4/2	MZ2/1	MZ2/2	MZ1/1	A5/1	A5/2	A5/3	A5/4	A5/5	A5/6	A13/1	A13/2	A35/1	A35/2	A35/3	A35/4
SiO_2	51.05	52.27	52.86	52.47	51.54	52.09	51.88	52.47	52.53	53.35	52.36	52.15	52.28	51.87	51.77	52.89	53.01	52.37	51.98
TiO_2	0.39	0.39	0.06	0.06	0.35	0.35	0.35	0.36	0.37	0.25	0.35	0.36	0.38	0.26	0.26	0.30	0.23	0.28	0.33
Al_2O_3	1.52	1.45	1.72	1.70	1.47	1.43	1.27	1.22	1.12	1.16	1.19	1.11	1.26	1.62	1.17	1.24	1.28	1.17	1.16
FeO	7.65	7.11	7.53	7.36	7.43	7.09	10.58	9.64	9.59	9.23	10.09	9.55	10.07	11.40	12.12	8.75	8.60	8.60	9.17
MnO	0.17	0.17	0.23	0.23	0.23	0.23	0.29	0.23	0.28	0.26	0.23	0.24	0.28	0.29	0.29	0.23	0.25	0.23	0.28
MgO	14.62	14.83	14.74	14.58	14.67	14.70	13.42	14.15	14.11	13.65	14.64	13.94	14.61	14.71	14.64	14.58	13.89	14.46	14.39
CaO	22.90	22.75	22.21	22.44	22.46	22.97	21.69	21.24	21.42	21.86	21.20	21.82	21.07	19.04	18.12	21.79	22.12	22.21	21.77
Na_2O	0.21	0.21	0.25	0.25	0.26	0.26	0.10	0.26	0.31	0.25	0.28	0.27	0.33	0.05	0.05	0.38	0.36	0.27	0.34
Cr_2O_3	0.15	0.15	0.20	0.22	0.23	0.23	0.04	0.02	0.04	0.01	0.02	0.05	0.01	0.02	0.02	0.06	0.02	0.02	0.02
NiO	0.05	0.05	0.05	0.05	0.06	0.06	0.05	0.03	0.03	0.05	0.05	0.01	0.04	0.03	0.03	0.04	0.06	0.04	0.06
TOTAL	98.71	99.38	99.85	99.36	98.70	99.41	99.67	99.62	99.79	100.07	100.41	99.50	100.33	99.29	98.47	100.26	99.82	99.65	99.50
Si	1.930	1.951	1.962	1.958	1.943	1.947	1.956	1.967	1.967	1.987	1.953	1.962	1.952	1.954	1.969	1.965	1.977	1.960	1.954
Ti	0.011	0.011	0.002	0.002	0.010	0.010	0.010	0.010	0.010	0.007	0.010	0.010	0.011	0.008	0.008	0.008	0.006	0.008	0.009
Al	0.068	0.064	0.075	0.075	0.065	0.063	0.057	0.054	0.049	0.051	0.052	0.049	0.055	0.072	0.052	0.054	0.056	0.052	0.051
Fe	0.242	0.222	0.234	0.230	0.235	0.222	0.334	0.302	0.300	0.287	0.315	0.300	0.314	0.359	0.386	0.272	0.268	0.269	0.288
Mn	0.005	0.005	0.007	0.007	0.008	0.008	0.010	0.007	0.009	0.008	0.007	0.008	0.009	0.009	0.009	0.007	0.008	0.007	0.009
Mg	0.825	0.826	0.816	0.812	0.825	0.820	0.755	0.791	0.788	0.758	0.814	0.782	0.813	0.827	0.831	0.807	0.772	0.807	0.806
Ca	0.927	0.910	0.883	0.897	0.907	0.920	0.876	0.853	0.859	0.872	0.847	0.880	0.843	0.769	0.739	0.867	0.884	0.891	0.877
Na	0.016	0.016	0.018	0.018	0.020	0.020	0.007	0.019	0.023	0.018	0.020	0.020	0.024	0.004	0.004	0.027	0.026	0.020	0.025
Cr	0.004	0.004	0.006	0.007	0.007	0.007	0.001	0.001	0.001	0.000	0.001	0.001	0.000	0.001	0.001	0.002	0.001	0.001	0.001
Ni	0.002	0.002	0.002	0.002	0.002	0.002	0.002	0.001	0.001	0.002	0.002	0.000	0.001	0.001	0.001	0.001	0.002	0.001	0.002
TOTAL	4.031	4.012	4.005	4.008	4.021	4.018	4.008	4.005	4.008	3.990	4.021	4.012	4.022	4.004	3.999	4.012	4.001	4.015	4.023
At %En	41.37	42.19	42.22	41.88	41.97	41.80	38.42	40.63	40.44	39.52	41.19	39.85	41.26	42.29	42.51	41.48	40.13	41.02	40.90
Fs	12.14	11.35	12.09	11.85	11.93	11.31	16.98	15.53	15.42	14.99	15.93	15.32	15.96	18.39	19.72	13.97	13.94	13.69	14.62
Wo	46.49	46.46	45.69	46.27	46.10	46.89	44.60	43.84	44.13	45.49	42.88	44.84	42.78	39.32	37.77	44.56	45.93	45.29	44.48
MMF	0.773	0.788	0.777	0.780	0.779	0.787	0.693	0.723	0.724	0.725	0.721	0.722	0.721	0.697	0.683	0.748	0.742	0.750	0.737
Al/Cr	15.11	14.51	12.21	11.02	9.13	9.27	47.70	90.93	41.74	172.92	88.70	33.09	187.83	121.49	87.21	30.81	95.40	87.21	86.46

CLINOPYROXENE ANALYSES AND STRUCTURAL FORMULAE BASED ON SIX OXYGENS

	A35/5	A38/1	A38/2	A48/1	A48/2	A52/1	A91/1	A91/2	A91/3	A100/1	A108/1	A108/2	A155/1	A155/2	A155/3	A155/4	A155/5	A193/1	A193/2
SiO_2	52.21	52.37	52.91	52.54	52.92	52.56	52.98	53.12	53.39	52.65	53.02	52.61	52.92	52.43	52.19	52.43	52.35	52.26	51.80
TiO_2	0.31	0.29	0.30	0.32	0.36	0.23	0.22	0.22	0.22	0.30	0.24	0.22	0.33	0.31	0.93	0.32	0.33	0.28	0.28
Al_2O_3	1.19	1.14	1.34	1.24	1.16	1.06	1.26	1.21	1.24	1.12	1.42	1.36	1.17	1.08	1.42	1.13	1.01	1.37	1.67
FeO	9.50	8.73	8.29	9.62	9.60	9.34	9.69	7.85	8.93	7.60	7.33	7.39	7.99	8.48	9.67	7.66	7.65	8.03	8.08
MnO	0.22	0.25	0.22	0.30	0.26	0.29	0.24	0.24	0.24	0.20	0.24	0.24	0.24	0.25	0.26	0.23	0.22	0.26	0.26
MgO	14.64	14.01	14.03	13.84	14.19	15.56	15.18	14.33	14.75	14.23	14.44	14.73	15.17	15.69	15.98	15.46	15.47	14.45	14.34
CaO	21.35	23.05	22.87	21.76	22.03	20.61	21.16	22.69	21.65	22.93	22.95	22.39	22.04	20.88	20.58	22.06	22.11	22.88	22.65
Na_2O	0.32	0.29	0.33	0.22	0.28	0.32	0.41	0.41	0.41	0.15	0.38	0.41	0.26	0.23	0.10	0.30	0.33	0.12	0.12
Cr_2O_3	0.02	0.04	0.02	0.03	0.04	0.04	0.02	0.02	0.04	0.03	0.05	0.06	0.03	0.04	0.06	0.06	0.03	0.03	0.06
NiO	0.04	0.03	0.03	0.02	0.05	0.04	0.05	0.05	0.05	0.05	0.05	0.05	0.07	0.03	0.07	0.01	0.06	0.08	0.08
TOTAL	99.80	100.69	100.34	99.89	100.89	100.05	101.20	100.14	100.91	99.26	100.12	99.96	100.22	99.42	101.26	99.66	99.56	99.75	99.34
Si	1.956	1.963	1.965	1.967	1.963	1.958	1.955	1.972	1.969	1.971	1.965	1.958	1.962	1.959	1.925	1.954	1.954	1.952	1.943
Ti	0.009	0.008	0.008	0.009	0.010	0.007	0.006	0.006	0.006	0.008	0.007	0.006	0.009	0.009	0.026	0.009	0.009	0.008	0.008
Al	0.053	0.050	0.059	0.055	0.051	0.047	0.055	0.053	0.054	0.049	0.062	0.060	0.051	0.048	0.062	0.050	0.044	0.060	0.074
Fe	0.298	0.271	0.258	0.301	0.298	0.291	0.299	0.244	0.275	0.238	0.227	0.246	0.248	0.265	0.298	0.239	0.239	0.251	0.254
Mn	0.007	0.008	0.007	0.010	0.008	0.009	0.007	0.008	0.008	0.006	0.008	0.008	0.008	0.008	0.008	0.008	0.007	0.009	0.009
Mg	0.817	0.775	0.777	0.772	0.784	0.864	0.834	0.793	0.810	0.794	0.798	0.817	0.838	0.874	0.878	0.859	0.861	0.805	0.803
Ca	0.857	0.917	0.910	0.873	0.875	0.822	0.837	0.903	0.856	0.920	0.912	0.893	0.875	0.836	0.813	0.881	0.884	0.916	0.910
Na	0.023	0.021	0.024	0.016	0.020	0.024	0.029	0.030	0.030	0.011	0.027	0.030	0.019	0.017	0.007	0.022	0.024	0.009	0.009
Cr	0.001	0.001	0.001	0.001	0.001	0.001	0.001	0.001	0.001	0.001	0.001	0.002	0.001	0.001	0.002	0.002	0.001	0.001	0.002
Ni	0.001	0.001	0.001	0.001	0.001	0.002	0.001	0.002	0.002	0.002	0.002	0.002	0.002	0.001	0.002	0.000	0.002	0.002	0.002
TOTAL	4.021	4.014	4.009	4.001	4.012	4.024	4.025	4.010	4.012	4.001	4.010	4.020	4.012	4.016	4.021	4.022	4.026	4.013	4.015
At %En	41.45	39.49	39.95	39.68	40.07	43.69	42.31	40.88	41.73	60.68	41.18	41.79	42.74	44.25	44.14	43.41	43.39	40.83	40.82
Fs	15.09	13.81	13.24	15.48	15.21	14.71	15.19	12.57	14.19	12.19	11.75	12.56	12.63	13.42	14.99	12.07	12.04	12.72	12.90
Wo	43.45	46.70	46.81	44.84	44.72	41.60	42.49	46.55	44.08	47.12	47.07	45.66	44.63	42.33	40.87	44.52	44.57	46.44	46.28
MMF	0.733	0.741	0.751	0.719	0.725	0.748	0.736	0.765	0.746	0.769	0.778	0.769	0.772	0.767	0.747	0.782	0.783	0.762	0.760
Al/Cr	88.70	42.48	99.88	61.62	43.23	39.50	63.11	60.62	46.58	55.65	42.63	28.96	58.14	40.25	35.28	28.08	50.19	68.08	41.74

CLINOPYROXENE ANALYSES AND STRUCTURAL FORMULAE BASED ON SIX OXYGENS

	A193/3	A208/1	A208/2	A213/1	A213/2	A238/1	A245/1	A245/2	A245/3	A245/4	A247/1	A247/2	A255/1	A257/1	A257/2	A266/1	A266/2	A284/1	A284/2
SiO_2	53.07	52.63	53.17	52.81	53.15	51.46	51.48	52.61	52.26	52.52	52.72	52.44	53.34	53.56	53.05	52.91	52.88	53.46	53.15
TiO_2	0.28	0.28	0.28	0.29	0.35	0.56	0.24	0.24	0.18	0.19	0.28	0.28	0.28	0.32	0.32	0.34	0.23	0.33	0.36
Al_2O_3	1.45	1.47	1.32	1.99	1.39	2.09	1.25	1.05	1.28	1.08	1.28	1.11	1.39	1.09	1.09	1.50	1.30	1.40	1.44
FeO	10.52	7.48	7.08	6.82	7.56	14.93	9.91	11.23	10.55	10.46	9.90	9.40	7.41	8.43	8.26	6.45	6.10	6.53	6.73
MnO	0.26	0.26	0.26	0.16	0.22	-	0.28	0.33	0.27	0.30	0.26	0.26	0.26	0.23	0.23	0.17	0.23	0.19	0.21
MgO	16.17	15.11	15.15	14.15	15.35	12.61	12.30	12.90	12.29	12.71	12.82	13.39	15.43	15.21	15.01	14.85	14.71	15.67	15.28
CaO	18.46	22.56	23.01	22.86	21.13	17.79	22.41	20.58	22.89	22.94	22.73	22.80	21.90	22.01	22.30	23.13	23.50	22.07	22.18
Na_2O	0.12	0.11	0.11	0.39	0.30	-	0.24	0.06	0.22	0.13	0.12	0.12	0.11	0.22	0.22	0.27	0.33	0.21	0.21
Cr_2O_3	0.02	0.07	0.08	0.03	0.08	0.11	0.04	0.04	0.04	0.06	0.04	0.06	0.18	0.12	0.12	0.25	0.27	0.28	0.29
NiO	0.08	0.07	0.02	0.05	0.04	-	0.02	0.07	0.01	0.01	0.07	0.07	0.07	0.06	0.06	0.07	0.04	0.07	0.02
TOTAL	100.43	100.04	100.48	99.55	99.57	99.55	98.17	99.11	99.99	100.40	100.22	99.92	100.37	101.25	100.66	99.94	99.59	100.21	99.87
Si	1.963	1.952	1.960	1.963	1.972	1.955	1.971	1.991	1.969	1.970	1.973	1.966	1.965	1.966	1.961	1.959	1.965	1.967	1.965
Ti	0.008	0.008	0.008	0.008	0.010	0.016	0.007	0.007	0.005	0.005	0.008	0.008	0.008	0.009	0.009	0.009	0.006	0.009	0.010
Al	0.063	0.065	0.058	0.087	0.061	0.094	0.056	0.047	0.057	0.048	0.057	0.049	0.060	0.047	0.047	0.065	0.057	0.061	0.063
Fe	0.326	0.232	0.218	0.212	0.235	0.474	0.317	0.355	0.332	0.328	0.310	0.295	0.228	0.259	0.255	0.200	0.190	0.201	0.208
Mn	0.008	0.008	0.008	0.005	0.007	-	0.009	0.011	0.009	0.010	0.009	0.009	0.008	0.007	0.007	0.005	0.007	0.006	0.007
Mg	0.891	0.836	0.832	0.784	0.849	0.714	0.702	0.728	0.690	0.711	0.715	0.748	0.847	0.832	0.827	0.820	0.815	0.859	0.842
Ca	0.732	0.896	0.909	0.910	0.840	0.724	0.919	0.834	0.924	0.922	0.911	0.916	0.865	0.866	0.883	0.918	0.936	0.870	0.879
Na	0.009	0.008	0.009	0.028	0.022	-	0.018	0.004	0.014	0.009	0.009	0.009	0.009	0.016	0.016	0.019	0.024	0.015	0.015
Cr	0.001	0.002	0.003	0.001	0.002	0.003	0.001	0.001	0.001	0.002	0.001	0.002	0.006	0.003	0.004	0.007	0.008	0.008	0.008
Ni	0.002	0.002	0.001	0.002	0.001	-	0.001	0.002	0.000	0.000	0.002	0.002	0.002	0.002	0.002	0.002	0.001	0.002	0.001
TOTAL	4.002	4.010	4.006	3.999	3.998	3.980	4.002	3.980	4.005	4.005	3.994	4.005	3.998	4.007	4.012	4.005	4.008	3.997	3.997
At %En	45.74	42.55	42.46	41.12	44.13	37.34	36.21	37.95	35.46	36.24	36.93	38.19	43.67	42.53	42.08	42.31	42.00	44.52	43.66
Fs	16.71	11.81	11.14	11.12	12.20	24.80	16.37	18.54	17.08	16.74	16.00	15.06	11.77	13.23	12.99	10.31	9.77	10.41	10.79
Wo	37.55	45.64	46.40	47.76	43.67	37.86	47.42	43.52	47.47	47.02	47.07	46.76	44.56	44.24	44.93	47.37	48.23	45.07	45.55
MMF	0.732	0.783	0.792	0.787	0.783	0.601	0.689	0.672	0.675	0.684	0.698	0.717	0.788	0.763	0.764	0.804	0.811	0.810	0.802
Al/Cr	108.07	27.58	22.03	98.88	25.90	28.32	46.58	39.13	47.70	26.83	38.46	27.58	10.91	13.54	13.54	8.94	7.18	7.45	7.40

CLINOPYROXENE ANALYSES AND STRUCTURAL FORMULAE BASED ON SIX OXYGENS

	A284/3	A284/4	A284/5	A290/1	A295/1	A295/2	A305/1	A305/2	A308/1	A308/2	A309/1	A319/1	A319/2	A327/1	A334/1	A334/2	A334/3	A346/1	A346/2
SiO_2	53.50	52.80	53.22	53.09	54.67	53.05	51.86	52.20	52.67	53.86	53.63	54.72	53.99	53.61	52.47	51.20	52.33	53.47	55.23
TiO_2	0.31	0.27	0.26	0.67	0.60	0.63	0.34	0.34	0.13	0.13	0.36	0.23	0.87	1.42	0.26	0.26	0.26	1.03	0.32
Al_2O_3	1.38	1.19	1.33	1.25	1.12	1.68	1.54	1.54	1.15	0.93	1.46	0.67	1.22	1.43	1.74	1.41	1.41	1.83	0.85
FeO	6.22	6.43	6.62	7.41	9.33	10.36	6.53	6.58	7.06	5.99	6.39	6.78	7.31	6.67	8.09	8.27	8.80	5.99	6.94
MnO	0.17	0.19	0.18	0.18	0.22	0.28	0.18	0.18	0.18	0.18	-	0.20	0.20	0.16	0.24	0.24	0.24	0.18	0.14
MgO	15.90	15.51	15.46	14.61	16.62	16.98	14.97	14.92	15.60	15.22	16.18	13.99	13.58	14.58	14.08	13.85	14.06	14.19	14.51
CaO	22.36	22.27	22.03	21.51	18.91	18.11	22.51	21.98	22.42	23.48	22.41	23.41	22.78	21.56	22.62	22.58	22.65	22.50	23.32
Na_2O	0.33	0.26	0.31	-	-	-	0.17	0.17	0.20	0.20	0.71	-	-	-	0.23	0.23	0.23	-	-
Cr_2O_3	0.27	0.24	0.27	0.22	0.20	0.23	0.36	0.27	0.21	0.28	0.23	0.04	0.21	0.32	0.42	0.22	0.14	0.21	0.14
NiO	0.05	0.08	0.02	0.03	0.08	0.08	0.05	0.05	0.08	0.08	-	-	-	-	0.08	0.08	0.08	0.01	0.04
TOTAL	100.49	99.24	99.70	98.97	101.75	101.39	98.51	98.23	99.69	100.34	101.37	100.04	99.96	99.75	100.23	98.34	100.20	99.41	101.48
Si	1.962	1.965	1.969	1.980	1.981	1.941	1.949	1.962	1.957	1.980	1.952	2.017	1.992	1.976	1.951	1.947	1.952	1.975	2.006
Ti	0.009	0.008	0.007	0.019	0.016	0.017	0.010	0.010	0.004	0.004	0.010	0.006	0.024	0.039	0.007	0.007	0.008	0.029	0.009
Al	0.060	0.052	0.058	0.055	0.048	0.072	0.068	0.068	0.050	0.040	0.063	0.029	0.053	0.062	0.076	0.063	0.062	0.080	0.036
Fe	0.191	0.200	0.205	0.231	0.283	0.317	0.205	0.207	0.220	0.184	0.195	0.209	0.226	0.206	0.252	0.263	0.275	0.185	0.211
Mn	0.005	0.006	0.006	0.006	0.007	0.009	0.006	0.006	0.006	0.006	-	0.006	0.006	0.005	0.007	0.007	0.008	0.006	0.004
Mg	0.869	0.860	0.853	0.812	0.896	0.926	0.839	0.836	0.864	0.833	0.878	0.769	0.747	0.801	0.780	0.787	0.782	0.781	0.786
Ca	0.879	0.888	0.873	0.860	0.734	0.710	0.906	0.885	0.892	0.925	0.874	0.924	0.900	0.851	0.901	0.920	0.906	0.891	0.908
Na	0.023	0.019	0.022	-	-	-	0.012	0.012	0.017	0.015	0.050	-	-	-	0.017	0.016	0.017	-	-
Cr	0.008	0.007	0.008	0.006	0.006	0.007	0.011	0.008	0.006	0.008	0.007	0.001	0.006	0.009	0.012	0.007	0.004	0.006	0.004
Ni	0.001	0.002	0.001	0.001	0.002	0.002	0.002	0.002	0.002	0.002	-	-	-	-	0.003	0.002	0.002	0.000	0.001
TOTAL	4.007	4.007	4.002	3.970	3.975	4.002	4.008	3.996	4.019	3.999	4.028	3.962	3.954	3.949	4.006	4.019	4.016	3.953	3.965
At %En	44.84	44.16	44.16	42.68	46.89	47.42	43.00	43.35	43.73	42.90	45.10	40.41	39.88	43.11	40.37	39.95	39.86	42.08	41.26
Fs	9.84	10.27	10.61	12.15	14.77	16.23	10.52	10.73	11.11	9.48	9.99	10.99	12.04	11.07	13.01	13.36	14.00	9.97	11.07
Wo	45.32	45.57	45.23	45.17	38.35	36.35	46.48	45.91	45.15	47.63	44.90	48.60	48.08	45.82	46.62	46.70	46.14	47.96	47.67
MMF	0.820	0.811	0.806	0.778	0.760	0.745	0.803	0.802	0.797	0.819	0.819	0.786	0.768	0.796	0.756	0.749	0.740	0.809	0.788
Al/Cr	7.62	7.39	7.34	8.47	8.35	10.89	6.38	8.50	8.16	4.78	9.46	24.97	8.66	6.66	6.18	9.14	15.12	12.99	8.94

PLAGIOCLASE ANALYSES AND STRUCTURAL FORMULAE BASED ON EIGHT OXYGENS

SAMPLE	SiO_2	Al_2O_3	FeO	CaO	Na_2O	K_2O	TOTAL	Si	Al	Fe	Ca	Na	K	TOTAL	An	Ab	Or
MZ7/1:I	50.30	31.85	0.41	14.86	3.04	0.18	100.64	2.284	1.702	0.016	0.723	0.267	0.011	5.004	72.19	26.71	1.10
MZ7/2:C	51.28	31.30	0.43	14.29	3.53	0.22	101.04	2.318	1.664	0.016	0.692	0.308	0.013	5.011	68.29	30.40	1.31
MZ7/3:I	51.95	31.31	0.48	13.85	3.69	0.22	101.49	2.334	1.654	0.018	0.667	0.320	0.013	5.006	66.66	32.03	1.32
MZ7/4:I	52.07	31.29	0.35	13.88	3.68	0.22	101.49	2.338	1.651	0.014	0.668	0.319	0.013	5.003	66.78	31.91	1.32
MZ7/5:I	50.57	31.54	0.35	14.93	2.98	0.19	100.56	2.296	1.687	0.013	0.727	0.262	0.012	4.997	72.63	26.22	1.16
MZ4/1:I	50.67	31.80	0.49	15.03	2.65	0.18	100.81	2.294	1.694	0.019	0.729	0.233	0.011	4.980	74.97	23.90	1.13
MZ4/2:C	50.04	31.86	0.40	15.26	3.00	0.18	100.74	2.274	1.704	0.015	0.744	0.264	0.011	5.012	72.99	25.93	1.08
MZ4/3:C	50.02	31.81	0.43	15.20	2.67	0.18	100.31	2.279	1.707	0.017	0.742	0.237	0.011	4.992	74.98	23.91	1.12
MZ4/4:C	50.37	31.83	0.54	14.95	2.76	0.18	100.62	2.287	1.701	0.021	0.727	0.243	0.012	4.991	74.04	24.72	1.24
MZ4/5:I	50.90	31.53	0.46	14.71	2.71	0.22	100.52	2.308	1.683	0.018	0.715	0.238	0.013	4.975	74.02	24.66	1.32
MZ2/1:C	50.81	31.53	0.37	14.59	2.85	0.22	100.36	2.307	1.686	0.014	0.710	0.251	0.014	4.982	72.84	25.73	1.43
MZ2/2:C	51.14	31.58	0.45	14.41	3.09	0.22	100.89	2.312	1.680	0.017	0.699	0.270	0.012	4.989	71.25	27.52	1.23
MZ2/3:C	50.93	31.61	0.43	14.88	3.20	0.22	101.27	2.300	1.678	0.017	0.720	0.279	0.013	5.007	71.17	27.58	1.25
MZ2/4:I	51.08	31.58	0.45	14.83	3.02	0.22	101.18	2.307	1.677	0.017	0.717	0.263	0.012	4.992	72.30	26.54	1.16
MZ2/5:I	51.15	31.62	0.41	14.76	3.34	0.22	101.49	2.305	1.674	0.015	0.712	0.291	0.013	5.010	70.08	28.68	1.24
MZ1/1:C	54.24	29.08	0.31	11.77	4.51	0.39	100.30	2.447	1.545	0.012	0.569	0.394	0.022	4.989	57.71	40.02	2.28
MZ1/2:C	54.82	29.11	0.29	11.88	4.78	0.39	101.27	2.450	1.535	0.011	0.569	0.413	0.019	4.998	56.82	41.25	1.93
MZ1/3:C	54.16	29.32	0.39	12.33	4.24	0.39	100.83	2.435	1.551	0.015	0.594	0.368	0.022	4.985	60.32	37.42	2.27
MZ1/4:I	54.41	29.29	0.25	12.08	4.28	0.39	100.70	2.445	1.549	0.010	0.582	0.373	0.018	4.976	59.80	38.31	1.88
MZ1/5:I	54.56	29.34	0.36	12.14	4.45	0.39	101.24	2.442	1.544	0.014	0.583	0.385	0.022	4.990	58.86	38.89	2.25
A5/1:I	54.25	29.10	0.47	12.04	4.49	0.30	100.65	2.441	1.543	0.018	0.580	0.392	0.017	4.992	58.67	39.59	1.74
A5/2:I	54.31	29.19	0.33	11.56	4.62	0.27	100.27	2.447	1.550	0.012	0.558	0.404	0.016	4.987	57.11	41.30	1.59

PLAGIOCLASE ANALYSES AND STRUCTURAL FORMULAE BASED ON EIGHT OXYGENS

SAMPLE	SiO_2	Al_2O_3	FeO	CaO	Na_2O	K_2O	TOTAL	Si	Al	Fe	Ca	Na	K	TOTAL	An	Ab	Or
A5/3:I	54.78	28.92	0.32	11.49	4.74	0.28	100.53	2.461	1.532	0.012	0.553	0.413	0.016	4.987	56.32	42.05	1.63
A5/4:C	52.28	30.23	0.61	13.29	3.71	0.19	100.31	2.370	1.615	0.023	0.645	0.326	0.011	4.991	65.69	33.19	1.12
A5/5:C	52.81	29.96	0.29	12.42	3.89	0.22	99.59	2.400	1.605	0.011	0.605	0.343	0.013	4.976	62.98	35.69	1.33
A5/6:C	53.72	28.96	0.36	12.80	4.34	0.33	100.51	2.427	1.542	0.014	0.620	0.380	0.019	5.002	60.82	37.32	1.87
A5/7:I	54.70	28.58	0.36	11.91	4.82	0.35	100.71	2.460	1.515	0.014	0.574	0.420	0.020	5.003	56.58	41.44	1.98
A35/1:I	54.23	28.47	0.46	11.18	4.73	0.25	99.32	2.466	1.526	0.017	0.545	0.417	0.015	4.986	55.80	42.72	1.49
A35/2:I	54.09	28.92	0.54	11.65	4.69	0.27	100.16	2.445	1.541	0.020	0.564	0.411	0.016	4.998	56.94	41.48	1.57
A35/3:C	52.79	29.13	0.31	12.16	4.38	0.28	99.05	2.416	1.571	0.012	0.596	0.389	0.016	5.001	59.55	38.82	1.63
A35/4:C	53.40	28.84	0.31	11.88	4.58	0.35	99.36	2.435	1.550	0.012	0.580	0.405	0.020	5.003	57.71	40.26	2.02
A35/5:C	53.46	29.04	0.63	12.21	4.24	0.33	99.91	2.427	1.554	0.024	0.594	0.373	0.019	4.992	60.22	37.84	1.94
A35/6:C	52.60	29.82	0.57	12.81	3.76	0.24	99.80	2.392	1.598	0.022	0.624	0.332	0.014	4.982	64.37	34.19	1.44
A35/7:C	53.62	29.03	0.37	12.06	4.54	0.30	99.92	2.432	1.552	0.014	0.586	0.399	0.017	5.000	58.45	39.82	1.73
A35/8:C	54.54	28.99	0.37	11.96	4.57	0.31	100.74	2.450	1.535	0.014	0.576	0.398	0.018	4.990	58.06	40.15	1.79
A48/1:I	54.34	29.52	0.27	12.37	4.70	0.32	101.52	2.429	1.551	0.010	0.592	0.405	0.018	5.007	58.31	39.89	1.79
A48/2:I	54.58	29.20	0.32	12.04	4.56	0.22	100.92	2.447	1.541	0.012	0.579	0.395	0.013	4.986	58.65	40.08	1.27
A48/3:I	54.29	29.41	0.29	12.47	4.71	0.33	101.50	2.429	1.547	0.011	0.598	0.406	0.019	5.010	58.39	39.71	1.89
A48/4:C	54.20	29.81	0.40	12.96	4.58	0.25	102.20	2.413	1.558	0.015	0.618	0.393	0.015	5.012	60.26	38.31	1.44
A48/5:C	54.32	29.26	0.36	12.31	4.51	0.33	101.09	2.437	1.544	0.013	0.592	0.391	0.019	4.996	59.07	39.05	1.88
A48/6:I	53.73	29.27	0.28	12.00	4.73	0.33	100.33	2.428	1.558	0.011	0.581	0.414	0.019	5.010	57.29	40.83	1.87
A91/1:C	54.16	29.93	0.31	12.43	4.44	0.34	101.60	2.418	1.570	0.012	0.595	0.383	0.020	4.998	59.60	38.41	2.00
A91/2:I	52.98	30.13	0.28	12.95	4.71	0.32	101.37	2.382	1.592	0.011	0.624	0.408	0.018	5.035	59.37	38.88	1.75
A91/3:I	53.01	29.96	0.29	12.74	4.57	0.34	100.91	2.390	1.589	0.011	0.616	0.398	0.020	5.025	59.53	38.53	1.95

PLAGIOCLASE ANALYSES AND STRUCTURAL FORMULAE BASED ON EIGHT OXYGENS

SAMPLE	SiO_2	Al_2O_3	FeO	CaO	Na_2O	K_2O	TOTAL	Si	Al	Fe	Ca	Na	K	TOTAL	An	Ab	Or
A91/4:I	53.24	29.92	0.30	12.51	4.38	0.34	100.69	2.400	1.588	0.012	0.604	0.383	0.020	5.007	60.01	37.99	2.00
A91/5:C	51.71	29.87	0.38	14.04	3.57	0.34	99.91	2.360	1.607	0.015	0.687	0.317	0.020	5.005	67.12	30.95	1.93
A108/1:C	51.09	30.76	0.33	14.10	3.34	0.26	99.88	2.331	1.654	0.013	0.689	0.295	0.015	4.997	68.94	29.55	1.51
A108/2:C	52.39	30.35	0.36	13.71	3.75	0.31	100.86	2.364	1.614	0.014	0.663	0.328	0.018	5.001	65.71	32.52	1.77
A108/3:I	52.22	29.19	0.38	13.49	3.73	0.33	99.34	2.392	1.576	0.015	0.662	0.331	0.019	4.995	65.38	37.71	1.90
A108/4:C	51.83	29.47	0.89	13.41	3.39	0.24	99.23	2.379	1.594	0.034	0.659	0.302	0.014	4.982	67.62	30.94	1.44
A108/5:I	51.87	30.50	0.38	13.98	3.55	0.25	100.53	2.350	1.629	0.014	0.679	0.312	0.014	4.998	67.53	31.03	1.44
A108/6:C	51.85	28.91	0.60	14.20	3.50	0.25	99.31	2.383	1.566	0.023	0.699	0.312	0.015	4.997	68.17	30.40	1.43
A108/7:C	51.75	30.13	0.42	13.89	3.81	0.27	100.26	2.354	1.615	0.016	0.677	0.336	0.016	5.014	65.81	32.67	1.52
A108/8:C	51.83	30.32	0.44	14.14	3.62	0.28	100.62	2.350	1.620	0.017	0.687	0.318	0.016	5.008	67.26	31.16	1.59
A155/1:C	53.18	30.00	0.25	12.81	3.95	0.29	100.48	2.399	1.595	0.009	0.619	0.345	0.017	4.985	63.09	35.21	1.70
A155/2:C	52.94	29.97	0.21	12.62	4.04	0.33	100.11	2.397	1.599	0.008	0.612	0.355	0.019	4.990	62.09	35.97	1.93
A155/3:C	52.75	30.10	0.25	13.00	3.82	0.28	100.20	2.388	1.606	0.009	0.630	0.335	0.016	4.985	64.21	34.14	1.65
A155/4:C	52.54	29.89	0.23	12.47	4.16	0.33	99.62	2.392	1.604	0.009	0.608	0.368	0.019	5.000	61.10	36.97	1.93
A155/5:C	52.85	30.04	0.34	12.93	3.70	0.27	100.23	2.390	1.601	0.013	0.627	0.324	0.016	4.972	64.82	33.57	1.61
A208/1:C	51.48	31.60	0.34	14.91	3.19	0.21	101.72	2.312	1.667	0.013	0.717	0.277	0.013	4.999	71.26	27.49	1.25
A208/2:C	52.71	30.45	0.30	13.72	3.71	0.25	101.14	2.371	1.611	0.012	0.661	0.322	0.014	4.992	66.25	32.31	1.44
A208/3:C	51.38	31.23	0.30	14.81	3.20	0.21	101.13	2.319	1.658	0.012	0.716	0.280	0.013	4.998	71.00	27.74	1.25
A208/4:I	52.09	30.96	0.32	14.22	3.59	0.27	101.45	2.342	1.636	0.012	0.685	0.312	0.016	5.004	67.64	30.77	1.58
A244/1:C	50.72	31.41	0.25	15.12	3.13	0.12	100.75	2.300	1.676	0.009	0.735	0.275	0.007	5.003	72.26	27.05	0.68
A244/2:C	52.13	30.89	0.22	14.08	3.65	0.23	101.20	2.347	1.636	0.009	0.679	0.317	0.014	5.001	67.21	31.42	1.36
A244/3:C	51.72	30.94	0.28	14.48	3.48	0.19	101.09	2.334	1.642	0.011	0.700	0.303	0.011	5.002	69.01	29.91	1.08

PLAGIOCLASE ANALYSES AND STRUCTURAL FORMULAE BASED ON EIGHT OXYGENS

SAMPLE	SiO_2	Al_2O_3	FeO	CaO	Na_2O	K_2O	TOTAL	Si	Al	Fe	Ca	Na	K	TOTAL	An	Ab	Or
A244/4:C	52.26	31.28	0.25	14.25	3.72	0.16	101.92	2.338	1.643	0.009	0.683	0.321	0.010	5.006	67.36	31.69	0.96
A245/1:C	51.95	31.08	0.22	14.08	3.19	0.13	100.65	2.344	1.653	0.008	0.681	0.279	0.007	4.973	70.37	28.85	0.77
A245/2:C	52.31	30.79	0.26	13.56	3.82	0.18	100.92	2.356	1.634	0.010	0.654	0.334	0.010	4.999	65.55	33.42	1.04
A247/1:C	52.36	31.04	0.17	14.23	3.53	0.15	101.48	2.349	1.637	0.006	0.684	0.306	0.009	4.990	68.51	30.63	0.86
A247/2:I	51.29	31.36	0.18	14.71	3.43	0.01	100.98	2.316	1.666	0.007	0.712	0.300	0.001	5.001	70.30	29.64	0.06
A247/3:I	51.82	31.49	0.18	14.27	3.66	0.00	101.42	2.327	1.662	0.007	0.686	0.318	0.000	5.000	68.37	31.63	0.00
A247:4:C	50.58	31.66	0.21	15.25	3.23	0.14	101.06	2.289	1.685	0.008	0.739	0.283	0.008	5.014	71.74	27.48	0.76
A247/5:C	50.94	31.44	0.23	14.80	3.10	0.20	100.71	2.308	1.676	0.009	0.719	0.217	0.012	4.995	71.75	27.09	1.15
A247/6:I	51.57	31.24	0.22	14.62	3.29	0.20	101.14	2.325	1.657	0.008	0.707	0.287	0.012	4.996	70.30	28.50	1.20
A255/1:C	52.56	30.83	0.14	13.75	3.85	0.22	101.34	2.359	1.627	0.006	0.662	0.334	0.013	5.001	65.59	33.10	1.30
A255/2:C	50.47	31.23	0.16	14.97	3.35	0.18	100.36	2.298	1.676	0.006	0.730	0.296	0.010	5.017	70.46	28.53	1.01
A255/3:C	52.80	29.45	0.18	14.09	3.97	0.22	100.70	2.388	1.570	0.007	0.683	0.348	0.013	5.009	65.42	33.36	1.22
A255/4:I	52.03	29.83	0.21	14.92	3.66	0.20	100.84	2.357	1.592	0.008	0.724	0.321	0.012	5.014	68.50	30.41	1.09
A255/5:I	52.98	28.41	0.45	14.33	3.92	0.22	100.31	2.410	1.523	0.017	0.698	0.346	0.013	5.007	66.08	32.71	1.21
A255/6:I	51.25	28.90	0.92	14.50	3.57	0.17	99.31	2.364	1.571	0.035	0.716	0.319	0.010	5.016	68.52	30.53	0.96
A255/7:C	52.57	29.45	0.35	13.87	3.92	0.17	100.33	2.386	1.575	0.013	0.674	0.345	0.010	5.004	65.53	33.51	0.96
A255/8:I	52.43	30.26	0.20	13.92	3.63	0.25	100.69	2.368	1.611	0.008	0.674	0.318	0.014	4.993	66.97	31.60	1.43
A266/1:I	51.61	31.45	0.19	14.23	3.33	0.25	101.06	2.326	1.667	0.007	0.687	0.291	0.014	4.993	69.25	29.30	1,45
A266/2:I	51.85	30.38	0.15	13.69	3.32	0.21	99.60	2.362	1.632	0.006	0.668	0.294	0.012	4.975	68.57	30.18	1.25
A266/3:C	52.11	31.09	0.14	14.07	3.63	0.20	101.24	2.344	1.644	0.006	0.678	0.315	0.011	4.998	67.48	31.38	1.14
A266/4:C	53.57	30.37	0.16	12.81	3.91	0.25	101.06	2.400	1.601	0.006	0.615	0.339	0.015	4.976	63.51	34.96	1.53
A266/5:C	51.99	31.59	0.16	14.69	3.26	0.24	101.92	2.326	1.660	0.006	0.704	0.282	0.014	4.992	70.41	28.17	1.43

PLAGIOCLASE ANALYSES AND STRUCTURAL FORMULAE BASED ON EIGHT OXYGENS

SAMPLE	SiO_2	Al_2O_3	FeO	CaO	Na_2O	K_2O	TOTAL	Si	Al	Fe	Ca	Na	K	TOTAL	An	Ab	Or
A266/6:I	52.62	30.62	0.14	13.69	3.49	0.23	100.79	2.370	1.623	0.006	0.661	0.305	0.014	4.978	67.48	31.11	1.41
A284/1:C	51.40	30.24	0.33	13.37	4.06	0.32	99.72	2.350	1.629	0.013	0.655	0.360	0.019	5.025	63.37	34.82	1.81
A284/2:C	50.70	31.03	0.31	14.34	3.30	0.24	99.92	2.315	1.670	0.012	0.701	0.292	0.014	5.004	69.62	28.99	1.39
A284/3:C	52.30	30.34	0.27	13.21	3.82	0.33	100.27	2.370	1.620	0.010	0.641	0.336	0.019	4.997	64.39	33.70	1.92
A284/4:C	52.13	30.43	0.37	13.48	3.61	0.31	100.33	2.363	1.626	0.014	0.655	0.317	0.018	4.992	66.14	32.05	1.81
A284/5:C	51.10	30.80	0.39	13.65	3.53	0.23	99.70	2.334	1.658	0.015	0.668	0.313	0.013	5.000	67.20	31.45	1.35
A284/6:C	52.92	29.96	0.26	12.58	3.98	0.33	100.03	2.398	1.600	0.010	0.611	0.350	0.019	4.987	62.35	35.70	1.95
A284/7:C	51.77	30.52	0.26	13.23	3.39	0.23	99.40	2.362	1.641	0.010	0.647	0.300	0.013	4.974	67.37	31.24	1.39
A284/8:C	52.51	30.30	0.24	13.00	3.70	0.30	100.05	2.380	1.619	0.009	0.631	0.325	0.017	4.982	64.83	33.39	1.78
A295/1:C	52.49	30.32	0.23	13.44	3.61	0.30	100.39	2.374	1.616	0.009	0.651	0.317	0.017	4.985	66.11	32.13	1.76
A295/2:I	52.39	29.89	0.23	13.69	3.49	0.32	100.01	2.380	1.601	0.009	0.666	0.307	0.019	4.982	67.15	30.98	1.87
A295/3:I	52.19	30.21	0.32	13.50	3.81	0.27	100.29	2.367	1.614	0.012	0.656	0.335	0.016	5.001	65.15	33.25	1.61
A295/4:I	52.69	30.22	0.21	13.26	4.08	0.27	100.72	2.378	1.605	0.008	0.641	0.357	0.016	5.006	63.23	35.18	1.59
A295/5:I	51.50	30.22	0.34	13.79	3.74	0.27	99.86	2.350	1.625	0.013	0.675	0.331	0.016	5.011	66.02	32.38	1.59
A295/6:C	51.18	30.19	0.27	13.81	3.60	0.27	99.32	2.346	1.633	0.011	0.678	0.321	0.016	5.006	66.79	31.60	1.61
A308/1:C	51.00	30.25	0.32	14.02	3.91	0.27	99.77	2.334	1.632	0.012	0.688	0.348	0.016	5.031	65.39	33.06	1.55
A308/2:C	51.42	31.17	0.26	14.17	3.83	0.21	101.06	2.323	1.656	0.010	0.686	0.334	0.013	5.022	66.40	32.37	1.23
A308/3:I	51.30	31.07	0.29	14.65	3.08	0.21	100.60	2.325	1.657	0.011	0.711	0.270	0.013	4.988	71.53	27.19	1.28
A308/4:I	52.65	30.09	0.35	13.67	3.48	0.21	100.45	2.381	1.602	0.014	0.662	0.305	0.013	4.977	67.59	31.12	1.29
A308/5:I	52.88	30.09	0.32	13.85	3.51	0.21	100.86	2.383	1.596	0.012	0.669	0.306	0.013	4.978	67.76	30.96	1.28
A308/6:C	51.57	31.30	0.24	14.61	3.03	0.21	100.96	2.327	1.662	0.009	0.706	0.264	0.013	4.981	71.85	26.86	1.29
A308/7:I	52.75	30.65	0.32	13.61	3.52	0.21	101.06	2.371	1.621	0.012	0.656	0.306	0.013	4.978	67.27	31.44	1.29

PLAGIOCLASE ANALYSES AND STRUCTURAL FORMULAE BASED ON EIGHT OXYGENS

SAMPLE	SiO_2	Al_2O_3	FeO	CaO	Na_2O	K_2O	TOTAL	Si	Al	Fe	Ca	Na	K	TOTAL	An	Ab	Or
A319/1:C	51.75	30.97	0.25	14.06	3.47	0.22	100.72	2.339	1.649	0.009	0.681	0.304	0.013	4.995	68.25	30.48	1.27
A319/2:C	51.86	30.75	0.21	13.97	3.58	0.34	100.71	2.345	1.639	0.008	0.677	0.314	0.020	5.002	66.99	31.07	1.94
A319/3:C	52.10	30.65	0.23	13.80	3.83	0.27	100.88	2.352	1.630	0.009	0.667	0.335	0.016	5.009	65.55	32.92	1.53
A319/4:C	50.35	31.36	0.21	15.12	3.03	0.19	100.26	2.294	1.684	0.008	0.738	0.268	0.011	5.003	72.59	26.32	1.09
A319/5:I	52.33	30.38	0.16	13.58	3.81	0.25	100.51	2.366	1.619	0.006	0.658	0.334	0.014	4.998	65.38	33.19	1.43
A327/1:I	53.13	30.61	0.27	13.34	3.72	0.29	101.36	2.380	1.613	0.010	0.640	0.322	0.017	4.983	65.39	32.86	1.75
A327/2:I	52.55	30.59	0.30	13.91	3.36	0.29	100.99	2.366	1.620	0.011	0.671	0.293	0.017	4.979	68.38	29.87	1.75
A327/3:C	51.91	30.62	0.26	14.22	3.53	0.29	100.83	2.347	1.629	0.010	0.689	0.309	0.017	5.002	67.84	30.46	1.70
A327/4:I	52.74	30.71	0.31	13.53	3.73	0.29	101.30	2.368	1.621	0.012	0.651	0.323	0.017	4.992	65.64	32.63	1.73
A346/1:I	50.91	29.77	0.17	14.53	3.25	0.21	98.84	2.346	1.621	0.007	0.717	0.292	0.012	4.996	70.19	28.60	1.21
A346/2:C	50.99	31.90	0.23	14.77	3.04	0.17	101.09	2.300	1.693	0.009	0.714	0.265	0.010	4.991	72.19	26.76	1.05
A346/3:C	50.86	31.74	0.17	14.86	3.09	0.21	100.93	2.299	1.689	0.007	0.720	0.271	0.012	4.998	71.79	27.00	1.21
A346/4:C	50.00	31.70	0.15	15.39	2.72	0.21	100.17	2.280	1.703	0.006	0.752	0.241	0.012	4.995	74.79	23.99	1.21
A346/5:I	50.79	31.76	0.17	14.83	3.20	0.21	100.96	2.297	1.690	0.006	0.719	0.280	0.012	5.004	71.13	27.67	1.20

APPENDIX 8

Basic program to compute elemental strontium and Sr isotope ratios of two-component mixtures, using the method outlined by Faure (1977).

```
100 REMark Program to compute elemental
110 REMark Sr and Sr isotope ratios of
120 REMark two-component mixtures.
130 REMark using eqns. 7.2 & 7.9 of
140 REMark       Faure, G.(1977)
150 REMark PRINCIPLES OF ISOTOPE GEOLOGY:
160 REMark  John Wiley & sons, New York
170 INPUT"Conc. of Sr in component A ? ";Xa
171 INPUT"Sr Ro of component A ? ";Roa
180 INPUT"Conc. of Sr in component B ? ";Xb
200 INPUT"Sr Ro of component B ? ";Rob
210 CLS
220 INPUT"Component ratio A/(A+B) ? ";f
230 PRINT"f","Rom","Sr(mixture)":PRINT
250  Xm=f*(Xa-Xb)+Xb
260  Rom=(Roa*(Xa*f/Xm))+(Rob*(Xb*(1-f)/Xm))
290  Rom=(INT((Rom+5E-5)*10000))/10000
300 PRINT f,Rom,Xm
320 REMark Rom is the initial ratio of
330 REMark the mixture of components A+B
340 REMark Xm is the concentration of
350 REMark elemental Sr in the mixture
360 REMark A+B
```

APPENDIX 9

The computer program MULTIFRACT, which simulates crystallization by Rayleigh fractionation, equilibrium crystallization or orthocumulate fractionation. The formulae employed are as follows:

1. Rayleigh fractionation: $$\frac{C_L}{C_o} = F^{(D-1)}$$

2. Equilibrium crystallization: $$\frac{C_L}{C_o} = \frac{1}{D(1-F)+F}$$

3. Orthocumulate fractionation: $$\frac{C_L}{C_o} = F^{(D-1)(1-X)}$$

Where C_L is the concentration of an element in successive derivative liquids, C_o is the concentration of the element in the parental liquid, F is the weight proportion of liquid remaining in the magma chamber, and D is the bulk distribution coefficient. In the case of equation 3 (orthocumulate fractionation), X is the fraction of intercumulus liquid trapped between the cumulus grains. The formula for orthocumulate fractionation is a modified Rayleigh equation, after Campbell (1987). The composition of the solid phase yielded for different values of C_L is given by the formula:

$$C_S = C_L \times D$$

Note: The program is written in Sinclair SUPERBASIC, as implemented on the Sinclair QL and ICL OPD computers. SUPERBASIC is a non-standard BASIC, employing many PASCAL-like features.

```
100 REMark ******************************
110 REMark * MULTIFRACT :  A program to  *
120 REMark * simulate crystallization by *
130 REMark * Rayleigh fractionation,     *
140 REMark * equilibrium crystallization *
150 REMark * or orthocumulate fractional *
160 REMark * crystallization processes.  *
165 REMark * Output is to a printer.     *
170 REMark ******************************
175 REMark
180 REMark Open channel to printer, set up
190 REMark screen, & dimension variables.
195 REMark
200 OPEN£5,ser1c
210 WINDOW 512,202,0,0:CLS
220 DIM n$(2,2),ic(2),bd(2),mfactor(2)
225 DIM clst(2),fic(2)
230 mfactor(1)=1:mfactor(2)=1
240 bd(1)=0:bd(2)=0:magno=1
245 REMark
250 REMark Enter initial data.
255 REMark
260 PRINT"One or two elements may be ";
270 PRINT"input: If two are input, the "
280 PRINT"first is the numerator for ";
290 PRINT"the ratio calculation."
300 PRINT
310 INPUT "One or two elements? ";noel
320 CLS
330 INPUT "Name of first element? ";n$(1)
340 IF noel =2 THEN
350  INPUT"Name of second element? ";n$(2)
360 END IF
370 CLS
380 DEFine PROCedure frepeat
390  magno=magno+1
400  GO TO 420
410 END DEFine frepeat
420 FOR i=1 TO noel
430  PRINT n$(i);" initial ";
440  INPUT"concentration (in ppm)? ";ic(i)
450  IF magno>1 THEN
451   fic(i)=ic(i)
460   ic(i)=(ic(i)*mf)+mfactor(i)
470  END IF
480 END FOR i
490 CLS
500 PRINT "Initial liquid fraction of ";
510 PRINT"magma No.";magno;" ? ";
520 INPUT li
530 PRINT "Final liquid fraction of ";
540 PRINT"magma No.";magno;" ? ";
550 INPUT fi
560 IF li<fi THEN
570  PRINT"Final liquid fraction must be";
580  PRINT" less than initial fraction !"
590  CLS:GO TO 500
600 END IF
610 CLS
620 PRINT "Fractionation increments : ";
630 INPUT "permitted range 0.01 to 1 ";inc
640 increments=((li-fi)/inc)+1
650 CLS
660 IF inc <1E-2 OR inc > 1 THEN GO TO 620
```

```
670 PRINT "Number of solid phases ";
680 INPUT "fractionating?";s
690 CLS
700 DIM sol$(s,4),dis(s,noel),d(s,noel)
710 DIM prop(s)
720 bd(1)=0:bd(2)=0
730 FOR i = 1 TO s
740  INPUT !"Name of phase "& i !;sol$(i)
750  PRINT "Modal proportion of ";sol$(i);
760  PRINT" in rock (as a fraction of 1)";
770  INPUT" ? ";prop(i)
780  FOR j = 1 TO noel
790   PRINT"Distribution coefficient ";
800   PRINT"for " & n$(j);" ? ";
810   INPUT d(i,j)
820   dis(i,j)=d(i,j)*prop(i)
830   bd(j)=bd(j)+dis(i,j)
840  END FOR j
850  CLS
860 END FOR i
870 frac_type
880 DEFine PROCedure frac_type
890  PRINT"The following types of ";
900  PRINT"crystallization are possible:"
910  PRINT" 1. Rayleigh fractionation"
920  PRINT" 2. Equilibrium xtllization"
930  PRINT" 3. Orthocumulate fractional ";
940  PRINT"xtlization (e.g.Campbell,1986)"
950  INPUT"Enter option (1,2 or 3)";choice
960  IF choice=3 THEN
970   PRINT"Enter proportion of ";
980   PRINT"intercumulus liquid (as a ";
990   INPUT"fraction of 1)";x
1000  END IF
1010 END DEFine frac_type
1011 REMark ******************************
1012 REMark Calculate & print results.
1013 REMark ******************************
1020 DIM c(increments,noel),dat(increments)
1030 DIM cl(increments,noel)
1040 PRINT£5
1050 IF magno=1 THEN
1060  PRINT£5,"Magma No. ";magno
1070 ELSE
1080   PRINT£5,"Magma/mixture No. ";magno
1090 END IF
1100 SELect ON choice
1110  ON choice=1
1120   PRINT£5,"Rayleigh fractionation"
1130  ON choice=2
1140   PRINT£5,"Equilibrium xtlization"
1150  ON choice=3
1160   PRINT£5,"Orthocumulate fractional";
1170   PRINT£5," xtlization: proportion ";
1180   PRINT£5,"of intercumulus fluid=";x
1190  ON choice=REMAINDER
1200   PRINT"Bad parameter: try again!"
1210   frac_type
1220 END SELect
1230 FOR i=1 TO noel
1240  PRINT£5,"Initial concentration of ";
1250  PRINT£5,n$(i);" in new magma = ";
1251  PRINT£5,fic(i);"ppm"
```

```
1260  IF magno>1 THEN PRINT£5,"Conc. in";
1270  PRINT£5," mixture = ";ic(i);"ppm"
1280 END FOR i
1290 PRINT£5,"Crystallizing the ";
1300 PRINT£5,"following";
1310 PRINT£5," minerals in proportions: "
1320 FOR i=1 TO s
1330  PRINT£5,sol$(i);" = ";prop(i);"; ";
1340 END FOR i
1350 PRINT£5
1360 PRINT£5,"Distribution coefficients :"
1370 FOR i=1 TO s
1380  FOR j=1 TO noel
1390   PRINT£5, n$(j);" into ";sol$(i);
1400   PRINT£5," = ";d(i,j);"; ";
1410  END FOR j
1420  PRINT£5
1430 END FOR i
1440 FOR i=1 TO noel
1450  PRINT£5,"Bulk D(";n$(i);")=";bd(i),
1460 END FOR i
1470 PRINT£5:PRINT£5
1480 IF noel=1 THEN
1490  PRINT£5,"Fractionating ";n$(1)
1500 ELSE
1510  PRINT£5,"Fractionating the ratio ";
1520  PRINT£5,n$(1);"/";n$(2)
1530 END IF
1540 PRINT£5:PRINT£5
1550 PRINT£5,"F","Cs"
1560 PRINT£5
1570 loops=1
1580 FOR i=li TO fi STEP -inc
1590  FOR j=1 TO noel
1600   SELect ON choice
1610    ON choice=1
1620     rfrac
1630    ON choice=2
1640     eqxtl
1650    ON choice=3
1660     orthfrac
1700   END SELect
1710   cl(i,j)=c(i,j)/bd(j)
1720  END FOR j
1730  IF noel=2 THEN
1740   dat(i)=c(i,1)/c(i,2)
1750  ELSE
1760   dat(i)=c(i,j)
1770  END IF
1810  lprint_using"x.xx",i;
1820  lprint_using"xxxx.xxx",dat(i)
1830  PRINT£5
1850  loops=loops+1
1860 END FOR i
1870 CLS
1880 PRINT"Do you want to repeat the ";
1890 PRINT"fractionation of the current "
1900 PRINT"magma with new parameters ? ";
1910 INPUT"(Y or N) ? ";frept$
1920 IF frept$="Y" OR frept$="y" THEN
1930  magno=magno-1
1940  mixr
1950 END IF
1960 CLS
1970 PRINT" A new influx may be modelled";
```

```
1980 PRINT"  at a chosen point in the "
1990 PRINT" fractionation path of the ";
2000 PRINT"previous magma, simply by"
2010 PRINT" selecting the appropriate ";
2020 PRINT"value of F from the printed ";
2030 PRINT"output:":PRINT
2040 PRINT" Enter the required F value ";
2050 PRINT"(a value for F>1 will ";
2060 INPUT"terminate the program): ";fval
2070 IF fval>1 THEN STOP
2080 PRINT
2090 PRINT"At F=";fval;" in the previous";
2100 PRINT" magma, the concentrations of";
2110 PRINT" the elements were as ";
2120 PRINT"follows: ":PRINT
2130 FOR i=1 TO noel
2140  PRINT n$(i),cl(fval,i)
2141  clst(i)=cl(fval,i)
2150 END FOR i
2151 mixr
2152 DEFine PROCedure mixr
2160 PRINT£5:PRINT£5
2170 PRINT£5,"New magma intruded at F = ";
2180 PRINT£5,fval;" in previous magma."
2190 PRINT"Complete mixing of the new ";
2200 PRINT"magma with the residual "
2210 PRINT"liquid in the chamber is ";
2220 PRINT"assumed."
2230 PRINT"To calculate an appropriate ";
2240 PRINT"mixing ratio, enter a value "
2250 PRINT"for the new influx as a ";
2260 PRINT"fraction of (new magma + ";
2270 INPUT"residue):";mf
2280 PRINT£5,"Ratio new:old magma: ";mf
2290 FOR i=1 TO noel
2300  mfactor(i)=(cl(fval,i)*(1-mf))
2301  IF frept$="Y" OR frept$="y" THEN
2302   mfactor(i)=(clst(i)*(1-mf))
2303   PRINT£5,"Concentration of ";n$(i);
2304   PRINT£5," in magma ";magno;" at F";
2305   PRINT£5,fval;" is ";clst(i);"ppm"
2306   GO TO 2340
2307  END IF
2310  PRINT£5,"Concentration of ";n$(i);
2320  PRINT£5," in magma ";magno;" at F=";
2330  PRINT£5,fval;" is ";cl(fval,i);"ppm"
2340 END FOR i
2350 CLS
2360 frepeat
2365 END DEFine mixr
9000 REMark ******************************
9010 REMark Simple Rayleigh fractionation
9020 REMark ******************************
9030 DEFine PROCedure rfrac
9040  c(i,j)=ic(j)*(i^((bd(j)-1)))*bd(j)
9050  RETurn c(i,j)
9060 END DEFine rfrac
9070 REMark ******************************
```

```
9080 REMark Equilibrium crystallization
9090 REMark ****************************
9100 DEFine PROCedure eqxtl
9110  fac=ic(j)*bd(j)
9120  c(i,j)=(1/(bd(j)*(1-i)+i))*fac
9130  RETurn c(i,j)
9140 END DEFine eqxtl
9150 REMark ****************************
9160 REMark Orthocumulate fractionation
9170 REMark ****************************
9180 DEFine PROCedure orthfrac
9190  fac=ic(j)*bd(j)
9200  c(i,j)=(i^((bd(j)-1)*(1-x)))*fac
9210  RETurn c(i,j)
9220 END DEFine orthfrac
```

Input and output data for the program MULTIFRACT,
as used in Fig. 33.

Magma No. 1
Orthocumulate fractional xtlization: proportion of intercumulus fluid=.3
Initial concentration of V in new magma = 0ppm
 mixture = 150ppm
Initial concentration of Cr in new magma = 0ppm
 mixture = 250ppm
Crystallizing the following minerals in proportions:
plag = .7; opx = .23; cpx = 7E-2;
Distribution coefficients :
V into plag = 0; Cr into plag = 0;
V into opx = .3; Cr into opx = 2;
V into cpx = 1.5; Cr into cpx = 10;
Bulk D(V)=.174 Bulk D(Cr)=1.16

Fractionating the ratio V/Cr

F	Cs
0.95	0.093
0.90	0.097
0.85	0.101
0.80	0.105
0.75	0.110
0.70	0.115
0.65	0.121
0.60	0.128
0.55	0.136
0.50	0.145
0.45	0.156
0.40	0.169
0.35	0.186
0.30	0.207
0.25	0.234
0.20	0.273
0.15	0.333
0.10	0.441
0.05	0.712

New magma intruded at F = .3 in previous magma.
Ratio new:old magma: .7
Concentration of V in magma 1 at F=.3 is 847.9042ppm
Concentration of Cr in magma 1 at F=.3 is 178.7412ppm

Magma/mixture No. 2
Rayleigh fractionation
Initial concentration of V in new magma = 150ppm
Conc. in mixture = 359.3713ppm
Initial concentration of Cr in new magma = 250ppm
Conc. in mixture = 228.6224ppm
Crystallizing the following minerals in proportions:
plag = .6; opx = .25; cpx = .15;
Distribution coefficients :
V into plag = 0; Cr into plag = 0;
V into opx = .3; Cr into opx = 2;
V into cpx = 1.5; Cr into cpx = 10;
Bulk D(V)=.3 Bulk D(Cr)=2

Fractionating the ratio V/Cr

F	Cs
0.95	0.257
0.90	0.282
0.85	0.311
0.80	0.345
0.75	0.385
0.70	0.432
0.65	0.490
0.60	0.562
0.55	0.651
0.50	0.766
0.45	0.916
0.40	1.119
0.35	1.405
0.30	1.826
0.25	2.489
0.20	3.637
0.15	5.931
0.10	11.817
0.05	38.394

New magma intruded at F = .25 in previous magma.
Ratio new:old magma: .4
Concentration of V in magma 2 at F.25 is 2925.933ppm
Concentration of Cr in magma 2 at F.25 is 11.43112ppm

Magma/mixture No. 3
Rayleigh fractionation
Initial concentration of V in new magma = 200ppm
Conc. in mixture = 1835.56ppm
Initial concentration of Cr in new magma = 300ppm
Conc. in mixture = 126.8587ppm
Crystallizing the following minerals in proportions:
plag = .65; opx = .25; cpx = .1;
Distribution coefficients :
V into plag = 0; Cr into plag = 0;
V into opx = .3; Cr into opx = 2;
V into cpx = 1.5; Cr into cpx = 10;
Bulk D(V)=.225 Bulk D(Cr)=1.5

Fractionating the ratio V/Cr

F	Cs
0.95	2.317
0.90	2.482
0.85	2.670
0.80	2.885
0.75	3.132
0.70	3.420
0.65	3.759
0.60	4.163
0.55	4.651
0.50	5.252
0.45	6.007
0.40	6.981
0.35	8.277
0.30	10.074
0.25	12.711
0.20	16.894
0.15	24.379
0.10	40.883
0.05	98.936

New magma intruded at F = .25 in previous magma.
Ratio new:old magma: .4
Concentration of V in magma 2 at F.25 is 2925.933ppm
Concentration of Cr in magma 2 at F.25 is 11.43112ppm

Magma/mixture No. 3
Orthocumulate fractional xtlization: proportion of intercumulus fluid=.15
Initial concentration of V in new magma = 200ppm
Conc. in mixture = 1835.56ppm
Initial concentration of Cr in new magma = 300ppm
Conc. in mixture = 126.8587ppm
Crystallizing the following minerals in proportions:
plag = .6; opx = .28; cpx = .12;
Distribution coefficients :
V into plag = 0; Cr into plag = 0;
V into opx = .3; Cr into opx = 2;
V into cpx = 1.5; Cr into cpx = 10;
Bulk D(V)=.264 Bulk D(Cr)=1.76

Fractionating the ratio V/Cr

F	Cs
0.95	2.317
0.90	2.482
0.85	2.669
0.80	2.883
0.75	3.129
0.70	3.416
0.65	3.754
0.60	4.156
0.55	4.642
0.50	5.240
0.45	5.991
0.40	6.959
0.35	8.247
0.30	10.033
0.25	12.651
0.20	16.802
0.15	24.223
0.10	40.564
0.05	97.933

ACKNOWLEDGEMENTS

From 1981 to 1983, this project was financed by the Council for Scientific and Industrial Research, initially within the framework of the National Geoscience Programme, but latterly under the auspices of the C.S.I.R. Research Grants Division. During 1984, a temporary lecturing appointment in the Department of Geology at Rhodes University provided financial support. A grant from the Hugh Kelly Foundation financed the strontium isotope analyses incorporated in this thesis.

The management of Johannesburg Consolidated Investment Corporation (J.C.I.) authorized the sampling of surface exploration boreholes SK2 and SK4. In this regard, Drs. M.J. Viljoen and C.A. Lee are particularly thanked for their help in locating the relevant core, and for their advice regarding the sampling thereof. J.C.I. also authorized field visits to R.P.M. Union Section, during the course of which samples were collected, both on surface and underground. The management and staff of Union Section are thanked for their hospitality during these visits. The Mine Chief Geologist, Mr. P.M. Coetzer, and his staff, in particular N.P. Hatch and T. Davis, were instrumental in making these trips worthwhile.

This project was jointly suppervised by Prof. H.V. Eales and Dr. I.M. Reynolds. Prof. Eales, in particular, has read various drafts of this thesis, and his advice and suggestions are reflected in many of the ideas expressed here. Although Dr. Reynolds gave general guidance during the course of this study, his help in the investigation of the Fe-rich ultramafic pegmatites is acknowledged in particular. Other members of staff in the Geology Department at Rhodes University also contributed in various ways. Dr. J.S. Marsh, in particular, is thanked for his assistance, not least for his constructive criticism of early drafts of the manuscript.

Dr. F.J. Kruger, of the Bernard Price Institute, University of the Witwatersrand, performed the strontium isotope analyses, and is thanked for valuable discussions of the results. My fellow research students, particularly R.N. Scoon and M.J. Botha, contributed much by way of discussion.

I am particularly grateful to my wife, Des, for her support and patience during what must have been, for her, a long and tedious process.

REFERENCES

Atkins, F.B. (1969) Pyroxenes of the Bushveld Intrusion, South Africa : J. Petrology, **Vol. 10**, pp. 222-249.

Albee, A.L. & Ray, L. (1970) Correction factors for electron probe microanalysis : Analyt. Chem., **Vol. 42**, pp. 1408-1414.

Barnes, S.J. (1986) The effect of trapped liquid crystallization on cumulus mineral compositions in layered intrusions : Contrib. Miner. Petrol., **Vol. 93**, pp. 524-531.

Bence, A.E. & Albee, A.L. (1968) Empirical correction factors for the electron microanalysis of silicates and oxides : J. Geology, **Vol. 76**, pp. 382-403.

Buchanan, D.L. (1975) The petrography of the Bushveld Complex intersected by boreholes in the Bethal area : Trans. Geol. Soc. South Africa, **Vol. 78**, pp. 335-348.

Buddington, A.F. (1936) Gravity stratification as a criterion in the interpretation of certain intrusives of the northwestern Adirondacks: Rept. 16th Internat. Geol. Congr., Washington, pp. 347-352.

Butcher, A.R. (1985) Channelled metasomatism in Rhum layered cumulates - evidence from late-stage veins : Geol. Mag., **Vol. 122**, pp. 503-518.

Cameron, E.N. (1971) Problems of the eastern Bushveld Complex : Fortshr. Mineral., **Vol. 48**, pp. 86-108.

Cameron, E.N. (1978) The Lower Zone of the eastern Bushveld Complex in the Olifants River Trough : J. Petrology, **Vol. 19**, pp. 437-462.

Cameron, E.N. & Desborough, G.A. (1964) Origin of certain magnetite-bearing pegmatites in the eastern part of the Bushveld Complex, South Africa : Econ. Geol., **Vol. 59**, pp. 197-225.

Cameron, M. & Papike, J.J. (1981) Structural and chemical variations in pyroxenes : Amer. Miner., **Vol. 66**, pp. 1-50.

Cameron, W.E., Nisbet, E.G. & Dietrich, V.J. (1979) Bonninites, komatiites and ophiolite basalts : Nature, **Vol. 280**, pp. 550-553.

Campbell, I.H. (1977) A study of macro-rhythmic layering and cumulate processes in the Jimberlana intrusion, Western Australia, Part 1: The Upper Layered Series : J. Petrolgy, **Vol. 18**, pp. 183-215.

Campbell, I.H. (1978) Some problems with the cumulus theory : Lithos, **Vol. 11**, pp. 311-323.

Campbell, I.H. (1987) Distribution of orthocumulate textures in the Jimberlana Intrusion : J. Geology, **vol. 95**, pp. 35-54.

Campbell, I.H., Roeder, P.L. & Dixon, J.M. (1978) Crystal bouyancy in basaltic liquids and other experiments with a centrifuge furnace : Contrib. Miner. Petrol., **Vol. 67**, pp. 369-378.

Campbell, I.H., Naldrett, A.J. & Barnes, S.J. (1983) A model for the origin of the platinum-rich sulfide horizons in the Bushveld and Stillwater Complexes : J. Petrology, **Vol. 24**, pp. 133-165.

Cawthorn, R.G. (1983) Magma addition and possible decoupling of major and trace element behaviour in the Bushveld Complex, South Africa: Chem. Geol., **Vol. 39**, pp. 335-345.

Cawthorn, R.G., Biggar, G.M., Graham, A., Ford, C.E., Sharpe, M.R. & Davies, G. (1979) Experimental petrological data on the parental magmas of the Bushveld Complex : Inst. Geol. Res. Bushveld Complex, Univ. Pretoria, **Res. Rept. 18**, 17pp.

Coertze, F.J. (1958) Intrusive relationships and ore deposits in the western part of the Bushveld Igneous Complex : Trans. Geol. Soc. South Africa, **Vol. 61**, pp. 387-392.

Coertze, F.J. (1960) Anorthosite emplaced in a shear zone in gabbro of the Bushveld Igneous Complex : Trans. Geol. Soc. South Africa, **Vol. 63**, pp. 75-81.

Coertze, F.J. (1970) The geology of the western part of the Bushveld Igneous Complex : Geol. Soc. South Africa, **Spec. Publ. 1**, pp. 5-20.

Coertze, F.J. (1974) The geology of the basic portion of the western Bushveld Igneous Complex : Geol. Surv. South Africa, **Mem. 66**, 148pp.

Coertze, F.J. & Schumann, F.W. (1962) The basic portion and associated minerals of the Bushveld Igneous Complex north of Pilanesberg : Geol. Surv. South Africa, **Bull. 38**, 48pp.

Cousins, C.A. (1959) Discussion of Feringa, G.; The geological succession in a portion of the northwestern Bushveld (Union Section) and its interpretation : Trans. Geol. Soc. South Africa, **Vol. 62**, pp. 233-236.

Cousins, C.A. (1960) Discussion of Coertze, F.J.; Anorthosite emplaced in a shear zone in gabbro of the Bushveld Igneous Complex : Trans. Geol. Soc. South Africa, **Vol. 63**, pp. 83-84.

Cox, K.G., Bell, J.D. & Pankhurst, R.J. (1979) The interpretation of igneous rocks, George Allen & Unwin, London, 450pp.

Crawford, A.J., Beccaluva, L. & Serri, G. (1981) Tectono-magmatic evolution of the West Phillipine-Mariana region and the origin of bonninites : Earth Planet. Sci. Lett., **Vol. 54**, pp. 346-356.

Daly, R.A. (1928) Bushveld Igneous Complex of the Transvaal : Bull. Geol. Soc. Amer., **Vol. 39**, pp. 703-768.

Davies, G., Cawthorn, R.G., Barton, J.M.Jr. & Morton, M. (1980) Parental magma to the Bushveld Complex : Nature, **Vol. 287**, pp. 33-35.

De Klerk, W.J. (1982) The geology, geochemistry and silicate mineralogy of the Upper Critical Zone of the north-western Bushveld Complex at Rustenburg Platinum Mines, Union Section : Unpubl. M.Sc. Thesis, Rhodes University.

Donaldson, C.H. (1977) Laboratory duplication of comb layering in the Rhum pluton : Min. Mag., **Vol. 41**, pp. 323-336.

Drake, M.J. & Weill, D.F. (1975) Partition of Sr, Ba, Ca, Y, Eu^{2+}, Eu^{3+} and other REE between plagioclase feldspar and magmatic liquid: an experimental study : Geochim. Cosmochim. Acta, **Vol. 39**, pp. 689-712.

Dunham, A.C. & Wadsworth, W.J. (1978) Cryptic layering in the Rhum layered intrusion : Min. Mag., **Vol. 42**, pp. 347-356.

Eales, H.V., Marsh, J.S., Mitchell, A.A., de Klerk, W.J., Kruger, F.J. and Field, M. (1986) Some geochemical constraints upon models for the crystallization of the Upper Critical Zone - Main Zone interval, northwestern Bushveld Complex : Min. Mag., **Vol. 50**, pp. 567-582.

Erlank, A.J., Allsop, H.L., Duncan, A.R. & Bristow, J.W. (1980) Mantle heterogeneity beneath southern Africa: evidence from the volcanic record : Phil. Trans. Roy. Soc. London, **Vol. 297**, pp. 295-307.

Evenson, N.M., Hamilton, P.J. & O'Nions, R.K. (1978) Rare-earth abundances in chondritic meteorites : Geochim. Cosmochim. Acta, **Vol. 42**, pp. 1199-1212.

Ferguson, J. & Botha, E. (1963) Some aspects of layering in the basic part of the Bushveld Complex : Trans. Geol. Soc. South Africa, **Vol. 66**, pp. 259-278.

Feringa, G. (1959) The geological succession in a portion of the northwestern Bushveld (Union Section) and its interpretation : Trans. Geol. Soc. South Africa, **Vol. 62**, pp. 219-232.

Fleet, M.E., Bilcox, G.A. & Barnett, R.L. (1980) Oriented magnetite inclusions in pyroxenes from the Grenville province : Canad. Miner., **Vol. 18**, pp. 89-99.

Frey, F.A., Green, D.H. & Roy, S.D. (1978) Integrated models of basalt petrogenesis: a study of quartz tholeiites to olivine melilites from south eastern Australia utilizing geochemical and experimental petrological data : J. Petrology, **Vol. 19**, pp. 463-513.

Gough, D.I. & van Niekerk, C.B. (1959) A study of the palaeomagnetism in the Bushveld Complex : Phil. Mag., **Vol. 4**, p. 126-136.

Griffin, W.L. & Murthy, V.R. (1969) Distribution of K, Rb, Sr and Ba in some minerals relevant to basalt genesis : Geochim. Cosmochim. Acta, **Vol. 33**, pp. 1389-1414.

Groeneveld, D. (1970) The structural features and the petrography of the Bushveld Complex in the vicinity of Stoffberg, eastern Transvaal : Geol. Soc. South Africa, **Spec. Publ. 1**, p. 36-45.

Hall, A.L. (1932) The Bushveld Complex of the central Transvaal : Geol. Surv. South Africa, **Memoir 28**, 510pp.

Hamilton, J. (1977) Sr isotope and trace element studies of the Great Dyke and Bushveld mafic phase and their relationship to early magma genesis in southern Africa : J. Petrology, **Vol. 18**, pp. 24-52.

Harmer, R.E. & Sharpe, M.R. (1984) Field relations and strontium isotope systematics of the marginal rocks of the Bushveld Complex : Inst. Geol. Res. Bushveld Complex, Univ. Pretoria, **Res. Rept. 50**, 52pp.

Henderson, P. (1982) Inorganic Geochemistry (1st edn.) : Pergammon, Oxford, 353pp.

Hickey, R.L. & Frey, F.A. (1982) Geochemical characteristics of bonninite series volcanics: implications for their source : Geochim. Cosmochim. Acta, **Vol. 46**, pp. 2099-2115.

Hunter, D.R. & Hamilton, P.J. (1978) The Bushveld Complex : In: Evolution of the earth's crust. (D.H. Tarling, ed.), Academic Press, pp. 107-173.

Huppert, H.E. & Sparks, R.S.J. (1980) The fluid dynamics of a basaltic magma chamber replenished by influx of hot, dense ultrabasic magma : Contrib. Miner. Petrol., **Vol. 75**, pp. 279-289.

Huppert, H.E. & Sparks, R.S.J. (1984) Double diffusive convection due to crystallization in magmas : Ann. Rev. Earth Planet. Sci., **Vol. 12**, pp. 11-37.

Irvine, T.N. (1970) Heat transfer during solidification of layered intrusions: 1: Sheets and sills : Canad. J. Earth Sci., **Vol. 7**, pp. 1030-1061.

Irvine, T.N. (1977a) Origin of chromitite layers in the Muskox intrusion and other layered intrusions : Geology, **Vol. 5**, pp. 273-277.

Irvine, T.N. (1977b) Chromite crystallization in the join Mg_2SiO_4 - $CaMgSi_2O_6$ - $CaAl_2Si_2O_6$ - $MgCr_2O_4$ - SiO_2 : Carnegie Inst., Washington, **Ybk. 76**, pp. 465-472.

Irvine, T.N. (1980a) Magmatic infiltration metasomatism, double-diffusive fractional crystallization and adcumulus growth in the Muskox Intrusion and other layered intrusions. In : Physics of magmatic processes (R.B. Hargraves, ed.), Princeton, pp. 325-383.

Irvine, T.N. (1980b) Magmatic density currents and cumulus processes : Amer. J. Sci., **Vol. 280A**, pp. 1-58.

Irvine, T.N. (1981) A liquid-density controlled model for chromite formation in the Muskox Intrusion : Carnegie Inst. Washington, **Ybk. 80**, pp. 317-324.

Irvine, T.N. (1982) Terminology for layered intrusions : J. Petrology, **Vol. 23**, pp. 127-162.

Irvine, T.N. & Smith, C.H. (1967) The ultramafic rocks of the Muskox Intrusion, Northwestern Territories, Canada : In: Ultramafic and related rocks. (P.J. Wyllie, ed.), Wiley, New York, pp. 38-49.

Irvine, T.N., Keith, D.W. & Todd, S.G. (1983) The J-M platinum-palladium reef of the Stillwater Complex, Montana : II. Origin by double-diffusive convective magma mixing and implications for the Bushveld Complex : Econ. Geol., **Vol. 78**, pp. 1287-1334.

Irvine, T.N. & Sharpe, M.R. (1983) Source rock compositions and depths of origin of Bushveld and Stillwater magmas : Carnegie Inst. Washington, **Ybk. 81**, pp. 294-303.

Jackson, E.D. (1961) Primary textures and mineral associations in the ultramafic zone of the Stillwater Complex, Montana : U.S. Geol Surv., **Prof. Paper 358**, 106pp.

Jaupart, C., Brandeis, G. & Allegre, C.J. (1984) Stagnant layers at the bottom of convecting magma chambers : Nature, **Vol. 308**, pp. 535-538.

Klemm, D.D., Ketterer, S., Reichhardt, F., Steindl, J. & Weber-Diefenbach, K. (1985) Implications of vertical and lateral compositional variations across the Pyroxenite Marker and its associated rocks in the upper part of the Main Zone in the eastern Bushveld Complex : Econ. Geol., **Vol. 80**, pp. 1007-1015.

Kruger, F.J. (1982) The petrology of the Merensky Cyclic Unit and associated rocks and their significance in the evolution of the western Bushveld Complex : Unpubl. Ph. D. Thesis, Rhodes University.

Kruger, F.J. & Marsh, J.S. (1982) Significance of $^{87}Sr/^{86}Sr$ ratios in the Merensky Cyclic Unit of the Bushveld Complex : Nature, **Vol. 298**, pp. 53-55.

Kruger, F.J., Cawthorn, R.G., Meyer, P.S. & Walsh, K.L. (1986) Sr-isotopic, chemical and mineralogical variations across the Pyroxenite Marker and in the Upper Zone of the western Bushveld Complex : Geol. Soc. South Africa, Geocongress '86, Extended Abstracts, pp. 609-612.

Kruger, F.J., Cawthorn, R.G. & Walsh, K.C. (in press) Strontium isotopic evidence against magma addition in the Upper Zone of the Bushveld Complex : Earth Planet. Sci. Lett.

Lee, C.A. & Sharpe, M.R. (1979) Spheroidal pyroxenite aggregates in the Bushveld Complex - a special case of silicate liquid immiscibility : Earth Planet. Sci. Lett., **Vol. 44**, pp. 295-310.

Liebenberg, C.J. (1961) The trace elements of the rocks of the Bushveld Igneous Complex: Part II: The different rock types : Univ. Pretoria, **Publ. 13**, 65pp.

Lombaard, A.F. (1949) Die geologie van die Bosveldkompleks langs Bloedrivier :Trans. Geol. Soc. South Africa, **Vol. 52**, pp. 343-376.

Lombaard, B.V. (1934) On the differentiation and relationships of the rocks of the Bushveld Complex : Trans. Geol. Soc. South Africa, **Vol. 37**, pp. 5-32.

Loney, R.A. & Himmelberg, G.R. (1983) Structure and petrology of the La Perouse gabbro intrusion, Fairweather Range, southeastern Alaska : J. Petrology, **Vol. 24**, pp. 377-423.

Marais, C.L. (1977) An investigation of the Pyroxenite Marker and the associated rocks in the Main Zone of the eastern Bushveld Complex : Unpubl. M.Sc. Thesis, Univ. Pretoria.

Markgraaff, J. (1976) Pyroxenes of the western Bushveld Complex : Trans. Geol. Soc. South Africa, **Vol. 79**, pp 217-224.

Marsh, J.S. (1979) A manual for X-ray fluorescence determination of major and trace elements in natural silicate rock materials : Unpubl. Manual, Rhodes Univ., 41pp.

Masuda, A., Nakamura, N. & Tanaka, T. (1973) Fine structures of mutually normalized rare-earth patterns of chondrites : Geochim. Cosmochim. Acta, **Vol. 37**, pp. 239-248.

McBirney, A.R. & Noyes, R.M. (1979) Crystallization and layering of the Skaergaard Intrusion : J. Petrology, **Vol. 20**, pp. 487-554.

McCarthy, T.S. & Cawthorn, R.G. (1980) Changes in initial $^{87}Sr/^{86}Sr$ ratio during protracted fractionation in igneous complexes : J. Petrology, **Vol. 21**, pp. 245-264.

McSween, H.Y. (1980) Mineralogy and petrology of the Dutchman's Creek gabbroic intrusion, South Carolina; reply : Amer. Miner., **Vol. 65**, pp. 1304-1306.

Meyer, G. (1969) Some petrological aspects of the mafic rocks from borehole sections between the Merensky Reef and the Main Zone gabbro in the western and eastern Bushveld Complex : Unpubl. M.Sc. Thesis, Univ. Potchefstroom.

Molyneux, T.G. (1970) A geological investigation of the Bushveld Complex in Sekhukhuneland and part of the Steelpoort valley, eastern Transvaal, with particular reference to the oxide minerals : Unpubl. D.Sc. Thesis, Univ. Pretoria.

Molyneux, T.G. (1974) A geological investigation of the Bushveld Complex in Sekhukhuneland and part of the Steelpoort valley : Trans. Geol. Soc. South Africa, **Vol. 77**, pp. 329-338.

Morse, S.A. (1979) Kiglapait geochemistry I : Systematics, sampling, and density : J. Petrology, **Vol. 20**, pp. 555-590.

Morse, S.A. (1986) Convection in aid of adcumulus growth: J. Petrology, **Vol. 27**, pp. 1183-1214.

Nel, H.J. (1940) The basal rocks of the Bushveld Igneous Complex, north of Pretoria : Trans. Geol. Soc. South Africa, **Vol. 43**, pp. 37-68.

Nesbitt, R.W., Mastins, H., Stolz, G.W. & Bruce, D.R. (1976) Matrix corrections in trace element analyses by X-ray fluorescence: an extension of the Compton scattering technique to long wavelengths : Chem. Geol., **Vol. 18**, pp. 203-213.

Norrish, K. & Hutton, J.T. (1969) An accurate X-ray spectrographic method for the analysis of a wide range of geological samples : Geochim. Cosmochim. Acta, **Vol. 33**, pp. 431-453.

Pankhurst, R.J. (1969) Strontium isotope studies related to petrogenesis in the Caledonian basic igneous province, N.E. Scotland : J. Petrology, **Vol. 10**, pp. 115-143.

Paster, T.P., Schauwecker, D.S. & Haskin, L.A. (1974) The behaviour of some trace elements during the solidification of the Skaergaard layered series : Geochim. Cosmochim. Acta, **Vol. 38**, pp. 1549-1577.

Pearce, J.A. & Norry, M.J. (1979) Petrogenetic implications of Ti, Zr, Y and Nb variations in volcanic rocks : Contrib. Miner. Petrol., **Vol. 69**, pp. 33-47.

Philpotts, J.A. & Schnetzler, C.C. (1970) Phenocryst-matrix partition coefficients for K, Rb, Sr and Ba, with applications to anorthosites and basalt genesis : Geochim. Cosmochim. Acta, **Vol. 34**, pp. 307-322.

Raal, F. (1965) The transition between the Main and Upper Zones of the Bushveld Igneous Complex in the western Transvaal : Unpubl. M.Sc. Thesis, Univ. Pretoria.

Reynolds, I.M. & Scoon, R.N. (1983) The iron-titanium oxide mineralogy of some ultramafic pegmatites from the Critical and Main Zones of the Bushveld Complex : Symposium on the Bushveld Complex (abstr.), Pretoria.

Reynolds, R.C. (1967) Estimation of mass absorption coefficients by Compton scattering: Improvements of the method : Amer. Miner., **Vol. 52**, pp. 1493-1502.

Scoon, R.N. (1985) Discordant bodies of postcumulus, ultramafic rock in the Upper Critical Zone of the Bushveld Complex : Iron-rich ultramafic pegmatite bodies at Amandelbult and the Driekop platiniferous ultramafic pipe :Unpubl. Ph. D. Thesis, Rhodes University, 257pp.

Sharpe, M.R. (1981) The chronology of magma influxes to the eastern compartment of the Bushveld Complex as exemplified by its marginal border groups : J. Geol. Soc. London, **Vol. 138**, pp. 307-326.

Sharpe, M.R. (1985) Strontium isotope evidence for preserved density stratification in the Main Zone of the Bushveld Complex, South Africa : Nature, **Vol. 316**, pp. 119-126.

Sharpe, M.R. (1986) REE and isotopic evidence for multiple parental magmas to the Bushveld Complex. Univ. Pretoria, Inst. Geol. Res. Bushveld Complex, Ann. Rept., 1985/86, pp. 51-62.

Sharpe, M.R. & Irvine, T.N. (1983) Melting relations of two Bushveld chilled margin rocks and implications for the origin of chromite : Carnegie Inst. Washington, **Ybk. 82**, pp. 295-300.

Sharpe, M.R., Irvine, T.N., Mysen, B.O. & Hazen, R.M. (1983) Density and viscosity characteristics of melts of Bushveld chilled margin rocks : Carnegie Inst. Washington, **Ybk. 82**, 301-305.

Smith, J.R. and Larsen, S.B. (1985) Two-dimensional study of a layered intrusion - the Hyllingen Series, Norway : Geol. Mag., **Vol. 122**, pp. 97-124.

South African Committee for Stratigraphy (SACS) (1980) Stratigraphy of South Africa. Part 1 (Comp. L.E.Kent). Lithostratigraphy of the Republic of South Africa, South West Africa/Namibia, and the Republics of Bophuthatswana, Transkei and Venda : Handbk. Geol. Surv. South Africa, **8**.

Sparks, R.S.J. & Huppert, H.E. (1984) Density changes during fractional crystallization of basaltic magmas: Fluid dynamic implications : Contrib. Miner. Petrol., **Vol. 85**, pp. 300-309.

Sparks, R.S.J., Meyer, P. & Sigurdson, H. (1980) Density variations among mid-ocean ridge basalts: implications for magma-mixing & the scarcity of primitive lavas : Earth Planet. Sci. Lett., **Vol. 46**, pp. 419-430.

Sparks, R.S.J., Huppert, H.E., Kerr, R.C., McKenzie, D.P. & Tait, S.R. (1985) Postcumulus processes in layered intrusions : Geol. Mag., **Vol. 122**, pp. 555-568.

Stormer, J.C. (1983) The effects of recalculation on estimates of temperature and oxygen fugacity from analyses of multicomponent non-titanium oxides : Amer. Mineral., **Vol. 68**, pp. 116-594.

Streckeisen, A.L. (1973) Plutonic rocks: Classification and nomenclature recommended by the IUGS subcommission on the systematics of igneous rocks : Geotimes, **Oct. 1973**, pp. 26-30.

Tait, S.R., Huppert, H.E. & Sparks, R.S.J. (1984) The role of compositional convection in the formation of adcumulate rocks: Lithos, **Vol. 17**, pp. 139-146.

Todd, S.G., Keith, D.W., Le Roy, L.W., Schissel, D.J., Mann, E.L. & Irvine, T.N. (1982) The J-M platinum-palladium reef of the Stillwater Complex, Montana. I: Stratigraphy and petrology : Econ. Geol., **Vol. 77**, p. 1454-1480.

Turner, J.S. & Gustafson, L.B. (1978) The flow of hot saline solutions from vents in the sea floor - some implications for massive sulphide and other ore deposits ; Econ. Geol., **Vol. 73**, pp 1082-1100.

Twist, D. (1985) Geochemical evolution of the Rooiberg silicic lavas in the Loskop Dam area, southeastern Bushveld : Econ. Geol., **Vol. 80**, pp 1153-1165.

Van den Berg, J.J. (1946) Petrofabric analysis of the Bushveld gabbro from Bon Accord : Trans. Geol. Soc. South Africa, **Vol. 49**, pp. 144-204.

Van der Merwe, M.J. (1976) The layered sequence of the Potgietersrus limb of the Bushveld Complex : Econ. Geol., **Vol. 71**, pp. 1337-1351.

Vermaak, C.F. (1976) The Merensky Reef - Thoughts on its environment and genesis : Econ. Geol., **Vol. 71**, pp. 1270-1298.

Viljoen, M.J. & Burvenich, T. (1983) Some magnetic stratigraphic anomalies in the Bushveld Complex : Symposium on the Bushveld Complex (abstr.), pp. 88-90.

Viljoen, M.J. & Feuchtwanger, T. (1977) The northern gap area of the B.I.C., results of a thermal scanner survey and a summary of available information : J.C.I. Fundamental Res., **Rept. 65 (unpubl.)**, 14pp.

Viljoen, M.J. & Scoon, R.N. (1985) The distribution and main geologic features of discordant bodies of iron-rich ultramafic pegmatite in the Bushveld Complex : Econ. Geol., **Vol. 80**, pp. 1109-1128.

Visser, J.N.J. (1964) Analyses of rocks, minerals and ores : Geol. Surv. South Africa, **Handbk. 5**, 409pp.

Von Gruenewaldt, G. (1966) The geology of the Bushveld Igneous Complex east of the Kruis River cobalt occurrence, north of Middelburg, Transvaal : Unpubl. M.Sc. Thesis, Univ. Pretoria.

Von Gruenewaldt, G. (1971) A petrographical and mineralogical investigation of the Bushveld Igneous Complex in the Tauteshoogte-Roossenekal area of the eastern Transvaal : Unpubl. D.Sc. Thesis, Univ. Pretoria.

Von Gruenewaldt, G. (1972) The origin of the roof rocks of the Bushveld Complex between Tauteshoogte & Paardekop in the eastern Transvaal: Trans. Geol. Soc. South Africa, **Vol. 75**, pp. 121-134.

Von Gruenewaldt, G. (1973) The Main and Upper Zones of the Bushveld Complex in the Roossenekal area, eastern Transvaal : Trans. Geol. Soc. South Africa, **Vol. 76**, pp. 207-227.

Von Gruenewaldt, G. (1979) A review of some recent concepts on the Bushveld Complex, with particular reference to sulphide mineralization : Canad. Miner., **Vol. 17**, pp. 233-256.

Von Gruenewaldt, G. & Weber-Diefenbach, K. (1977) Coexisting Ca-poor pyroxenes in the Main Zone of the Bushveld Complex : Contrib. Miner. Petrol., **Vol. 65**, pp. 11-18.

Wager, L.R. (1963) The mechanism of adcumulus growth in the layered series of the Skaergaard intrusion : Min³ Soc. America, **Spe. Paper 1**, pp. 73-85.

Wager, L.R. & Brown, G.M. (1968) Layered igneous rocks : Oliver & Boyd, Edinburgh, 588pp.

Wager, L.R., Brown, G.M. & Wadsworth, W.J. (1960) Types of igneous cumulates : J. Petrology, **Vol. 1**, pp. 73-85.

Wager, L.R. & Deer, W.A. (1939) Geological investigation in east Greenland: Part III. The petrology of the Skaergaard intrusion, Kangerdlugssuaq, East Greenland : Meddelelser Om Grønland, **Bd. 105, No. 4**, 343pp.

Wagner, P.A. (1929) The Platinum Deposits and Mines of South Africa : Oliver & Boyd, Edinburgh, 362pp.

Walraven, F. (1985) Genetic aspects of the granophyric rocks of the Bushveld Complex : Econ. Geol³, **Vol. 80**, pp. 1166-1180.

Walraven, F. & Darracott, B.W. (1976) Quantitative interpretation of a gravity profile across the western Bushveld Complex : Trans. Geol. Soc. South Africa, **Vol. 79**, pp. 22-26.

Willemse, J. (1959) The "floor" of the Bushveld Igneous Complex and its relationships, with special reference to the eastern Transvaal : Trans. Geol. Soc. South Africa, **Vol. 62**, pp. 21-83.

Willemse, J. (1964) A brief outline of the geology of the Bushveld Igneous Complex. In : The geology of some ore deposits in southern Africa, Vol. 2 (S.H. Haughton, ed.), Geol. Soc. South Africa, pp. 91-128.

Willemse, J. (1969) The geology of the Bushveld Complex, the largest repository of magmatic ore deposits in the world : Econ. Geol. **Monogr. 4**, pp. 1-22.

Zeck, H.P., Shenouda, H.H., Ronsbo, J.G. & Poorter, R.P.E. (1982) Hypersthene-ilmenite (magnetite) symplectites in coronitic olivine-gabbronorites : Lithos, **Vol. 15**, pp. 173-182.